Exploring Microbial Adhesion Through Targeted Design of Bacterial Probes and Substrates in AFM-based Force Spectroscopy

Dissertation

zur Erlangung des Grades

des Doktors der Naturwissenschaften

der Naturwissenschaftlich-Technischen Fakultät

der Universität des Saarlandes

von

Christian Spengler

Saarbrücken

2018

Tag des Kolloquiums:	07.12.2018
Dekan:	Prof. Dr. Gregor Jung
Berichterstatter:	Prof. Dr. Karin Jacobs
	Prof. Dr. Markus Bischoff
	Prof. Dr. Manfred Radmacher
Vorsitz:	Prof. Dr. Volkhard Helms
Akad. Mitarbeiter:	Dr. Mariusz Radtke

Kurzzusammenfassung

Das Verständnis und die Kontrolle bakterieller Adhäsion ist in vielen Lebensbereichen hoch relevant. Da sich frühere Studien diesen Fragestellungen meist mit klassischen Adsorptionsexperimenten genähert haben, wurden quantitative Messungen der Wechselwirkungen zwischen Bakterien und Grenzflächen bisher nur für eine begrenzte Anzahl von Systemen durchgeführt. In dieser Arbeit wurde deshalb Rasterkraftmikroskopie-basierte Kraftspektroskopie mit Einzelbakteriensonden eingesetzt, um Adhäsionskräfte zwischen Bakterien und verschiedenartigen Oberflächen zu bestimmen. Als Grundlage wurde die Adhäsion von *Staphylococcus aureus* auf sehr gut und sehr schlecht benetzbaren Oberflächen charakterisiert und der Einfluss verschiedener Zellwandmoleküle auf die Adhäsion bestimmt. Mit diesem Wissen wurde eine Methode zur Messung der Kontaktfläche zwischen Bakterien und flachen Oberflächen entwickelt und es wurde gezeigt, dass die Haftkraft eines Individuums nicht von der Größe seiner Kontaktfläche abhängt. Eine Erklärung dafür liefert die Tatsache, dass die Haftfähigkeit heterogen über die bakterielle Zelloberfläche verteilt ist, was durch Experimente auf periodischen Strukturen gezeigt wurde. Auf unregelmäßig strukturierten Oberflächen wurde gezeigt, dass die Stärke der Bakterienadhäsion sensitiv auf nanoskalige Oberflächenrauheiten ist. Außerdem wurde gezeigt, dass sich *Streptococcus mutans* Zellen ihrem natürlichen, oralen Habitat anpassen, indem sich ihre Haftfähigkeit in Speichel erhöht.

Abstract

Understanding and, therewith, controlling bacterial adhesion is highly relevant in many areas of life. Since earlier studies approached these questions mostly with classical adsorption experiments, quantitative measurements of the interactions between bacterial cells and interfaces have so far only been carried out for a limited number of systems. Hence, in this thesis, atomic force microscopy-based single cell force spectroscopy was used to determine adhesion forces of bacterial cells to different types of surfaces. As a basis, the adhesion of *Staphylococcus aureus* cells to very hydrophilic and strongly hydrophobic surfaces was characterized for a high number of individual cells and the influence of certain groups of cell wall molecules on adhesion was determined. With this knowledge, a method for measuring the contact area between bacterial cells and flat surfaces was developed and it was shown that the adhesive strength of an individual cell does not depend on its contact area. This may be explained by the fact that the adhesion capability is heterogeneously distributed over the cell surface, which was shown by experiments on periodically structured surfaces. Irregularly structured surfaces were used to show that the adhesive strength of bacterial cells is sensitive to nanoscale surface roughnesses. Additionally, it was shown that *Streptococcus mutans* cells adapt to their natural oral habitat in terms of an enhanced adhesion capability in a salivary environment.

Contents

Abbreviations

B. subtilis *Bacillus subtilis*

E. coli *Escherichia coli*

P. aeruginosa *Pseudomonas aeruginosa*

P. fluorescens *Pseudomonas fluorescens*

S. aureus *Staphylococcus aureus*

S. carnosus *Staphylococcus carnosus*

S. epidermidis *Staphylococcus epidermidis*

S. mutans *Streptococcus mutans*

AFM atomic force microscope

AOI area of interest

CWA cell wall anchored

EPS extracellular polymeric substances

GlcNAc N-acetylglucosamine

HAP hydroxyapatite

LTA lipoteichoic acid

MC simulation Monte Carlo simulation

MSCRAMM microbial surface components recognizing adhesive matrix molecules

MurNAc N-acetylmuramic acid

OTS octadecyltrichlorosilane

PBP penicillin binding protein

PBS phosphate-buffered saline

PDMS polydimethylsiloxane

PMMA poly(methyl methacrylate)

RMS root mean square

SAM self-assembling monolayer

SCFS single cell force spectroscopy

SEM scanning electron microscopy

SERAM secretable expanded repertoire adhesive molecules

TBS tris-buffered saline

THB Todd Hewitt broth

TSB tryptic soy broth

WLC worm-like chain

WTA wall teichoic acid

XPS x-ray photoelectron spectroscopy

1. Introduction

Bacteria and especially bacterial biofilms are – for numerous reasons and in various fields – of high importance in today's world.

On the one hand, these biofilms can be useful and, therefore, highly welcome. For example, they are essential for daily life applications, such as bioreactors used in wastewater treatment or similar devices [151, 189].

On the other hand, bacterial biofilms can be an undesirable nuisance as they cause problems in industry and medicine [61]. Regarding the latter, biofilms can lead to severe health problems that require lengthy treatments. Especially after implantations, biofilms formed by staphylococci, such as *Staphylococcus aureus* (*S. aureus*) and *Staphylococcus epidermidis* (*S. epidermidis*), often cause commonly termed device-related infections, which are difficult to treat and often require additional surgeries [191, 270].

Hence, the understanding and, therewith, the management of biofilms and their formation are of great interest in many areas of life. The first and most fundamental step in the formation of a biofilm is usually the contact and subsequent attachment of bacterial cells to an interface. As a consequence, one method to prevent the formation or modify the structure of biofilms is the control of bacterial adhesion at interfaces. Therefore, investigating, modeling, and understanding bacterial adhesion – especially of *S. aureus* cells – to solid surfaces is the main objective of this work.

However, in reality, the bacterial cells themselves as well as the environmental conditions, under which adhesion takes places, are highly complex and need to be studied in detail. For example, the bacterial cell wall contains a large number of proteins, by far not all of which are sufficiently characterized in terms of their number or physical properties [70, 71, 113, 193, 231, 264]. Hence, their role in the adhesion process remains unclear to date. As a direct consequence, the size and shape of the actual contact area between bacterial cells and hard surfaces is also unknown. In addition, the natural liquid environment of the cells, such as various body fluids (e. g. saliva, blood), can change properties of the substrates by creating a conditioning layer and/or influencing the metabolism of the cells. While the effect of conditioning layers has been investigated on various types of surfaces [162, 259, 245], the response of bacterial cells to their liquid environment – especially with regard to their adhesion behaviour – has hardly been studied so far. Other important parameters in reality are physical properties of the surface, such as its structure and morphology, which affect both the conditioning layers and the interaction between bacterial cells and substrate. Although numerous studies focused on different aspects of the surface morphology upon bacterial adhesion [136, 198, 282], literature lacks a comprehensive investigation of surface roughness in the nanorange – as it is the case for many surfaces in reality [5] – on the actual adhesion force of *S. aureus* cells.

The present thesis addresses these open questions by reducing the complexity of the system. The technique of choice is atomic force microscope (AFM)-based force spec-

troscopy with single bacterial probes, which enables quantitative measurements of the interactions between bacterial cells and surfaces during the whole process of adhesion (attachment and detachment). In order to investigate cellular properties and environmental parameters relevant for adhesion as described above, the bacterial probe as well as the substrate, are separately modified in a controlled manner.

For the bacterial cells, genetic and chemical tools of modification are used: knock-out mutant cells help to identify certain factors of *S. aureus* cells important for adhesion. In addition, *Streptococcus mutans* (*S. mutans*) cells are enzymatically treated to study the effect of environmental conditions on the adhesion of these cells.

The surfaces are modified in terms of surface energy and topography: by locally varying surface hydrophobicity, the bacterial contact area to flat surfaces is quantified. Periodically structured surfaces are used to identify highly adhesive spots of the bacterial cell. Additionally, nano-roughened surfaces help to elucidate the influence of surface morphologies with sizes typical for many implant materials on the adhesion and viability of *S. aureus* cells.

A great strength of the experimental setup in this work is that different scenarios can be investigated with one and the same bacterial cell. In this way, effects emanating from individual properties of the studied cell can be excluded. Furthermore, a systematic change in the order of the surfaces and conditions examined helps to distinguish general aspects from systematic errors caused by alteration of the bacterial cells.

2. Overview and Connectivity

The present work encompasses eight manuscripts of which five have already been published in peer-reviewed scientific journals. The main objective of these publications is the development of a detailed comprehension of the bacterial adhesion process to various substrates under different conditions.

The publications of **Thewes et al. in *The European Physical Journal E* 2015** (Addendum I) and **Kann et al. in *Analytic Chemistry* 2016** (Addendum II) demonstrate the potential of the experimental method: it is shown that AFM-based force spectroscopy is a versatile tool for the investigation of microorganisms and is in particular powerful in bacterial adhesion studies when using single bacterial cells as force sensors. These two publications form the technical basis for the studies described in the following.

The AFM-based force spectroscopy studies in this thesis have two main focal points: a) understanding the adhesion of bacteria to well-controlled, tailored surfaces and b) characterizing bacterial adhesion in the oral cavity and its typical surrounding (other cells, saliva, teeth). Thereby, the studies in the oral cavity are closer to the natural environment than the cases studied in a). However, the model surfaces in a) are so well characterized that adhesion can be theoretically modeled, since the relevant forces can be calculated (e. g. from the dielectric properties of the materials involved). Furthermore, in a), Monte Carlo simulations describing bacterial adhesion are possible.

ad a): For the experiments presented in the first unpublished manuscript of **Spengler et al.** in Addendum III, the bacterial cells are genetically modified to investigate which groups of cell wall macromolecules are involved in bacterial adhesion to abiotic surfaces.

By locally modifying the surface energies of these abiotic surfaces, the size of the contact area of staphylococcal cells to these substrates is determined and further investigated in the publication of **Spengler et al. in *Nanoscale* 2017** (Addendum IV).

This knowledge about the contact area size can help to interpret the results presented in the second unpublished manuscript of **Spengler et al.** in Addendum V where it is shown that nano-rough surfaces can reduce bacterial adhesion and affect their viability.

Another method of reducing bacterial adhesion is presented in the manuscript of **Lang et al.** (submitted to *Nature Materials*) in Addendum VI: surfaces coated with spider silk proteins inhibit bacterial adhesion and growth while allowing mammalian cells to adhere and proliferate.

ad b): In the publication of **Zeitz et al. in *ACS Applied Materials & Interfaces* 2016** (Addendum VII) a recipe for the production along with a detailed characterization of tailored samples made of hydroxyapatite (HAP) used for important experiments approaching *in vivo* conditions is presented. The corresponding measurements and results on these surfaces using enzymatically modified oral bacteria are presented in the publication

of **Spengler et al. in** *Journal of Molecular Recognition* **2017** (Addendum VIII).

Formally, the thesis is hereinafter divided into the following chapters:

- The chapter **'Background and State of the Art'** introduces the theoretical concepts as well as the organisms important for the thesis and gives an overview of recent findings in the scientific fields covered by the work.

- The chapter **'Material and Methods'** describes the substrates, experimental techniques and ways of data analysis used to understand and reproduce the results of this work. In addition, information is provided on specific materials and modified techniques not listed in the publications.

- The chapter **'Results and Discussion'** condenses the results that are presented in the publications in the addenda, as well as the outcomes of further experiments which are still unpublished. The findings are arranged thematically in three chapters: 'Adhesion Behaviour of *S. aureus* to Flat, Abiotic Surfaces', 'Adhesion to Structured Surfaces', and 'Adhesion in the Oral Environment'.

- The chapter **'Conclusions'** summarizes the results of the presented work and highlights their relevance for and connection to ongoing as well as future projects.

3. Background and State of the Art

3.1 Forces in Biological Adhesion

In nature, there are fundamentally only four forces – or more general, interactions[1]. The *strong interaction* and *weak interaction* are responsible for the stability of atoms because they act between elementary particles inside atoms while *gravity* always attractively acts between all objects with a mass not equal to zero. The remaining force is the *electromagnetic interaction*, which acts between all particles that have – at least temporarily – a (partial) charge or a magnetic momentum. For the this thesis, strong and weak interactions do not play a role since sub-atomic effects are not investigated. Due to the microscopic size of the objects and processes examined, gravity is also negligible.

Therefore, since the electromagnetic force is the only relevant interaction in this work, it makes sense to describe this force in more detail. This section categorizes electromagnetic interactions and presents various facets of the same concepts with special focus on the interactions relevant for the processes in this thesis.

Since all of the following forces – with the exception of chemical bonds – act between different molecules, they are often referred to as **intermolecular forces**.

More details can be found in a variety of textbooks and reviews on this subject, which

---

[1]In this section, no rigorous differentiation between the terms 'force' and 'interaction' will be used, since, most of the time, general aspects and no exact formulas of the terms are described.

form the basis of this section [37, 131, 150, 171, 261].

The text is designed to be easily readable without 'mathematical distractions'. For quantitative formulas, which are supported by calculations fitting experimental values, reference is made in particular to the textbook of J. Israelachvili [131].

As mentioned, *chemical bonds* do not fall in the category of intermolecular forces because they act between atoms and, hence, are responsible for several atoms to form a molecule in the first place. Therefore, here, chemical bonds will be explained rather superficially. Most often, they are divided into three groups: *metallic bonds*, *ionic bonds* and *covalent bonds*.

Metallic bonds are formed when the electrons of the binding atoms are not tightly connected to the atomic kernel but freely mobile, as it is the case in metals. Then, the electrons of many atoms build a negatively charged 'electron sea' around the positively charged atomic kernels of the atoms, and a stable material emerges. Notably, in biological systems, metallic bonds are very rare.

Ionic bonds exist between atoms that exchange electrons to reach a more stable and, therefore, preferred state each. This state is called 'noble gas configuration' and is defined by a certain number of electrons in the outer shell of the atom. So, if one atom has too many outer electrons, and the other atom has the same number of 'missing' electrons, they can exchange their electrons. Afterwards, the atoms have a positive or negative charge, re-

spectively, and are, therefore, attracted to each other, resulting in an ionic bond.

In contrast, when two atoms form a covalent bond, they do not exchange electrons but 'share' one or more electrons to reach a more favorable state. Therefore, covalent bonds are – unlike ionic bonds – always directed. Inside organic molecules, such as proteins or the bacterial cell wall, covalent bonds are the dominant form of interaction [27].

3.1.1 Hydrogen Bonds

Sometimes, hydrogen bonds are also counted among chemical bonds, but, in contrast to chemical bonds that act between atoms, hydrogen bonds act between different molecules and are, therefore, presented individually here.

If a hydrogen atom is covalently bound to an atom of high electronegativity, the resulting molecule has a partially positive charge near the hydrogen atom and a partially negative charge near the other atom. If two of these atoms – of the same or of different kind – come close together, the partial charges attract each other, and a hydrogen bond is formed. Classically, the difference in electronegativity needed for a hydrogen bond to form is only present when the involved hydrogen atom is bound to an oxygen, nitrogen or fluorine atom, but also other functional groups such as isocyanides and carbon monoxide can act as hydrogen bond donors or acceptors [4].

Hydrogen bonds are the reason for the cohesion of water, where every molecule has in average 3.5 (from four theoretically possible) hydrogen bonds to neighboring water molecules [19]. Additionally, water molecules can form hydrogen bonds to surfaces or immersed particles.

3.1.2 Van der Waals Forces

In literature, the term *van der Waals forces* is used variably. For this thesis, all forces that emerge from molecular dipoles – regardless of the dipoles' origins – are termed van der Waals forces.[2] The dipoles can have different origins resulting in different names for the subcategories of van der Waals forces: if two permanent dipoles interact, van der Waals forces are often termed *Keesom interactions*. If a permanent dipole induces a second dipole, the interactions are called *Debye interactions*. Finally, if two interacting dipoles form due to thermal fluctuations inside molecules, this is called *London (dispersion) interaction* [164].

Van der Waals interactions are present between all bodies and are always attractive. Nevertheless, if two objects interact through a medium, it can appear that the objects repel each other, because the interaction between one body and the medium is stronger than the interaction between the two bodies themselves.

In general, two different ways of calculating van der Waals potentials are common: the *Hamaker approach* and the *Lifshitz approach*. In the Hamaker approach, van der Waals forces are assumed to be additive, and, therefore, forces between two objects can be calculated as the sum of all forces between atoms and molecules of the objects [105]. However, in general, the assumption of pairwise additivity of van der Waals interactions is not valid and, therefore, not applicable to all systems. In this case, the Lifshitz approach could be more suitable. There, van der Waals forces are calculated by macroscopic properties, such as dielectric functions and refractive indices of the interacting objects [158]. However, for com-

---

[2]In some textbooks, the term van der Waals forces is solely used for interactions involving permanent dipoles while interactions resulting from fluctuating dipoles are called London dispersion forces.

plex systems, such as e. g. bacteria, a complete set of optical properties may be hardly accessible.

The distance dependency of van der Waals forces is strongly dependent on the geometry of the interacting objects: while the interaction potential for two atoms in a distance d is proportional to d^{-6} and, therefore, very short-ranging, the potential between an atom and a (half-infinite) surface is proportional to d^{-3}. The potential for a sphere interacting with a surface scales with d^{-1} and can be assumed to be rather long-ranging.

Van der Waals forces have been shown to influence biological adhesion and adsorption of objects that differ in size by several orders of magnitude [102, 166, 168].

3.1.3 Electrostatic Double Layer Forces

Due to its high dielectric constant, water is a good solvent for ions. Therefore, different objects – may they be flat surfaces or differently shaped particles – in liquids often exhibit surface charges [37]. The origin of these charges is twofold: either ions leave the surface into the solution or they bind to the surface stemming from the solution. Then, the charges attract counter ions from the solution, and, consequently, the commonly termed *double layer* emerges.

One of the first calculations of the electric double layer was done by Gouy and Chapmann for planar surfaces and later by Debye and Hückel for spherical objects [63, 97, 43]. In these studies, several assumptions are made: ions in the diffuse part bear a unit charge, resulting in a homogeneous charge distribution. The polar medium is a symmetrical electrolyte and affects the double layer only through its dielectric constant [37, 216].

In the calculations, counterions in solution are subject of thermal motion, and the Poisson-Boltzmann equation relates charge density and electric potential distribution. This leads to sufficiently good results under certain conditions.

However, this theory bears certain weaknesses. For example, the finite size of ions is neglected. Additionally, it is a mean field theory, disregarding the discrete nature of a charge. Furthermore, non-coulombic interactions, such as the hydration shell, are neglected. Also, assuming the solvent to be continuous with a homogeneous permittivity is not adequate for high electric fields. Moreover, surfaces are assumed to be molecularly flat which is certainly wrong for real situations [37, 216].
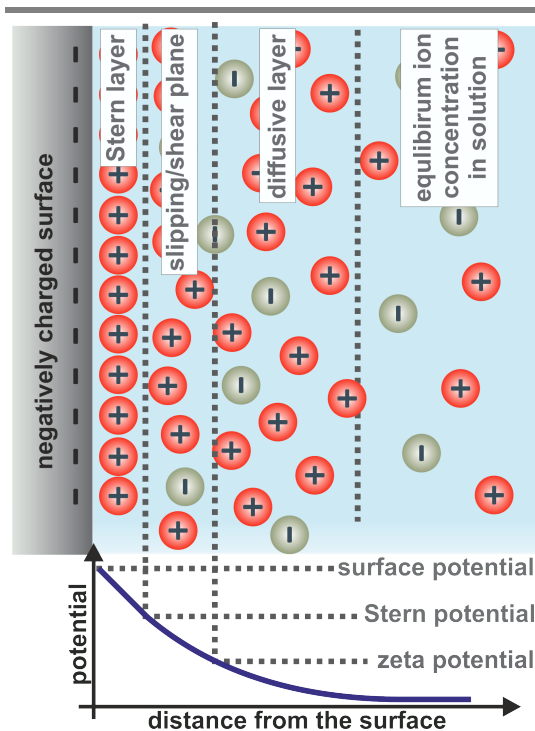
Figure 3.1. The electric double-layer (see text for details).

Stern overcomes the weaknesses of the Gouy-Chapmann model by introducing an immovable bound layer of counterions directly at the surface at a distance of an ionic diameter, as shown in Figure 3.1 [144, 237]. After this layer, another layer of more loosely bound ions follows. The end of this layer is called slipping or shear plane [144].[3] It is also the location of the Zeta potential. There, hydrodynamic motion perpendicularly to the surface and also rotation start being possible. At larger distance to the surface, a diffusive layer of ions is followed by the equilibrium ion concentration in the solution.

Inside the Stern layer, the potential decays linearly and afterwards exponentially. The decay length is called *Debye length*, which is solely dependent on the properties of the solvent, such as temperature, ionic strength, and dielectric constant [131].

Under physiological conditions, – which are present for all experiments in this work – the Debye length can be calculated to be in the order of 10 nm [37, 150].

However, if two objects with electrical double layers come close enough, their potentials can overlap and the objects feel what is called a double layer force. This force is essentially different from simple Coulombic forces due to the presence of ions in the medium that can screen the field of the surface [37]. The strength of these forces is – similar to the van der Waals forces (see Paragraph 3.1.2) – dependent on the geometry of the objects [150].

There were several improvements of the Stern layer concept taking into account more properties of the charged particles and the solvent, which will not be discussed here [30, 52,

98, 174]. Also, in recent works, it was possible to measure double layer forces in detail by surface force apparatus or AFM [90, 205].

3.1.4 DLVO Theory

The DLVO theory – named after Derjaguin, Landau, Verwey and Overbeck [65, 265] – combines the ideas of the electrostatic double layer forces and the van der Waals forces by adding both potentials (see Figure 3.2).
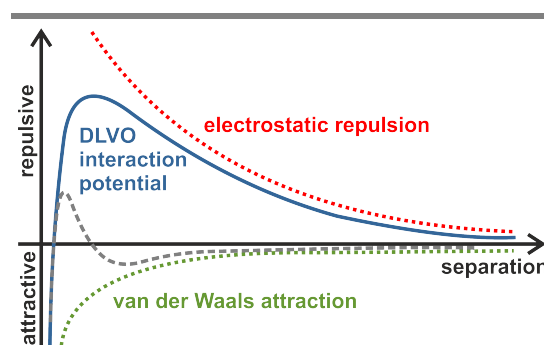
Figure 3.2. The DLVO potential: the blue line gives the sum of the electrostatic potential (here: red, repulsive) and the van der Waals potential (here: green, attractive). The gray line shows how the resulting potential can change for varying ion concentrations or different surface charges.

Depending on different properties of the objects and the solutions, the shape of the resulting potential may differ. However, there is almost always a minimum near the surface, but there can also be a secondary energy minimum at a certain distance from the surface (see gray dashed line in Figure 3.2).

Of note, the classic DLVO theory only considers long-range interactions and neglects short-range contributions. To overcome this weakness, the extended DLVO theory (xDLVO theory) was developed and accounts for short range electron-donor/electron-acceptor inter-

---

[3]Some studies and textbooks neglect the shear plane and define the Zeta potential at the end of the Stern layer. Although not correct in general, it can – depending on the system and surface charge – give good results.

actions, which summarize Lewis acid-base interactions [155] and osmotic interactions [260, 262]. These interactions are often orders of magnitude stronger than classic DLVO forces, but decay much faster in space. Therefore, the extended theory gives for certain systems much better results. However, since the experimental systems in this thesis feature – like most biological systems – a high complexity and inhomogeneity, simple equations for these interactions cannot be formulated.

3.1.5 Hydrophilic and Hydrophobic Interaction

Hydrophilic repulsion and hydrophobic attraction are two forces in water that cannot be explained by the DLVO theory. They have been measured decades ago [124, 132], but are still under heavy investigation and controversially discussed today [69, 72, 107, 242].[4]

To get a simple molecular picture of what might cause these interactions, the following scenario shall be considered: whenever a solvent (not necessarily water) is brought in small confinement, short ranged forces are present. In that case, the solvent cannot be assumed continuous anymore and its molecular character comes into play [150, 131]. As a consequence, – depending on the solvent and the properties of the surfaces confining the molecules – forces arise that cannot be explained by van der Waals or electrical double layer interactions at small separations [131]. Hence, these forces are termed *structural forces* or *solvation forces*.

There are several theories explaining the origin of these forces in general for different

molecules in confinement. They all have in common that the molecules near interfaces have to order themselves into layered structures and that the ordering gives – calculated for the most simplified case of spherical particles between flat surfaces in two dimensions – rise to a potential oscillating with distance to the surface between repulsion and attraction [37]. The periodicity of the oscillations are the molecules' sizes while the envelope of the oscillations is decaying exponentially. Thereby, the total range and the decay length depend on various properties of the solvent.

In the case of water, the situation is even more complicated: water cannot be treated as a simple solvent of spherical molecules, but rather as a complex H-bonded network, and arising forces must be – at least partially – attributed to effects of polar cohesion [261]. Nevertheless, also water molecules can undergo ordering effects near interfaces, a fact that has been experimentally confirmed [238]: while, at hydrophilic surfaces, the molecules can form H-bonds with the surface (for example, in the case of silicon oxide, with free OH-groups), this is not possible at hydrophobic surfaces. As a consequence, near a hydrophilic surface, a stable molecular surface-bound layer emerges. At a hydrophobic surface, however, the molecules reorient so that one of their OH-vector points perpendicular and the other parallel to the surfaces in such a way that each molecule has to 'sacrifice' only one H-bond [238].

Consequently, many publications and textbooks described the hydrophilic repulsion and the hydrophobic attraction as a special case of a structural force in water, sometimes even with the help of *depletion forces* [150], that will be introduced later. However, many experiments that found interactions of different

---

[4]The fact that the interaction was and is not fully understood becomes especially evident by its often used notion as *hydrophobic effect*, a term that was originally used for the immiscibility of hydrophobic substances in water, a purely entropic effect [131, 143].

strengths and distance dependences led to more possible explanations. In his famous textbook, Israelachvili mentioned three of them [131]: '*vapor bridges* due to the attractive capillary (Laplace pressure) force between bridging nanoscopic bubbles; *water structure* as an attraction solvation (hydration) force associated with changes in the density or ordering of water between two approaching hydrophobic surfaces; and *electrostatic*, as an attractive electrostatic van der Waals-like force between correlated charges or dipoles at the surfaces.'

Of note, the existence of a rather long-ranged hydrophobic interaction caused by sub-micron bubbles, is doubtful and is often attributed to non-homogeneous hydrophobicities due to very sensitive surface preparation techniques. Rather, a short-ranged hydrophobic interaction may cause the formation of these bubbles which than cause capillary forces between solids they are attached to [48, 69, 72].

The rest of this paragraph focuses on the forces that arise when the solvent is water. Therefore, general geometric arguments, as described above, are neglected and the force is traced back to the network of water molecules and is assumed to be hydrogen bond driven [261].

This way, the description and possible explanation of the hydrophilic repulsion and hydrophobic attraction are based on a recent publication by Donaldson et al. [69]. In their work, one single potential is introduced that is able to describe both situations, only differing in the sign in the otherwise same equation, in which the interaction potential decays exponentially.

The current understanding, described in the paper, is that an inherent hydrophobic interaction has a range of 10–20 nm with a decay length of 0.3–1 nm, a statement that is cor-

roborated by a variety of experiments (for example measured by dynamic AFM or surface force apparatus [107, 242]). Surprisingly, the hydrophilic repulsion is exactly in the same range, which has been experimentally determined many times (for example, measured between strongly hydrophilic silica sheets [124]).

The fact that the shape and strength of the potential is suitable for both (hydrophilic and hydrophobic) cases, leads the authors to the conclusion that its origin must be attributed to an inherent property of the water network and seems to be hydrogen bond driven. Pure structural forces or depletion forces seem unlikely because some studies did not find a depleted density directly at a hydrophobic interface at all [42], or the range of the ordering is much smaller than the measured interaction distance [238].

For the hydrophilic case, the explanation of the situation appears to be rather clear [69]: it 'appears due to the confinement of hydrated ions or thermally mobile protrusions and the hydration of such moieties, with the decay length and/or [...] magnitude being positively correlated with the size and coverage of the ions or protrusions.'

In the case of the hydrophobic interaction, the situation remains less clear, and possible explanations could be the following [69]: '[...] we hypothesize that the longer-ranged nature of the force is due to long-range correlations from dipolar, angular, or proton-hopping correlations among water molecules confined between hydrophobic surfaces. This hypothesis is supported by recent theoretical calculations that show a similar functional form for the hydrophobic interaction.' Indeed, in the mentioned theoretical work, it is found by analysis of MD simulations that dipole correlations can exhibit a long-range behaviour [140].

10

To conclude this paragraph, it is to say that there are, without doubt, interactions in water that cannot be explained by the DLVO theory. They are repulsive between hydrophilic and attractive between hydrophobic objects. Most probably, these interactions are of very short range and originate from different effects that are all caused by the character of liquid water as a hydrogen bond driven cohesive network. These effects are by far not completely understood and remain subject of present and future studies.

3.1.6 Steric Forces and Born Repulsion

To prevent objects from getting infinitesimally close to each other, a – very general – repulsion has to act at small distances. This repulsion is most often called *steric interaction* or *Born repulsion*.[5] The interaction is a direct consequence of the Pauli principle, stating that two electrons – or more generally, two fermions – cannot be in the same quantum state [197].

Therefore, strictly speaking, this interaction is not intermolecular, but 'inter-subatomistic' with a quantum-mechanic origin. Nevertheless, it is introduced here because it adds an important term to the overall intermolecular potential.

To date, no general equation for the distance dependence of the Born repulsion exists. Three most common, more or less empirical, dependences are the *hard core potential* (zero for separations above a critical distance and infinite below that distance), an inverse power law, or an exponentially decaying potential [131].

In the 'Lennard-Jones potential', the born repulsion is most often accounted for by a term

proportional to $1/r^{12}$ [138, 152].[6] This has practical reasons because, in this case, the repulsive part of the potential is proportional to the square of the attractive part which scales with $1/r^6$.

3.1.7 Specific Interactions

In many studies, specific interactions are considered as very strong interactions of unknown or almost 'magical' origin [261]. Of course, this is not true, and, – also in these systems – the same forces as described above have to act. The remarkable strength of these forces is often a consequence of the very good geometrical fit between the two (or more) interaction bodies (*lock-and-key*, *ligand-receptor*, *dock, lock and latch* [200], *collagen hug* [161]) and the amplifying effect of several non-specific forces acting simultaneously. In medicine, for example, specific interactions are especially important for the detection of drug-targets [129]. However, they differ markedly for varying systems and are, therefore, not discussed in detail here.

3.1.8 Entropic Forces

Entropy is a fundamental quantity in statistical physics, which is connected to the number of a system's *microstates* [87, 149, 244]. Simply put, a microstate is a unique microscopic configuration of the system. The probability of finding the system in a specific microstate is identical for all possible microstates. In other words, all possible microstates are (energetically) equivalent. The intrinsic reason for a

---

[5]Also, the terms hard 'core repulsion' or 'exchange repulsion' can be found in literature [131].

[6]As value for the exponent, 12 is the most common choice, but it can also be smaller up to 6 [131]. For example, in dewetting experiments, it was shown that a term proportional to $1/r^8$ is able to describe the repulsive part of the potential for thin polymer films on silicon surfaces with different oxide layer thicknesses [224].

system to change its microstate is its temperature, which causes thermal fluctuations.

A *macrostate*, in contrast, is a more general property of the system. Every possible macrostate of the system can be represented by a different number of microstates. It holds that, a macrostate that is represented by more microstates has a higher entropy than a macrostate represented by rather few microstates.

The Second law of thermodynamics states that, in a closed system, entropy cannot decrease and, therefore, forces exist that drive the system into an – in terms of entropy – more favorable state [51]. These forces are called *entropic forces*. It is worth mentioning, that these forces do not drive the system into an energetically more favorable state and are, therefore, of distinctly different origin than classical forces.

In the following paragraphs, three examples of entropic forces relevant for the thesis are given.

Entropic Steric Repulsion

It can be observed that covering dispersed particles with polymers can stabilize the dispersion by hindering flocculation and simultaneously increase the solutions osmotic pressure by creating a repulsive force [84, 271].

The reason for this observation is *entropic steric repulsion* of the particles, or more exactly, of their polymeric coating: the surface polymers undergo thermal fluctuations, whose free available space is reduced when the particles come too close to each other. Therefore, the number of possible configurations of a certain macrostate would decrease and the dispersion's entropy would lower. Consequently, in order to prevent this, an entropic repulsive force between the particles occurs. The force-distance dependence is a quantity of the spe-

cific system, but can usually be described by an exponentially decaying potential [37, 131].

Depletion Forces

It was found that the interaction of small dispersed particles is influenced by other dissolved molecules although there is no direct interaction between the particles and the dissolved molecules [14, 15].

The reason for this is a force commonly referred to as *depletion force*: when the distance between two particles is in the range of or smaller than the size of the dissolved molecules, these molecules cannot enter the space between the particles. Consequently, their free accessible volume and, along with that, the entropy decreases. The result is an attractive force between the particles with a range of the diameter of the dissolved molecules. The strength of the force can be calculated by the osmotic pressure of the molecules in the solution.

Entropic Restoring Force in Polymers

When a polymer is stretched, restoring forces emerge that can be explained by the polymer's tendency to increase its entropy.

The polymer can, in a simple model, be assumed as an *ideal chain* (also termed *freely-jointed chain*). In this case, the polymer's monomers are considered as rigid rods of a fixed length, which can move freely at their bonds and do not interact with each other. This means that their position and orientation is completely independent of the state of all other monomers. Therefore, the polymer's configuration is equivalent to a random walk caused by Brownian motion [188].

In this model, the state of the whole polymer can be related to a value of entropy which is,

in the simplest case, represented by its end-to-end-vector [208]. The state represented by the most configurations is obviously the state when the end-to-end-vector equals zero.

Consequently, this 'coil' is the state of highest entropy. Analogously, the case of a completely stretched polymer is represented by only one configuration making it the state with the highest entropy. Hence, whenever the polymer is stretched, an entropic force occurs that drives it to a more coiled state. In a first approximation, the restoring force can be assumed linear, which is why polymers are often termed *entropic springs*.

A more sophisticated model, relatively well suitable for stiffer polymers, is the commonly termed *worm-like chain model* [175, 277]. In this case, the monomers are considered as isotropic rods that are continuously flexible. The force-elongation dependence cannot be determined analytically, but there are approximations that resemble the numerically derived solution quite well for small as well as for large forces [175].

In this thesis, the macromolecules in the bacterial cell wall can be, simply put, considered as polymers with restoring forces of entropic origin.

3.2 Bacteria

A very general way to categorize life on Earth is to divide it into three domains, namely eukaryots, archea, and eubacteria, of which the latter are the subject of this thesis.

Eubacteria are single cells that lack a nucleus and several cell organelles, but have a cell wall made of peptidoglycan. For reasons of simplicity – although not entirely correct[7] – they will be hereinafter referred to as bacteria.

The easiest way to classify bacteria is by their shape: there are rod-shaped cells (with differences in their symmetry or shape at the end of the rod), spiral-shaped cells, comma-shaped cells (vibrons), and spherical cells. The latter are the organisms studied in this thesis, called cocci. They can be further classified by the way the cells aggregate as diplococci (in most cases, two cells clustering), streptococci (a chain of cells), and staphylococci (bunchy clusters of cells).

Another important property to differentiate bacterial cells, especially when investigating their adhesion properties, is based on their cell wall and the response to a certain staining technique [99]: while gram-negative cells have a thin peptidoglycan layer between an outer and an inner membrane, gram positive bacteria do not have an outer membrane, but a much thicker layer of peptidoglycan (see Section 3.3).

This section provides a short overview about the bacteria and their properties used for the experiments in this thesis. More detailed descriptions and explanations can be found in various textbooks, e. g. [39, 122, 185, 219].

---

[7]The kingdom of archae also includes bacteria, which have several distinct differences from eubacteria, e. g. cell walls lacking peptidoglycan.

3.2.1 Staphylococci

Staphylococci[8] are spherical bacteria that form bunchy colonies because they divide along varying axes. They are gram-positive and include more than 40 different species. Most of these species are coagulase-positive, meaning they produce enzymes that promote fibrin formation. The two representatives of this genus used for the experiments in this work are *S. aureus* and *Staphylococcus carnosus* (*S. carnosus*) presented in the following paragraphs.

Staphylococcus aureus

S. aureus[9] is a yellow/goldish pigmented, amotile representative of the genus *Staphylococcus*. The species is maybe the most prominent representative of this genus because it is responsible for many infections and severe diseases, such as skin/wound infections, sepsis, toxication, endokarditis, or pneumoia.

S. aureus is part of the 'normal' microflora in humans [280]: it can be found in about half of the population's nasopharrygeal areas, of which 20–25 % are colonized permanently. By contrast, 20 % of the population are never colonized [263]. The carriers have an increased risk to develop an infection caused by *S. aureus* [269] while the risk to have an infection with severe consequences is reduced among them [278]. Currently, methicillin-resistant variants of *S. aureus* are the predominant hospital-acquired pathogens [119, 142, 145].

Staphylococcus carnosus

S. carnosus[10] was found in dry sausage and firstly described in 1982 [222]. It is nowadays used as a meat starter culture due to several of its functions in the ripening of dry sausage [21, 157, 182]: it reduces nitrate to nitrite [186] and then partially further to ammonia [187].

S. carnosus shares a comparably low DNA sequence homology with *S. aureus* and other staphylococci and lacks most of the mobile genetic elements found in pathogenic stapylococcal species. Consequently, it does not produce toxins, haemolysins, protein A, coagulase, or clumping factors typical for many *S. aureus* strains [272] (see Paragraph 3.3.3).

Because of the mentioned properties, *S. carnosus* is, in this work, often used as a counterpart or 'negative control' to pathogenic bacterial cells.

3.2.2 Streptococci

Streptococci[11] are gram-positive, spherical bacteria that divide along one single axis and, therefore, grow in chains or pairs. In this thesis, one pathogenic representative of this genus, namely *S. mutans*, has been used.

Streptococcus mutans

S. mutans was originally isolated from human carious teeth by J. K. Clarke in 1924 [50] and later completely described by A. L. Coykendall [56].

It is thought to be the most important perpetrator of caries in humans [104, 163]. *S. mutans* cells have a variety of virulence factors that are among others responsible for the growth of oral pellicles. The cells build extracelullar glucans

---

[8]Greek *staphyle*, grape.
[9]Latin *aureus*, golden.

[10]Latin *carnis*, meat.
[11]Greek *streptos*, easily bent.

from sucrose in bolus helping the cells adhering to enamel [36].

Additionally, *S. mutans* degrades carbohydrates to lactic acids, which results in a drop of pH value, causing demineralization of teeth [36]. The cells themselves, in contrast, can sustain very acidic milieus by the active secretion of protons [36].

3.3 The Bacterial Cell Wall

In this work, only gram-positive bacteria were studied. Therefore, this section focuses on the cell wall of gram-positive bacterial cells, which is markedly different from gram-negative ones. For the latter, the reader is referred to specific textbooks [122, 219].

The cell wall of gram-positive bacteria is a highly complex and dynamic structure, including several different constituents. In total, the cell wall can make up to 70 % of the cell's entire mass. The main features are shown in Figure 3.3: the outer part of the cell is built by one large molecule called peptidoglycan being separated from the cell-interior by a lipid-membrane. Bound to the peptidoglycan, there are wall teichoic acids (WTAs) and intercalated to the cell membrane there are lipoteichoic acids (LTAs). At different locations, a variety of proteins can be found. They are either strongly bound or loosely attached and can have different properties and functions [227]. The main constituents of the cell wall will be further explained later in this chapter.

The bacterial cell wall has several functions, such as forming the shape of bacteria, acting as a permeability barrier (in both directions), hosting virulence factors, and – most importantly for this thesis – making contact to surfaces.

It has been found that the cell wall shows a certain spatial heterogeneity, which may be caused by stochastic processes in gene expression and cell division [40, 38]. Similar effects may manifest in the emergence of adhesion nano-domains in fungi [8].

3.3.1 Peptidoglycan

Peptidoglycan (also termed murein) is a polymer and the main component of the bacterial cell wall. It envelops the whole cell body as one giant macromolecule, often referred to as sacculus [73]. Peptidoglycan is only observed in bacteria, meaning that no other organism is able to produce this type of macromolecule.

It consists of two single sugars, N-acetylglucosamine (GlcNAc) and N-acetylmuramic acid (MurNAc). These chains are usually 10–100 disaccharide units long and, therefore, way too short for enveloping the whole cell. Hence, the cell wall consists of many of these chains that are cross-linked by oligo peptides with a length of three to five amino acids that can vary between different species (e. g. l-alanine, d-alanine, l-lysine, d-glutamine acid, meso-diaminopimelic acid) [122]. They bind to the carboxyl group of GlcNAc and cross-link between each other.

In gram-positive cells, the peptidoglycan can be up to 40 layers thick (15–80 nm) [122]. Besides this first level of cross-linking depicted in Figure 3.3, there is also a higher level cross-linking between the chains in different directions [268]. One group of proteins responsible for the second order cross-linking are the penicillin binding proteins (PBPs).

A lack in one specific representative of these proteins, namely PBP4, leads to a reduced stiffness of the cell wall [167]. Furthermore, the absence of certain other proteins causes delocalization of PBPs and, therefore, negatively influences cell size regulation in *S. aureus* [139]. Of note, methicillin-
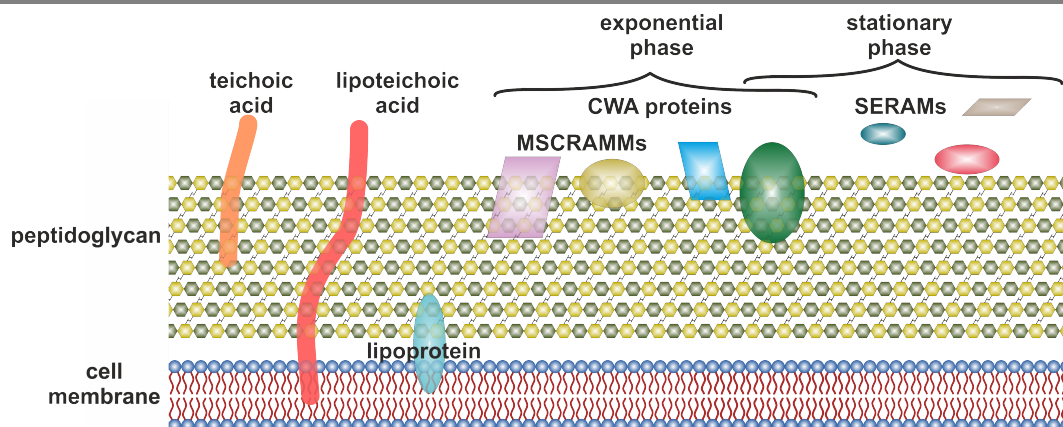
Figure 3.3. The cell wall of the gram-positive bacterium *S. aureus* (after [33]).

resistant strains of *S. aureus* distinguish themselves from methicillin-susceptible strains by the presence of an additional penicillin binding protein, PBP2A [110, 62].

A decreased cell wall stiffness is also essential for cell enlargement (for example, immediately after cell division) and reached by peptidoglycan hydrolases [279]. Also, cell division itself is dependent on peptidoglycan architecture and its properties determined by several additional proteins [17, 32, 255].

3.3.2 Wall Teichoic Acids and Lipoteichoic Acids

In general, teichoic acids are glycopolymers, firstly discovered in 1958 [12]. While LTAs are linked to the cell membrane by hydrophobic interactions, WTAs are covalently bound to the cell wall's peptidoglycan. The genes responsible for the latter are called *tag* (*teichoic acid glycerols*) genes, which can be knocked-out to investigate the influence of WTAs on different processes [34].

About 10 % of the MurNAc residues of peptidoglycan have an attached WTA of 40 to 60 polyol repeats. Hence, WTAs can make up to 60 % of the cell wall mass [34].

Teichoic acids have various tasks in the bacterial cell wall [283]: for example, they are temporal and spatial regulators of peptidoglycan cross-linking in *S. aureus*, play an important role in cell shape determination, and are required for some resistances in *S. aureus* [16, 26, 34, 199].

WTAs form a dense network of negative charges where the attachment of d-alanine residues is an important mechanism by which the bacterial cell controls its cell wall charge [34, 241].

WTAs and most LTAs reach through the cell wall and are exposed to the exterior and, therefore, participate in adhesion as it will be shown in this thesis [276, 284, 217].

3.3.3 Proteins

The bacterial cell wall contains a large number of proteins (studies found over 400 different types [70, 71, 113, 193, 231, 264]) whereby one certain protein can fulfill multiple functions, and where many functions are fulfilled by different proteins simultaneously. By far

not all of these proteins are sufficiently characterized. This means that for many proteins, especially, their role in the adhesion process remains unclear to date.

In general, it is difficult to provide numbers for the prevalence of certain individual proteins because – similar as other cell wall molecules – proteins are not equally distributed over the cell envelop but rather form clusters [76].

Because they are most relevant for the thesis at hand, this paragraph focuses on proteins of *S. aureus* [195]. One way to categorize the proteins is by the time in the cell cycle when the are expressed [169]. In exponential growth phase, most proteins relevant for adhesion are produced. A big group of them is the family of *microbial surface components recognizing adhesive matrix molecules (MSCRAMM)*, but also many other cell wall anchored (CWA) proteins that are covalently linked to the cell wall are expressed in this stage [53, 82]. In the stationary phase, expression of most CWA proteins is turned down, while the production of another group of adhesion molecules, the *secretable expanded repertoire adhesive molecules (SERAM)*, is enhanced.

In the following, some important members of the different groups and their main properties and functions are shortly presented. In literature, more detailed reviews can be found that focus on different aspects, such as e. g. on the quantification of proteins' interaction forces [89, 117, 135].

One CWA protein is Protein A, which can bind to several ligands by different binding mechanisms and can, thereby, cause inflammations, endovascular infections and endocarditis [89].

Another CWA protein from the MSCRAMM family is clumping factor A (ClfA, 90–100 kDa), which binds to ligands by the dock, lock and latch mechanism and

is an important adhesin and immune evasion factor [89] while Clumping factor B (ClfB, 120–130 kDa) is more important for colonization and can successfully bind to fibrinogen or fibrin [11, 91] but also to cytokeratin and loricrin [286]. The fibronectin binding protein A (180–220 kDa) is one of the main adhesion factors that can – besides fibronectin – also bind to elastin and fibrinogen and promotes blood clots [11, 29]. As an important invasion factor [10], it induces a zipper-like phagocytosis [2, 252].

The iron-regulated surface protein (IsdA, 30 kDa) is part of the iron acquisition of the cell and can bind to heme and several other ligands [251]. The *S. aureus* surface protein G (SasG, 190 kDa) plays an important role in biofilm formation because it binds to the extracellular matrix and, therefore, also promotes cell-cell aggregation [94]. A similar task is fulfilled by the biofilm associated protein b (Bap, 256 kDa), which is only found in bovine isolates and very sensitive to the cell's calcium level [13].

Some proteins from the SERAM family that play a role in adhesion are, for example, the fibrinogen binding protein A (FbA, 34 kDa), coagulase (Coa, 60–70 kDa), the von Willebrand factor binding protein (vWbp, 66 kDa), and the extracellular adherence protein (Eap, 60–70 kDa) [44]. It has been shown that SERAM proteins are secreted to the extracellular environment and can partially rebind to the cell surface and, therefore, have a big influence on adhesion [202]. The von Willebrand factor binding protein adheres best under high shear flow and, by this, induces fibrin clot formation in damaged endothelium which is important for wound closure [49, 249]. The extracellular adherence protein fulfills many functions, such as adhesion to epithelial cells [93] where it can promote internalization [101, 106], and ef-

fects migration as well as proliferation of these cells [35, 77].

3.4 Bacterial Biofilms

Biofilms, in general, are aggregates of microorganisms together with extracellular substances that form on virtually all interfaces [75]. This way, biofilms develop properties that make them the most abundant and successful form of life on Earth. Therefore, since the discovery of the concept of biofilms by Henrici and Zobell in the 1930s [114, 288], they have been heavily studied by many researchers. Consequently, many detailed reviews exist [86, 103, 165, 177], and only a short overview about some properties of biofilms is given here.

Biofilms can be formed by different organisms, such as bacteria, fungi, algae and archaea [177]. Usually, more than one species can be found, but most often bacteria dominate in biofilms. The focus of this section is on bacterial biofilms. They can form on many different types of interfaces, such as the solid-liquid, liquid-liquid, solid-gaseous, liquid-gaseous interface, and, as a consequence, on virtually every place on Earth. This makes them important for many different fields of life.

On the one hand, biofilms can be beneficial. For example, one can find them on ants where they exist in symbioses with the animal and serve as a protection against environmental influences [59]. Moreover, biofilms can be used to recover metals [31], or for wastewater treatment [189]. Today, biofilms are also often a key component of bioreactors where they have various beneficial functions [151].

On the other hand, in many places biofilms can be unwanted and cause problems. For example, biofilms are often found on ship hulls where they amplify hydrodynamic friction and, therefore, heavily increase fuel consumption

[61]. In many pipes, the formation of biofilms is a big problem because they reduce flow rates and are hard to remove [223]. Biofilms produced by the bacteria studied in this thesis are especially relevant in medical fields because they can form inside the human body, for example, on artificial surfaces, such as all kinds of implants and catheters, but also on natural surfaces, such as teeth or mucosals. Inside the human body, infectious biofilms are often the origin of severe diseases, commonly termed *device related infections* [54, 55, 103, 211].

A fully developed biofilm offers the embedded cells protection against antibiotics, disinfectants, host's immune defense, pH-extremes, high salt concentrations, hydraulic stress, toxic metal ions, desiccation, biocides, and even ultraviolet radiation [86, 103]. This explains why biofilms are such a big problem, for example on implants: when an infectious biofilm is formed, the only way to remove it, is often a surgery to replace the implant. Even if the strain *per se* has no resistance against antibiotics, their use may not be successful against a mature biofilm, probably due to the presence of a subpopulation of cells called persisters. Recent studies even show that the formation of biofilms can be fostered by low levels of some antibiotics [141]. The benefits for the bacteria in a biofilm go even further: the involved cells can have a high potential to adapt to external conditions (nutrient supply) by genetic regulation and selection and, therefore, develop new phenotypes even more successful in colonization [218].

The bacterial lifestyle in a biofilm is essentially different from the situation in a planctonic state: because of the favorable environments, the cell density in a biofilm can be 1,000–10,000 times higher than in free liquid phase [54]. This is possible because – despite being a close aggregation of individuals

– diffusion coefficients of many dissolved substances are comparable to their diffusion coefficients in the aqueous phase [85].

Besides living organisms, 50–90 % of the biofilm's mass consist of extracellular polymeric substances (EPS) [86]. The EPS build a matrix that has a locally varying density and is made of polysaccharides, proteins, nucleic acids, and lipids [86].[12] These components are the debris of dead cells or actively produced by the living organisms [177]. The EPS matrix is responsible for the retention of extracellular enzymes and other cell ingredients, for example, DNA being used as an adhesin [86, 266].

The formation of biofilms can be divided into different steps. The exact number of these steps as well as precise borders between them are not clearly defined, but are, in general, the following (see Figure 3.4): it starts with a surface contact of the bacterial cells [196]. Then, the cells adhere firmly and start to produce extracellular substances. After a certain time of growth and differentiation, often termed as maturation phase, a dispersal of cells occurs, for which three strategies exist: *swarming/seeding dispersal*, *clumping dispersal*, *surface dispersal* [103].

One method to prevent or modify biofilms is the understanding and control of bacterial adhesion to interfaces, which is the focus of this work. General aspects of bacterial adhesion will be briefly discussed in the following section, inspired by different textbooks (e. g., [159]).

---

[12]Also, humic substances can be found in some biofilms, that are not subject of this thesis [86]

3.5 Bacterial Adhesion

3.5.1 Specific Mechanisms

If the substrate on which bacterial adhesion takes place is already covered by certain types of molecules (most often proteins), several characteristic and additionally so-called *specific interactions* between the bacterial cell and the substrate can be observed.

With the help of force-distance curves recorded with single cells or single molecule force spectroscopy, many very characteristic interactions between different molecules can be identified [7, 120]. For example, an 'unzipping' of proteins results in force-distance curves with a characteristic force plateau of non-zero force [9]. By the shape of force distance curves, it is also possible to differentiate between the existence and rupture of single or multiple bonds [257].

Some proteins have specific mechanisms that allow them to preferentially interact with proteins of the very same kind; such interactions are called *homophilic* interactions and have been found in some types of bacteria [116]. Another specific mechanism is the *dock, lock and latch* mechanism that involves conformational changes in the proteins to increase the interaction area between binding partners [200]. The *collagen hug* is an example between the collagen binding protein and a collagen covered surface [161]. In some cases, specific bonds can be strengthened by externally acting forces: for example, in *catch bonds*, the receptor–ligand complex deforms under certain values of external forces in a way that strengthens the binding. Therefore, the bond's lifetime increases under flow conditions (see Figure 3.5) [64, 230].

As mentioned, these mechanisms and interactions only occur between specific inter-
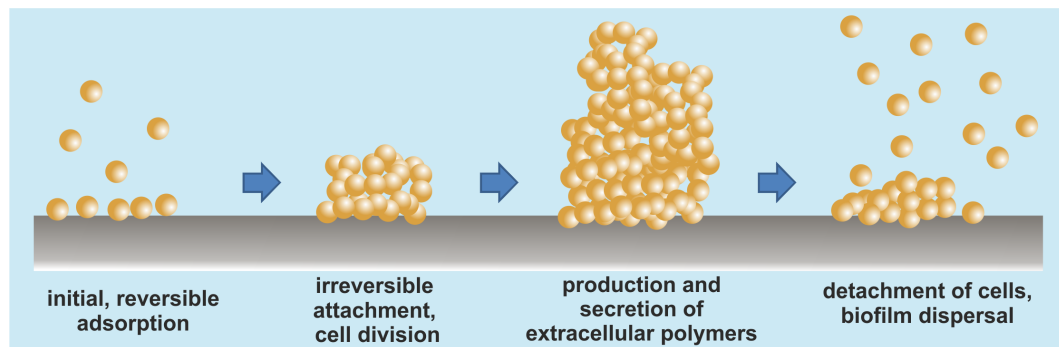
Figure 3.4. Growth of a bacterial biofilm.
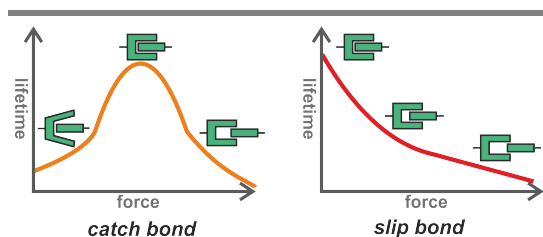
Figure 3.5. The catch bond mechanism (sketch adapted from a figure by Sokurenko et al. [230]): an external force increases the lifetime of the bond by 'tightening' the bond's configuration (left). In contrast, classical *slip bonds* weaken continuously under increasing external forces (right).

action partners that are located on the bacterial cell wall (or, for some studies, directly coated on the cantilever) and on the studied substrate. As a consequence, for the thesis at hand mostly dealing with abiotic or uncoated surfaces, these interactions are not of predominant importance.

3.5.2 Modeling Bacterial Interaction With Flat Surfaces

Since bacteria are no simple hard spheres, but rather 'living patchy colloids' [267], several quite elaborate models of bacterial adhesion have been published recently.

Since biofilms were found to have viscoelastic properties, this concept was also transferred to the contact of single bacterial cells to solid surfaces [210]. However, for rather quick attachment and detachment processes, as the case in most force spectroscopy measurements with single bacterial cells, the viscous part of the contact can be neglected [256, 167].

Considering the bacterial cell made of different layers with differing elastic properties, Chen et al. developed a promising model of the adhesion process to hard, flat surfaces [47]: the contact between cell and surface is solely established by a cylinder of constant volume that deforms under external load. In this model, for different amotile bacterial strains[13], the contact almost always solely exists between the surface and a rather soft outermost layer of the bacterial cell that is said to consist of proteinaceous surface appendages or extracellular polymeric substances [47]. With the help of this model, long-range bacterial adhesion forces can be explained by van der Waals interactions, whose strength increases along with an enlargement of the contact area between cell and surface upon increasing loading forces [46].

---

[13]The studied cells did not have flagella to initiate adhesion.

The strength of this model is the consideration of a certain inhomogeneity of the bacterial cell wall. However, the drawback of the model is that this heterogeneity is limited to the radial direction of the spherical cell. In-plane inhomogeneities, such as clusters of adhesins in the cell wall, or different mechanical properties or lengths of single proteins in the cell wall are not considered at all. One reason for the fact that, in their experiments, Chen et al. do not observe effects of the properties mentioned above could be attributed to their way of preparing bacterial probes: the bacteria, already immobilized on the cantilever, are dried for two minutes, which is likely to alter the proteinaceous cell wall layer and change its original properties, such as heterogeneity in several aspects [47, 46]. This might also explain why no cell-individual adhesion behaviour is observed.

A very detailed model was introduced by Thewes et al.: the bacterial cell is modeled as a hard (incompressible) sphere[14] that is decorated with a large number of springs symbolizing adhesion mediating macromolecules [248]. These springs have randomly distributed spring constants, lengths, and also random positions on the surface of the sphere. The process of adhesion is described by thermal fluctuations of these springs, which can bind to the surface via a square potential as soon as their ends come close enough to the substrate. As the cell approaches the surface, the probability of having more binding molecules increases. If the number of adhering molecules is large enough, the overall restoring force of the molecular springs is strong enough to 'pull' the cell body to the surface, even without further external actuation ('snap-to-contact'). In this

way, experimental force-distance curves can be reproduced in Monte Carlo simulations (MC simulations) for approach and retraction of the cell [248].

Another strength of the Model by Thewes et al. is the fact that it can simulate specific force-distance curves that were obtained by thoughtfully designing the experiment: instead of approaching the bacterial cell to the surface until a positive force (i.e. an 'upward' deflection of the cantilever because the cell is pressed onto the surface) is reached, the cantilever is retracted already at a certain negative force during the 'snap-to-contact'. This way 'partitioned force-distance curves' can be recorded which can be reproduced with high accuracy in MC simulations using the model of Thewes et al. [248].

A similar model was developed and studied by Ostvar et al.: the bacterial cell wall is considered to have a certain roughness that accounts for differing lengths of surface molecules. This roughness was approximately determined by AFM measurements to be in the range of 10–20 nm [194]. In the model, the surface molecules are represented by polymers that can either behave like Hookean springs or according to the worm-like chain (WLC) model. At the end of each spring, a bead is located that can directly bind to the surface via a Lennard-Jones potential. Upon retraction, every single polymer can either unbind by the bead escaping the potential or the polymer itself can rupture. With the help of this model, retraction parts of experimental force-distance curves obtained with *S. epidermidis* cells on glass could be reproduced [194, 45].

Both of the latter models have their specific advantages: the model of Thewes et al. is capable of exactly reproducing approach (especially the 'snap-to-contact') as well as retraction parts of force-distance curves and ac-

---

[14]The validity of this assumption is supported by measurements showing the elastic modulus of the cells being in the MPa range [167].

counts for several mechanical properties of cell wall macromolecules [248]. The model of Ostvar et al. uses a more realistic surface potential and considers the surface macromolecules not only as springs but rather as polymers with non-linear energy functions [194].

Nevertheless, there is plenty of room for improvements of those models: for example, the macromolecules fluctuate in the models – if at all – only in one dimension while, in reality, they probably explore the complete three-dimensional space. Implementing more degrees of freedom in the models seems not to be necessary for describing adhesion to smooth substrates, but it may important to understand and model contact formation and breaking on rougher surfaces. As a consequence, interactions between different molecules when they come close to each other during thermal fluctuations at the bacterial cell wall might also become relevant for future, more accurate models.

Additionally, more experimental details such as experimentally determined mechanical properties of cell wall macromolecules or their density and inhomogeneity (for example, in the division plane) should be considered to improve the models in the future.

Another important aspect in model improvement is to estimate the number of interacting surface macromolecules. For this purpose, the exact knowledge about the cell wall area that is in contact with the surface seems to be an important step to improve the model. Furthermore, this knowledge is essential to include substrate parameters such as surface roughness into the model for being able to describe adhesion to non-ideal surfaces.

A first step in the direction of estimating the properties and, especially, the number of tethering cell wall macromolecules was taken by Thewes et al. [246]: thereto, the above described model of Thewes et al. was modified in a way that the tethering surface macromolecules were not to be considered as simple springs but as ideal polymers. To account for the spatial extend of real cell wall polymers, a minimum length l_0 was defined, below that, a polymer chain causes repulsion according to Hooke's law with a spring constant according to the Gaussian approximation for small extensions of ideal polymers [208]. If the polymer is stretched above the threshold length l_0, the potential energy w is calculated according to the WLC approach [175]. Concretely, the energy w of the polymers is given in units of $k_b T$ with Boltzmann constant k_b and temperature T as follows:

$$w(l) = \begin{cases} \frac{(l-l_0)^2}{b}\left(\frac{1}{M} + \frac{1}{2(M-(l-l_0))}\right) & \text{if } l < l_0 \\ \frac{3}{2Mb}(l-l_0)^2 & \text{if } l \geq l_0 \end{cases},$$

where M is the contour length and b the *Kuhn length* of the polymer. Besides M and b, the polymer surface density and the depth of the square binding potential are free parameters of the model. The threshold length l_0 was chosen to be $2 \cdot \sqrt{b \cdot M/6}$, which is twice radius of gyration of an ideal linear polymer [208].

With this model, it was possible to achieve a very good match between simulated curves and experimental curve for both, hydrophobic and hydrophilic, surfaces (see Figure 3.6). To do so, contour lengths were chosen uniformly distributed between 60 nm and 300 nm as well as Kuhn lengths uniformly distributed between 0.072 nm and 0.36 nm. The only parameters in the model that differed for hydrophobic and hydrophilic surfaces were the depth of the binding potential (that had a range of 3 nm) and the density of polymers on the surface of the sphere (that had a radius of 500 nm). To re-

22
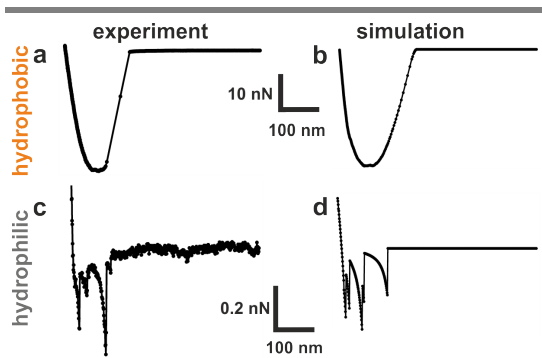
Figure 3.6. Retraction parts of representative force-distance curves that were experimentally obtained on a hydrophobic (a) and a hydrophilic (c) surface compared to curves simulated according to the improved model from N. Thewes with a high protein density ($3.2 \cdot 10^{-2}\,\mathrm{nm}^{-2}$) and low depth ($-18\,k_b\mathrm{T}$) of the binding potential (b) and a low protein density ($2.2 \cdot 10^{-5}\,\mathrm{nm}^{-2}$) and large depth ($-54\,k_b\mathrm{T}$) of the binding potential (d). Figure slightly adapted from Reference [246].

produce the curves on hydrophilic surfaces, a protein density of $3.2 \cdot 10^{-2}\,\mathrm{nm}^{-2}$ (one polymer per $31.3\,\mathrm{nm}^2$) and a potential of $-18\,k_b\mathrm{T}$ was used. On the hydrophilic surfaces, the density was $2.2 \cdot 10^{-5}\,\mathrm{nm}^{-2}$ (one polymer per $4.5 \cdot 10^4\,\mathrm{nm}^2$) and potential was $-54\,k_b\mathrm{T}$. In other words, on hydrophobic surfaces about three orders of magnitude more polymers bind due to a factors of three weaker potential as on hydrophilic surfaces.

So far, the improved model cannot be considered to be quantitatively exactly true because only a limited number of parameters have been studied by MC simulations. In general, it seems hardly possible to achieve 'completeness of the model' in near future because physical properties of bacterial cells and its surface polymers as input for the MC simulations are still largely unknown.

Nevertheless, the model is able to reproduce the fundamental shape of force-distance curves on hydrophobic and hydrophilic surfaces. Therefore, it seems that at least one very general aspect can be deduced from the improved model: on hydrophobic surfaces, much more molecules contribute to bacterial adhesion than on hydrophilic surfaces. This single fact, will be important for the interpretation of more data obtained from a systematic statistical analysis of the adhesion of *S. aureus* cells on flat hydrophobic and hydrophilic surfaces (see Chapter 5) [246].

3.5.3 Experimental Techniques to Investigate Bacterial Adhesion

'Traditional' methods to investigate bacterial adhesion are mainly adsorption experiments in well plates or flow chamber measurements.

In well plate adsorption experiments, the surfaces of interest are inserted into typical well plates and 'brought in contact' with bacterial solutions. Thereby, the bacteria are either immersed in pure buffer or even in nutrient where they are allowed to divide and actively colonize the surfaces. After a certain 'incubation time', the surfaces are taken out of the wells and rinsed to detach non-adsorbed cells. In a last step, the bacteria are visualized by optical microscopy, and their number in a certain area is counted. This way, a large number of individual cells can be investigated simultaneously, but the procedure – especially the step of rinsing the surface – is rather 'uncontrolled' since the force acting on single cells can only be estimated.[15]

In the flow chamber, a bacterial solution with a given concentration (usually achieved by adjusting the optical density) is flushed over a surface of interest. By a good choice of the

---

[15]For spherical cells, the force exerted by the three phase contact line was estimated to be in the range of $10^{-7}\,\mathrm{N}$ per cell [96].

chamber's geometry and flow rates, a laminar flow profile can be achieved. After a certain time, the number of attached cells in a certain area is recorded by optical microscopy with or without staining. Some studies intentionally fill the flow chamber with air and let the three-phase contact line travel over the surface to detach weakly bound cells before counting the final number of bacteria. In the flow chamber setup, the adsorption process of individual cells seems to be more controlled compared to adsorption processes in well plates. Additionally, adhesion kinetics can be recorded by imaging the surface over time. Also, the rinsing or flushing of the surface is more controllable: either a high flow rate can be used to detach weakly bound bacteria, or a single air bubble can be flushed trough the chamber with constant, adjustable speed.

Nevertheless, while both methods mentioned above can collect data of large numbers of cells simultaneously, they are not able to precisely measure or control forces acting on individual cells. To achieve such a high force control, common methods are optical tweezers [81, 287] or AFM [74]. While both methods, have essentially the same advantages in terms of precise force and position control, the latter has – to address the questions in this thesis – fewer requests on the system itself. Therefore, AFM-based force spectroscopy with a single cell bacterial probe is the method of choice to investigate adhesion properties of individual bacterial cells in this thesis. Of note, – because it is only possible to investigate one specific cell at a time – this method needs a certain number of single experiments to gain enough statistics to draw conclusions about general properties of a specific bacterial species.

3.5.4 Substrate Properties Influencing Bacterial Adhesion

In literature, there many studies that investigate which parameters of abiotic surfaces influence bacterial adhesion. Here, some of them are reviewed with focus on the substrates properties related to the studies and results of this thesis. Note, that these results have mostly been achieved on 'clean' surfaces and can be superimposed by other effects such as protein layers on top of the surfaces.

Substrates Stiffness

While the effect of substrate's stiffness is well-investigated for eucaryotic cells [78, 79, 67], there is only a limited number of studies concerning bacterial adhesion.

It is reported that the adhesion of *S. epidermidis* and *Escherichia coli* (*E. coli*) is positively correlated with the stiffness ($\approx$ 1, 10, 40, and 100 MPa of Young's modulus tested) of polyelectrolyte multilayer thin films [156]. Also, the growth of *E. coli* biofilm colonies is faster on softer ($E = 30$ kPa) than on stiffer ($E = 150$ kPa) polyelectrolyte multilayers [215].

Song et al. used polydimethylsiloxane (PDMS) of different stiffness (achieved by different degrees of cross-linking) and found that stiffer surfaces promote bacterial adhesion and growth, while simultaneously decreasing the antibiotic susceptibility of *E. coli* and *Pseudomonas aeruginosa* (*P. aeruginosa*) [232].

Contact Angle and Surface Energy

On a molecular scale, considering bacterial adhesion solely governed by the tethering of cell wall macromolecules to the substrate, the adhesion of *S. aureus* (and other gram-positive species) is dominated by hydrophobic interac-

tions [23, 240, 247]: the lower the molecular surface energy, the stronger and more numerous are single bonds, and the stronger is the overall adhesion force of the whole cell.

In contrast to these observations, several studies claim that surface energy and especially so-called *super-hydrophobicity* reduces bacterial adhesion [80, 203, 243]. Of note, the experiments in these studies do not measure actual adhesion forces in liquid medium. Rather, the effect of surface properties on the retention of bacteria after incubation for a certain time in bacterial solution is investigated. The observed super-hydrophobicity in these studies is achieved by imposing a certain roughness on the hydrophobic surfaces. Therefore, it is rather a macroscopic property and not present on a microscopic level where tethering of cell wall macromolecules occurs.

The effect of surface roughness on bacterial adhesion and retention will be discussed in more detail in the following paragraphs.

Surface Structure and Roughness

One important aspect influencing bacterial adhesion is the topography or morphology of the underlying surface. Concerning this parameter, it is of high importance to identify typical length scales of the surface morphology and put them in relation to the cell size, which is for most bacteria in the range of one to a few micrometers. When studying the influence of surface topography, it can be discriminated between surfaces with regular – and often intentionally produced – structures and surface on which the structures are rather random.

Regular Structures and Surface Patterns
There are a number of studies investigating the effect of surface structures of different sizes for many different types of bacteria. Here, a short overview about recent studies will be presented, starting with the smallest regular structures.

It was shown for *Pseudomonas fluorescens* (*P. fluorescens*), a $0.5–1.0 \times 1–3\,\mu m$ rod-shaped gram-negative bacterium, that the cells order themselves along the offered grooves when placed in channels of approximately 900 nm in depth and width made of different metals [66]. A similar effect was observed for *S. aureus*, *E. coli* and *P. fluorescens* in grooves of $0.5–4\,\mu m$ in width [170]. Additionally, it was observed that, in total, less cells adhere to these structures, especially when the pattern size was smaller than the cell size [170]. Very similarly, *P. aeruginosa* and *E. coli* order according to small posts (height $\approx 2\,\mu m$, width $\approx 0.3\,\mu m$) that are placed at distances of $0.9–4\,\mu m$ on polymer replicas [121]. For *E. coli* and *P. aeruginosa* among others, on patterned silica and alumina surfaces with pattern sizes of $1–2\,\mu m$, besides the already mentioned ordering, also changes in cell morphology were observed [125].

The largest structures that initiate ordering of cells (*E. coli*, *Bacillus subtilis* (*B. subtilis*), *S. epidermidis*) seem to be trenches and squares of $5–10\,\mu m$. There, also a reduced adhesion in total was observed [198].

Even on surfaces that are not densely covered with small obstacles, bacteria prefer these obstacles and adsorb with regard to the structures. This was recently shown for nickel pillars of different geometry with a size of about 500 nm and distances of about $10\,\mu m$ for *S. aureus* cells [136].

Of note, in all of the above mentioned studies, the effect of surface morphology was investigated in a way that the bacterial cells were allowed to freely adsorb to the substrates (sometimes followed by further cell division), and then, the number of cells and their dis-

tribution on the surface were recorded. The recorded patterns and even the change in morphology were most often attributed to the goal of maximizing the contact area between cell and surface. This way of investigation is different from the experiments in this thesis where the force present between cells and the surface after contact formation is measured.

For the sake of completeness, very large grooves (10–40 μm) on PDMS perpendicular to the flow direction in a flow chamber experiment show that *P. aeruginosa* and *P. fluorescens* adsorb preferentially at the downstream edges of the grooves [220]. Because of the large difference in the sizes of surface structures and cells, a preferred adsorption on specific edges would most likely not be found under static conditions.

Randomly Structured Rough Surfaces

In 2000, it was found on steel surfaces that the adhesion behavior of streptococci was independent of the surface roughness in the range of 0.5 to 3.3 μm [88]. In the following years, especially titanium was used to investigate the influence of surface roughness in more detail.

Several studies found that the adhesion of *S. aureus*, *P. aeruginosa* and *E. coli* is weaker on rougher surfaces. In these works, root mean square (RMS) surface roughnesses were in the range of 0.7 to 12 nm[16] [133, 204, 254].

If the differences in mean roughness are much larger (6 nm compared to 830 nm), an opposite effect can be observed for *S. epidermidis* on titanium [282]. In contrast, when comparing roughnesses below 1 nm on titanium, different studies found no correlation between the roughness and the adhesive

---

[16]For comparison: a mirror-polished high quality Si wafer exhibits an RMS roughness below 0.2 nm.

strength, but this was also dependent on the studied type of bacteria [134, 253].

Similar to the results mentioned above, Singh et al. found that the adhesion capability of *S. aureus* and *E. coli* cells on titanium and its oxides shows a maximum for varying roughness: it rises with increasing roughness for RMS values below 20 nm and drops with increasing roughness above 20 nm (measured up to 33 nm) [228, 229].

A recent study on nano-structured PDMS with RMS roughnesses between 12 nm and 36 nm found again less adhesion on rough surfaces, and this effect was much more pronounced for *S. aureus* than for *E. coli* [160].

Again, these experiments did not measure the actual force needed to separate the cells from the surface but studied the adsorption behavior of the cells from solution to the surfaces. Also, some of these studies neglect the chemical characterization of the surfaces (for example, the oxide layer thickness for metal substrates) before and after roughening. Therefore, the observed effects may be the superposition of changes in surface morphology and chemistry.

To conclude this section, there is a need for studies addressing the influence of roughness arising from structures smaller than the bacterial cells [22] on the actual strength of adhesion in terms of adhesion forces or adhesion energies.

3.5.5 Adhesion in the Oral Cavity

According to the German Federal Statistical Office, the costs of dentures in Germany in 2015 were about 7.4 million Euros. Probably, the largest part of these costs was caused by diseases initiated by bacteria in the oral cavity.

The bacteria unfold their harmful potential by attaching to surfaces in the oral cavity and

the consecutive formation of biofilms. During their metabolism, the cells produce different acids that lower the pH value either in the complete oral cavity or only in restricted areas close to their adsorption site, which can lead to typical carious infections [112]. When sufficiently large parts of the tooth material are degraded, it cannot be refilled naturally and medical treatments, such as fillings or dentures, are inevitable.

The origin of caries is the fact that HAP, the mineral component of teeth, which accounts for up to 95 % of the tooth mass, demineralizes at a pH value of around 5.5 or less [60, 176]. That means that if the pH value, even if only locally, drops below that limit, teeth start to degrade steadily [112]. Of note, not only caries but also other, more directly life-threatening infections such as endocarditis or meningitis can be caused by bacteria from the oral cavity [1, 180].

Consequently, the adhesion of bacteria in the oral cavity is of great interest in medicine and healthcare and is, therefore, often studied by dentists [108]. Thereby, the adhesion to real teeth and typical implant materials has been investigated: for example, it has been found that biofilms on dental titanium are influenced by topography and hydrophobicity of these surfaces [6]. Moreover, strategies to inhibit bacterial adhesion on artificial tooth surfaces using polymeric coatings were recently proposed [58].

An often overlooked aspect is that, *in vivo*, bacteria in the oral cavity are exposed to many conditions specific for this environment. For example, they are in permanent contact to saliva. This natural body fluid is of great complexity and involves a variety of different components [154]. Of them, proteins are the main organic component of saliva whereas many of them have different functions (*multifunctional-*

ity), and many functions are covered by different proteins (*functional redundancy*) [154].

The adhesion of different salivary proteins to HAP has been studied for a long time, and specific binding domains of certain proteins could be identified [137]. Not only for HAP, but also for dental implant materials, protein adsorption has been investigated as a function of different parameters, such as pH value, surface hydrophobicity, or contact time [184, 183]. For some model proteins, also the competition in adsorption between different proteins and their mutual interference on dental titanium could be shown [273]. The presence of these proteins is likely to have an influence on bacterial adhesion to oral surfaces as it also has been shown for other substrates and conditioning films [162, 245].

Thereby, it has to be differentiated between (free) salivary components in the liquid phase and (pre-)adsorbed proteins on the surfaces of relevance. In reality, of course, most often, both conditions are present at the same time: the bacterial cells in saliva interact with free proteins while other proteins adsorb to the surfaces.

The effect of adsorbed proteins on bacterial adhesion has been investigated in detail: for example, it has been discovered that a certain protein called P1 adhesin, of *S. mutans* specifically binds to salivary agglutinin, a conditioning film of different salivary components [240]. It was also shown that upon first attachment of bacteria to salivary conditioning films, *bond strengthening* occurred, meaning that the strength of adhesion increased with time (in the order of tens of seconds), most likely due to specific interaction between bacterial cell factors and components of the conditioning layer [259].

The presence of different types of salivary components has been investigated on the

biofilm level: it has been shown that the presence of sucrose can enhance the growth of *S. mutans* biofilms while it was inhibited by fluid-phase agglutinin in the absence of sucrose [3]. However, on the single bacterial level, the influence of fluid-phase proteins or sugars or even a complete salivary environment has not been investigated so far.

4. Material and Methods

This chapter describes the materials used (surfaces, chemicals, bacterial strains), experimental techniques and methods of data analysis that are important for understanding the results of the work. To ensure good reproducibility, at the end of this chapter, an alphabetically sorted list of all manufacturers of materials and devices used can be found.

4.1 Substrates and Cleaning

This section provides detailed information about the surfaces used for the experiments in this thesis. Due to the high sensitivity of the measurements to surface properties, extensive cleaning of the surfaces was inevitable. Therefore, also the cleaning procedures for all surfaces used are described in detail to ensure maximal reproducibility of the presented results.

4.1.1 Silicon-Based Substrates

Several different surfaces that are based on silicon wafers are introduced in this subsection together with the cleaning procedures used.

Bare Silicon

As a smooth flat and very hydrophilic surface, bare silicon wafers with (100) crystal orientation were used. By default, they are polished to mean square surface roughness of less than $0.1\,nm$ (after cleaning, see below). Their surface energy is $64(1)\,mJ/m^2$, resulting in an advancing water contact angle of $7(2)°$ and complete wetting for receding droplets [247]. The

streaming potential of these surfaces was determined to be $-104.4(4)\,mV$ at pH 7 [25]. Furthermore, the substrates are p-doted, resulting in an electric resistivity of $10\text{–}20\,\Omega cm$.

To remove surface contaminations, the surfaces were immersed in peroxymonosulfuric acid ('piranha acid') made of equal parts of H_2SO_4 (conc.) and H_2O_2 (30 %, nonstabilized) for 30 min. Afterwards, to remove leftovers of the acids, the surfaces were placed in hot ultrapure water (with a conductivity of less than $0.6\,\mu S/cm$) for one hour while the water was refreshed every 20 min. If necessary, the substrates were then dried under a stream of nitrogen with a purity of 99.999 %.

Hydrophobized Silicon

To change the properties of a surface, the use of self-assembling monolayers (SAMs) is a common and often convenient method [172]. In order to render the bare silicon wafers very hydrophobic, they were covered by a SAM of CH_3-terminated silanes according to a standard recipe published by Lessel et al. [153]. The silane used is octadecyltrichlorosilane (OTS) having 18 carbon atoms in its backbone and, therefore, a tail length of approximately $2.2\,nm$ [233]. The end of the chain is terminated by a CH_3-group. This silane is known to produce very dense and robust SAMs even when prepared at room temperature [41]. The surface treatment results in a surface energy of $24(1)\,mJ/m^2$ and a streaming potential of $-80.0(1)\,mV$ at pH 7 [25]. Consequently, the advancing water contact angle is $111(1)°$ and the receding one $107(2)°$ indicating the

high chemical and topographical homogeneity of the surface. Accordingly, the RMS surface roughness is almost unchanged as compared to the bare silicon surface (0.12(2) nm).

The hydrophobized surfaces were cleaned in an ultrasonic bath of ethanol and acetone subsequently for 5 min each and dried under a stream of nitrogen with a purity of 99.999 %.

Partially Hydrophobized Silicon Samples

The partially hydrophobized surfaces used in the publication in Addendum IV were produced by preserving one part of the surface while silanizing the remaining surface area.

In order to achieve this, one part of the surface was covered by a thin film of poly(methyl methacrylate) (PMMA) with a molecular weight of 14.3 kg/mol (glass transition temperature $T_g \approx 101\,°C$ [146, 24]) in the following way: first, the the PMMA film was prepared on a fresh mica sheet by spin coating ($\omega = 3,000$ rpm) from a solution of PMMA in toluene (concentration $c = 70$ mg/ml) resulting – after the evaporation of the solvent – in a thin, glassy film of about 350–450 nm thickness. Then, the mica was carefully immersed in a bath of ultrapure water under an angle of approximately 45°. Thereby, the water detaches the glassy polymer film by 'creeping' between the hydrophobic polymer and the hydrophilic mica. The polymer film then floats on the water surface, and the mica is discarded. By carefully pulling on the polymer film with tweezers, it is possible to brake the film into several parts that have, at the line of breakage, well-defined straight edges. One of these parts is now taken up by a cleaned piece of silicon and carefully taken out of the water. After the remaining water has evaporated, the film has a stable state on the silicon surface. To enhance the smoothness of the edge of the polymer film, the sample is heated to 130 °C for 5 min.

In the next step, the partially PMMA-covered silicon is silanized according to the recipe of Lessel et al. with a few modifications: the surface is not treated with water vapor and it is only once immersed into the silane solution for 10 min. Afterwards, the polymer film on the surface is removed by rinsing with chloroform. This procedure results in a surface with a very sharp interface between a silanized part and a part of bare silicon as characterized in more detail in the publication in Addendum IV.

The cleaning of this surface is slightly modified according to cleaning of completely silanized surfaces: firstly, the surface is gently wiped with a nonabrasive cellulose-fiber wipers soaked in ethanol and acetone, subsequently. Then, to remove particles of the tissue, the surface is treated with a stream of carbon dioxide crystals ('snowjet') [20, 226]. Afterwards, the surface is cleaned in an ultrasonic bath of 1 % of the cleaning agent Mucasol in ultrapure water for 3 min and the Mucasol is removed by an ultrasonic bath in ultrapure water for 5 min where the water is exchanged three times.

By modifying the recipe described above, it is also possible to produce narrow (width $w \approx 200$ nm) stripes of OTS on a silicon surface. To achieve this, the silicon wafer is completely covered by a very thin (height $h = 5$–10 nm) PMMA film following the same protocol as described above (or by directly spin coating the silicon surface) but with a lower concentration of PMMA in toluene, namely 5.5 mg/ml. Then, with the help of an AFM operating in contact mode, 'scratches' are made into the PMMA film while it is heated to a temperature of 80–100 °C. When heating the sample to 160 °C for 30 min afterwards, the polymer film partially dewets from the silicon at the position of the scratch resulting in

a groove with smooth edges (see Figure 4.1 a). After cooling the sample to room temperature again, the uncovered part of the silicon can be silanized as described above, which results in a slim stripe of silanes (see Figure 4.1 b). The surfaces that are partially silanized this way can, for example, be used to characterize the shape of the bacterial contact area in more detail than it is done in the publication in Addendum IV.
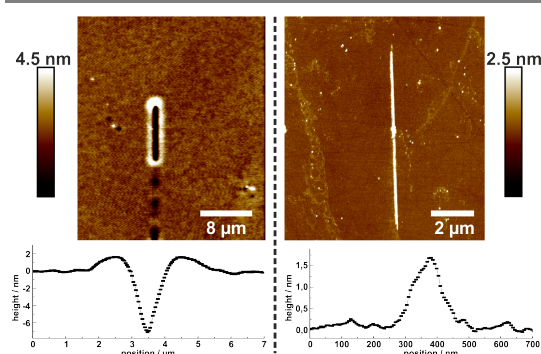
Figure 4.1. AFM image and averaged cross-section of a dewetted scratch in the polymer film (left) and a silanized stripe on a bare silicon surface (right).

Roughened Silicon Surfaces

The general recipe to impose a roughness on silicon surfaces is extracted from a publication of Koynov et al. [147] and modified by F. Nolle [192]. In short: cleaned silicon substrates were covered by physical vapor deposition (at 10^{-5} mbar in an Univex 300 device) with a gold layer of a nominal thickness of 2 nm as determined by a quartz crystal microbalance. Notably, the gold does not form a homogeneous layer but rather a well-known pattern of nano-sized clusters (see Figure 4.2).
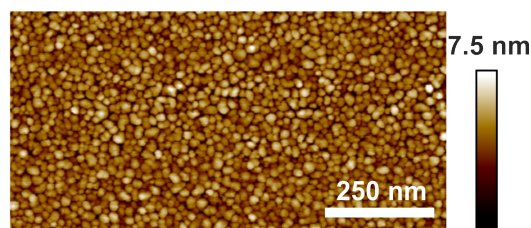
Figure 4.2. AFM image of gold clusters on a bare silicon surface.

The gold-covered substrates were further processed in the laboratories of Prof. Dr. Helmut Seidel at Saarland University. The substrates were etched in a mixture of fluoric acid (40 %), hydrogen peroxide (35 %), and deionized water for different times (90 s, 180 s and 360 s). The acid was removed by rinsing with ultrapure water and the gold cluster by immersing the substrates in aqua regia (1:3 mixture of nitric acid and hydrochloric acid). This procedure results in different rough surfaces with RMS roughnesses of 7 nm, 24 nm and 35 nm. A detailed characterization of the roughened substrates (by AFM and scanning electron microscopy (SEM)) can be found in the publication in Addendum V.

4.1.2 Hydroxyapatite Samples

Investigating interactions of biomolecules and microorganisms with tooth surfaces is an important topic in life sciences. However, real teeth feature some properties that make them a non-ideal substrate for experimental research [274]: for example, their chemical composition and structure heavily depend on external factors, such as the dietary habits or genetic background of the individual person (or animal) they were taken from. HAP pellets combine the high biological relevance with well-definedness and reproducibility. They

are made of the same material as the mineral component of natural teeth, but – in contrast to real teeth – are very smooth, highly dense, stable, mostly chemically inert, and well-characterized. The properties and the synthesis of HAP samples are described in detail in the publication in Addendum VII.

The samples were used for several experiments and before every set of experiments treated in the following way: to remove possible contaminations from storage and to ensure the high quality low roughness of the surface, the last polishing step explained in the publication was repeated (polishing for several minutes with polishing solution containing diamonds with sizes of 30 nm). Then, in order to remove possible contaminations from the polishing step, the samples were etched for 7 s in sodium acetate buffer (pH 4.5) in an ultrasonic bath. Possible leftovers of the etching solution were then removed by extensively rinsing the samples and placing them in an ultrasonic bath of ultrapure water.

After every set of experiments, HAP samples were cleaned in an ultrasonic bath of 1 % Mucasol in ultrapure water for 3 min, afterwards rinsed with ultrapure water, and dried under a stream of nitrogen before storing them in a clean room environment. To test whether Mucasol might change the surface chemistry or contaminate the sample, x-ray photoelectron spectroscopy (XPS) experiments have been performed, which showed that the surface is not influenced by the cleaning agent.

4.1.3 Corrugated Surfaces

To investigate the influence of regularly structured surfaces on the adhesion of bacteria, also sinusoidally corrugated PDMS surfaces were used. The substrates were produced by the group of Prof. Andreas Fery according to a published recipe [123, 236, 235]. Briefly,

PDMS was produced by mixing Sylgard 184 Base and Sylgard 184 Curing Agent in a mass ratio of 10:1. After casting approximately 5 mm thick films, they were heated to 80 °C for 24 h to achieve the best possible cross-linking. Afterwards, smaller pieces were stretched in a costume-made setup and oxidized in an air plasma (1 mbar, 18 W, PDC-32 G device) in the extended state. After relaxing, the substrates exhibit a wrinkled surface as shown in Figure 4.3. For our applications, the strain and oxidation time were adjusted in a way that results in wavelengths of 2635 nm and 2718 nm and amplitudes of 239 nm and 181 nm. Except for the sinusoidal structure, the PDMS itself is very smooth on small scales featuring an RMS roughness of less than 0.5 nm.[1]
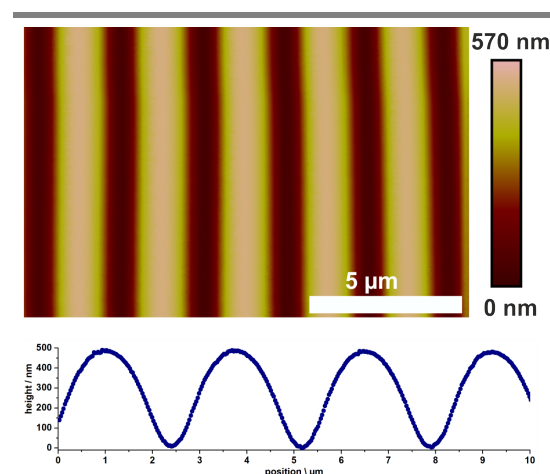
Figure 4.3. AFM image and cross-section of the sinusoidal structured PDMS surface.

---

[1]The roughness was determined by AFM in a square area with a size of 1 μm^2.

4.2 Bacterial Strains and Growth Conditions

For the experiments with *S. aureus* cells in this work, the strain SA113 (also termed ATCC 35556, derived from the laboratory strain NCTC 8325), which was firstly isolated by S. Iordanescu, was used [130]. It is widely used in staphylococcal research since it can also accept *E. coli* DNA [115, 148]. Here, it is chosen because of its strong ability to form biofilms and the broad knowledge of its properties [57, 100, 250, 281].

As a non-pathogenic representative of the genus *Staphylococcus*, *S. carnosus* strain TM300 was used. The genome of this strain was fully decoded in 2009 and, unlike *S. aureus*, encodes only a few mobile elements; thus, it is believed to have a high stability [207].

For the experiments imitating processes in the oral environment, *S. mutans* strain ATCC 25175 (NCTC 10449) was used.

The staphylococcal cells were, for the long term, stored as a glycerol stock at $-20\,°C$ that was renewed after one year at the latest by a sample from a deeply frozen ($-80\,°C$) stock solution. For the experiments, cells from the frozen stock were streaked on blood agar plates and cultured for 3 days at $37\,°C$ in normal atmosphere. These plates were used no longer than two weeks. The day before the experiments, one colony from the plate was transferred into 5 ml of sterile tryptic soy broth (TSB) and cultured overnight at $37\,°C$ and 150 rpm. From this solution, 40 µl were transferred into 4 ml of fresh TSB and cultured for another 2.5 h under the same conditions to obtain cells in exponential growth phase. In this phase, the homogeneity of the bacterial culture is maximal and would decrease for longer incubation times because the proportion

of dead and/or damaged cells increases [209] and because some cells start to produce capsules [178]. Furthermore, the production of the majority of adhesins is maximal in exponential growth phase [109].

From this final solution, about 1 ml was extracted and washed in the following way: the suspension was centrifuged at 17,000 g, and the supernatant was replaced by sterile phosphate-buffered saline (PBS) of pH 7.3 and vortexed for 10 s. This washing step was repeated two more times to remove leftovers of the nutrient and other extracellular substances. To achieve a concentration suitable for the fabrication of single cell probes, the final solution was diluted to an optical density at 600 nm of 0.2–0.3, placed at $4\,°C$, and used no longer than 6 hours.

For the *S. mutans* cells, the procedure was similar, with the following differences: cells were plated on mitis salivarius agar, cultured in Todd Hewitt broth (THB) [18, 95], and, because of the different growth time of this species compared to the used staphylococci, culturing steps in liquid medium lasted for 24 and 16 hours.

4.3 Atomic Force Microscopy-based Force Spectroscopy

While classically, the AFM is used to scan the surface of interest in order to gain information of topographical – or even mechanical, chemical, electrical, or magnetic – properties on every point of the surface, in force spectroscopy, the AFM tip is approached to and then retracted from the surface at one specific position and the cantilever's deflection during approach and retraction is monitored [225].

This way, force-distance curves as sketched in Figure 4.4 can be obtained. With these curves, different properties of the system can be measured: for example, the 'adhesion force', is defined by the absolute minimum of the force-distance curve giving the maximum absolute force value needed to detach the probe from the substrate. Thereby, the traveled distance of the cantilever in one direction is termed 'ramp size'. The integral of the force over distance gives the 'adhesion energy'. Both, the adhesion force and adhesion energy, are, in this thesis, used to characterize the 'adhesive strength' of the specific probe. The distance between a functionalized tip and the surface when the last contact breaks is called 'rupture length'. For certain systems, in the approach part of the force-distance curve, a distinct 'snap-to-contact' ('snap-in') can be observed, which is characterized by its 'snap-in force' and 'snap-in distance'. The 'force trigger' is the maximal force with which the probe is pressed to the surface and can be adjusted by the experimenter to be suitable for the particular system. Another important parameter that was varied in many experiments of this work is the 'surface delay time' describing the (additional) time for which the probe is pressed to the surface with the chosen force trigger[2].

There are some new scanning techniques, such as the Peak Force QNM®mode, that use fast-recorded force-distance curves for image generation. This technique simultaneously provides information about mechanical properties and – with the help of these – also improves image quality. Therefore, this mode was used for imaging eucaryotic cells and to characterize their shape and surface characteristics in the publication in Addendum II.

---

[2]A surface delay time of 0 s stands for a very short contact time below 100 ms [23].
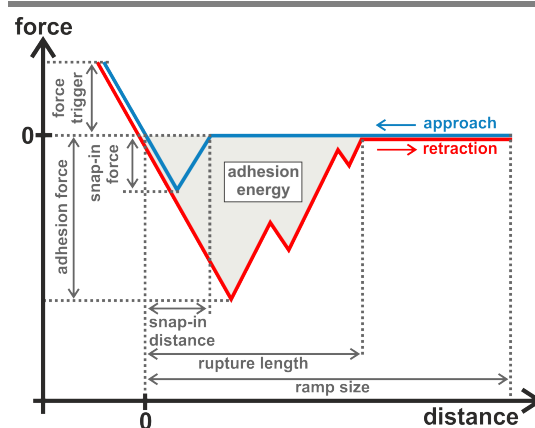
Figure 4.4. Principle of a force-distance curve with all used measures and parameters to characterize bacterial adhesion (see text for details).

Today, the data that can be obtained from force-distance curves increases continuously. Many of these measures are rather complex and not very expressive on their own. However, in combination with many other parameters and the help of huge statistics, interesting correlations between features in force-distance curves and actual material properties can be revealed [68].

By combining AFM-based force spectroscopy with other methods, researchers start to simultaneously gain information about different properties, which has been impossible before, and new research routes open up. For example, commonly termed tip-enhanced Raman spectroscopy combines the chemical information of Raman spectroscopy with the lateral precision of the AFM [285, 239].

AFM can also be combined with infrared spectroscopy: in this case, the cantilever acts as a sensor for the adsorption of the sample in the infrared regime and provides chemical information with nanoscale lateral precision [173].

4.3.1 Calibration of Cantilevers

Obviously, to gain quantitative information about the forces acting between a (functionalized) cantilever and a substrate, a precise knowledge about the mechanical properties of the cantilever is inevitable. In theory, these properties can be calculated with the knowledge of the exact geometry and material of the cantilever. However, in reality, for several reasons such as the lack of exact information about the cantilever thickness, the force sensors are calibrated before every experiment.

For AFM-based force spectroscopy, two parameters are particularly important: the deflection sensitivity[3] and the spring constant, the former having the unit nm/V and connecting the cantilever's deflection to the voltage on the photo-diode.

For the calibration of the deflection sensitivity, the cantilever is pressed onto a hard (much harder than typical spring constants, in practice, often sapphire or silicon) surface, and from the linear relationship between displacement of the piezoelectric crystal driving the cantilever and the recorded voltage, the deflection sensitivity can be obtained [28].

The calibration of the cantilever's spring constant turns out to be more complex. One way of calibrating is the commonly termed *thermal tune* method [128]. Thereby, the cantilever is considered to be a simple harmonic oscillator with one degree of freedom undergoing thermal fluctuations. By measuring the vibrations of the cantilever for a certain time and analyzing its frequency spectrum, the spring constant can be calculated. Notably, the calculated value depends on several factors, such as laser spot size, and *z*-displacement piezo calibration [212].

Therefore, another method was proposed by Sader et al., firstly for rectangular and later for various shapes of cantilevers [214, 213, 212]. For the calculation of the spring constant, the cantilever's plain geometry, its resonance frequency, and its *Q* factor are used. To reduce errors in the calibration of spring constants even further in a systematic way, Sader proposed to compare and standardize thermal tune measurements from many AFM users globally [212]. It has been shown that this method, commonly termed as *Sader method*, significantly reduces calibration errors if enough data for the cantilever in use is accessible.

However, even if the cantilever's spring constant is known exactly, calibration can go wrong because the deflection sensitivity is error-prone: if the surface or the cantilever are contaminated, the procedure described above does not result in an exact value for the deflection sensitivity when linearly fitting *z*-displacement versus voltage on the photo diode. Furthermore, the deflection sensitivity is dependent on the surrounding medium (liquid or air) and the position of the laser spot on the cantilever. For the sake of completeness: the error caused by the tilt of the cantilever should be small [111, 127].

To overcome these problems, Schillers et al. proposed a technique called *Standardized Nanomechanical Atomic Force Microscopy Procedure* [221]. In this method, precalibrated cantilevers are used whose spring constants were exactly determined by laser Doppler vibrometry.[4] From this real value of the spring constant and the value determined by the AFM via thermal tune, a correction factor for the deflection sensitivity is determined. It was shown that this method drastically re-

---

[3]One may also find other terms, such as inverse optical lever sensitivity.

[4]It was shown that force constant calibration with laser Doppler vibrometry features very high accuracy [92].

duces errors in the measurements of elastic moduli over a variety of laboratories [221].

In all experiments for the thesis at hand, spring constants and deflection sensitivities were – *i. a.* due to the novelty of the presented methods of Sader and Schillers – determined in the 'classical' way. Nevertheless, it was taken care that the calibration was always done identically and as close as possible under the same conditions as the actual experiment. For example, the calibration of the deflection sensitivity was done in the same buffer that was also used for the measurements and also the laser spot size and position was not changed between calibration and measurement. Furthermore, the thermal tune was always performed at a distance of at least 100 nm between cantilever and surface to make sure that the cantilever oscillates freely and is not influenced by the surface potential. Therefore, systematic errors should be small and not influencing the results of the work.

4.4 Bacterial Probes and 'Bacterial' Force-Distance Curves

4.4.1 Technique

The development of a 'recipe' for the production of stable bacterial probes for reliable adhesion measurements of single bacterial cells was part of this thesis and is described in the publication in Addendum I.

In short, single bacterial cells were immobilized on a tip-less AFM cantilever (MLCT-O) coated with a thin layer of dopamine. The cells were proven to be in a living state (as indicated by viability staining) after measurements.[5]

---

[5] An exception are the measurements on roughened surfaces where a contact killing of bacterial cells was observed [179].
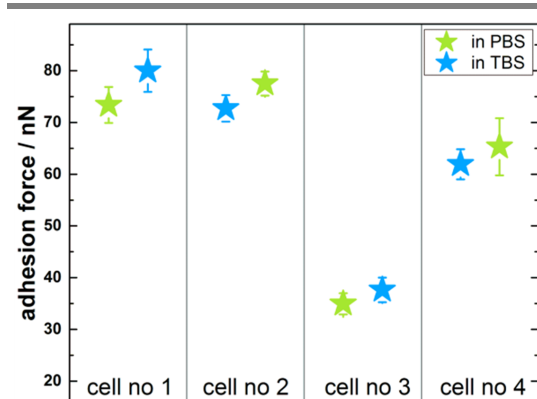
Figure 4.5. Mean adhesion forces of four individual *S. aureus* cells obtained from 50 force-distance curves in each buffer.

All single cell force spectroscopy (SCFS) measurements were performed in PBS. Nevertheless, also the use of another buffer not containing phosphate ions, tris-buffered saline (TBS), gives the same results as it was shown for four individuals of *S. aureus* adhering to a hydrophobic surface (see Figure 4.5).

A very important strength of the experiments in this thesis is the fact that one and the same bacterial cell can be used to investigate different scenarios. For example, one individual cell can be used to test its adhesion strength to several different surfaces under the same conditions. Also, the influence of other parameters, such as the temperature, the ionic strength or the nutrient content of the buffer can be tested in one single experiment with the same cell.

Thereby, the order of the different conditions is changed systematically to ensure that the observed effects are intrinsic and not caused by the specific experimental procedure. For example, when probing the adhesion to different substrates, the order of the substrates is changed for every measurement. Additionally,

at the end of a experimental series, – after every surface has been probed – the adhesion to the first substrate is measured again to ensure that it has not changed, for example due to alteration in the bacterial cell wall.

4.4.2 Data Analysis – Curve Correction

How raw data of SCFS measurements are converted into a 'meaningful' format is explicitly described in the publication in Addendum I. There, it is especially detailed how the traveled distance of the cantilever and the voltage on the photodiode is converted into the acting force and the distance between cell and surface.

Here, the focus is on defining the distance between cell and surface – from now on called separation – because it may be important in order the interpret some of the results presented in the publication in Addendum V. The original experimental value for calculating the separation is the traveled distance of the cantilever. Since the bacterial cells have cell wall components of different dimensions and mechanical properties, in reality, a separation of 0 nm cannot be defined mutually. Rather, one has to decide what is considered as the point of contact between cell and surface.

For all SCFS measurements presented in the thesis at hand, this point in the retraction part of the force-distance curve is calculated as follows[6]: in the case of no adhesion between cell and surface, a linear function is fitted from the last data point where the force is a factor of two larger than the maximal force value of the baseline and the first point where it is below 0 N. Then, the values of the traveled distance are shifted in a way that this linear function

---

[6]In the actual analysis program, the procedure is slightly more complex because some exceptions have to be included. Nevertheless, the general statement given in the text is valid.

goes through the origin of the coordinate system. In the case of measurable adhesion between cell and surface, the points for the linear fit are calculated slightly different: 'going backwards' from the last point of contact – defined as the last point where the force has an absolute value that is a factor of two larger than the maximal force value of the baseline –, the last point where the actual force value is below 0 N and the first point where the force value is larger than 0 N are used, and the correction is done as described above.

For the approach curve, the method is equivalent, also taking into account the occurrence or absence of a snap-in event.

The last step to obtain the real separation is as follows: when a force is acting on the cantilever, the deflection of the cantilever – accessible by knowing the deflection sensitivity, spring constant and measured voltage on the photo detector – is added to or subtracted from the corrected distance, depending on the sign of the force value.

For rough surfaces, as used in the publication in Addendum V, calculating the separation as described above can lead the certain problems (see Figure 4.6): since for every adhesion event it is not known if, or to which extent, the bacterial cell wall or the proteinaceous outer layer is penetrated by the 'spikes' on the rough surface, the point of zero distance is rather undefined, and, can additionally change for every curve. The variations of the value can be the size of the surface features, i. e. in the range of 30–100 nm [248]. Since values of rupture lengths and, even more important, snap-in distances lie also in this range, their absolute values as well as relative values from different curves are not reliable. This should not be a problem for measurements on locally flat sur-
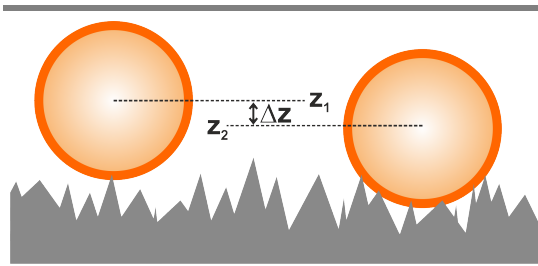
Figure 4.6. Illustration of the difficulty in properly defining the cell-surface separation on rough substrates: the cell on the left side already experiences a force at a height z_1 due to the contact to one single 'peak' whereas the cell on the right does not directly sense the substrate until it is at height z_2 where it already interacts with several surface features.

faces (as they are performed for all other publications in the addenda).

4.5 Parallel Plate Flow Chamber Experiments

Before AFMs were apt to determine adhesion forces, parallel flow plate experiments were widely used to investigate bacterial adhesion to all kind of surfaces. The principle of these experiments is simple: a dispersion of bacterial cells is flushed trough a chamber having a geometry allowing the solution to exhibit a laminar flow profile in a defined area of interest (AOI) in the chamber. When the solution is flushed trough the chamber within this AOI, the bacterial cells adsorb to the boundaries of the chamber, which is often constructed in such a way that the top of the chamber is transparent and the bottom part can be replaced by different substrates. The number of cells and their position on the respective surface can be observed by optical microscopy, with or without staining the cells beforehand. Using this procedure, it is possible to measure the adhesion

of the examined cells to the material which the boundaries of the chamber are made of. In this setup, it is possible to change flow velocity or optical density of the bacterial suspension easily to confirm results under varying conditions. Furthermore, different liquids and drugs can be flushed trough the cell before or after the bacteria to study the effect of surface conditioning or cell treatment on the adhesion properties.

Compared to AFM-based force spectroscopy, flow chamber measurements rather give an adhesion probability (*How high is the chance that cells adsorb on the given surface?*) instead of an actual adhesive strength (*How hard is it to remove the cells from the surface?*). Moreover, no qualitative information about micro- or nanoscopic adhesion mechanisms can be obtained.

Nevertheless, a big advantage of flow chamber measurements compared to SCFS is that a much higher number of individual cells can be probed in a given time. This can be useful when studying the effect of certain drugs or other conditions on bacteria that can cause very cell individual responses and, therefore, need big statistics. For this reason, in the thesis at hand, flow chamber measurements are used in the experiments presented in the publication in Addendum V to investigate the effect of surface roughness on bacterial viability for many cells.

Manufacturer Information of the Used Materials and Devices

Acetone 99.9 % p. a., Thermo Fischer Scientific, Waltham, MA, USA

AFM Bioscope Catalyst, Bruker-Nano, Santa Barbara, CA, USA

Carbon dioxide filter TEM Filter Inc., Nampa, ID, USA

Cellulose-fiber wipers Kimwipes, Kimberly-Clark Corporation, Dallas, TX, USA

Dopamine 99 %, Merck, Darmstadt, Germany (former Sigma-Aldrich St. Louis, MO, USA)

Ethanol 99,8 % absolute, VWR International, Radnor, PA, USA

Hydrochloric acid Bernd Kraft GmbH, Duisburg, Germany

Hydrogen peroxide 30 % p. a., nonstabilized, Merck, Darmstadt, Germany

Mitis salivarius agar home-made with the following components: MS Agar Medium (Acumedia), Sucrose, Bacitracin (both Merck, Darmstadt, Germany), Potassium tellurite (VWR International, Radnor, PA, USA)

Mucasol Merz Pharma, Frankfurt am Main, Germany

Nitric acid 65 %, ORG Laborchemie GmbH, Bunde, Germany

Nitrogen 5.0, Air Liquide S. A., Paris, France or Praxair, Danbury, CT,

OTS Merck, Darmstadt, Germany (former Sigma-Aldrich St. Louis, MO, USA)

PBS Merck, Darmstadt, Germany (former Sigma-Aldrich St. Louis, MO, USA)

Physical vapor deposition device Univex 300, Leybold Heraeus, Köln, Germany

Plasma cleaner PDC-32 G Harrick Plasma, Ithaca, NY, USA

PMMA PSS Polymer Standards Service GmbH, Mainz, Germany

polishing solution 30 nm diamond polishing suspension MSY 0-0.03, Microdiamant, Lengwil, Switzerland

Si-Wafer Siltronic AG, Burghausen, Germany

Sulfuric acid 75 % selectipure, BASF, Ludwigshafen am Rhein, Germany

Sylgard 184 Dow Corning, Midland, MI, USA

THB Merck, Darmstadt, Germany (former Sigma-Aldrich St. Louis, MO, USA)

Tipp-less AFM cantilevers MLCT-O, Bruker-Nano, Santa Barbara, CA, USA

TSB VWR International, Radnor, PA, USA

Toluene LiChrosolv, Merck, Darmstadt, Germany

Ultrapure water Thermo Fischer Scientific, Waltham, MA, USA

Viability staining BacLight Bacterial Viability Kit, Thermo Fischer Scientific, Waltham, MA, USA (former Invitro Molecular Probes, Eugene, OR, USA)

5. Results and Discussion

This chapter presents the main results of the thesis. Thereto, the most important observations of the respective studies are shown as figures and briefly discussed. Further details are given in the respective publications in the addenda of the document.

In addition, this chapter presents and discusses results that have not yet made their way into publishable manuscripts, namely the influence of temperature on the snap-in event and the adhesion of *S. aureus* cells to sinusoidal structured surfaces. Although these results are not yet substantial enough to be published alone and need further complementary experiments to enhance their relevance for the work, they can help to understand and interpret the main results of the thesis.

Part of the results already published is the establishment of a reliable procedure for SCFS, the method of choice for investigating bacterial adhesion in this work. Parts of it are described in Chapter 4 of this thesis. Therefore, it is not explained here again. More details can be found in the publication in Addendum I.

5.1 Adhesion Behaviour of *S. aureus* to Flat, Abiotic Surfaces

Considering the adhesion of *S. aureus* to solid surfaces as examined in this work, several aspects and quantities exist that are described and discussed in this section.

5.1.1 General Adhesion Properties to Hydrophobic and Hydrophilic Surfaces

The adhesion of *S. aureus* to very hydrophilic silicon surfaces and strongly hydrophobic OTS surfaces was characterized by measurements of more than 120 individual bacterial cells.

Distinct differences between hydrophobic and hydrophilic surfaces were found (see Figure 5.1). On a first sight, the shape of the force-distance curves is very different for both types of surfaces: on hydrophobic surfaces, the curves are quite 'smooth' and the shape is very reproducible for different adhesion events of the same cell (see Figure 5.1 a). On hydrophilic surfaces, in contrast, the retraction parts of the curves show 'spiky' features and the shape varies for different curves, even of one and the same cell (see Figure 5.1 b). Furthermore, while the adhesive strength to hydrophobic surfaces is not sensitive to additional surface delay time of the cells on the substrate, on the hydrophilic surfaces, the adhesion markedly increases when an additional surface delay time of 5 s (as compared to no additional surface delay time) is applied (note the different scale bars in Figure 5.1 b and d). In fact, on the hydrophilic surfaces, without additional surface delay time, almost no adhesion occurs. Therefore, in the following, for hydrophilic surfaces, only values gained with additional surface delay time of 5 s are discussed.

What was already visible for one cell, becomes even clearer when comparing measurements of over 50 individuals on each surface
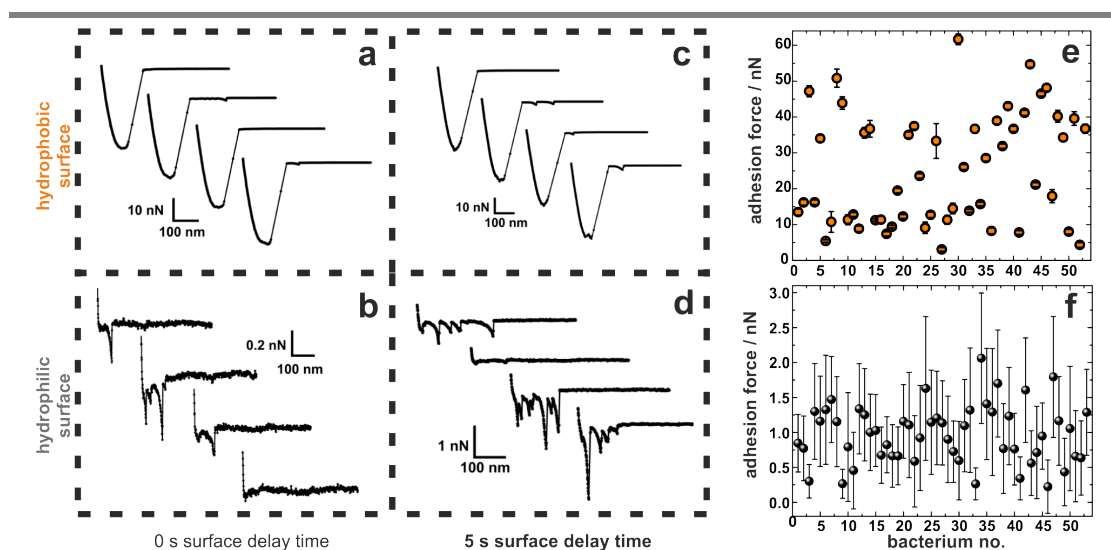
Figure 5.1. a)–d) Exemplary retraction parts of force-distance curves for one *S. aureus* cell on hydrophobic (OTS, upper row) and hydrophilic (native silicon, lower row) surfaces with surface delay times of 0 s (a and b) and of 5 s (c and d). e), f) Mean values (circles) and standard deviations (error bars) of adhesion forces on hydrophobic (OTS, top) and hydrophilic (native silicon, bottom) surfaces. Data were obtained from at least 50 force-distance curves for every individual cell on the respective substrate.

(see Figure 5.1 e and f): the adhesion force on hydrophobic surfaces is at least one order of magnitude higher than on hydrophilic surfaces. Furthermore, – in line with the findings regarding the shape reproducibility of force-distance curves – the value of adhesion force gained from several curves shows distinctly lower standard deviations on hydrophobic surfaces as compared to hydrophilic surfaces (see error bars in Figure 5.1 e and f). In contrast, the mean values of adhesion force vary much more between different individual cells on hydrophobic surfaces as compared to hydrophilic surfaces. In fact, the experiments reveal a bimodal distribution of adhesion forces for *S. aureus* cells on hydrophobic surfaces (see Figure 5.1 e). This may be attributed to the age of the cell wall area that made contact with the substrate as discussed in detail in the publication in Addendum III.

Furthermore, a distinct snap-in event on hydrophobic surfaces can be observed that is not present on hydrophilic surfaces. The range, in terms of cell-surface distance, of this snap-in event as well as the rupture length, the cell-surface distance at which the last contact breaks, were measured with high statistical significance.

All presented measurements could be interpreted and explained by the 'improved adhesion model' of Thewes et al. (see Paragraph 3.5.2) [246]: the adhesion of *S. aureus* cells to hydrophobic as well as to hydrophilic smooth surfaces can be solely described by tethering cell wall macromolecules that behave like 'ideal polymers'. Consequently, the main difference between the adhesion to hydrophobic and hydrophilic surfaces is the number of adhering polymers. While on hydrophilic surfaces, their number is very high, it is low on

hydrophilic surfaces. Therefore, on hydrophobic surfaces, a snap-to-contact occurs, the adhesion force is rather high, and stochastic fluctuations are suppressed resulting in smooth, reproducible curve shapes. On hydrophilic surfaces, in contrast, the result is a rather low adhesion force combined with strong variations in the shapes of the curves.

In a next step, these results combined with the 'improved adhesion model' of Thewes et al. could be used to speculate about the involved interactions on both substrates: on hydrophobic surfaces, obviously, the hydrophobic interaction seems to be the main reason for the tethering of macromolecules while on the hydrophilic surface, the formation of hydrogen bonds seems more likely, as described in the following.

The hydrophobic interaction is virtually always present between a hydrophobic surface and any hydrophobic patch in the tethering macromolecules wherefore a 'hydrophobic bond' can form instantaneously as soon as the distance between the surface and the hydrophobic patch is small enough. In our experiments, it seems that very many of these bonds formed in every force-distance measurement due to a high number of (at least) partially hydrophobic molecules in the bacterial cell wall.

Hydrogen bonds, in contrast, are directional (see Section 3.1.1) and, therefore, need a certain time to be formed. Hence, the explanation for the low adhesion and varying curve shapes may be twofold: Either, the number of macromolecules in the cell wall that were able to exhibit hydrogen bonds is quite low, or there are, in principle, many such molecules, but during one force-distance measurement the time to form multiple hydrogen bonds is too short. The fact, that with increasing surface delay time, the adhesive strength increases, is a strong hint that the latter explanation is at least

partially true and that cell wall molecules exist which participate in adhesion to both types of surfaces.

Still, it is not clear which particular molecules are in line for the purpose of adhesion. However, the knowledge about the described general adhesive behaviour of *S. aureus* cells can be used as a basis to tackle this question when combined with experiments using specifically designed mutant cells that are presented in the next paragraph.

5.1.2 Influence of Certain Groups of Cell Wall Molecules

As described in Section 3.2, the surface of a bacterial cell consists of a variety of molecules that can be categorized by different means, such as by their chemical building blocks (e. g. proteins, sugars), or by their functions (e. g. adhesion, transport). Additionally, all these molecules can have differences in their connection to the cell's surface: they can be secreted by the cell, they can be covalently attached to the cell wall, or they can be rather weakly associated to the cell wall.

One aim of this work was to investigate which molecules, or rather which groups of molecules, participate in the adhesion process to abiotic surfaces in general. Although many cell wall molecules are identified, and their function was already elucidated as not primarily adhesive, they can also play a role in adhesion because it is well-known that multifunctional properties are common amongst the molecules in the bacterial cell wall [154].

The focus of this work was placed on the three following groups of surface macromolecules: i) covalently bound cell wall proteins, ii) WTAs, iii) and d-alanine residues in WTAs and LTAs. For this purpose, knock-out mutant cells of *S. aureus* were used in which
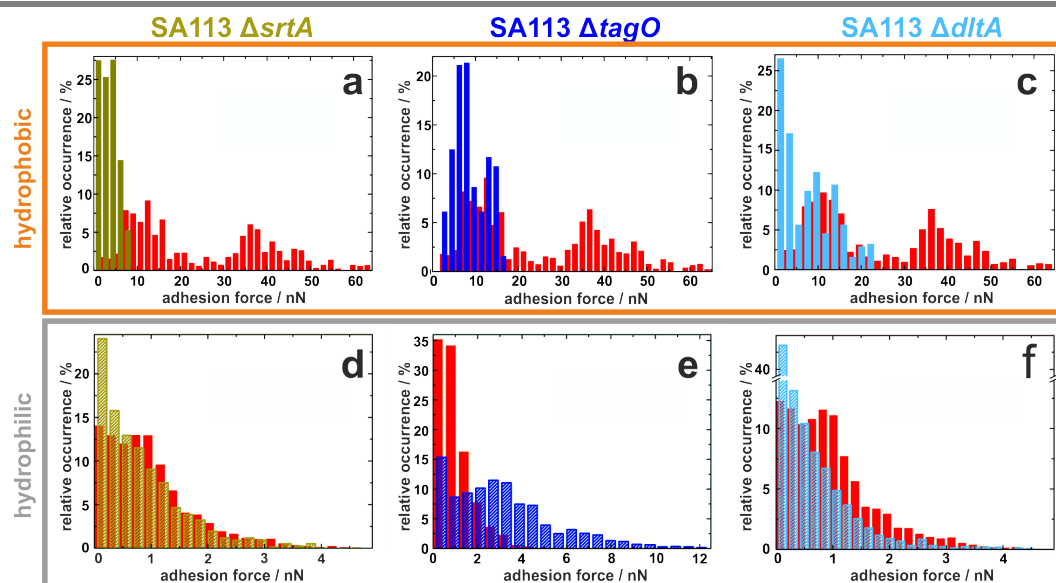
Figure 5.2. Comparison of adhesion forces of the three mutant strains to wild-type cells (red data) on hydrophobic (upper row) and hydrophilic (lower row) surfaces.

the respective groups of cell wall molecules were either modified or not present at all (in the case of i), SA113Δ*srtA* cells were used; for ii), SA113Δ*tagO* cells were used; for iii), SA113Δ*dltA* cells were used). As an additional comparison to the strongly pathogenic *S. aureus* cells, a non-pathogenic representative of the genus *Staphylococcus*, namely *S. carnosus*, was used. This organism is known to have in general much fewer surface molecules than *S. aureus*.

The experiments showed that it is not possible to identify one single group of cell wall macromolecules that is solely responsible for the adhesion of *S. aureus* (see Figure 5.2). On hydrophobic surfaces, the knock-out of every group of molecules markedly reduces the adhesion force (see Figure 5.2 a–c). Still, there seem to be many adhesive molecules left because adhesion forces show rather small standard deviations (and because the curve shapes were very reproducible, not shown here). Even

more notably, in every case, the knock-out of a certain group of molecules reduces the adhesion force by a factor greater than two-thirds. This means that the adhesion capability of the wild-type cells is not simply given by the sum of the adhesive properties of all molecule groups, but rather, the different groups seem to enhance each other's adhesive strength.

On hydrophilic surfaces, the adhesive strength is less reduced after knocking-out certain molecule groups compared to the situation on hydrophobic surfaces (see Figure 5.2 d–f). After knocking-out WTAs, adhesion is even enhanced (see Figure 5.2 e). The latter might be an effect of reduced electrostatic repulsion between cell and surface as it was also found in other studies [258, 201].

Altogether, it seems that on hydrophobic surfaces, adhesive strength is determined by the respective cell and its cell wall composition in terms of the number and density of cell wall macromolecules while on the hydrophilic

surface, the adhesive strength fluctuates for every adhesion event and may be driven by the stochastic process of 'bond formation' of rather few molecules.

The observed differences in adhesive strength between mutant and wild-type cells might come from the fact that the contact area between the particular mutant and a flat surface is different as compared to wild-type cells. For example, the high adhesion of the wild-type may arise from relatively large contact area. To test whether this hypothesis may be true, a technique for measuring the contact area between a single bacterial cell and a flat substrate was developed and is described in the next paragraph.

5.1.3 Bacterial Contact Area to Flat Surfaces

Not only for interpreting the experimental results concerning the adhesion of mutant cells in the previous paragraph, but also – as described in Paragraph 3.5.2 – for the modeling of bacterial adhesion in general, the knowledge about the size of the bacterial contact area to a solid surface is of fundamental interest. One of the main results of this work is the determination of the contact area of staphylococcal cells to abiotic surfaces as detailed in the publication in Addendum IV. Of note, the newly developed method to measure the contact area is not restricted to spherical cells or even bacteria. Given the fact that the adhesion of an individual is different on hydrophilic and hydrophobic surfaces, rod-shaped bacteria, yeasts, or even bigger cells can be investigated.

As a basis to measure the contact area, a tailored substrate was prepared: by partially hydrophobizing an originally hydrophilic silicon wafer, a surface with a very sharp interface

(with a width of less than 30 nm) between very high and extremely low surface energies was produced. SCFS measurements on varying positions on this surface provided data to determine the radius of the spherical contact area of *S. aureus* to be in the range of 150–350 nm depending on the individual cell (see Figure 5.3). This means that the size of the contact area is a very cell individual property, in a way that different cells of one and the same bacterial culture can have contact radii that vary by more than a factor of two. Notably, this is much more than the statistical deviations in the cell diameter for *S. aureus* cells that were determined by electron microscopy or can be found in literature [222, 181].
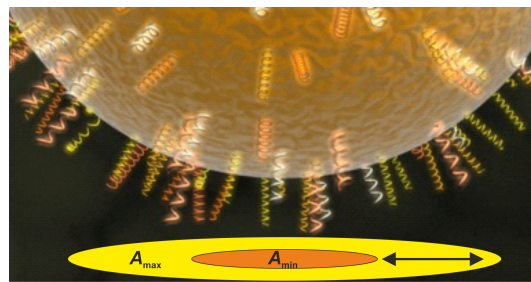
Figure 5.3. Comparison of the bacterial size and the maximal and minimal determined contact area size.

Surprisingly, no correlation was found between the size of the contact area of an individual cell and its adhesive strength. Especially, the non-pathogenic and weakly adhesive *S. carnosus* cells exhibit radii of the contact area that are in the very same range as the highly adhesive *S. aureus* cells. But also within one strain, there was no correlation found between contact area size of an individual and its adhesive capability.

Furthermore, the measured size of the contact area for bacterial cells is much higher

45

than for hard spheres of similar diameter (see the Electronic Supplementary Information of the publication in Addendum IV). To test whether simple models established for the contact between hard spheres and flat surfaces may be suitable for bacteria, the cells were pressed onto the surface with different loading forces. In the classical contact models, the loading force is directly connected to the size of the contact area. However, the experiments showed that the response of the bacterial cells on varying loading forces (up to two orders of magnitude) is also very cell-individual and not predictable. Therefore, it can be concluded that the contact between bacterial cells and flat surfaces cannot be described by simple contact models, such as e. g. the Hertzian model [118].

These results – once more – corroborate the fact that bacterial adhesion should be considered to be solely mediated by bacterial cell wall macromolecules and not as a rather simple contact of a sphere with a surface. Hence, the adhesion properties are highly dependent on individual properties of the tethering macromolecules as well as on the overall macromolecular density of the cell wall. To further investigate the tethering of these macromolecules during thermal fluctuations, experiments at different temperatures were performed that are presented in the next paragraph.

5.1.4 Influence of Temperature on the Snap-in Event

The snap-in event on hydrophobic surfaces is considered to emerge from thermally fluctuating surface macromolecules on the bacterial cell wall which randomly come in contact with the surface, then bind by hydrophobic interactions and act as entropic springs [247, 248]. If the number of these molecules and their total

binding strength and restoring force is strong enough, the molecules 'pull' the whole cell in close contact with the surface. The distance between cell and substratum at which this snap-in event starts is called snap-in separation and the exerted force is the snap-in force (see Section 4.3).

Consequently, the temperature of the system that defines the thermal energy of each molecule and, thus, the thermal fluctuations of the surface macromolecules should influence the snap-in separation and the snap-in force.
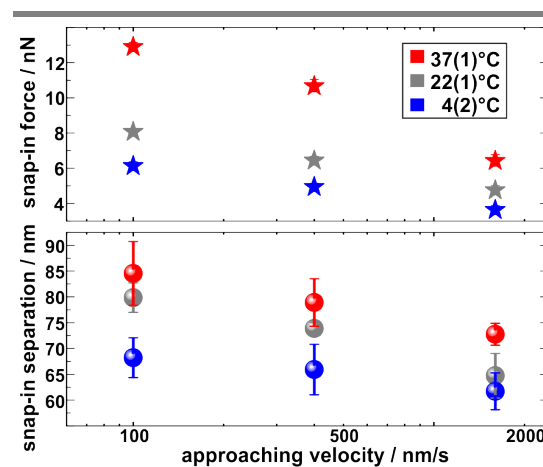
Figure 5.4. Influence of the system's temperature on the snap-in force and snap-in separation of one *S. aureus* cell on OTS for three different approaching velocities. The symbols (stars and spheres) and error bars give the mean values and standard deviations of the experimental measures calculated from 25 force-distance curves each. (Note: the error bars of the snap-in forces are smaller than the symbol size.)

To test this hypothesis, SCFS measurements with *S. aureus* cells on an OTS surface were performed for three different temperatures, namely at room temperature (22(1) °C, like all other experiments in this thesis), at 4(2) °C and at 37(1) °C. Since snap-in force and snap-

in separation depend on the approaching velocity of the cell toward the sample for the same reasons as described above, the experiments were performed at three different approaching velocities (100 nm/s, 400 nm/s and 1600 nm/s) [247].

The results are depicted in Figure 5.4 and qualitatively confirm the hypothesis: at higher temperatures, snap-in separations as well as snap-in forces increase. This effect can be observed at all approaching velocities tested.

Of note, these experiments were only performed with one individual cell and are, therefore, to be regarded as preliminary. To increase their significance, the measurements should be repeated with a larger number of cells. Furthermore, the experimental parameters, such as the temperature and approaching velocity, should be varied in different ways to exclude systematic errors.

However, even if these aspects are taken into account and further experiments will be performed, the quantitative interpretation of the data might be challenging for several reasons: i) the number of molecules in the cell wall that tether to the surface is not known, ii) the distribution of mechanical properties (e. g. length, stiffness) of the molecules is not known, iii) it is even unclear whether for each adhesion event, the number and the types of tethering molecules is constant.

Consequently, an analytically derived dependence of snap-in separation (or snap-in force) and temperature that could be fitted to the experimental data cannot be provided here. Nevertheless, the measurements showed a clear correlation between these parameters and, thus, strongly corroborate the hypothesis that macromolecular tethering is driven by thermal fluctuations.

So far the adhesion of *S. aureus* cells to smooth abiotic surfaces has been characterized and important surface parameters such as the wettability as well as other measures, e. g. the contact area on these surfaces, have been determined. In reality, however, many abiotic materials (e. g. implants materials) show a certain morphology on the surface [5]. Consequently, it is of interest to investigate if and how the presented findings on smooth substrates translate to 'rough' abiotic surfaces. Some aspects of this question are answered in the following.

5.2 Adhesion to Structured Surfaces

In literature, there are many studies investigating bacterial adhesion to structured surfaces (see Paragraph 3.5.4). However, many previous works focused on rather large (i. e. larger than a bacterial cell) morphological features and monitored the adsorption of bacterial cells relative to these structures. Thereby, it was often neglected how bacteria can be detached from the surfaces. Furthermore, substrates were often not sufficiently characterized in terms of their surface composition and chemistry. For the experiments presented here, the focus was on measuring the actual forces between bacterial cells and rough surfaces during attachment and detachment. The surface roughness was in the nano-range, as it is the case for various materials in real applications [5]. Silicon-based substrates were used because they can be well-characterized and results can be compared to the findings on smooth surfaces of the same kind. Additionally, thoughtfully structured surfaces were used to investigate general aspects of bacterial adhesion.

5.2.1 Nanorough Silicon

To investigate the influence of surface roughness on bacterial adhesion and viability, silicon wafers were etched for different periods of time, resulting in rough surfaces with 'spiky' structures and RMS roughnesses of 7 nm, 24 nm, and 35 nm. These roughnesses in the nano-range – and thus smaller than the diameter of bacterial cells or their contact areas – has consequences for the adhesive strength and viability of *S. aureus* on hydrophilic and hydrophobic surfaces, as discussed in the publication in Addendum V.

First, it should be mentioned that all surfaces used were characterized in great detail by Minkowski functionals, which were determined from height data of AFM images. This analysis showed that all surfaces are morphological equivalent and only the spatial dimensions of the surfaces structures increase for substrates with higher RMS roughness.

As on smooth wafers with different surface energies (see Paragraph 5.1.1), also on rough substrates, adhesion forces are much higher with lower standard deviations on hydrophobic surfaces compared to hydrophilic surfaces. Nevertheless, in principle, adhesion forces determined on hydrophilic and hydrophobic surfaces show similar dependencies on the surface roughness (see Figure 5.5 a and b): the higher the surface RMS roughness, the lower the adhesion force of *S. aureus* on these surfaces. Anyway, certain differences between the two sets of substrates (hydrophilic vs. hydrophobic) could be observed: while the adhesion forces on the hydrophilic substrates are almost identical for to two roughest substrates, the mean adhesion force on the hydrophobic surfaces differ for all investigated roughnesses. However, on the hydrophobic substrates, the mean adhesion force on the smooth surface

is the same as it is on the surface with 7 nm RMS roughness and, on the rougher surfaces, the mean adhesion forces decrease to approximately 60 % and 40 % on the surfaces with RMS values of 24 nm and 35 nm, respectively.

Assuming that thermally fluctuating bacterial cell wall macromolecules have an average thermal extension of about 50 nm [248], these results can be quantitatively explained by calculating the actual accessible surface area in dependence of the height from the top of the surface. For example, it showed that on the surface with an RMS roughness of 24 nm the cell wall macromolecules could reach about 50 % percent of the surface as compared to a smooth wafer. This fits well with the adhesion force data, because on the surface with 24 nm RMS roughness the adhesion force was also reduced to about 56(18) %.

In addition, the experiments on the hydrophobic substrates also showed an interesting correlation between the adhesion force on the smooth and rough surfaces (see Figure 5.5 c): the higher the adhesion force on the smooth surface, the lower the relative decrease of the adhesion force on the rough surfaces. In other words: if a cell has a rather low adhesion force on the smooth surface, the percentage decrease on the rough surfaces is greater than for cells that initially showed strong adhesion on the smooth surface. These observations could also be explained by the assumption that the pure number of tethering molecules of certain lengths is responsible for the adhesive strength and that this number must be quite high on hydrophobic surfaces (for details, see the publication in Addendum V).

Besides the adhesive strength, also the cells' viability was determined after SCFS and, additionally, in flow chamber measurements. Comparing both types of experiments, distinct differences were found that are also dependent on
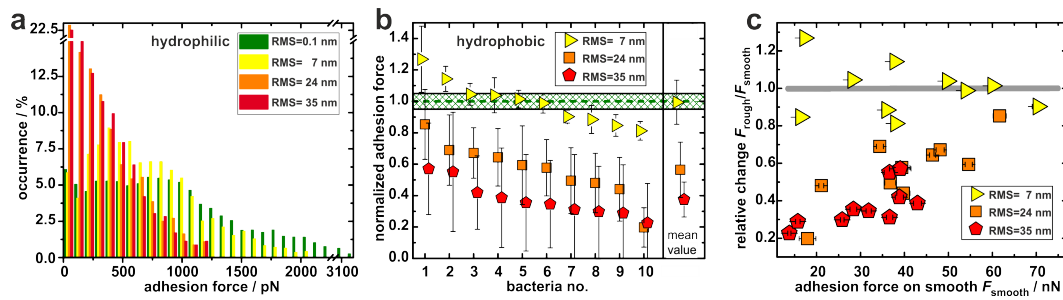
Figure 5.5. a) Histograms of adhesion forces of several *S. aureus* cells to hydrophilic surfaces of different roughnesses. b) Adhesion forces of several *S. aureus* cells to hydrophobic surfaces of different roughnesses (normalized to their adhesion force on smooth surfaces symbolized by the greenly shaded box). c) Relative change of the adhesion force on the rough hydrophobic surfaces in dependence of the adhesion force on the smooth hydrophobic surface.

the surface energy of the rough substrates. On the one hand, on the hydrophobic surface, after SCFS as well as during flow chamber experiments, some fraction of cells (approx. two-third after SCFS and approx. one-third in flow chamber measurements) were killed. On the other hand, SCFS killed all tested cells on the hydrophilic surface, whereas these surfaces did not affect the cells' viability in flow chamber experiments. These effects are attributed to differences in external forces on the cells and their individual cell wall robustness as it is discussed extensively in the publication in Addendum V.

The results regarding adhesion on the rough surfaces are similar to outcomes of other studies using surfaces with comparable RMS values that performed 'classical' adsorption experiments [228]. However, our SCFS experiments provide quantitative information about adhesion forces in dependence of surface roughness for two very different surface energies. Consequently, our results can help to design or modify surfaces where bacterial adhesion should be fostered or inhibited.

Considering the presented results on rough surfaces, the question arises whether the adhesive capability of one cell is the same on every spot of the cell's surface, i. e. everywhere within the contact area with the 'spiky' surface. One method to answer this question would be to immobilize the cells and to map their surfaces with functionalized AFM tips. Another method that is presented in the next section makes use of well-designed structured surfaces.

5.2.2 Sinusoidal Surface Structures

Purposeful structured surfaces were used to investigate if the adhesion capability of bacteria is heterogeneously distributed over their cell wall, a fact that is, for example, known for eucaryotic cells, which have specific spots of high adhesiveness (focal adhesion points) [190]. To do so, the adhesion of *S. aureus* cells on sinusoidal structured PDMS surfaces (characterized in Paragraph 4.1.3) was measured.

Thereby, single force-distance curves, with a lateral distance of 25 nm between each other, along a straight line, in direction of the sinu-

soidal structure were recorded. Because it was not possible to image the surface during force spectroscopy, another 'data channel' was used to gain lateral information about the position at the surface: for every curve, the 'absolute' height value (defined by internal settings of the instrument) at the moment when retraction started was recorded. As it can be seen in Figure 5.6 (orange line), these data show a certain regularity with the same periodicity as the sinusoidal surface structure. Therefore, with the help of these data, every force-distance curve can be assigned to a specific point relative to the sine structure on the surface.[1]
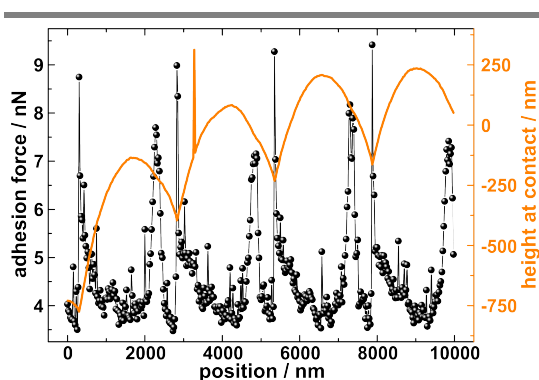
Figure 5.6. Adhesion force of one individual cell of *S. aureus* (black spheres) and height of the piezo electric crystal holding the cantilever at contact between cell and surface (orange line) in dependence of the position on sinusoidal structured PDMS.

Figure 5.6 exemplary shows the measured adhesion forces of one individual *S. aureus* cell together with the respective data of the height channel at the start of retraction from 400 sin-

---

[1]Notably, the data from the height sensor are not sinusoidal. This may be attributed to the fact that the probe (the bacterial cell) was not point-shaped but has a width of around 1 μm. Nevertheless, the data could be used to locate force-distance curves relative to the sine structure: local maxima were assigned to antinodes and minima to wave troughs of the sine.

gle force-distance curves with a lateral distance of 25 nm. In this visualization already, a certain regularity in the values of adhesion force is observable. For example, the highest adhesion forces always occur in the valleys of the surface.
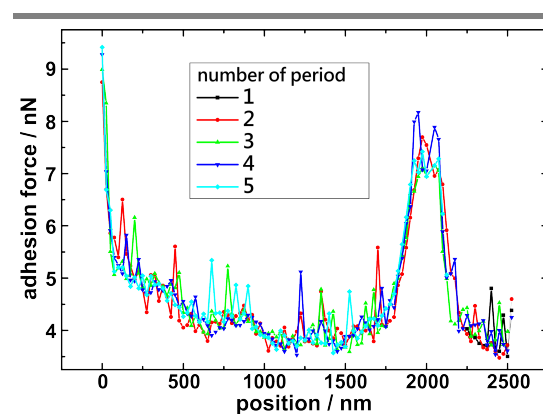
Figure 5.7. Overlay of the adhesion forces of one *S. aureus* cell measured on five different periods of the sinusoidal structured PDMS. (force trigger: 300 pN, ramp size: 800 nm, tip velocity: 800 nm/s)

The regularity becomes even clearer when the data of this specific cell are displayed as an overlay of each period on the sinusoidal surface as depicted in Figure 5.7. Differences in adhesion forces at the same point relative to the surface structure (same *x* value in Figure 5.7) are relatively small, as it is known for *S. aureus* cells adhering to flat hydrophobic surfaces [234].

However, the values of adhesion force vary for different positions on the period of the sine. This might be a combination of two effects: first, the contact area between cell and surface is not constant for different positions on one period. In the valley of the sine (in the graph located at $x = 0$ nm), for example, the contact area is most likely maximal. This easily explains the high values of adhesion force at

the beginning and end of the x-axis. On the maximum of the sine, contrarily, the contact area might be minimal. Secondly, the forces may vary on different positions because the angle between the local surface normal in the direction of the cantilever's retraction path is changed. At the maxima and minima of the surface, this angle is 0 ° while it could be up to 49 ° at the steepest point of the surface[2].

More interestingly, the measured data of adhesion force for different points do not reproduce the symmetry of the sinusoidal surface at all. Even if the contact area is not constant for different positions and the force depends on actual pulling directions, for a simple sphere (or even a sphere decorated with a homogeneous polymer layer), the measured values should be identical regardless if the right or left side of the – perfectly symmetrical – surface structure was in contact with the sphere. Obviously, this is not the case for the tested bacterial cell. In quite contrast, the cell shows a local maximum of adhesion at around $x = 2000$ nm while the corresponding symmetrical values at around $x = 700$ nm are much smaller.

The results of additional measurements with several individual bacterial cells are shown in Figure 5.8: the adhesion forces of five different cells were averaged over five periods of the sinusoidal PDMS surface and plotted against the position relative to the surface structure (where $x = 0$ nm is the minimum of the sine, see Figure 5.8 a). For all tested cells, the standard deviations on corresponding positions are small, and the data do not show the symmetry expected for homogeneous spheres. This asym-

metry is pronounced to a different extent for different individuals: while the cells in Figure 5.8 b and c have very peculiar variations in the adhesion forces at different relative positions, these variations are smaller for the cells depicted in Figure 5.8 d–f. Notably, the severity of the asymmetry is independent of the general adhesive strength of the individual cell (see different y-scales in Figure 5.8 b–f).

These measurements clearly demonstrated, for the first time, that the adhesion capability of *S. aureus* cells is heterogeneously distributed over the cell wall of individual cells. In particular, there can be certain areas that have a very high adhesive strength compared to the rest of the cell wall.

The reasons for this heterogeneity can be various. For example, it is possible that the age of the cell wall has a particular influence. It is known that there is a correlation between the production of certain adhesins and the cell cycle (see Paragraph 3.3.3). Therefore, it is possible that, for example, very recently built parts of the cell wall (e. g. near the septum) have a high local density of adhesion mediating proteins. It is also likely that under certain conditions adhesive macromolecules could be actively accumulated on specific spots on the cell wall when there is a need for high adhesive strength.

In order to gain further insights into the heterogeneity of the cell wall and its influence on adhesion, for future experiments, bacterial cells could be used in which certain parts of the cell wall are fluorescently labeled according to certain properties, such as their age [279]. The results of presented measurements on sinusoidal surfaces also hint to another possible explanation of the fact that different individual cells of *S. aureus* as well as *S. carnosus* show large differences in their

---

[2]To correct the forces for this error and, for example, to give normal forces seems difficult because of two reasons: i) the contact was not point-wise and the size of the contact area is unknown, ii) adhesion mediating cell wall molecules can stretch and change their direction with respect to the surface and the pulling direction.
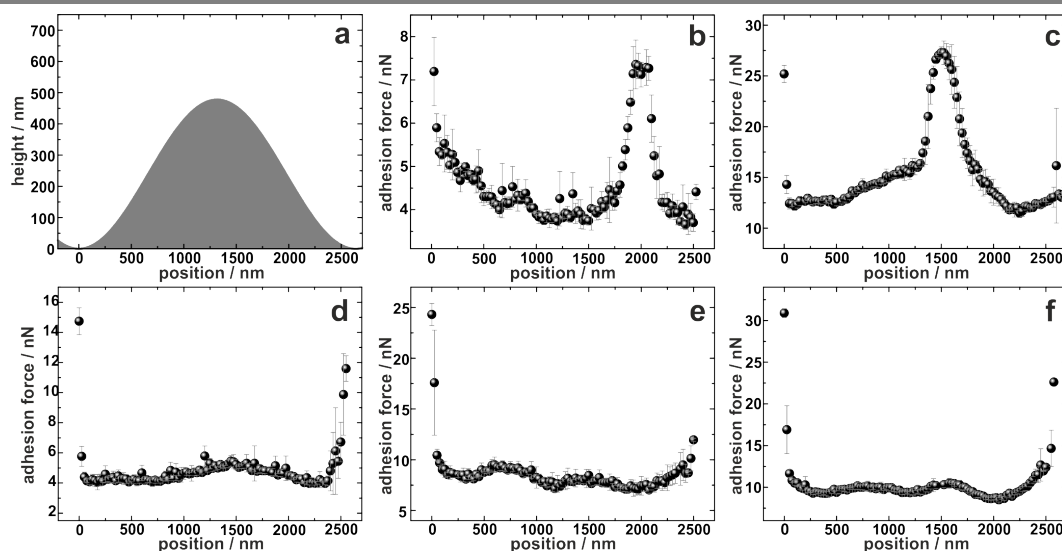
Figure 5.8. a) One exemplary period of the sinusoidal structured PDMS surface. b)–f) Average adhesion force of five individuals of *S. aureus* in dependence of the relative position on the surface according to the structure in a).

adhesive strength to flat hydrophobic surfaces (see Paragraph 5.1.3) [234].

An alternative way of structuring a surface is to coat it a with layer of another 'material'. Thereto, various materials could be used, e. g. polymer films, nanoparticles, or biological molecules. In the next paragraph, the ability of one specific group of biological molecules, namely spider silk proteins, to reduce bacterial adhesion is presented.

5.2.3 Adhesion to Spider Silk Coatings

To examine the effect of spider silk proteins on the adhesion of bacterial cells, silanized glass surfaces were covered with thin protein layers and the adhesion forces to these surfaces were compared to the adhesion forces to bare silanized glass substrates. For the experiments, two types of silk proteins were used:

i) fibroin, that was regenerated from the domestic silkmoth *Bombyx mori*, served as reference for a silk produced by insects [206]. ii) fibroin eADF4(C16), a well-establisehd recombinant spider silk protein, was synthesized based on 16 repeat units of the consensus sequence of core domain of fibroin originating from the dragline silk of the European garden spider *Araneus diadematus* [126].

By SCFS, it was shown that the fibrion produced by *Bombyx mori* reduces the adhesion of *S. aureus* cells by about a factor of six (three) for surface delay times of 0 s (5 s). Coatings of the synthetic eADF4(C16) have an even more drastic effect on adhesion: the adhesion force is reduced to approximately 2 % (8 %) for surface delay times of 0 s (5 s).

In addition, it was shown that these coatings are not only effective against *S. aureus*, but also against other bacterial species (*S. mutans*) and fungi, while simultaneously offering a good surface for the adherence and prolifera-

tion of mammalian cells. More details about the experiments, results and implications of spider silk materials can be found in the manuscript in Addendum VI.

So far, the adhesion of bacterial cells to abiotic surfaces and its dependence on different surface properties, such as hydrophobicity and morphology, has been presented. Consequently, in a next step, the system's complexity was increased by using surfaces that more closely resemble 'real' natural materials.

5.3 Adhesion in the Oral Environment

To mimic the situation in the oral cavity, *S. mutans* as bacteria and HAP pellets as surfaces were used the SCFS measurements. The HAP surfaces served as a substitute for real teeth with several benefits as compared to them: the HAP surfaces were polished to a very low roughness of less than 1 nm so that topographic effects (as shown to be important in Section 5.2) can be excluded. Real teeth, in contrast, have a hierarchically structured surface composed of crystallites with a size in the micron range [83]. The HAP substrates are completely inorganic and, therefore, not subject to any natural organic degradation processes. Additionally, every real tooth has its own 'history' (dependent of the individual that is was taken from and its health, diet, and exposition to other environmental influences [275]) whereas this does not apply to the HAP samples that are produced from well-known chemicals after a standard recipe.

In the publication in Addendum VII an exact recipe for the production and final treatment of these samples is given. Additionally, an elaborate characterization of these surfaces in terms

of chemical composition and surface properties can be found.

5.3.1 Influence of Saliva Inoculation

To mimic not only teeth surfaces but to study also the effect of the liquid environment in the oral cavity, experiments with *S. mutans* after exposure to human saliva were conducted. The results are presented in the publication in Addendum VIII. More precisely, several SCFS measurements were done on HAP in a first step. Then, the same cell was immersed in filtered human saliva for 30 min and afterwards rinsed thoroughly. Finally, the adhesion of the same cell on HAP was measured again.

In general, regardless of the saliva treatment, the adhesive strength of *S. mutans* to HAP is rather weak but increases with longer surface delay times (up to 5 s were used for these experiments). Experiments also showed certain variations: for some curves, there is no adhesion at all whereas there are distinct adhesive events for other curves.
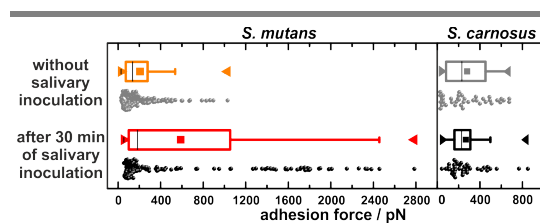
Figure 5.9. Boxplot representation of the adhesion forces of ten individuals of *S. mutans* (and for comparison, of five individuals of *S. carnosus*) determined from about 800 single force-distance curves before and after saliva inoculation (for a surface delay time of 5 s).

After the cells were exposed to saliva, the number of these adhesive events increases significantly for *S. mutans* cells (see Figure 5.9). In these events, also the adhesion force, ad-

hesion energy, and rupture length increase. In fact, the adhesion energy increases most strongly because it is – simply spoken – the combination and 'multiplication' of increased adhesion forces and rupture lengths. These effects are more pronounced for longer surface delay times.

In very contrast to *S. mutans* cells, the effect of enhanced adhesive strength cannot be observed or is much less pronounced for *S. carnosus* cells. For example, while adhesion energies of both species were in the same range before inoculation, they differ by one order of magnitude or more after inoculation (see Figure 5.9).

The experiments discussed in the publication in Addendum VIII showed that *S. mutans* cells adapt well to their natural environment, the oral cavity. This adaption could achieved either by the specific accumulation of adhesive molecules from the saliva or by production of these substances by the cells themselves when they are exposed to salivary components.

In addition, these results may have an impact on the methodology of future research: in adhesion experiments, not only the cells and surfaces of interest should be carefully chosen, but also the medium in which experiments are performed. This is particularly important as the measured effects may not be limited to bacteria in the oral, salivary environment, but may also apply to cells that naturally occur in other typical locations, such as the bloodstream or the urinary tract.

6. Conclusions

6.1 Summary

In the present thesis, the understanding of bacterial adhesion to solid surfaces was improved by experiments that specifically addressed different aspects of the bacterial attachment and detachment process.

The method of choice was AFM-based force spectroscopy with single bacterial cells. In the course of this work, a recipe for SCFS was established that is universal and not restricted to certain surfaces, liquid media, or specific types of cells. In fact, one and the same cell can be used to directly determine the effect of changing parameters. To study adhesion in detail, the bacterial cells, as well as the surfaces, were modified in certain ways suitable to investigate specific aspects of adhesion.

As a basis for all experiments, the adhesion of *S. aureus* to hydrophilic and hydrophobic surfaces was extensively characterized. Not only adhesion force but also different other measures (snap-in separation, rupture length, ...) were analyzed. Thereby, it was shown that on hydrophobic surfaces, adhesive strength is mainly determined by the pure number of tethering cell wall macromolecules, while on hydrophilic surfaces, in every single adhesion event, only few stochastic binding processes play the major role. Consequently, adhesion to low energy surfaces is much stronger than to high energy surfaces. Further, by using knockout mutant cells, it was shown that not only one type of molecules but rather many different groups of cell wall macromolecules are involved in the process of adhesion.

By using tailored substrates of locally differing surface energy, the contact area between staphylococcal cells and flat surfaces could be determined experimentally for the first time. The results can help to improve state-of-the-art models capturing bacterial adhesion and show in particular that Hertzian contact mechanics are not sufficient to describe biological adhesion phenomena. Moreover, it was shown that the contact area is a cell-individual property and does not correlate with the adhesive strength of the cells.

Adhesion measurements on regularly structured low-energy surfaces showed that the adhesion ability is not only cell-specific but also heterogeneously distributed over the surface of individual cells: while some parts of the cell envelope may exhibit relatively high adhesion, other equivalent regions could be much less adhesive. The origin of this heterogeneous cell wall properties might be the different age of various parts of the cell wall.

The use of nano-rough surfaces revealed that the adhesiveness of *S. aureus* cells is sensitive to differences in surfaces roughness with dimensions in the size range of the cell wall macromolecules. On hydrophobic and hydrophilic surfaces, greater roughnesses led to reduced adhesion of individual cells. This loss of adhesive strength on hydrophobic surfaces could be directly related to the reduction of accessible surface area for fluctuating cell wall macromolecules of certain lengths. In addition, the surfaces had an influence on the viability of the cells: depending on the surface energy and the experimental method, different

fractions of cells were killed on the nano-rough surfaces, most likely due to a loss of cell wall integrity after penetration by sharp surface features.

Experiments in which *S. mutans* cells were enzymatically treated by exposure to a salivary environment showed that the adhesive power of the cells can adapt to external factors. This might be an evolutionary advantageous property that is not limited to the tested cells but can be transferred to many other species and experimental conditions.

6.2 Outlook

Several follow-up experiments directly related to the experiments of this work are conceivable which would directly complement some of the results. For example, the contact area of other cell types could be measured with the same experimental setup. Going into more detail, the exact shape of the contact area could be gauged with the help of the OTS stripes introduced in the materials section. Furthermore, the heterogeneous distribution of adhesion ability should also be verified for hydrophilic surfaces.

The universality of the concepts presented should be investigated by other cells. Gram-negative bacterial cells can be used to test whether their adhesion shows the same differences on hydrophobic and hydrophilic surfaces. Cells of different shapes can also be tested for the size of their contact area. In particular, these experiments are not limited to bacteria and can also be performed with other organisms in which, for example, *candida albicans* stands to reason.

Another aspect is certainly the step of getting from the laboratory *in vitro* system gradually closer to the real *in vivo* situation. In a first step, this could include the use of more 'real life' surfaces, which means that they are,

for example, conditioned by pre-adsorbed layers of proteins or other molecules, such as sugars or lipids. With regard to these layers, rather specific interactions are to be expected, which do not play a role in the experiments presented in this thesis.

In vivo situations also include the measurements of forces between cells and surfaces after prolonged contact time. Especially in biofilms, the bacterial cells live for days or even longer in this environment and are, additionally, in contact with extracellular substances of many other organisms.

A promising way to explore these rather complex scenarios is the coupling of different experimental techniques. For example, the combination of AFM and high-resolution fluorescence microscopy seems to have enormous potential to investigate forces in microbial colonies under *in vivo* conditions.

Altogether, the mentioned future experiments can have different effects. They can lead to improvements in the theoretical model of bacterial adhesion and – on the more application-oriented site – help to design surfaces or processes that can promote or hinder microbial adhesion, viability, and growth.

Bibliography

[1] J Abranches, L Zeng, M Bélanger, P H Rodrigues, P J Simpson-Haidaris, D Akin, W A Dunn Jr, A Progulske-Fox, and R A Burne. Invasion of human coronary artery endothelial cells by *Streptococcus mutans* OMZ175. *Oral Microbiology and Immunology*, **24**(2):141–145, 2009.

[2] F Agerer, S Lux, A Michel, M Rohde, K Ohlsen, and C R Hauck. Cellular invasion by *Staphylococcus aureus* reveals a functional link between focal adhesion kinase and cortactin in integrin-mediated internalisation. *Journal of Cell Science*, **118**(10):2189–2200, 2005.

[3] S Ahn, S Ahn, Z T Wen, L J Brady, and R A Burne. Characteristics of biofilm formation by *Streptococcus mutans* in the presence of saliva. *Infection and Immunity*, **76**(9):4259–4268, 2008.

[4] I Alkorta and J Elguero. Non-conventional hydrogen bonds. *Chemical Society Reviews*, **27**(2):163–170, 1998.

[5] R K Alla, K Ginjupalli, N Upadhya, M Shammas, R K Ravi, and R Sekhar. Surface Roughness of Implants: A Review. *Trends in Biomaterials and Artificial Organs*, **25**(3):112–118, 2011.

[6] A Almaguer-Flores, R Olivares-Navarrete, M Wieland, L A Ximénez-Fyvie, Z Schwartz, and B D Boyan. Influence of topography and hydrophilicity on initial oral biofilm formation on microstructured titanium surfaces *in vitro*. *Clinical Oral Implants Research*, **23**(3):301–307, 2011.

[7] D Alsteens, A Beaussart, S El-Kirat-Chatel, R M A Sullan, and Y F Dufrêne. Atomic force microscopy: a new look at pathogens. *PLoS Pathogens*, **9**(9):e1003516, 2013.

[8] D Alsteens, M C Garcia, P N Lipke, and Y F Dufrêne. Force-induced formation and propagation of adhesion nanodomains in living fungal cells. *Proceedings of the National Academy of Sciences*, **107**(48):20744–20749, 2010.

[9] D Alsteens, C B Ramsook, P N Lipke, and Y F Dufrêne. Unzipping a Functional Microbial Amyloid. *ACS Nano*, **6**(9):7703–7711, 2012.

[10] N Alva-Murillo, J E López-Meza, and A Ochoa-Zarzosa. Nonprofessional phagocytic cell receptors involved in *Staphylococcus aureus* internalization. *BioMed Research International*, **2014**:247, 2014.

[11] R A S Ariëns, T-S Lai, J W Weisel, C S Greenberg, and P J Grant. Role of factor XIII in fibrin clot formation and effects of genetic polymorphisms. *Blood*, **100**(3):743–754, 2002.

[12] J J Armstrong, J Baddiley, J G Buchanan, B Carss, and G R Greenberg. Isolation and structure of ribitol

phosphate derivatives (teichoic acids) from bacterial cell walls. *Journal of the Chemical Society (Resumed)*, pages 4344–4354, 1958.

[13] M J Arrizubieta, A Toledo-Arana, B Amorena, J R Penadés, and Í Lasa. Calcium Inhibits Bap-Dependent Multicellular Behavior in *Staphylococcus aureus*. *Journal of Bacteriology*, **186**(22):7490–7498, 2004.

[14] S Asakura and F Oosawa. On Interaction between Two Bodies Immersed in a Solution of Macromolecules. *The Journal of Chemical Physics*, **22**(7):1255–1256, 1954.

[15] S Asakura and F Oosawa. Interaction between particles suspended in solutions of macromolecules. *Journal of Polymer Science Part A: Polymer Chemistry*, **33**(126):183–192, 1958.

[16] M L Atilano, P M Pereira, J Yates, P Reed, H Veiga, M G Pinho, and S R Filipe. Teichoic acids are temporal and spatial regulators of peptidoglycan cross-linking in *Staphylococcus aureus*. *Proceedings of the National Academy of Sciences*, **107**(44):18991–18996, 2010.

[17] R G Bailey, R D Turner, N Mullin, N Clarke, S J Foster, and J K Hobbs. The Interplay Between Cell Wall Mechanical Properties and the Cell Cycle in *Staphylococcus aureus*. *Biophysical Journal*, **107**(11):2538–2545, 2014.

[18] C J Baker, D J Clark, and F F Barrett. Selective broth medium for isolation of group B streptococci. *Applied Microbiology*, **26**(6):884–885, 1973.

[19] P Ball. Water as an Active Constituent in Cell Biology. *Chemical Reviews*, **108**(1):74–108, 2008.

[20] S Banerjee, C C Lin, S Su, H F Chung, W Brandt, and K Tang. Cryogenic aerosol cleaning of photomasks. *Photomask and Next-Generation Lithography Mask Technology XII*, pages 90–99, 2005.

[21] C Barriere, S Leroy-Sétrin, and R Talon. Characterization of catalase and superoxide dismutase in *Staphylococcus carnosus* 833 strain. *Journal of Applied Microbiology*, **91**(3):514–519, 2001.

[22] K Bazaka, R J Crawford, and E P Ivanova. Do bacteria differentiate between degrees of nanoscale surface roughness? *Biotechnology Journal*, **6**(9):1103–1114, 2011.

[23] A Beaussart, S El-Kirat-Chatel, P Herman, D Alsteens, J Mahillon, Pl Hols, and Y F Dufrêne. Single-Cell Force Spectroscopy of Probiotic Bacteria. *Biophysical Journal*, **104**(9):1886–1892, 2013.

[24] R B Beevers and E F T White. Physical properties of vinyl polymers. Part 1.—Dependence of the glass-transition temperature of polymethylmethacrylate on molecular weight. *Transactions of the Faraday Society*, **56**:744–752, 1960.

[25] M Bellion, L Santen, H Mantz, H Hähl, A Quinn, A Nagel, C Gilow, C Weitenberg, Y Schmitt, and K Jacobs. Protein adsorption on tailored substrates: long-range forces and conformational changes. *Journal of Physics: Condensed Matter*, **20**(40):404226, 2008.

[26] A Bera, R Biswas, S Herbert, E Kulau-zovic, C Weidenmaier, A Peschel, and F Götz. Influence of Wall Teichoic Acid on Lysozyme Resistance in *Staphylococcus aureus*. *Journal of Bacteriology*, **189**(1):280–283, 2007.

[27] J M Berg, J L Tymoczko, and L Stryer. *Biochemie*. Spektrum Akademischer Verlag, 2003.

[28] Bharat Bhushan. *Springer Handbook of Nanotechnology*. Springer, 2017.

[29] R J Bingham, E Rudiño-Piñera, N A G Meenan, U Schwarz-Linek, J P Turkenburg, M Höök, E F Garman, and J R Potts. Crystal structures of fibronectin-binding sites from *Staphylococcus aureus* FnBPA in complex with fibronectin domains. *Proceedings of the National Academy of Sciences*, **105**(34):12254–12258, 2008.

[30] J O'M Bockris, MAV Devanathan, and K Muller. On the structure of charged interfaces. *Proceedings of the Royal Society A: Mathematical, Physical and Engineering Sciences*, **274**(1356):55–79, 1963.

[31] K Bosecker. Bioleaching: metal solubilization by microorganisms. *FEMS Microbiology Reviews*, **20**(3-4):591–604, 1997.

[32] A L Bottomley, A F Kabli, and A F Hurd. *Staphylococcus aureus* DivIB is a peptidoglycan-binding protein that is required for a morphological checkpoint in cell division. *Molecular Microbiology*, **94**(5):1041–1046, 2014.

[33] L Brown, J M Wolf, R Prados-Rosales, and A Casadevall. Through the wall: extracellular vesicles in Gram-positive bacteria, mycobacteria and fungi. *Nature Reviews Microbiology*, **13**(10):620–630, 2015.

[34] S Brown, J P Santa Maria Jr, and S Walker. Wall Teichoic Acids of Gram-Positive Bacteria. *Annual Review of Microbiology*, **67**(1):313–336, 2013.

[35] S Bur, K T Preissner, M Herrmann, and M Bischoff. The *Staphylococcus aureus* Extracellular Adherence Protein Promotes Bacterial Internalization by Keratinocytes Independent of Fibronectin-Binding Proteins. *Journal of Investigative Dermatology*, **133**(8):2004–2012, 2013.

[36] F Burkhardt and S al Dahouk. *Mikrobiologische Diagnostik: Bakteriologie-Mykologie-Virologie-Parasitologie*, volume 34. Georg Thieme Verlag, 2009.

[37] H-J Butt and M Kappl. *Surface and Interfacial Forces*. Wiley-VCH, 2010.

[38] L Cai, N Friedman, and X S Xie. Stochastic protein expression in individual cells at the single molecule level. *Nature*, **440**(7082):358–362, 2006.

[39] N A Campbell and J B Reece. *Biologie*. Pearson Studium, 2015.

[40] M Campos and C Jacobs-Wagner. Cellular organization of the transfer of genetic information. *Current Opinion in Microbiology*, **16**(2):171–176, 2013.

[41] J M Castillo, M Klos, K Jacobs, M Horsch, and H Hasse. Characterization of Alkylsilane Self-Assembled Monolayers by Molecular Simulation. *Langmuir*, **31**(9):2630–2638, 2015.

[42] D Chandler. Interfaces and the driving force of hydrophobic assembly. *Nature*, **437**(7059):640–647, 2005.

[43] D L Chapman. LI. A contribution to the theory of electrocapillarity. *The London, Edinburgh, and Dublin Philosophical Magazine and Journal of Science*, **25**(148):475–481, 1913.

[44] T Chavakis, K Wiechmann, K T Preissner, and M Herrmann. *Staphylococcus aureus* interactions with the endothelium. *Thrombosis and Haemostasis*, **94**(02):278–285, 2005.

[45] Y Chen, H J Busscher, H C van der Mei, and W Norde. Statistical Analysis of Long- and Short-Range Forces Involved in Bacterial Adhesion to Substratum Surfaces as Measured Using Atomic Force Microscopy. *Applied and Environmental Microbiology*, **77**(15):5065–5070, 2011.

[46] Y Chen, A K Harapanahalli, H J Busscher, W Norde, and H C van der Mei. Nanoscale Cell Wall Deformation Impacts Long-Range Bacterial Adhesion Forces on Surfaces. *Applied and Environmental Microbiology*, **80**(2):637–643, 2014.

[47] Y Chen, W Norde, H C van der Mei, and H J Busscher. Bacterial Cell Surface Deformation under External Loading. *mBio*, **3**(6):e00378–12, 2012.

[48] H K Christenson and P M Claesson. Direct measurements of the force between hydrophobic surfaces in water. *Advances in Colloid and Interface Science*, **91**(3):391–436, 2001.

[49] J Claes, T Vanassche, M Peetermans, L Liesenborghs, C Vandenbriele, K Vanhoorelbeke, D Missiakas, O Schneewind, M F Hoylaerts, R Heying, and P Verhamme. Adhesion of *Staphylococcus aureus* to the vessel wall under flow is mediated by von Willebrand factor–binding protein. *Blood*, **124**(10):1669–1676, 2014.

[50] J K Clarke. On the Bacterial Factor in the Aetiology of Dental Caries. *British journal of experimental pathology*, **5**(3):141–147, 1924.

[51] R Clausius. Über verschiedene für die Anwendung bequeme Formen der Hauptgleichungen der mechanischen Wärmetheorie. *Annalen der Physik und Chemie*, **201**(7):353–400, 1865.

[52] B E Conway. Transition from "supercapacitor" to "battery" behavior in electrochemical energy storage. *Journal of The Electrochemical Society*, **138**(6):1539–1548, 1991.

[53] P Cossart and R Jonquières. Sortase, a universal target for therapeutic agents against Gram-positive bacteria? *Proceedings of the National Academy of Sciences*, **97**(10):5013–5015, 2000.

[54] J W Costerton, K J Cheng, G G Geesey, T I Ladd, J C Nickel, M Dasgupta, and T J Marrie. Bacterial biofilms in nature and disease. *Annual Reviews in Microbiology*, **41**(1):435–464, 1987.

[55] J W Costerton, P S Stewart, and E P Greenberg. Bacterial biofilms: a common cause of persistent infections. *Science*, **284**(5418):1318–1322, 1999.

[56] A L Coykendall. Proposal to Elevate the Subspecies of *Streptococcus mutans* to Species Status, Based on Their Molecular Composition. *International Journal of Systematic and Evolutionary Microbiology*, **27**(1):26–30, 1977.

[57] C Cucarella, C Solano, J Valle, B Amorena, Í Lasa, and J R Penadés. Bap, a *Staphylococcus aureus* surface protein involved in biofilm formation. *Journal of Bacteriology*, **183**(9):2888–2896, 2001.

[58] X Cui, Y Koujima, H Seto, T Murakami, Y Hoshino, and Y Miura. Inhibition of Bacterial Adhesion on Hydroxyapatite Model Teeth by Surface Modification with PEGMA-Phosmer Copolymers. *ACS Biomaterials Science & Engineering*, **2**(2):205–212, 2016.

[59] C R Currie. A Community of Ants, Fungi, and Bacteria: A Multilateral Approach to Studying Symbiosis. *Annual Review of Microbiology*, **55**(1):357–380, 2001.

[60] C Dawes. What is the critical ph and why does a tooth dissolve in acid? *Journal-Canadian Dental Association*, **69**(11):722–725, 2003.

[61] C C C R De Carvalho. Biofilms: recent developments on an old battle. *Recent Patents on Biotechnology*, **1**(1):49–57, 2007.

[62] B L De Jonge, Y S Chang, D Gage, and A Tomasz. Peptidoglycan composition of a highly methicillin-resistant Staphylococcus aureus strain. The role of penicillin binding protein 2A. *Journal of Biological Chemistry*, **267**(16):11248–11254, 1992.

[63] P Debye and E Hückel. The theory of electrolytes. I. Lowering of freezing point and related phenomenaInterionic Attraction. *Phys. Z.*, **24**, 1923.

[64] M Dembo, D C Torney, K Saxman, and D Hammer. The reaction-limited kinetics of membrane-to-surface adhesion and detachment. *Proceedings of the Royal Society B*, **234**(1274):55–83, 1988.

[65] B V Derjaguin and L Landau. Theory of the Stability of Strongly Charged Lyophobic Sols and of the Adhesion of Strongly Charged Particles in Solutions of Electrolytes. *Acta Physicochim. URSS*, **14**(6):633–662, 1941.

[66] C Díaz, P L Schilardi, R C Salvarezza, and M Fernández Lorenzo de Mele. Nano/microscale Order Affects the Early Stages of Biofilm Formation on Metal Surfaces. *Langmuir*, **23**(22):11206–11210, 2007.

[67] D E Discher, P Janmey, and Y Wang. Tissue Cells Feel and Respond to the Stiffness of their Substrate. *Science*, **310**(5751):1139–1143, 2005.

[68] M E Dokukin and I Sokolov. Nanoscale compositional mapping of cells, tissues, and polymers with ringing mode of atomic force microscopy. *Scientific Reports*, **7**(1):11828, 2017.

[69] S H Donaldson Jr, A Røyne, K Kristiansen, M V Rapp, S Das, M A Gebbie, D W Lee, P Stock, M Valtiner, and J Israelachvili. Developing a General Interaction Potential for Hydrophobic and Hydrophilic Interactions. *Langmuir*, **31**(7):2051–2064, 2014.

[70] A Dreisbach, K Hempel, G Buist, M Hecker, D Becher, and J M van Dijl. Profiling the surfacome of *Staphylococcus aureus*. *Proteomics*, **10**(17):3082–3096, 2010.

[71] A Dreisbach, J M van Dijl, and G Buist. The cell surface proteome of *Staphylococcus aureus*. *Proteomics*, **11**(15):3154–3168, 2011.

[72] W A Ducker and D Mastropietro. Forces between extended hydrophobic solids: Is there a long-range hydrophobic force? *Current Opinion in Colloid & Interface Science*, **22**:51–58, 2016.

[73] Y F Dufrêne. Atomic Force Microscopy in Microbiology: New Structural and Functional Insights Into the Microbial Cell Surface. *mBio*, **5**(4):e01363–14, 2014.

[74] Y F Dufrêne and A E Pelling. Force nanoscopy of cell mechanics and cell adhesion. *Nanoscale*, **5**(10):4094–*–4104, 2013.

[75] W M Dunne. Bacterial adhesion: seen any good biofilms lately? *Clinical Microbiology Reviews*, **15**(2):155–166, 2002.

[76] V Dupres, D Alsteens, G Andre, and Y F Dufrêne. Microbial nanoscopy: a closer look at microbial cell surfaces. *Trends in Microbiology*, **18**(9):397–405, 2010.

[77] J Eisenbeis, H Peisker, C S Backes, S Bur, S Hölters, N Thewes, M Greiner, C Junker, E C Schwarz, M Hoth, K Junker, K T Preissner, K Jacobs, M Herrmann, and M Bischoff. The extracellular adherence protein (Eap) of Staphylococcus aureus acts as a proliferation and migration repressing factor that alters the cell morphology of keratinocytes. *International Journal of Medical Microbiology*, **307**(2):116–125, 2017.

[78] A J Engler, S Sen, H L Sweeney, and D E Discher. Matrix elasticity directs stem cell lineage specification. *Cell*, **126**(4):677–689, 2006.

[79] N Eroshenko, R Ramachandran, V K Yadavalli, and R R Rao. Effect of substrate stiffness on early human embryonic stem cell differentiation. *Journal of Biological Engineering*, **7**(1):7, 2013.

[80] E Fadeeva, V K Truong, M Stiesch, B N Chichkov, R J Crawford, J Wang, and E P Ivanova. Bacterial retention on superhydrophobic titanium surfaces fabricated by femtosecond laser ablation. *Langmuir*, **27**(6):3012–3019, 2011.

[81] E Fällman, S Schedin, J Jass, M Andersson, B E Uhlin, and O Axner. Optical tweezers based force measurement system for quantitating binding interactions: system design and application for the study of bacterial adhesion. *Biosensors and Bioelectronics*, **19**(11):1429–1437, 2004.

[82] D K Fimereli, K D Tsirigos, Z I Litou, T D Liakopoulos, P G Bagos, and S J Hamodrakas. Cw-pred: a hmm-based method for the classification of cell wall-anchored proteins of gram-positive bacteria. In *Hellenic Conference on Artificial Intelligence*, pages 285–290. Springer, 2012.

[83] A G Fincham, J Moradian-Oldak, and J P Simmer. The Structural Biology

of the Developing Dental Enamel Matrix. *Journal of Structural Biology*, **126**(3):270–299, 1999.

[84] E W Fischer. Orientierte Kristallisation des Polyäthylens auf Steinsalz. *Colloid & Polymer Science*, **159**(2):108–118, 1958.

[85] H C Flemming and J Wingender. Biofilme—die bevorzugte Lebensform der Bakterien: Flocken, Filme und Schlämme. *Biologie in unserer Zeit*, **31**(3):169–180, 2001.

[86] H-C Flemming and J Wingender. The biofilm matrix. *Nature Reviews Microbiology*, **8**(9):623–633, 2010.

[87] T Fließbach. *Statistische Physik*. Spektrum Akademischer Verlag, 1991.

[88] S H Flint, J D Brooks, and P J Bremer. Properties of the stainless steel substrate, influencing the adhesion of thermo-resistant streptococci. *Journal of Food Engineering*, **43**(4):235–242, 2000.

[89] T J Foster, J A Geoghegan, V K Ganesh, and M Höök. Adhesion, invasion and evasion: the many functions of the surface proteins of *Staphylococcus aureus*. *Nature Reviews Microbiology*, **12**(1):49–62, 2014.

[90] J Fréchette and T K Vanderlick. Double Layer Forces over Large Potential Ranges as Measured in an Electrochemical Surface Forces Apparatus. *Langmuir*, **17**(24):7620–7627, 2001.

[91] V K Ganesh, E M Barbu, C C S Deivanayagam, B Le, A S Anderson, Y V Matsuka, S L Lin, T J Foster, S V L

Narayana, and M Höök. Structural and Biochemical Characterization of *Staphylococcus aureus* Clumping Factor B/Ligand Interactions. *Journal of Biological Chemistry*, **286**(29):25963–25972, 2011.

[92] R S Gates and J R Pratt. Accurate and precise calibration of AFM cantilever spring constants using laser Doppler vibrometry. *Nanotechnology*, **23**(37):375702, 2012.

[93] B V Geisbrecht, B Y Hamaoka, B Perman, A Zemla, and D J Leahy. The Crystal Structures of EAP Domains from *Staphylococcus aureus* Reveal an Unexpected Homology to Bacterial Superantigens. *Journal of Biological Chemistry*, **280**(17):17243–17250, 2005.

[94] J A Geoghegan, R M Corrigan, D T Gruszka, P Speziale, J P O'Gara, J R Potts, and T J Foster. Role of Surface Protein SasG in Biofilm Formation by *Staphylococcus aureus*. *Journal of Bacteriology*, **192**(21):5663–5673, 2010.

[95] O G Gold, H V Jordan, and J Van Houte. A selective medium for *Streptococcus mutans*. *Archives of Oral Biology*, **18**(11):1357–1364, 1973.

[96] C Gómez-Suárez, H J Busscher, and H C van der Mei. Analysis of Bacterial Detachment from Substratum Surfaces by the Passage of Air-Liquid Interfaces. *Applied and Environmental Microbiology*, **67**(6):2531–2537, 2001.

[97] M Gouy. Sur la constitution de la charge électrique à la surface d'un électrolyte. *Journal of Physics*, **9**:457, 1913.

[98] D C Grahame. The Electrical Double Layer and the Theory of Electrocapillarity. *Chemical Reviews*, **41**(3):441–501, 1947.

[99] C Gram. Über die isolierte Färbung der Schizomyceten in Schnitt-und Trocken-präparaten. *Fortschritte der Medizin*, **2**:185–189, 1884.

[100] M Gross, S E Cramton, F Götz, and A Peschel. Key Role of Teichoic Acid Net Charge in *Staphylococcus aureus* Colonization of Artificial Surfaces. *Infection and Immunity*, **69**(5):3423–3426, 2001.

[101] A Haggar, M Hussain, H Lönnies, M Herrmann, A Norrby-Teglund, and J-I Flock. Extracellular Adherence Protein from *Staphylococcus aureus* Enhances Internalization Into Eukaryotic Cells. *Infection and Immunity*, **71**(5):2310–2317, 2003.

[102] H Hähl, F Evers, S Grandthyll, M Paulus, C Sternemann, P Loskill, M Lessel, A K Hüsecken, T Brenner, M Tolan, and K Jacobs. Subsurface Influence on the Structure of Protein Adsorbates as Revealed by in Situ X-ray Reflectivity. *Langmuir*, **28**(20):7747–7756, 2012.

[103] L Hall-Stoodley, J W Costerton, and P Stoodley. Bacterial biofilms: from the Natural environment to infectious diseases. *Nature Reviews Microbiology*, **2**(2):95–108, 2004.

[104] S Hamada and H D Slade. Biology, Immunology, and Cariogenicity of *Streptococcus mutans*. *Microbiological Reviews*, **44**(2):331–384, 1980.

[105] H C Hamaker. The London—van der Waals attraction between spherical particles. *Physica*, **4**(10):1058–1072, 1937.

[106] M Hammel, D Němeček, J A Keightley, G J Thomas, and B V Geisbrecht. The *Staphylococcus aureus* extracellular adherence protein (Eap) adopts an elongated but structured conformation in solution. *Protein Science*, **16**(12):2605–2617, 2007.

[107] M U Hammer, T H Anderson, A Chaimovich, M S Shell, and J Israelachvili. The search for the hydrophobic force law. *Faraday Discussions*, **146**:299–308, 2010.

[108] C Hannig and M Hannig. The oral cavity—a key system to understand substratum-dependent bioadhesion on solid surfaces in man. *Clinical Oral Investigations*, **13**(2):123–139, 2009.

[109] L G Harris, S. J. Foster, and R G Richards. An introduction to Staphylococcus aureus, and techniques for identifying and quantifying S. aureus adhesins in relation to adhesion to biomaterials: review. *European Cells and Materials*, **4**:39–60, 2002.

[110] B J Hartman and A Tomasz. Low-affinity penicillin-binding protein associated with beta-lactam resistance in *Staphylococcus aureus*. *Journal of Bacteriology*, **158**(2):513–516, 1984.

[111] L O Heim, M Kappl, and H-J Butt. Tilt of Atomic Force Microscope Cantilevers: Effect on Spring Constant and Adhesion Measurements. *Langmuir*, **20**(7):2760–2764, 2004.

[112] M Helfman. Chemical aspects of dentistry. *Journal of Chemical Education*, **59**(8):666–668, 1982.

[113] K Hempel, J Pané-Farré, A Otto, S Sievers, M Hecker, and D Becher. Quantitative Cell Surface Proteome Profiling for SigB-Dependent Protein Expression in the Human Pathogen *Staphylococcus aureus* via Biotinylation Approach. *Journal of Proteome Research*, **9**(3):1579–1590, 2010.

[114] A T Henrici. Studies of Freshwater Bacteria: I. A Direct Microscopic Technique. *Journal of Bacteriology*, **25**(3):277–187, 1933.

[115] S Herbert, A-K Ziebandt, K Ohlsen, T Schäfer, M Hecker, D Albrecht, R Novick, and F Götz. Repair of Global Regulators in *Staphylococcus aureus* 8325 and Comparative Analysis with Other Clinical Isolates. *Infection and Immunity*, **78**(6):2877–2889, 2010.

[116] P Herman-Bausier, S El-Kirat-Chatel, T J Foster, J A Geoghegan, and Y F Dufrêne. *Staphylococcus aureus* Fibronectin-Binding Protein A Mediates Cell-Cell Adhesion Through Low-Affinity Homophilic Bonds. *mBio*, **6**(3):e00413–15, 2015.

[117] P Herman-Bausier, C Formosa-Dague, C Feuillie, C Valotteau, and Y F Dufrêne. Forces guiding staphylococcal adhesion. *Journal of Structural Biology*, **197**(1):65–69, 2017.

[118] Heinrich Hertz. Über die Berührung fester elastischer Körper. *Journal für die reine und angewandte Mathematik*, **92**:156–171, 1882.

[119] A I Hidron, J R Edwards, J Patel, T C Horan, D M Sievert, D A Pollock, and S K Fridkin. Antimicrobial-resistant pathogens associated with healthcare-associated infections: annual summary of data reported to the National Healthcare Safety Network at the Centers for Disease Control and Prevention, 2006–2007. *Infection Control & Hospital Epidemiology*, **29**(11):996–1011, 2008.

[120] P Hinterdorfer and Y F Dufrêne. Detection and localization of single molecular recognition events using atomic force microscopy. *Nature Methods*, **3**(5):347–355, 2006.

[121] A I Hochbaum and J Aizenberg. Bacteria pattern spontaneously on periodic nanostructure arrays. *Nano Letters*, **10**(9):3717–3721, 2010.

[122] H Hof and R Dörries. *Medizinische Mikrobiologie*. Thieme, 2014.

[123] A Horn, H G Schoberth, Se Hiltl, A Chiche, Q Wang, A Schweikart, A Fery, and A Böker. Nanostructured wrinkled surfaces for templating bio-nanoparticles—controlling and quantifying the degree of order. *Faraday Discussions*, **143**:143–150, 2009.

[124] R G Horn, D T Smith, and W Haller. Surface forces and viscosity of water measured between silica sheets. *Chemical Physics Letters*, **162**(4-5):404–408, 1989.

[125] L C Hsu, J Fang, D A Borca-Tasciuc, R W Worobo, and C I Moraru. Effect of Micro- and Nanoscale Topography on the Adhesion of Bacterial Cells to Solid Surfaces. *Applied and Environmental Microbiology*, **79**(8):2703–2712, 2013.

65

[126] D Huemmerich, C W Helsen, S Quedzuweit, J Oschmann, R Rudolph, and T Scheibel. Primary Structure Elements of Spider Dragline Silks and Their Contribution to Protein Solubility. *Biochemistry*, **43**(42):13604–13612, 2004.

[127] J L Hutter. Comment on Tilt of Atomic Force Microscope Cantilevers: Effect on Spring Constant and Adhesion Measurements. *Langmuir*, **21**(6):2630–2632, 2005.

[128] J L Hutter and J Bechhoefer. Calibration of atomic-force microscope tips. *Review of Scientific Instruments*, **64**(7):1868–1873, 1993.

[129] P Imming, C Sinning, and A Meyer. Drugs, their targets and the nature and number of drug targets. *Nature reviews Drug discovery*, **5**(10):821–834, 2006.

[130] S Iordanescu and M Surdeanu. Two Restriction and Modification Systems in *Staphylococcus aureus* NCTC8325. *Microbiology*, **96**(2):277–281, 1976.

[131] J Israelachvili. *Intermolecular and Surface Forces*. Academic Press, third edition edition, 2011.

[132] J Israelachvili and R Pashley. The hydrophobic interaction is long range, decaying exponentially with distance. *Nature*, **300**(5890):341–342, 1982.

[133] E P Ivanova, V K Truong, J Y Wang, C C Berndt, R T Jones, I I Yusuf, I Peake, H W Schmidt, C Fluke, D Barnes, and R J Crawford. Impact of Nanoscale Roughness of Titanium Thin Film Surfaces on Bacterial Retention. *Langmuir*, **26**(3):1973–1982, 2009.

[134] E P Ivanova, V K Truong, H K Webb, V A Baulin, Js Y Wang, N Mohammodi, F Wang, C Fluke, and R J Crawford. Differential attraction and repulsion of *Staphylococcus aureus* and *Pseudomonas aeruginosa* on molecularly smooth titanium films. *Scientific Reports*, **1**:165, 2011.

[135] Z Jaglic, M Desvaux, A Weiss, L L Nesse, R L Meyer, K Demnerova, H Schmidt, E Giaouris, A Sipailiene, P Teixeira, M Kačániová, C U Riedel, and S Knøchel. Surface adhesins and exopolymers of selected foodborne pathogens. *Microbiology*, **160**(12):2561–2582, 2014.

[136] Z Jahed, P Lin, B B Seo, M S Verma, F X Gu, T Y Tsui, and M R K Mofrad. Responses of *Staphylococcus aureus* bacterial cells to nanocrystalline nickel nanostructures. *Biomaterials*, **35**(14):4249–4254, 2014.

[137] M Johnsson, M J Levine, and G H Nancollas. Hydroxyapatite Binding Domains in Salivary Proteins. *Critical Reviews in Oral Biology & Medicine*, **4**(3):371–378, 1993.

[138] J E Jones. On the Determination of Molecular Fields. II. From the Equation of State of a Gas. *Proceedings of the Royal Society A: Mathematical, Physical and Engineering Sciences*, **106**(738):463–477, 1924.

[139] A M Jorge, E Hoiczyk, J P Gomes, and M G Pinho. EzrA Contributes to the Regulation of Cell Size in *Staphylococcus aureus*. *PLoS ONE*, **6**(11):e27542, 2011.

[140] J M P Kanth, S Vemparala, and R Anishetty. Long-distance correlations in molecular orientations of liquid water and shape-dependent hydrophobic force. *Physical Review E*, **81**(2):021201, 2010.

[141] J B Kaplan, E A Izano, P Gopal, M T Karwacki, S Kim, J L Bose, K W Bayles, and A R Horswill. Low Levels of β-Lactam Antibiotics Induce Extracellular DNA Release and Biofilm Formation in *Staphylococcus aureus*. *mBio*, **3**(4):e00198–12, 2012.

[142] A W Karchmer and A S Bayer. Methicillin-Resistant *Staphylococcus aureus*: An Evolving Clinical Challenge. *Clinical Infectious Diseases*, **46**(S5):342–343, 2008.

[143] W Kauzmann. Some Factors in the Interpretation of Protein Denaturation. *Advances in Protein Chemistry*, **14**:1–63, 1959.

[144] B J Kirby and E F Hasselbrink. Zeta potential of microfluidic substrates: 1. Theory, experimental techniques, and effects on separations. *Electrophoresis*, **25**(2):187–202, 2004.

[145] R M Klevens, M A Morrison, J Nadle, S Petit, K Gershman, S Ray, L H Harrison, R Lynfield, G Dumyati, J M Townes, A S Craig, E R Zell, G E Fosheim, L K McDouglas, R B Carey, and S K Fridkin. Invasive Methicillin-Resistant *Staphylococcus aureus* Infections in the United States. *JAMA*, **298**(15):1763–1771, 2007.

[146] M Klos. Exploring the Boundary Condition of Polymeric Liquids–Experiments and MD Simulations. *Dissertation, Saarland University*, 2016.

[147] S Koynov, M S Brandt, and M Stutzmann. Black nonreflecting silicon surfaces for solar cells. *Applied Physics Letters*, **88**(20):203107, 2006.

[148] B N Kreiswirth, S Löfdahl, M J Betley, M O'Reilly, P M Schlievert, M S Bergdoll, and R P Novick. The toxic shock syndrome exotoxin structural gene is not detectably transmitted by a prophage. *Nature*, **305**(5936):709–712, 1983.

[149] L D Landau and E M Lifschitz. *Lehrbuch der theoretischen Physik – Statistische Physik*. Harri Deutsch, 1991.

[150] D Leckband and J Israelachvili. Intermolecular forces in biology. *Quarterly Reviews of Biophysics*, **34**(2):105–267, 2001.

[151] T O Leiknes and H Ødegaard. The development of a biofilm membrane bioreactor. *Desalination*, **202**(1-3):135–143, 2007.

[152] J E Lennard-Jones. Cohesion. *Proceedings of the Physical Society*, **43**(5):461–482, 1931.

[153] M Lessel, O Bäumchen, M Klos, H Hähl, R Fetzer, M Paulus, R Seemann, and K Jacobs. Self-assembled silane monolayers: an efficient step-by-step recipe for high-quality, low energy surfaces. *Surface and Interface Analysis*, **47**(5):557–564, 2015.

[154] M J Levine. Development of Artificial Salivas. *Critical Reviews in Oral Biology & Medicine*, **4**(3):279–286, 1993.

[155] G N Lewis. *Valence and the Structure of Atoms and Molecules*. Chemical Catalog Com.; New York, 1923.

[156] J A Lichter, M T Thompson, M Delgadillo, T Nishikawa, M F Rubner, and K J Van Vliet. Substrata Mechanical Stiffness Can Regulate Adhesion of Viable Bacteria. *Biomacromolecules*, **9**(6):1571–1578, 2008.

[157] H U Liepe and R Porobic. Influence of storage-conditions on sirvival rates and fermentative activity of lyophilized staphylococci. *Fleischwirtschaft*, **63**(11):1756–1757, 1983.

[158] E M Lifshitz. The theory of molecular attractive forces between solids. *Perspectives in Theoretical Physics*, pages 329–349, 1956.

[159] D Linke and A Goldmann, editors. *Bacterial Adhesion*. Springer Science+Media, 2011.

[160] L Liu, B Ercan, L Sun, K S Ziemer, and T J Webster. Understanding the Role of Polymer Surface Nanoscale Topography on Inhibiting Bacteria Adhesion and Growth. *ACS Biomaterials Science & Engineering*, **2**(1):122–130, 2015.

[161] Q Liu, K Ponnuraj, Y Xu, V K Ganesh, J Sillanpää, B E Murray, S V L Narayana, and M Höök. The *Enterococcus faecalis* MSCRAMM ACE Binds Its Ligand by the Collagen Hug Model. *Journal of Biological Chemistry*, **282**(27):19629–19637, 2007.

[162] Y Liu, J Strauss, and T A. Camesano. Adhesion forces between *Staphylococcus epidermidis* and surfaces bearing self-assembled monolayers in the presence of model proteins. *Biomaterials*, **29**(33):4374–4382, 2008.

[163] W J Loesche. Role of *Streptococcus mutans* in human dental decay. *Microbiological Reviews*, **50**(4):353–380, 1986.

[164] F London. The general theory of molecular forces. *Transactions of the Faraday Society*, **33**:8b–26, 1937.

[165] D López, H Vlamakis, and R Kolter. Biofilms. *Cold Spring Harbor Perspectives in Biology*, **2**(7):a000398, 2010.

[166] P Loskill, H Hähl, N Thewes, C T Kreis, M Bischoff, Mathias Herrmann, and Karin Jacobs. Influence of the Subsurface Composition of a Material on the Adhesion of Staphylococci. *Langmuir*, **28**(18):7242–7248, 2012.

[167] P Loskill, P M Pereira, P Jung, M Bischoff, M Herrmann, M G Pinho, and K Jacobs. Reduction of the peptidoglycan crosslinking causes a decrease in stiffness of the *Staphylococcus aureus* cell envelope. *Biophysical Journal*, **107**(5):1082–1089, 2014.

[168] P Loskill, J Puthoff, M Wilkinson, K Mecke, K Jacobs, and K Autumn. Macroscale adhesion of gecko setae reflects nanoscale differences in subsurface composition. *Journal of The Royal Society Interface*, **10**(78):20120587–20120587, 2012.

[169] F D Lowy. *Staphylococcus aureus* infections. *New England Journal of Medicine*, **339**(8):520–532, 1998.

[170] N Lu, W Zhang, Y Weng, X Chen, Y Cheng, and P Zhou. Fabrication of

PDMS surfaces with micro patterns and the effect of pattern sizes on bacteria adhesion. *Food Control*, **68**:344–351, 2016.

[171] H Lyklema. *Fundamentals of Interface and Colloid Science*, volume Volume 1. Academic Press, 2005.

[172] R Maoz and J Sagiv. On the formation and structure of self-assembling monolayers. I. A comparative atr-wettability study of Langmuir—Blodgett and adsorbed films on flat substrates and glass microbeads. *Journal of Colloid and Interface Science*, **100**(2):465–496, 1984.

[173] C Marcott, M Lo, K Kjoller, C Prater, and D P Gerrard. Applications of AFM-IR—Diverse Chemical Composition Analyses at Nanoscale Spatial Resolution. *Microscopy Today*, **20**(6):16–21, 2012.

[174] R A Marcus. On the Theory of Oxidation-Reduction Reactions Involving Electron Transfer. I. *The Journal of Chemical Physics*, **24**(5):966–978, 1956.

[175] J F Marko and E D Siggia. Stretching dna. *Macromolecules*, **28**(26):8759–8770, 1995.

[176] P Marsh and M Martin. *Oral Microbiology*, volume 1. Springer, 2013.

[177] M G Mazza. The physics of biofilms—an introduction. *Journal of Physics D: Applied Physics*, **49**(20):203001, 2016.

[178] S Meier, C Goerke, C Wolz, K Seidl, D Homerova, B Schulthess, J Kormanec, B Berger-Bachi, and

M Bischoff. σ^B and the σ^B-Dependent *arlRS* and *yabJ-spoVG* Loci Affect Capsule Formation in *Staphylococcus aureus*. *Infection and Immunity*, **75**(9):4562, 2007.

[179] J Mischo. Viabilität von *Staphylococcus aureus* auf Siliziumoberflächen mit variabler Rauheit. *Staatsexamensarbeit, Saarland University*, 2017.

[180] T J Mitchell. The pathogenesis of streptococcal infections: from Tooth decay to meningitis. *Nature Reviews Microbiology*, **1**(3):219–230, 2003.

[181] Monteiro, J M and Fernandes, P B and Vaz, F and Pereira, A R and Tavares, A C and Ferreira, M T and Pereira, P M and Veiga, H and Kuru, E and Van-Nieuwenhze, M S and Brun, Y V and Sérgio, R. Cell shape dynamics during the staphylococcal cell cycle. *Nature Communications*, **6**:8055, 2015.

[182] S C Morot-Bizot, S Leroy, and R Talon. Monitoring of staphylococcal starters in two French processing plants manufacturing dry fermented sausages. *Journal of Applied Microbiology*, **102**(1):238–244, 2007.

[183] C Müller, A Lüders, W Hoth-Hannig, M Hannig, and C Ziegler. Initial Bioadhesion on Dental Materials as a Function of Contact Time, pH, Surface Wettability, and Isoelectric Point. *Langmuir*, **26**(6):4136–4141, 2009.

[184] C Müller, J Wald, W Hoth-Hannig, N Umanskaya, D Scholz, M Hannig, and C Ziegler. Protein adhesion on dental surfaces—a combined surface analytical approach. *Analytical and Bio-*

analytical Chemistry, **400**(3):679–689, 2011.

[185] K Munk. *Mikribiologie*. Spektrum Akademischer Verlag, 2000.

[186] H Neubauer and F Götz. Physiology and interaction of nitrate and nitrite reduction in *Staphylococcus carnosus*. *Journal of Bacteriology*, **178**(7):2005–2009, 1996.

[187] H Neubauer, I Pantel, and F Götz. Molecular Characterization of the Nitrite-Reducing System of *Staphylococcus carnosus*. *Journal of Bacteriology*, **181**(5):1481–1488, 1999.

[188] R M Neumann. Entropic approach to Brownian movement. *American Journal of Physics*, **48**(5):354–357, 1980.

[189] C Nicolella, M C M Van Loosdrecht, and J J Heijnen. Wastewater treatment with particulate biofilm reactors. *Journal of Biotechnology*, **80**(1):1–33, 2000.

[190] C D Nobes and A Hall. Rho, rac, and cdc42 gtpases regulate the assembly of multimolecular focal complexes associated with actin stress fibers, lamellipodia, and filopodia. *Cell*, **81**(1):53–62, 1995.

[191] S Noimark, C W Dunnill, and M Wilson. The role of surfaces in catheter-associated infections. *Chemical Society Reviews*, **38**(12):3435–3448, 2009.

[192] F Nolle. Bakterienadhäsion auf nanostrukturierten Oberächen. *Master's Thesis, Saarland University*, 2017.

[193] A Olaya-Abril, I Jiménez-Munguía, L Gómez-Gascón, and M J Rodríguez-Ortega. Surfomics: Shaving live organisms for a fast proteomic identification of surface proteins. *Journal of Proteomics*, **97**:164–176, 2014.

[194] S Ostvar and B D Wood. Multi-scale Model Describing Bacterial Adhesion and Detachment. *Langmuir*, **32**(20):5213–5222, 2016.

[195] A Otto, J M van Dijl, M Hecker, and D Becher. The *Staphylococcus aureus* proteome. *International Journal of Medical Microbiology*, **304**(2):110–120, 2014.

[196] J Palmer, S Flint, and J Brooks. Bacterial cell attachment, the beginning of a biofilm. *Journal of Industrial Microbiology & Biotechnology*, **34**(9):577–588, 2007.

[197] W Pauli. Über den Zusammenhang des Abschlusses der Elektronengruppen im Atom mit der Komplexstruktur der Spektren. *Zeitschrift für Physik*, **31**(1):765–783, 1925.

[198] D Perera-Costa, J M Bruque, M L González-Martín, A C Gómez-García, and V Vadillo-Rodríguez. Studying the Influence of Surface Topography on Bacterial Adhesion Using Spatially Organized Microtopographic Surface Patterns. *Langmuir*, **30**(16):4633–4641, 2014.

[199] A Peschel, C Vuong, M Otto, and F Götz. The d-alanine residues of *Staphylococcus aureus* teichoic acids alter the susceptibility to vancomycin and the activity of autolytic enzymes. *Antimicrobial Agents and Chemotherapy*, **44**(10):2845–2847, 2000.

[200] K Ponnuraj, M G Bowden, S Davis, S Gurusiddappa, D Moore, D Choe, Y Xu, M Hook, and S V L Narayana. A "dock, lock, and latch" structural model for a staphylococcal adhesin binding to fibrinogen. *Cell*, **115**(2):217–228, 2003.

[201] A T Poortinga, R Bos, W Norde, and H J Busscher. Electric double layer interactions in bacterial adhesion to surfaces. *Surface science reports*, **47**(1):1–32, 2002.

[202] L M Prescott, J P Harley, and D A Klein. *Microbiology*. McGraw-Hill Higher Education, 2005.

[203] B J Privett, J Youn, S A Hong, J Lee, J Han, J H Shin, and M H Schoenfisch. Antibacterial fluorinated silica colloid superhydrophobic surfaces. *Langmuir*, **27**(15):9597–9601, 2011.

[204] S D Puckett, E Taylor, T Raimondo, and T J Webster. The relationship between the nanostructure of titanium surfaces and bacterial attachment. *Biomaterials*, **31**(4):706–713, 2010.

[205] R Raiteri, M Grattarola, and H-J Butt. Measuring Electrostatic Double-Layer Forces at High Surface Potentials with the Atomic Force Microscope. *The Journal of Physical Chemistry*, **100**(41):16700–16705, 1996.

[206] D N Rockwood, R C Preda, T Yücel, X Wang, M L Lovett, and D L Kaplan. Materials fabrication from *Bombyx mori* silk fibroin. *Nature Protocols*, **6**(10):1612, 2011.

[207] R Rosenstein, C Nerz, L Biswas, A Resch, G Raddatz, Stephan C Schuster, and F Götz. Genome Analysis of the Meat Starter Culture Bacterium *Staphylococcus carnosus* TM300. *Applied and Environmental Microbiology*, **75**(3):811–822, 2009.

[208] M Rubinstein and R H Colby. *Polymer Physics*. Oxford University Press, 2003.

[209] M Rüger, G Bensch, R Tüngler, and U Reichl. A flow cytometric method for viability assessment of *Staphylococcus aureus* and *Burkholderia cepacia* in mixed culture. *Cytometry Part A*, **81**(12):1055–1066, 2012.

[210] C J Rupp, C A Fux, and P Stoodley. Viscoelasticity of *Staphylococcus aureus* Biofilms in Response to Fluid Shear Allows Resistance to Detachment and Facilitates Rolling Migration. *Applied and Environmental Microbiology*, **71**(4):2175–2178, 2005.

[211] M A Ryder. Catheter-Related infections: It's All About Biofilm. *Topics in Advanced Practice Nursing Journal*, **5**(3):1–6, 2005.

[212] J E Sader, R Borgani, and C T Gibson. A virtual instrument to standardise the calibration of atomic force microscope cantilevers. *Review of Scientific Instruments*, **87**(9):093711, 2016.

[213] J E Sader, J A Sanelli, B D Adamson, J P Monty, X Wei, S A Crawford, J R Friend, I Marusic, P Mulvaney, and E J Bieske. Spring constant calibration of atomic force microscope cantilevers of arbitrary shape. *Review of Scientific Instruments*, **83**(10):103705, 2012.

[214] John E Sader, James W M Chon, and Paul Mulvaney. Calibration of rectangular atomic force microscope can-

tilevers. *Review of Scientific Instruments*, **70**(10):3967–3969, 1999.

[215] N Saha, C Monge, V Dulong, C Picart, and K Glinel. Influence of Polyelectrolyte Film Stiffness on Bacterial Growth. *Biomacromolecules*, **14**(2):520–528, 2013.

[216] B Salopek, D Krasic, and S Filipovic. Measurement and application of zeta-potential. *Rudarsko-geolosko-naftni zbornik*, **4**(1):147–151, 1992.

[217] J P Santa Maria, A Sadaka, S H Moussa, S Brown, Y J Zhang, E J Rubin, M S Gilmore, and S Walker. Compound-gene interaction mapping reveals distinct roles for *Staphylococcus aureus* teichoic acids. *Proceedings of the national academy of sciences*, **111**(34):12510–12515, 2014.

[218] K Sauer, A K Camper, G D Ehrlich, J W Costerton, and D G Davies. *Pseudomonas aeruginosa* Displays Multiple Phenotypes During Development as a Biofilm. *Journal of Bacteriology*, **184**(4):1140–1154, 2002.

[219] S Sauerbaum, H Hahn, G-D Burchard, S H E Kaufmann, and T F Schulz. *Medizinische Mikrobiologie and Infektiologie*. Springer, 2012.

[220] T R Scheuerman, A K Camper, and M A Hamilton. Effects of substratum topography on bacterial adhesion. *Journal of colloid and interface science*, **208**(1):23–33, 1998.

[221] H Schillers, C Rianna, J Schäpe, T Luque, H Doschke, M Wälte, J J Uriarte, N Campillo, G P A Michanetzis, J Bobrowska, A Dumitru, E T Herruzo, S Bovio, P Parot, M Galluzzi, A Podestà, L Puricelli, S Scheuring, Y Missirlis, R Garcia, M Odorico, J-M Teulon, F Lafont, M Lekka, F Rico, A Rigato, J-L Pellequer, H Oberleithner, D Navajas, and M Radmacher. Standardized Nanomechanical Atomic Force Microscopy Procedure (SNAP) for Measuring Soft and Biological Samples. *Scientific Reports*, **7**(1):5117, 2017.

[222] K H Schleifer and U Fischer. Description of a new species of the genus Staphylococcus: *Staphylococcus carnosus*. *International Journal of Systematic and Evolutionary Microbiology*, **32**(2):153–156, 1982.

[223] C U Schwermer, G Lavik, R M M Abed, B Dunsmore, T G Ferdelman, P Stoodley, A Gieseke, and D de Beer. Impact of Nitrate on the Structure and Function of Bacterial Biofilm Communities in Pipelines Used for Injection of Seawater into Oil Fields. *Applied and Environmental Microbiology*, **74**(9):2841–2851, 2008.

[224] R Seemann, S Herminghaus, and K Jacobs. Dewetting Patterns and Molecular Forces: A Reconciliation. *Physical Review Letters*, **86**(24):5534–5537, 2001.

[225] Y Seo and W Jhe. Atomic force microscopy and spectroscopy. *Reports on Progress in Physics*, **71**(1):016101, 2007.

[226] R Sherman and P Adams. Carbon Dioxide Snow Cleaning—The Next Generation of Clean. *Precision Cleaning 1996 Proceedings*, pages 290–299, 1996.

[227] T J Silhavy, D Kahne, and S Walker. The Bacterial Cell Envelope. *Cold*

Spring Harbor Perspectives in Biology, **2**(5):a000414, 2010.

[228] A V Singh, V Vyas, R Patil, V Sharma, P E Scopelliti, G Bongiorno, A Podesta, C Lenardi, W N Gade, and P Milani. Quantitative Characterization of the Influence of the Nanoscale Morphology of Nanostructured Surfaces on Bacterial Adhesion and Biofilm formation. *PLoS ONE*, **6**(9):e25029, 2011.

[229] A V Singh, V Vyas, T S Salve, D Cortelli, D Dellasega, A Podestà, P Milani, and W N Gade. Biofilm formation on nanostructured titanium oxide surfaces and a micro/nanofabrication-based preventive strategy using colloidal lithography. *Biofabrication*, **4**(2):025001, 2012.

[230] E V Sokurenko, V Vogel, and W E Thomas. Catch-bond mechanism of force-enhanced adhesion: counterintuitive, elusive, but... widespread? *Cell Host & Microbe*, **4**(4):314–323, 2008.

[231] N Solis, M R Larsen, and S J Cordwell. Improved accuracy of cell surface shaving proteomics in *Staphylococcus aureus* using a false-positive control. *Proteomics*, **10**(10):2037–2049, 2010.

[232] F Song and D Ren. Stiffness of Cross-Linked Poly(Dimethylsiloxane) affects Bacterial Adhesion and Antibiotic Susceptibility of Attached Cells. *Langmuir*, **30**(34):10354–10362, 2014.

[233] W Souheng, J Brandrup, E H Immergut, and E A Grulke. *Polymer Handbook*, volume Volume 6. John Wiley & Sons, 1999.

[234] C Spengler, N Thwes, F Nolle, M Bischof, and K Jacobs. Adhesion of *Staphylococcus aureus* and its Mutants to Abiotic Surfaces of Different Surface Energies. *unpublished*.

[235] C M Stafford, S Guo, C Harrison, and M Y M Chiang. Combinatorial and high-throughput measurements of the modulus of thin polymer films. *Review of Scientific Instruments*, **76**(6):062207, 2005.

[236] C M Stafford, C Harrison, K L Beers, A Karim, E J Amis, M R VanLandingham, H-C Kim, W Volksen, R D Miller, and E E Simonyi. A buckling-based metrology for measuring the elastic moduli of polymeric thin films. *Nature Materials*, **3**(8):545, 2004.

[237] O Stern. The theory of the electrolytic double-layer. *Z. Elektrochem.*, **30**:508–516, 1924.

[238] G Stirnemann, P J Rossky, J T Hynes, and D Laage. Water reorientation, hydrogen-bond dynamics and 2D-IR spectroscopy next to an extended hydrophobic surface. *Faraday Discussions*, **146**:263–281, 2010.

[239] R M Stöckle, Y D Suh, V Deckert, and R Zenobi. Nanoscale chemical analysis by tip-enhanced Raman spectroscopy. *Chemical Physics Letters*, **318**(1):131–136, 2000.

[240] R M A Sullan, J K Li, P J Crowley, L J Brady, and Y F Dufrêne. Binding Forces of Streptococcus mutans P1 Adhesin. *ACS Nano*, **9**(2):1448–1460, 2015.

[241] J G Swoboda, J Campbell, T C Meredith, and S Walker. Wall Teichoic acid Function, Biosynthesis, and Inhibition. *ChemBioChem*, **11**(1):35–45, 2010.

[242] R F Tabor, C Wu, F Grieser, R R Dagastine, and D Y C Chan. Measurement of the Hydrophobic Force in a Soft Matter System. *The Journal of Physical Chemistry Letters*, **4**(22):3872–3877, 2013.

[243] P Tang, W Zhang, Y Wang, B Zhang, H Wang, C Lin, and L Zhang. Effect of superhydrophobic surface of titanium on *Staphylococcus aureus* adhesion. *Journal of Nanomaterials*, **2011**:1–8, 2011.

[244] P L Taylor and J Tabachnik. Entropic forces—making the connection between mechanics and thermodynamics in an exactly soluble model. *European Journal of Physics*, **34**(3):729–736, 2013.

[245] A Thakur, A Chauhan, and M D P Willcox. Effect of lysozyme on adhesion and toxin release by *Staphylococcus aureus*. *Clinical & Experimental Ophthalmology*, **27**(3-4):224–227, 1999.

[246] N Thewes. Bacterial adhesion to abiotic surfaces: Atomic force spectroscopy and Monte Carlo simulations. *Dissertation, Saarland University*, 2016.

[247] N Thewes, P Loskill, P Jung, H Peisker, M Bischoff, M Herrmann, and K Jacobs. Hydrophobic interaction governs unspecific adhesion of staphylococci: a single cell force spectroscopy study. *Beilstein Journal of Nanotechnology*, **5**:1501–1512, 2014.

[248] N Thewes, A Thewes, P Loskill, H Peisker, M Bischoff, M Herrmann, L Santen, and K Jacobs. Stochastic binding of *Staphylococcus aureus* to hydrophobic surfaces. *Soft Matter*, **11**(46):8913–9046, 2015.

[249] L Thomer and O Schneewind. Pathogenesis of *Staphylococcus aureus* Bloodstream Infections. *Annual Review of Pathology: Mechanisms of Disease*, **11**(1):343–364, 2016.

[250] K M Thompson, N Abraham, and K K Jefferson. *Staphylococcus aureus* extracellular adherence protein contributes to biofilm formation in the presence of serum. *FEMS Microbiology Letters*, **305**(2):143–147, 2010.

[251] M T Tiedemann, N Muryoi, D E Heinrichs, and M J Stillman. Iron acquisition by the haem-binding Isd proteins in *Staphylococcus aureus*: studies of the mechanism using magnetic circular dichroism. *Biochemical Society Transactions*, **36**(6):1138–1143, 2008.

[252] S Tollis, A E Dart, G Tzircotis, and Rt G Endres. The zipper mechanism in phagocytosis: energetic requirements and variability in phagocytic cup shape. *BMC Systems Biology*, **4**(1):149, 2010.

[253] V K Truong, V T H Pham, A Medvedev, R Lapovok, Y Estrin, T C Lowe, V Baulin, V Boshkovikj, C J Fluke, R J Crawford, and E P Ivanova. Self-organised nanoarchitecture of titanium surfaces influences the attachment of *Staphylococcus aureus* and *Pseudomonas aeruginosa* bacteria. *Applied Microbiology and Biotechnology*, **99**(16):6831–6840, 2015.

[254] V K Truong, S Rundell, R Lapovok, Y Estrin, J Y Wang, C C Berndt, D G

Barnes, C J Fluke, R J Crawford, and E P Ivanova. Effect of ultrafine-grained titanium surfaces on adhesion of bacteria. *Applied Microbiology and Biotechnology*, **83**(5):925–937, 2009.

[255] R Turner, E Ratcliffe, R Wheeler, R Golestanian, J K Hobbs, and S J Foster. Peptidoglycan architecture can specify division planes in *Staphylococcus aureus*. *Nature Communications*, **1**:26, 2010.

[256] V Vadillo-Rodriguez, T J Beveridge, and J R Dutcher. Surface Viscoelasticity of Individual Gram-Negative Bacterial Cells Measured Using Atomic Force Microscopy. *Journal of bacteriology*, **190**(12):4225–4232, 2008.

[257] C Valotteau, V Prystopiuk, G Pietrocola, S Rindi, D Peterle, V De Filippis, T J Foster, P Speziale, and Y F Dufrêne. Single-Cell and Single-Molecule Analysis Unravels the Multifunctionality of the *Staphylococcus aureus* Collagen-Binding Protein Cna. *ACS Nano*, **11**(2):2160–2170, 2017.

[258] H C van der Mei, P Brokke, J Dankert, J Feijen, and H J Busscher. Influence of electrostatic interactions on the deposition efficiencies of coagulase-negative staphylococci to collector surfaces in a parallel plate flow chamber. *Journal of Dispersion Science and Technology*, **13**(4):447–458, 1992.

[259] H C van der Mei, M Rustema-Abbing, J de Vries, and H J Busscher. Bond Strengthening in Oral Bacterial Adhesion to Salivary Conditioning Films. *Applied and Environmental Microbiology*, **74**(17):5511–5515, 2008.

[260] C J Van Oss. Energetics of cell-cell and cell-biopolymer interactions. *Cell Biophysics*, **14**(1):1–16, 1989.

[261] C J van Oss. *Interfacial Forces in Aqueous Media*. CRC Press by Taylor & Francis Group, second edition edition, 2006.

[262] C J Van Oss, R F Giese, and P M Costanzo. Dlvo and non-dlvo interactions in hectorite. *Clays Clay Miner*, **38**(2):151–159, 1990.

[263] M F Q VandenBergh, E P F Yzerman, A van Belkum, H A M Boelens, M Sijmons, and H A Verbrugh. Follow-Up of *Staphylococcus aureus* Nasal Carriage after 8 Years: Redefining the Persistent Carrier State. *Journal of Clinical Microbiology*, **37**(10):3133–3140, 1999.

[264] C L Ventura, N Malachowa, C H Hammer, G A Nardone, M A Robinson, S D Kobayashi, and F R DeLeo. Identification of a Novel *Staphylococcus aureus* Two-Component Leukotoxin Using Cell Surface Proteomics. *PLoS ONE*, **5**(7):e11634, 2010.

[265] E J W Verwey and J T G Overbeek. *Theory of the Stability of Lyophobic Colloids*. Courier Corporation, 1999.

[266] S Vilain, J M Pretorius, J Theron, and V S Brözel. DNA as an adhesin: *Bacillus cereus* Requires Extracellular DNA to Form Biofilms. *Applied and Environmental Microbiology*, **75**(9):2861–2868, 2009.

[267] T Vissers, A T Brown, N Koumakis, A Dawson, M Hermes, J Schwarz-Linek, A B Schofield, J M French, V Koutsos, J Arlt, V A Martinze, and

W C K Poon. Bacteria as living patchy colloids: Phenotypic heterogeneity in surface adhesion. *Science Advances*, **4**(4):eaao1170, 2018.

[268] W Vollmer, D Blanot, and M A De Pedro. Peptidoglycan structure and architecture. *FEMS microbiology*, **32**(2):149–167, 2008.

[269] C Von Eiff, K Becker, K Machka, H Stammer, and G Peters. Nasal Carriage as a Source of *Staphylococcus aureus* Bacteremia. *New England Journal of Medicine*, **344**(1):11–16, 2001.

[270] C von Eiff, B Jansen, W Kohnen, and K Becker. Infections Associated with Medical Devices. *Drugs*, **65**(2):179–214, 2005.

[271] A Vrij. Polymers at interfaces and the interactions in colloidal dispersions. *Pure and Applied Chemistry*, **48**(4):471–483, 1976.

[272] E Wagner, J Doskar, and F Götz. Physical and genetic map of the genome of *Staphylococcus carnosus* TM300. *Microbiology*, **144**(2):509–517, 1998.

[273] J Wald, C Müller, M Wahl, M Kopnarski, and C Ziegler. ToF-SIMS investigations of adsorbed proteins on dental titanium. *Physica Status Solidi (a)*, **207**(4):831–836, 2010.

[274] J A Weatherell, C Robinson, and A S Hallsworth. Variations in the Chemical Composition of Human Enamel. *Journal of Dental Research*, **53**(2):180–192, 1974.

[275] J A Weatherell, C Robinson, and A S Hallsworth. Variations in the Chemical composition of Human Enamel. *Journal of Dental Research*, **53**(2):180–192, 1974.

[276] C Weidenmaier and A Peschel. Teichoic acids and related cell-wall glycopolymers in gram-positive physiology and host interactions. *Nature Reviews Microbiology*, **6**(4):276–287, 2008.

[277] A L Weisenhorn, H E Gaub, H G Hansma, R L Sinsheimer, G L Kelderman, and P K Hansma. Imaging single-stranded DNA, antigen-antibody reaction and polymerized Langmuir-Blodgett films with an atomic force microscope. *Scanning Microscopy*, **4**(3):511–516, 1990.

[278] H F L Wertheim, J Verveer, H A M Boelens, A Van Belkum, H A Verbrugh, and M C Vos. Effect of Mupirocin Treatment on Nasal, Pharyngeal, and Perineal Carriage of *Staphylococcus aureus* in Healthy Adults. *Antimicrobial Agents and Chemotherapy*, **49**(4):1465–1467, 2005.

[279] R Wheeler, R D Turner, R G Bailey, B Salamaga, S Mesnage, S A S Mohamad, E J Hayhurst, M Horsburgh, J K Hobbs, and S J Foster. Bacterial cell enlargement requires control of cell wall stiffness mediated by peptidoglycan hydrolases. *mBio*, **6**(4):e00660–15, 2015.

[280] R E O Williams. Healthy carriage of *Staphylococcus aureus*: its prevalence and importance. *Bacteriological Reviews*, **27**(1):56–71, 1963.

[281] J A Wu, C Kusuma, J J Mond, and J F Kokai-Kun. Lysostaphin Disrupts *Staphylococcus aureus* and *Staphylococcus epidermidis* Biofilms on Arti-

ficial Surfaces. *Antimicrobial Agents and Chemotherapy*, **47**(11):3407–3414, 2003.

[282] Y Wu, J P Zitelli, K S TenHuisen, X Yu, and M R Libera. Differential response of Staphylococci and osteoblasts to varying titanium surface roughness. *Biomaterials*, **32**(4):951–960, 2011.

[283] G Xia, T Kohler, and A Peschel. The wall teichoic acid and lipoteichoic acid polymers of Staphylococcus aureus. *International Journal of Medical Microbiology*, **300**(2):148–154, 2010.

[284] G Xia, T Kohler, and A Peschel. The wall teichoic acid and lipoteichoic acid polymers of *Staphylococcus aureus*. *International Journal of Medical Microbiology*, **300**(2):148–154, 2010.

[285] B-S Yeo, J Stadler, T Schmid, R Zenobi, and W Zhang. Tip-enhanced Raman Spectroscopy–Its status, challenges and future directions. *Chemical Physics Letters*, **472**(1-3):1–13, 2009.

[286] K Yoneda, T Nakagawa, O T Lawrence, J Huard, T Demitsu, Y Kubota, and R B Presland. Interaction of the Profilaggrin N-Terminal Domain with Loricrin in Human Cultured Keratinocytes and Epidermis. *Journal of Investigative Dermatology*, **132**(4):1206–1214, 2012.

[287] H Zhang and K-K Liu. Optical tweezers for single cells. *Journal of The Royal Society Interface*, **5**(24):671–690, 2008.

[288] C E Zobell and E C Allen. The Significance of Marine Bacteria in the Fouling of Submerged Surfaces. *Journal of bacteriology*, **29**(3):239, 1935.

Publications and Manuscripts

Addendum I – A Detailed Guideline for the Fabrication of Single Bacterial Probes Used for Atomic Force Spectroscopy

Authors: N. Thewes[1], P. Loskill[1], C. Spengler[1], S. Hümbert[1], M. Bischoff[2], and K. Jacobs[1]

[1] Department of Experimental Physics, Saarland University, 66041 Saarbrücken, Germany.
[2] The Institute of Medical Microbiology and Hygiene, Saarland University, 66421 Homburg/Saar, Germany.

Author contributions:
*The fabrication of 'bacterial probes' was developed by N. Thewes for single bacterial cells and the bacterial cluster probes were developed by P. Loskill and S. Hümbert. Protocols were drawn up by N. Thewes and **C. Spengler**. Experimental results were achieved by N. Thewes. The article was written by N. Thewes, **C. Spengler**, M. Bischoff and K. Jacobs. Scientific work was directed by M. Bischoff and K. Jacobs.*

Abstract - The atomic force microscope (AFM) evolved as a standard device in modern microbiological research. However, its capability as a sophisticated force sensor is not used to its full capacity. The AFM turns into a unique tool for quantitative adhesion research in bacteriology by using 'bacterial probes'. Thereby, bacterial probes are AFM cantilevers that provide a single bacterium or a cluster of bacteria as the contact-forming object. We present a step-by-step protocol for preparing bacterial probes, performing force spectroscopy experiments and processing force spectroscopy data. Additionally, we provide a general insight into the field of bacterial cell force spectroscopy.

Tips and Tricks

A detailed guideline for the fabrication of single bacterial probes used for atomic force spectroscopy

Nicolas Thewes[1,a], Peter Loskill[1,a], Christian Spengler[1], Sebastian Hümbert[1], Markus Bischoff[2], and Karin Jacobs[1,b]

[1] Experimental Physics, Campus E2 9, Saarland University, D-66123 Saarbrücken, Germany
[2] Institute of Medical Microbiology and Hygiene, Saarland University, D-66421 Homburg/Saar, Germany

Abstract. The atomic force microscope (AFM) evolved as a standard device in modern microbiological research. However, its capability as a sophisticated force sensor is not used to its full capacity. The AFM turns into a unique tool for quantitative adhesion research in bacteriology by using "bacterial probes". Thereby, bacterial probes are AFM cantilevers that provide a single bacterium or a cluster of bacteria as the contact-forming object. We present a step-by-step protocol for preparing bacterial probes, performing force spectroscopy experiments and processing force spectroscopy data. Additionally, we provide a general insight into the field of bacterial cell force spectroscopy.

1 Introduction

Infectious biofilms on implants or catheters cause serious medical problems that may lead to major medical intervention [1,2]. One key step in the development of a biofilm is the adhesion of bacteria to these medical devices. However, a fundamental understanding of the basic processes governing bacterial adhesion is still lacking [3]. Atomic force microscope (AFM) used in force spectroscopy mode is a promising technique to close this gap in knowledge. By attaching a single bacterium or a cluster of bacteria to an AFM cantilever, so called "bacterial probes" can be prepared, which allow studying the adhesion process of bacteria with nanometer spatial and piconewton force resolution [4–7].

This paper details a protocol for the fabrication of bacterial probes, both with a cluster of bacteria ("bacterial cluster probe", fig. 1a) or one single bacterium ("single bacterial probe", fig. 1b). Further, a detailed description of how to measure and process force spectroscopy data ("force/distance curves", fig. 1c) with bacterial probes will be given.

2 Bacterial cell force spectroscopy

Single cell force spectroscopy (SCFS) is a well-established method for the characterization of adhesive properties

Fig. 1. a) "Bacterial cluster probe", tipless cantilever covered with a large number of bacteria, b) "single bacterial probe", tipless cantilever with one single bacterial cell attached, c) representative force/distance curve taken with a single *S. aureus* cell adhering to a hydrophobized Si wafer in PBS buffer (for preparation of the hydrophobic substrate see ref. [8]). Approach (retraction) curve in blue (red).

of eukaryotic cells [9–12]. The concept of bacterial cell force spectroscopy is the logical continuation of SCFC to prokaryotic cells.

To perform AFM force spectroscopy experiments with bacterial probes, a single bacterium or a cluster of bacteria has to be immobilized on an AFM cantilever. For the immobilization, two parameters are of major importance, namely the geometry of the AFM tip and the selection of an appropriate glue, *i.e.* a glue that binds the bacteria strong enough to the cantilever to perform force measurements, without changing the properties of the bacterial cells.

ᵃ *Present address:* Dept. of Bioengineering and California Institute for Quantitative Biosciences (QB3), University of California at Berkeley, Berkeley, California 94720, USA.
ᵇ e-mail: k.jacobs@physik.uni-saarland.de
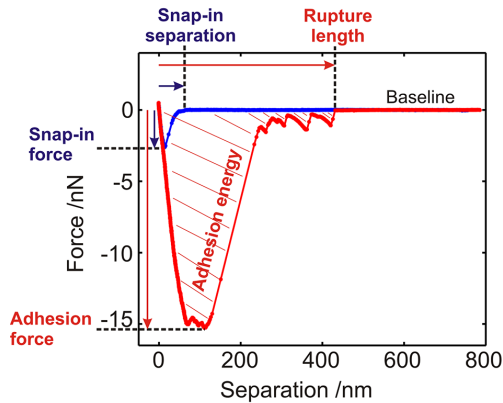
Fig. 2. Representative force/distance curve taken with a single *S. aureus* cell adhering on a hydrophobized Si wafer in PBS buffer. Approach (retraction) curve in blue (red). Fundamental measurands that characterize the bacterial adhesion process are highlighted.

The outcome of AFM force spectroscopy measurements with bacterial probes are called force/distance curves. Thereby, the force acting on the bacterium (attached to an AFM cantilever), is monitored as the cantilever (and the bacterium) is approached to the surface, pressed onto it with a certain maximum force (called "force trigger"), and retracted from the surface. Figure 1c and fig. 2 show a representative force/distance curve taken with a *Staphylococcus aureus* single bacterial probe; the approach and retraction curves are shown in blue and red, respectively. Force/distance curves allow to quantify bacterial adhesion by several means (cf. fig. 2): The range of attractive forces upon approach can be measured ("snap-in separation"), additionally the "snap-in force" is a measure for the strength of the attractive forces. During retraction, the lowest point of the curve determines the adhesion force of the bacterium and the distance where the adhesive contact is lost defines the "rupture length". Integrating over the area above the retraction curve provides the adhesion energy. Further quantitative parameters such as the separation of the adhesion peak, or the number and depth of secondary peaks can be evaluated depending on the experimental goal. Thus, AFM force spectroscopy with bacterial probes is a unique tool to gain access into bacterial adhesion in a quantitative manner.

2.1 Tip geometries

Various tip geometries can be used as a basis for bacterial probes. To implement experiments enabling both a large number of repetitions required in biological experiments and a large degree of control of experimental parameters, the number of immobilized bacteria needs to be controlled while keeping the preparation procedure as simple as possible. The most advanced bacterial probes feature one single immobilized bacterium (single bacterial probe) as this is the most precise way to characterize bacterial adhesion [7,13]. However, bacterial probes with a larger number of immobilized bacteria (bacterial cluster probes) may be used, as their preparation is less complex and time consuming [14,6]. When using bacterial cluster probes, on the one hand only measurements with the same bacterial probe are comparable, on the other hand the overall larger adhesion force and the averaging over many individual adhesion events can lead to better statistics of the measurements.

The most common tip geometry is the absence of a tip [5,15–18]. These so-called tipless cantilevers feature a large and accessible contact area. Functionalization with a glue and fixation of bacteria are straightforward in the case of tipless cantilevers.

Further typical tip geometries utilized as a basis for bacterial probes are spherical probes [19–21] and pyramidal tips [22–24]. Both spherical probes and pyramidal tips offer only a small contact area to the bacteria due to the curved and pointed geometry. Therefore, a high adhesive strength of the glue holding the bacteria onto the cantilevers is necessary. Moreover, it is challenging to place single bacteria at a specific spot, the apex of the tip or the topmost part of the sphere.

Here we detail a protocol using tipless cantilevers which possesses ease of use and, while using "single bacterial probes", ensures the comparability of different bacterial probes.

2.2 Immobilization methods

As mentioned above, the selection of the best suited glue is challenging due to two major requirements: On the one hand, bacteria have to be attached to the cantilever by a force that exceeds the adhesion force to the substrate under study. On the other hand, the viability and the properties of the bacterial cell wall that is not in contact with the cantilever should not be affected.

Various types of glues based on different binding mechanisms have been presented in the literature:

– Positively charged polymer coatings such as polyethyleneimine (PEI) [22,25] and poly-L-lysine (PLL) [16, 26] can be used, since the surfaces of both the bacterium and the cantilever, are negatively charged at a physiological pH. However, the effectivity of the electrostatic immobilization may decrease depending on the concentration of electrolytes.

– By using aminosilanes, -thiols [20,27], or (poly)dopamine (PDA) [28,5], the cantilevers can be functionalized with amino groups that can form strong, unspecific, covalent bonds with carboxyl groups that are accessible in the bacterial cell wall. Covalent binding between carboxyl and amino groups may be enhanced by 1-Ethyl-3-(3-dimethylaminopropyl)-carbodiimide/N-hydroxysuccinimide (EDC/NHS) treatment [29,30].

– Specific linkage can be achieved by coating the cantilevers with proteins serving as ligands for components of the bacterial cell wall (*i.e.* fibronectin-fibronectin binding proteins) [31,32]. Similarly, a commercially available cell adhesive protein derived from *Mytilus edulisi* (Cell-Tak^TM) was reported to be a suitable glue to immobilize bacterial cells [30,33].

Although approaches such as the use of regular glue (*e.g.* glass adhesive) have also been reported in the literature [15,34], a satisfactory fulfillment of the second requirement, the prevention of any alteration of the bacterium, is highly doubtful. The same is true for procedures involving a crosslinking via glutaraldehyde or formaldehyde [25,22], which are known to have an effect on the surface properties of the entire bacterium [35,36].

To immobilize bacterial cells, our protocol utilizes a polydopamin coating of AFM cantilevers that is inspired by a work by Lee *et al.* [37]. This coating combines ease of use with biological compatibility and durability [5,7,13].

2.3 Bacterial cluster force spectroscopy

The small size of bacterial cells makes their handling challenging, yet measuring the adhesion of bacterial cell clusters using "bacterial cluster probes" circumvents this problem [14,6]: These bacterial probes are much easier to produce, but lead to less controlled and less quantitative experimental results as the number of bacteria and the area of contact interacting with the respective surface is largely unknown. When comparing the adhesion to different surfaces, this problem can be handled by performing consecutive measurements on the surfaces of interest with the identical bacterial probe. The result, however, will always be a relative one, since absolute force values cannot be measured with this kind of probe. A comparison between different bacterial probes or different bacterial species is not possible [6]. Bacterial cluster probes are usually based on tipless cantilevers [18,6], some studies, however, describe the use of spherical tips [19] or even normal cantilevers, where the tip is covered with bacteria [23,14]. Another interesting approach is the application of an entire bacterial biofilm to a glass sphere attached to an AFM cantilever [38,39]. Regardless of the exact procedure, all of these bacterial cluster probes lack a certain level of control.

2.4 Single bacterial cell force spectroscopy

The problem of measuring adhesion in an absolute manner can be solved by controlling the number of adhering bacteria, at best by using only one bacterium ("single bacterial probes"). However, the accurate attachment of a single bacterium to an AFM cantilever is fairly impossible without adequate technical equipment, *e.g.* an AFM with an integrated inverted microscope [7,21] or a micromanipulation system [5,13]. The use of a single bacterial probe results in a highly controlled experiment in terms

of the load applied to the bacterium and the measured quantities, in particular the adhesion force. In addition, the viability of the characterized single bacterium can be checked by subsequent live/dead staining.

3 Experimental protocol

3.1 Fundamentals

3.1.1 AFM

We use a Bioscope Catalyst (Bruker-Nano, Santa Barbara, Ca, USA) for AFM bacterial cell force spectroscopy. Yet, the protocol detailed here does not require any special AFM model, except for the possibility of recording force/distance curves.

The following components are part of our AFM system:

1. BioScope Catalyst head ("head")

2. Nanoscope V controller ("controller")

3. BioScope Catalyst Electronics Interface Box ("E-Box")

4. BioScope Catalyst baseplate with sample holder plate ("sample holder")

5. EasyAlign for infrared laser alignment ("alignment station")

6. Joystick for controlling x, y, z motors

7. Nanoscope Software (version 8.15) ("software")

8. Probe holder for measurement in liquid

9. Mount for the probe holder while changing cantilever

10. Magnetic sample substrate clamps

3.1.2 Micromanipulation system

The components of our micromanipulation system are:

1. Inverted fluorescence light microscope Leica DMIL LED Flou

2. Micromanipulator Narishige MOM 202D

3. A homemade aluminum arm with a hole on its upper end (fig. 3a)

4. A small cross of PMMA that can be inserted into the aluminum arm (fig. 3b)

5. Double-sided adhesive tape

3.1.3 Cantilevers

The adhesion forces of bacteria can vary over a huge range of forces, from below 100 pN to several tenths of nN. Hence, some experience is necessary to identify the right cantilever spring constant, since stiff cantilevers allow the
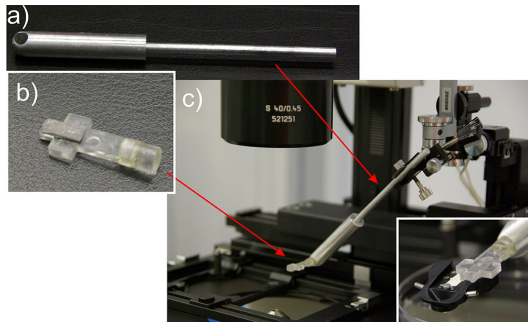
Fig. 3. a) Aluminium micromanipulation arm with a hole to insert the PMMA cross, b) PMMA cross with a small piece of double-sided adhesive tape, c) manipulation arm with PMMA cross inserted into the micromanipulator. The inset shows the cantilever holder attached to the PMMA cross.

measurement of higher forces but reduce the experimental resolution in terms of force. We use spring constants between 0.03 and 0.5 N/m depending on the expected forces during the adhesion process.

3.2 The protocol

3.2.1 Functionalization of the cantilever

This method of cantilever-functionalization is inspired by a publication by Lee *et al.* [37].

1. Take out as many cantilevers as you plan to use in today's experiment, and put them into a clean glass petri dish. The cantilever coating should be freshly prepared each day.

2. Cantilevers are cleaned in an air-plasma for 30 seconds, to get rid of any organic residues.

3. From now on, we perform every step under class 100 (less than 100 particles/ft^3) clean room conditions to reduce the risk of cantilever contamination (clean room conditions are helpful, yet might not be necessary).

4. Prepare a solution of 4 mg/ml dopamin hydrochloride (Sigma-Aldrich) in TRIS/HCL-Buffer (Sigma-Aldrich, 10 mMolar, pH 7.9 at 22 °C).

5. Dip the cantilevers vertically into the dopamin solution and store them for about one hour in the refrigerator.

6. Take the cantilevers out of the solution and rinse them carefully with ultrapure water (0.055 μS/cm at 26 °C).

7. Dry the cantilevers under vacuum (approx. 1 mbar) for about 15 minutes or under a laminar flow bench for at least one hour.

8. Proceed with the calibration of the cantilever.

3.2.2 Preparation of the substratum

The surface preparation very much depends on the type of substratum. Therefore, this issue is not detailed here. However, some fundamentals have to be obeyed irrespective of the exact surface: The surface has to be clean and inert concerning the used buffer solution and it must be fixed within the liquid cell (a petri dish or something similar) in order to prevent unwanted motion of the substratum. If using glue for fixation, it must not contaminate the buffer and should not dissolve. We use polystyrene of high molecular weight (780 kg/mol) dissolved in chloroform (in a concentration of 40-50 mg/ml), which works well in combination with polystyrene petri dishes. The chloroform evaporates fast and the residual polymer melt is a ideal non-dissolving glue.

3.2.3 Calibration of the cantilever

The calibration of the cantilever is a crucial step in AFM force spectroscopy. In order to be able to apply exact force values, calibration should be done before bacterial force spectroscopy measurements. If the single bacterium is attached using the AFM piezo drive, no difficulties will occur during this step (the protocol is the same) [21]. However, this protocol describes the attachment of a single bacterium via an external micromanipulation system. Therefore, the cantilever has to be removed from the AFM head after calibration. This step could result in a change of the deflection sensitivity since the laser spot has to be refocused after the reassembly of the cantilever into the AFM head. Yet, experience has shown that the deflection sensitivity does not change significantly if i) the laser position on the cantilever matches the position during calibration, which should be controlled by eye and ii) the laser sum is almost identical to before. In the following, we give step-by-step instructions for calibrating an AFM cantilever:

1. Check that AFM, computer, controller, and other AFM electronic devices as well as all necessary components of the optical microscope are turned on. Depending on the instruments, it may take a significant amount of time until *e.g.* thermal drifts have equilibrated.

2. Prepare everything for a contact mode experiment in liquid.

3. For the calibration of the cantilever, a hard (indeformable) sample should be used to determine the deflection sensitivity.

4. Insert the functionalized cantilever carefully into the cantilever holder that enables measurements in liquid and cover it with a droplet of liquid (*e.g.* PBS) to avoid contamination.

5. Integrate the cantilever holder into the AFM head.

6. Align the laser spot on the back of the cantilever maximising the sum of the voltage signal on the photodiode.

I. Addendum I – A Detailed Guideline for the Fabrication of Single Bacterial Probes Used for Atomic Force Spectroscopy

7. Place the cantilever over the hard sample surface to calibrate it.

8. Approach the surface to a distance of about $100\,\mu\mathrm{m}$ manually.

9. Give the AFM/cantilever some time to equilibrate, until a constant signal on the photodiode is reached.

10. Enter the deflection setpoint to approach the surface.

11. Start the approach.

12. As soon as the cantilever reaches the surface, change into ramp mode.

13. Give values for ramp rate (ramp size). Common values are between 0.5 and $1.5\,\mathrm{Hz}$ (600 to $1000\,\mathrm{nm}$).

14. Enter an approximate spring constant to perform the calibration force/distance curve. Usually, the value indicated by the manufacturer is sufficient at this point.

15. Enter a force trigger of 3–$8\,\mathrm{nN}$ (depending on the cantilever stiffness) and record one single force/distance curve.

16. To get a reliable value for the deflection sensitivity, a large, undisturbed, linear part in the contact regime of the force/distance curve is necessary. If the force curve does not exhibit an appropriate linear part, try a larger force trigger.

17. The deflection sensitivity is determined by calculating the inverse of the slope of the force/distance curve in the contact regime (this is usually implemented in the AFM software).

18. Update the deflection sensitivity.

19. Retract the cantilever from the surface.

20. To prepare for thermal tune, the influence of the surface must be excluded. Therefore, enlarge the distance between the surface and the cantilever. It should be at least $50\,\mu\mathrm{m}$.

21. Perform a thermal tune to determine the cantilever spring constant (details should be checked in the user manual of the respective AFM).

22. Update the spring constant and retract the cantilever completely.

23. Remove the cantilever holder (with cantilever) from the AFM. Care should be taken to maintain a small amount of liquid on the cantilever holder covering the cantilever to avoid contamination of the cantilever.

24. Go on with "attachment of bacteria".

3.2.4 Attachment of bacteria

In the following, we describe two different methods for attaching bacteria to a functionalized cantilever: i) A rather simple method to produce a bacterial probe with a cluster of attached bacteria, and ii) a more complex preparation for the attachment of a single bacterial cell to a tipless cantilever is detailed.

Bacterial cluster probe

1. Place the functionalized tipless cantilever on a hydrophobic surface. The side intended to carry the bacteria faces upwards.

2. Cover the cantilever with a droplet of bacterial solution ($\approx 60\,\mu\mathrm{l}$) and leave it in the refrigerator (to reduce Brownian motion) for at least one hour.

3. Remove the bacterial solution and rinse the cantilever carefully with PBS buffer to get rid of poorly attached bacteria.

4. By optical microscopy, verify that bacteria are attached close enough to the free end of the cantilever (not further away than roughly three bacterial diameters[1] to safely exclude cantilever/substrate interactions), while the cantilever stays in liquid the whole time. Ideally, this step is done using reflection optical microscopy. Alternatively, a transmission optical microscope can be used after integrating the cantilever into the cantilever holder for measurements in liquid and using a set-up similar to the one described in the section "single bacterial probe".

5. Integrate the cantilever into the probe holder for measurements in liquid and mount it to the AFM head.

6. Cover the cantilever immediately with a droplet of PBS to avoid drying.

Single bacterial probe

For the attachment of a single bacterium to a functionalized cantilever, a micromanipulation system is used. Stress due to capillary forces or drying should be avoided by maintaining bacterium as well as cantilever in liquid/buffer during the entire preparation procedure.

1. Put a plastic petri dish on the microscope of the micromanipulator.

2. Place a tiny droplet ($\approx 1\,\mu\mathrm{l}$) of bacterial solution on the petri dish.

3. Give the bacteria some minutes to sediment on the petri dish, without complete drying.

4. Insert the manipulation arm into the micromanipulator (cf. figs. 3a and c).

5. Put a small piece of the double-sided adhesive tape on the PMMA-cross (cf. fig. 3b).

6. Fix the cantilever holder with the cantilever and the covering droplet (resulting from the calibration step) on the PMMA-cross (cf. inset to fig. 3c)[2].

7. Insert the PMMA-cross with the cantilever holder into the aluminum arm (cf. fig. 3c).

---

[1] The cantilever is usually tilted by an angle α in the AFM, the upper limit of the distance l between the bacteria (with diameter d) and the free end of the cantilever can be calculated as $l = d/\sin(\alpha)$.

[2] The exact procedure of integrating the cantilever holder into the micromanipulator might differ, depending on type and design of the cantilever holder.

8. Place a droplet of PBS-buffer ($\approx 20\,\mu l$) on the tiny droplet covering the pre-attached bacteria.

9. Use a 10× objective/10× eyepiece of the microscope to bring the cantilever directly over the droplet and lower it into the droplet of bacterial solution.

10. Focus onto the bacteria lying on the petri dish and approach the cantilever to the surface until it is almost in focus.

11. Change to 40× or higher objective and use the precision control to place the cantilever straight above a single bacterium.

12. Lower the cantilever onto the single bacterial cell and press it gently (the pressure can be controlled by watching the light reflection off the cantilever, which should change only slightly) onto the bacterium.

13. Pull the cantilever immediately away from the surface again. Focus onto the cantilever to confirm the attachment of a single bacterial cell close enough to the free end of the cantilever (cf. bacterial cluster probe).

14. If the bacterium did not attach, repeat step 10 to 13.

15. Retract the cantilever from the surface and out of the droplet. Ensure that a small amount of buffer remains at the probe holder covering the cantilever. As the cantilever has to be covered by liquid the whole time, some more liquid might be added if the cantilever starts drying out.

16. Confirm again the attachment of the single bacterium close enough to the free end of the cantilever (see above). If the bacterium has detached, start again with step 8.

17. Remove the probe holder from the micromanipulator and insert it into the AFM head.

18. Go on with section "Force distance measurements with a bacterial probe".

3.3 Force distance measurements with a bacterial probe

1. Place the bacterial probe right above the surface on which the adhesion will be measured. At best, the droplet covering the cantilever and the liquid covering the surface do not touch at this step.

2. Use the AFM step motor to lower the cantilever towards the surface. Stop the movement about $100\,\mu m$ above the surface. Crashing the cantilever into the surface will at best only detach bacteria, but may destroy the cantilever.

3. Check the experimental parameters: AFM in "contact mode", set scan size to zero, choose a "deflection setpoint" that ensures a force of less than 1 nN.

4. Start the approach.

5. As soon as the approach is finished, change into force spectroscopy mode, this will retract the bacterium from the surface.

6. Set the parameter values for the force/distance measurements:
   - Define the total distance the piezo moves during the force/distance curve (this value may be called "ramp size"). The value for the ramp size depends on the expected rupture length (see above), common values for the ramp size are around $1\,\mu m$.
   - Define the number of data points while approaching/retracting, which constitutes —in combination with the ramp size— the z-resolution of the curve. The z-resolution should be at least one point per nm.
   - Define the number of full force/distance curves per second ("ramp rate"). In combination with the ramp size, the ramp rate defines the tip velocity. Typical values are between 0.5 and 1.5 Hz.
   - Define the speed of the piezo movement in z-direction. This defines in combination with the ramp size - the ramp rate.
   - Define the so called "trigger threshold" (this is the force value at which the cantilever/bacterium approach is stopped). Typical values are less than 0.5 nN.
   - Define a time span between stopping the approach and starting the retraction of the cantilever, *i.e.* a time of contact between bacterium and surface (this value is called "surface delay").
   - A second timespan may be defined that delays the start of a force/distance curve after full retraction of the preceding one.

7. Perform one single force/distance curve with the above-defined parameters.

8. Investigating the shape of the force/distance curve will help to decide whether the bacterium is still attached to the cantilever (cf. fig. 3 of ref. [13]) or not. However, as the shape of the force/distance curve depends on the combination of surface and bacterium, this may require some experience. If the bacterium becomes detached, attach a new one.

9. Run a number of force/distance measurements with one set of parameters. Take care that the same spot of the substratum is not probed twice to exclude influences of potential residues originating from preceding approaches. Some AFM offer an automatic realization of a number of force/distance curves on different spots.

10. Conduct additional sets of force/distance curves while changing the experimental parameters according to the respective experimental goal.

11. Take care that the last series of force/distance curves for a bacterial probe reproduce the parameters of the first series. That way, changes of the bacterial adhe-

sion properties due to the force measurements can be identified. The number of maximum force/distance curves per bacterial probe is usually limited due to fading effects (*i.e.* the adhesion strength of the bacterium may decrease due to repeated pull-off events, possibly by losing surface adhesins) or loss of the bacterium/bacteria. The influence of fading effects depends on the respective bacterium/surface combination, however, at least 100-150 curves per bacterial probe are usually possible.

12. If all measurements are finished, retract the cantilever from the surface.

13. In the case of single cell measurements, the existence of the single bacterium can be confirmed optically.

14. If the AFM is linked to an integrated inverse microscope, the presence of the single bacterium on the cantilever can be checked directly. Otherwise, the cantilever has to be removed from the AFM and reintegrated into the inverse microscope linked to the micromanipulator:

    (a) Use the motors to retract the cantilever as far as possible from the surface.

    (b) Remove the cantilever holder (with cantilever) from the AFM. It is important that some liquid (buffer) remains that covers the bacterial probe. This avoids losing the bacterium by capillary forces and prevents it from drying out. If the droplet covering the cantilever is tiny, add a small amount of buffer ($\approx 10\,\mu l$) with the pipette.

    (c) Insert holder and cantilever into the microscope set-up (specified in paragraph "Single bacterial probe").

    (d) Use the microscope to confirm the attachment of the single bacterium.

15. The cantilever may be reused by detaching the single bacterium and attaching a new one:

    (a) Put a plastic petri dish on the inverted microscope linked to the micromanipulator.

    (b) Use the 10× objective to approach the cantilever with the single bacterium towards the surface of the petri dish and stop a few micrometers before.

    (c) Use the 40× objective and carefully press the bacterium onto the surface until a slight deflection of the cantilever can be seen by a change in the cantilever light reflection.

    (d) Pulling the cantilever backwards over the surface (in the xy plane) will shear the bacterium off the cantilever.

    (e) Retract the cantilever from the surface. Make sure that a small amount of liquid remains on the petri dish covering the bacterium. The viability of this bacterium can then be checked by a live/dead stain in the following.

    (f) Repeat the "single bacterium probe" steps to attach a new bacterium.
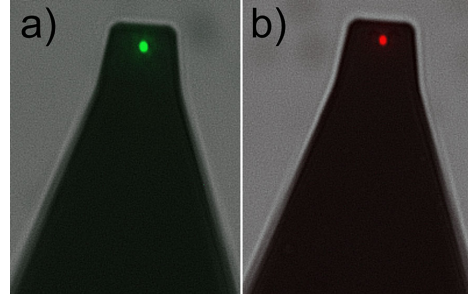
Fig. 4. a) Viable *Staphylococcus carnosus* cell attached to a tipless AFM cantilever. Staining was applied after one hundred force/distance curves. b) Ethanol-killed *S. carnosus* cell attached to a tipless AFM cantilever. Live/dead staining was performed as described in chapt. 3.4.

3.4 Viability of bacteria

The viability of the bacterium/bacteria either attached to the cantilever or the one sheared off on a petri dish (see previous paragraph) can be checked via a live/dead stain. However, as the shearing process may harm sensitive bacterial cell types, we recommend testing the viability directly on the cantilever.

1. Focus the fluorescence microscope on the bacterium lying on the petri dish or fixed to the cantilever.

2. Add a small amount of live/dead stain (*e.g.* Life Technologies GmbH, Germany) (about $20\,\mu l$) to the buffer covering the bacterium.

3. Shade all the surrounding light to avoid photobleaching and wait for ten minutes.

4. Verify the viability of the bacterium used in the force measurements by means of its color (cf. fig. 4).

3.5 Data calibration

The basic data recorded by the AFM during a force spectroscopy experiment are the voltage applied to the piezo controlling the movement in z-direction (z-piezo) and the voltage signal on the photodiode, quantifying the shift of the laser spot reflected from the back of the cantilever. A "height sensor" may give a second measure for the z-position of the cantilever. Based on the calibration, these outputs are then presented as a force *vs.* z-position curve. This is usually done automatically, nevertheless, we will go through it here:

1. The AFM internal calibration of the z-piezo converts the applied voltage into the dilatation of the piezo. However, users should be aware that the z-position is always a relative measure between the starting point and the actual position.

Publications and Manuscripts

Page 8 of 9   Eur. Phys. J. E (2015) **38**: 140
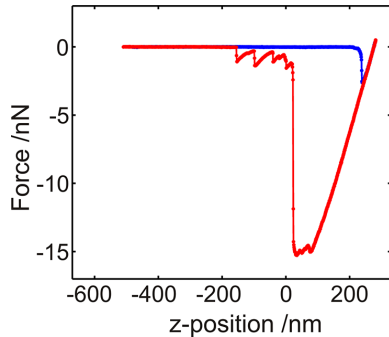
Fig. 5. Force/distance curve plotted as force *vs.* *z*-position after baseline correction. Approach (retraction) curve is shown in blue (red).

2. Two steps are performed to convert the voltage signal from the photodiode into the actual force exerted on the cantilever:

   – The deflection of the cantilever "*d*" in nm can be obtained by multiplying the voltage signal by the deflection sensitivity (see calibration of cantilever).

   – The force on the cantilever "*F*" in nN can be calculated by applying Hooke's law ($F = k \cdot d$), with the spring constant "*k*" of the cantilever (see calibration of cantilever).

3. Since the output of the photodiode is a relative measure, the baseline of the force distance curve — representing the zero-force part before/after contact— is often shifted along the *y*-axis. By applying an offset correction, the baseline can be brought in line with the *x*-axis (cf. fig. 5)

These three steps result in a calibrated force/distance curve in the form of a force *vs.* *z*-position plot (cf. fig. 5). For most subsequent analysis steps, however, the force *vs.* *z*-position representation is not ideal and rather a force "*F*" *vs.* separation "*s*" plot is required. One of the main disadvantages of AFM in general is that it lacks the ability to directly measure the separation between probe and surface since the system basically reports solely the *z*-position of the cantilever mount. Yet, if the point of zero separation *i.e.* the point of contact "z_0" between probe and surface can be accurately determined in the force/distance curve, it is possible to convert the *z*-position to the actual separation. In the case of a bacterium adhering to a hard surface, the point of contact can be assumed to be the point at which force is again zero after the snap-in event (cf. fig. 6a). To convert the force *vs.* *z*-position plot then into a force *vs.* separation plot, the following two steps are required (cf. fig. 6):
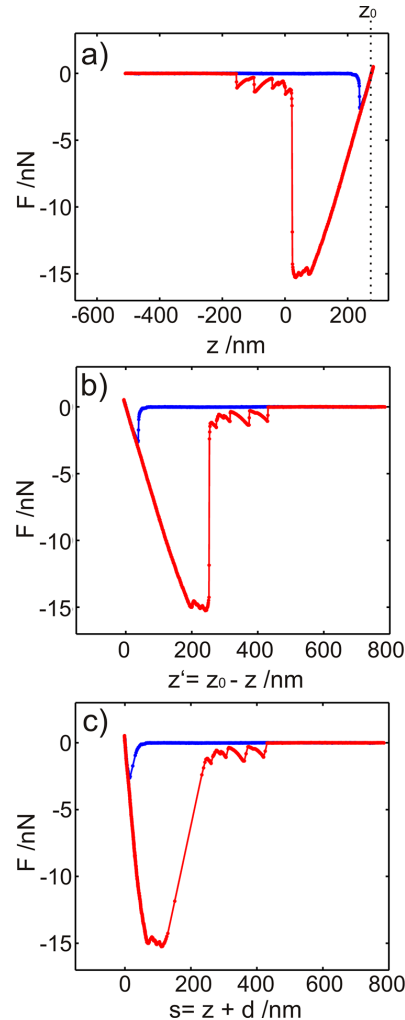
Fig. 6. Work steps for calculating a force (F) *vs.* separation (s) curve. a) Starting with a baseline-corrected force (F) *vs.* *z*-position (z) curve, b) a force (F) *vs.* *z*-position (z') curve with the respective point of contact is calculated and c) subsequently transformed into the force (F) *vs.* separation (s) curve.

1. Define the contact point z_0, in our case this is the point of zero force after the snap-in (cf. fig. 6a). Shift the force/distance curve along the *x*-axis by calculating $z' = z_0 - z$ (cf. fig. 6b).

2. The separation between the bacterium and the substrate surface is calculated by adding the deflection d to the shifted *z*-position z' (cf. fig. 6c).

The calculation can be done simultaneously for both approach and retraction part of the force/distance curve.

I. Addendum I – A Detailed Guideline for the Fabrication of Single Bacterial Probes Used for Atomic Force Spectroscopy

4 Conclusion

Here we present a simple and reproducible procedure to fabricate viable bacterial probes and to perform bacterial cell force spectroscopy measurements. The protocols presented describe the fabrication of both bacterial cluster probes, as well as single bacterial probes, in detail. Our approach allows for measurements with high precision and high throughput and features a simplicity with regards to applicability and equipment availability, which may pave the way for bacterial cell force spectroscopy as a standard technique in modern bacterial adhesion research.

References

1. A.E. Khoury, K. Lam, B. Ellis, J.W. Costerton, ASAIO J. **38**, M174 (1992).
2. J.W. Costerton, P.S. Stewart, E.P. Greenberg, Science **284**, 1318 (1999).
3. K. Hori, S. Matsumoto, Biochem. Engin. J. **48**, 424 (2010) ISSN 1369-703X, invited Review Issue 2010.
4. Y. Seo, W. Jhe, Rep. Prog. Phys. **71**, 016101 (2008).
5. S. Kang, M. Elimelech, Langmuir **25**, 9656 (2009).
6. P. Loskill, H. Haehl, N. Thewes, C.T. Kreis, M. Bischoff, M. Herrmann, K. Jacobs, Langmuir **28**, 7242 (2012).
7. A. Beaussart, S. El-Kirat-Chatel, P. Herman, D. Alsteens, J. Mahillon, P. Hols, Y. Dufrêne, Biophys. J. **104**, 1886 (2013).
8. M. Lessel, O. Bäumchen, M. Klos, H. Hähl, R. Fetzer, M. Paulus, R. Seemann, K. Jacobs, Surf. Interface Anal. **47**, 557 (2015).
9. M. Benoit, D. Gabriel, G. Gerisch, H.E. Gaub, Nat. Cell Biol. **2**, 313 (2000).
10. M. Benoit, H.E. Gaub, Cells Tissues Organs **172**, 174 (2002).
11. P.H. Puech, K. Poole, D. Knebel, D.J. Muller, Ultramicroscopy **106**, 637 (2006).
12. J. Helenius, C.P. Heisenberg, H.E. Gaub, D.J. Muller, J. Cell Sci. **121**, 1785 (2008).
13. N. Thewes, P. Loskill, P. Jung, H. Peisker, M. Bischoff, M. Herrmann, K. Jacobs, Beilstein J. Nanotechnol. **5**, 1501 (2014).
14. X. Sheng, Y. Peng Ting, S.O. Pehkonen, J. Colloid Interface Sci. **310**, 661 (2007).
15. W.R. Bowen, R.W. Lovitt, C.J. Wright, J. Colloid Interface Sci. **237**, 54 (2001).
16. N.P. Boks, H.J. Busscher, H.C. van der Mei, W. Norde, Langmuir **24**, 12990 (2008).
17. L. Mei, Y. Ren, H.J. Busscher, Y. Chen, H.C. van der Mei, J. Dental Res. **88**, 841 (2009).
18. W. Zhang, A.G. Stack, Y. Chen, Colloids Surf. B: Biointerfaces **82**, 316 (2011).
19. S.K. Lower, C.J. Tadanier, M.F.H. Jr., Geochim. Cosmochim. Acta **64**, 3133 (2000).
20. S.K. Lower, M.F. Hochella, T.J. Beveridge, Science **292**, 1360 (2001).
21. A. Beaussart, S. El-Kirat-Chatel, R.M.A. Sullan, D. Alsteens, P. Herman, S. Derclaye, Y.F. Dufrêne, Nat. Protocols **9**, 1049 (2014).
22. A. Razatos, Y.L. Ong, M.M. Sharma, G. Georgiou, Proc. Natl. Acad. Sci. U.S.A. **95**, 11059 (1998).
23. R.J. Emerson IV, T.S. Bergstrom, Y. Liu, E.R. Soto, C.A. Brown, W.G. McGimpsey, T.A. Camesano, Langmuir **22**, 11311 (2006).
24. T. Cao, H. Tang, X. Liang, A. Wang, G.W. Auner, S.O. Salley, K. Ng, Biotechnol. Bioengin. **94**, 167 (2006).
25. Y.L. Ong, A. Razatos, G. Georgiou, M.M. Sharma, Langmuir **15**, 2719 (1999).
26. W. Qu, H.J. Busscher, J.M. Hooymans, H.C. Van der Mei, J. Colloid Interface Sci. **358**, 430 (2011).
27. A.L. Neal, T.L. Bank, M.F. Hochella, K.M. Rosso, Geochem. Trans. **6**, 77 (2005).
28. H. Lee, J. Rho, P.B. Messersmith, Adv. Mater. **21**, 431 (2009).
29. E. Velzenberger, I. Pezron, G. Legeay, M.D. Nagel, K.E. Kirat, Langmuir **24**, 11734 (2008).
30. R.L. Meyer, X. Zhou, L. Tang, A. Arpanaei, P. Kingshott, F. Besenbacher, Ultramicroscopy **110**, 1349 (2010).
31. P. Kuusela, Nature **276**, 718 (1978).
32. A.W. Buck, V.G. Fowler Jr., R. Yongsunthon, J. Liu, A.C. DiBartola, Y.A. Que, P. Moreillon, S.K. Lower, Langmuir **26**, 10764 (2010).
33. G. Zeng, T. Mu ller, R.L. Meyer, Langmuir **30**, 4019 (2014).
34. W.R. Bowen, A.S. Fenton, R.W. Lovitt, C.J. Wright, Biotechnol. Bioengin. **79**, 170 (2002).
35. S.B. Velegol, B.E. Logan, Langmuir **18**, 5256 (2002).
36. G.A. Burks, S.B. Velegol, E. Paramonova, B.E. Lindenmuth, J.D. Feick, B.E. Logan, Langmuir **19**, 2366 (2003).
37. H. Lee, S.M. Dellatore, W.M. Miller, P.B. Messersmith, Science **318**, 426 (2007).
38. P.C. Lau, J.R. Dutcher, T.J. Beveridge, J.S. Lam, Biophys. J **96**, 2935 (2009).
39. P.C. Lau, T. Lindhout, T.J. Beveridge, J.R. Dutcher, J.S. Lam, J. Bacteriol. **191**, 6618 (2009).

Addendum II – Intracellular Delivery of Poorly Soluble Polyphenols: Elucidating the Interplay of Self-Assembling Nanocarriers and Human Chondrocytes

Authors: B. KANN[1,2], C. SPENGLER[3], K. CORADINI[4], L. A. RIGO[4], M. L. BENNINK[5], K. JACOBS[3], H. L. OFFERHAUS[2], R. C. R. BECK[4], M. WINDBERGS[1,6,7]

[1] Saarland University, Department of Biopharmaceutics and Pharmaceutical Technology, Campus A4.1, 66123 Saarbrücken, Germany.
[2] University of Twente, Optical Sciences Group, MESA+ Institute for Nanotechnology, P.O. Box 217, 7500 AE Enschede, The Netherlands.
[3] Saarland University, Experimental Physics, Campus E2.9, 66123 Saarbrücken, Germany.
[4] Programa de Pós-Graduação em Ciências Farmacêuticas, Faculdade de Farmácia, Federal University of Rio Grande do Sul (UFRGS), 90610-000, Porto Alegre, Rio Grande do Sul, Brazil.
[5] University of Twente, Nanobiophysics Group, MESA+ Institute for Nanotechnology, P.O. Box 217, 7500 AE Enschede, The Netherlands.
[6] Helmholtz Centre for Infection Research and Helmholtz Institute for Pharmaceutical Research Saarland, Department of Drug Delivery, Campus E 8.1, 66123 Saarbruecken, Germany.
[7] PharmBioTec GmbH, Department of Drug Delivery, Science Park 1, 66123 Saarbruecken, Germany.

Author contributions:
*Experiments were planned and experimental results were achieved by B. Kann, **C. Spengler**, K. Coradini, L. A. Rigo and M. L. Bennik. Data were analyzed by B. Kann, **C. Spengler**, K. Coradini, L. A. Rigo and M. L. Bennik, K. Jacobs, H. L. Offerhaus, R. C. R. Beck and M. Windbergs. The manuscript was written by B. Kann, **C. Spengler**, K. Coradini, L. A. Rigo, M. L. Bennik, K. Jacobs, H. L. Offerhaus, R. C. R. Beck and M. Windbergs. Scientific work was directed by K. Jacobs, H. L. Offerhaus, R. C. R. Beck and M. Windbergs.*

Abstract - Increased molecular understanding of multifactorial diseases paves the way for novel therapeutic approaches requiring sophisticated carriers for intracellular delivery of actives. We designed and characterized self-assembling lipid-core nanocapsules for coencapsulation of two poorly soluble natural polyphenols curcumin and resveratrol. The polyphenols were identified as high-potential therapeutic candidates intervening in the intracellular in flammation cascade of chondrocytes during the progress of osteoarthritis. To elucidate the interplay be-

tween chondrocytes and nanocapsules and their therapeutic effect, we pursued a complementary analytical approach combining label-free visualization with biological assays. Primary human chondrocytes did not show any adverse effects upon nanocapsule application and coherent anti-Stokes Raman scattering images visualized their intracellular uptake. Further, by systematically blocking different uptake mechanisms, an energy independent uptake into the cells could be identified. Additionally, we tested the therapeutic effect of the polyphenol-loaded carriers on inflamed chondrocytes. Treatment with nanocapsules resulted in a major reduction of nitric oxide levels, a well-known apoptosis trigger during the course of osteoarthritis. For a more profound examination of this protective effect on joint cells, we pursued studies with atomic force microscopy investigations. Significant changes in the cell cytoskeleton as well as prominent dents in the cell membrane upon induced apoptosis were revealed. Interestingly, these effects could not be detected for chondrocytes which were pretreated with the nanocapsules. Overall, besides presenting a sophisticated carrier system for joint application, these results highlight the necessity of establishing combinatorial analytical approaches to elucidate cellular uptake, the interplay of codelivered drugs and their therapeutic effect on the subcellular level.

analytical chemistry

Intracellular Delivery of Poorly Soluble Polyphenols: Elucidating the Interplay of Self-Assembling Nanocarriers and Human Chondrocytes

Birthe Kann,[†,‡] Christian Spengler,[§] Karine Coradini,[∥] Lucas A. Rigo,[∥] Martin L. Bennink,[⊥] Karin Jacobs,[§] Herman L. Offerhaus,[‡] Ruy C. R. Beck,[∥] and Maike Windbergs*[,†,#,∇]

[†]Saarland University, Department of Biopharmaceutics and Pharmaceutical Technology, Campus A4.1, 66123 Saarbruecken, Germany

[‡]University of Twente, Optical Sciences Group, MESA+ Institute for Nanotechnology, P.O. Box 217, 7500 AE Enschede, The Netherlands

[§]Saarland University, Experimental Physics, Campus E2.9, 66123 Saarbruecken, Germany

[∥]Programa de Pós-Graduação em Ciências Farmacêuticas, Faculdade de Farmácia, Federal University of Rio Grande do Sul (UFRGS), 90610-000, Porto Alegre, Rio Grande do Sul, Brazil

[⊥]University of Twente, Nanobiophysics Group, MESA+ Institute for Nanotechnology, P.O. Box 217, 7500 AE Enschede, The Netherlands

[#]Helmholtz Centre for Infection Research and Helmholtz Institute for Pharmaceutical Research Saarland, Department of Drug Delivery, Campus E 8.1, 66123 Saarbruecken, Germany

[∇]PharmBioTec GmbH, Department of Drug Delivery, Science Park 1, 66123 Saarbruecken, Germany

ABSTRACT: Increased molecular understanding of multifactorial diseases paves the way for novel therapeutic approaches requiring sophisticated carriers for intracellular delivery of actives. We designed and characterized self-assembling lipid-core nanocapsules for coencapsulation of two poorly soluble natural polyphenols curcumin and resveratrol. The polyphenols were identified as high-potential therapeutic candidates intervening in the intracellular inflammation cascade of chondrocytes during the progress of osteoarthritis. To elucidate the interplay between chondrocytes and nanocapsules and their therapeutic effect, we pursued a complementary analytical approach combining label-free visualization with biological assays. Primary human chondrocytes did not show any adverse effects upon nanocapsule application and coherent anti-Stokes Raman scattering images visualized their intracellular uptake. Further, by systematically blocking different uptake mechanisms, an energy independent uptake into the cells could be identified. Additionally, we tested the therapeutic effect of the polyphenol-loaded carriers on inflamed chondrocytes. Treatment with nanocapsules resulted in a major reduction of nitric oxide levels, a well-known apoptosis trigger during the course of osteoarthritis. For a more profound examination of this protective effect on joint cells, we pursued studies with atomic force microscopy investigations. Significant changes in the cell cytoskeleton as well as prominent dents in the cell membrane upon induced apoptosis were revealed. Interestingly, these effects could not be detected for chondrocytes which were pretreated with the nanocapsules. Overall, besides presenting a sophisticated carrier system for joint application, these results highlight the necessity of establishing combinatorial analytical approaches to elucidate cellular uptake, the interplay of codelivered drugs and their therapeutic effect on the subcellular level.

Because of a continuously growing understanding of origination and course of complex diseases on a molecular level, there is a high demand for sophisticated carrier systems allowing for intracellular delivery of active pharmaceutical ingredients (API) and thus treatment of such diseases on a subcellular level.

One example in this context is osteoarthritis, a multifactorial degenerative joint disease with a severe impact on life quality especially for the elderly population.[1] During the course of the disease, the chondrocytes within the cartilage tissue are inflamed, subsequently resulting in a breakdown of the connective tissue in the affected joint.[2−5] Despite this

knowledge, osteoarthritis is generally treated symptomatically using nonsteroidal, anti-inflammatory drugs limited to temporary effects without complete curing.[6,7] Recently, natural polyphenols gained considerable interest as therapeutic alternatives due to their anti-inflammatory, antioxidant, and chemo preventive potential.[3,8−10] It was shown that curcumin (diferuloylmethane) and resveratrol (*trans*-3,4′-trihydroxystilbene) have a protective effect on chondrocytes by modulating

the intracellular inflammation cascade.[6,11−13] Interestingly, this effect could even synergistically be increased by combining different polyphenols.[6,12] However, because of their low water solubility, the polyphenols were dissolved in organic solvents before application to cultivated chondrocytes.[6,11,14,15] Such organic solvents do not only artificially increase the solubility of the polyphenols but also increase the permeability of the chondrocytes. Thereby, the extent of intracellular uptake of the actives is artificially facilitated and increased which is not reflecting the *in vivo* situation in a human joint. To overcome these issues, we designed a delivery system for codelivery of resveratrol and curcumin based on self-assembling lipid-core nanocapsules (LNC) consisting of an oily core surrounded by a biocompatible and biodegradable shell of polycaprolactone (PCL).[16,17] These capsules provide protection and solubility enhancement for the lipophilic actives as well as a controlled release pattern.[18−20] Furthermore, a first study in a rat model of osteoarthritis showed promising results for LNC loaded with the polyphenols as a novel therapeutic approach.[21]

However, for in-depth understanding of such a novel approach for codelivery of two polyphenols, sophisticated analytics are required to elucidate cellular uptake and response. In terms of visualizing biological structures, research benefits from progress in microscopic techniques, especially in confocal laser scanning fluorescence microscopy for cell imaging. However, the technique requires biomarkers and these can cause misinterpretation of analytical results.[22,23] In addition to visualization, the analysis of cellular biomechanics upon drug application is important as inflammatory processes in osteoarthritic chondrocytes entail changes in their cell biomechanics and consequently their membrane structure.

In this study, we performed a multidisciplinary approach to bridge the aforementioned scientific gaps. We encapsulated resveratrol and curcumin in lipid-core nanocapsules and investigated their interactions with human primary chondrocytes. Further analysis focused on their therapeutic effects on the chondrocytes treated with a chemical NO-donor to induce apoptosis, thereby mimicking the conditions of diseased cells in osteoarthritic joints. To gain new insights, noninvasive and label-free coherent anti-Stokes Raman scattering (CARS) microscopy was used for visualization of interactions with chondrocytes and intracellular location of the capsules after uptake. Further, the cellular uptake process was elucidated by selective blocking of individual endocytosis pathways and subsequent CARS analysis. In addition, the therapeutic effect of the nanocapsules on chondrocytes was analyzed by a combination of bioassays and atomic force microscopy (AFM) to probe cellular nanobiomechanics and membrane structure as well as to investigate changes upon diseased state and therapeutic effects of the nanocapsules on human chondrocytes.

■ EXPERIMENTAL SECTION

Materials. Curcumin, poly(ε-caprolactone), sorbitan monostearate, 5-(N-ethyl-N-isopropyl) amiloride (ENIA), monensin sodium, chlorpromazine HCl, nystatin, sodium nitroprusside dehydrate (SNP), and methylthiazolyldiphenyl-tetrazolium bromide (MTT) as well as analytical solvents were purchased from Sigma-Aldrich. Grape seed oil was obtained from Delaware (Porto Alegre, Brazil). Resveratrol was supplied by Pharma Nostra (Anápolis, Brazil), and polysorbate 80 was acquired from Henrifarma (São Paulo, Brazil). All chemicals

and solvents were of pharmaceutical or HPLC grade and were used as received.

Preparation of Lipid-Core Nanocapsules. The protocol for LNC preparation was established by Jornada et al.[20] In brief, 27 mL of acetone including dissolved PCL (0.1 g), grape seed oil (165 μL) and sorbitan monostearate (0.0385 g) were injected into the aqueous phase (water 54 mL) containing polysorbate 80 (0.077g) under magnetic stirring at room temperature. Curcumin and/or resveratrol (5 or 2.5 mg) were part of the organic phase. Subsequently, acetone was eliminated under reduced pressure and the suspension was concentrated to a final volume of 10 mL. LNC containing 0.5 mg/mL of resveratrol (R-LNC) and curcumin (C-LNC) individually and in combination (Co-LNC) as well as polyphenol free nanocapsules were prepared. To investigate a possible dose dependent effect, LNC with 0.25 mg/mL of curcumin and resveratrol were fabricated additionally. For cell culture experiments a 50-fold dilution of LNC suspensions was used.

Characterization of Lipid-Core Nanocapsules. Physicochemical characteristics were acquired by photon correlation spectroscopy at a scattering angle of 173 °C for hydrodynamic size and polydispersity index (PdI) measurements and coupled with laser Doppler velocimetry to determine the zeta potential (Zetasizer Nano ZSP/SP, Malvern instruments, Malvern, U.K.). LNC suspensions were diluted in Milli-Q water (1/50) prior to measurements. The pH-value was directly determined from the LNC suspension using a calibrated potentiometer (VB-10, Denver Instrument Company, Colorado). Morphological characteristics were visualized by transmission electron microscopy (TEM) (JEM 2010, Tokyo, Japan). LNC suspensions, diluted in ultrapure water (200-fold) were placed on a specimen grid and counterstained with phosphotungstic acid hydrate (1% w/v). The microscope was operated at 200 kV. The *in vitro* release of resveratrol and curcumin from LNC was carried out by the dialysis bag method according to Coradini et al.[24] with minor modifications. A volume of 0.8 mL of the samples (Co-LNC, R-LNC, and C-LNC) were placed into a dialysis bag with a 10 kDa molecular weight cutoff and suspended into 80 mL of release medium (water/Tween 80/ethanol (80:2:20 v/v)). The samples ($n = 3$) were maintained at 37 °C under gentle agitation. At predetermined time intervals, 1 mL of release medium was withdrawn and replaced with fresh medium. The samples were diluted with mobile phase, filtered through a 0.45 μm membrane, and analyzed by the previously described HPLC method.[24]

Cell Culture Experiments. Human primary chondrocytes were purchased from PromoCell (Heidelberg, Germany) and cultured in chondrocyte growth medium (PromoCell) which was supplemented with 10% (v/v) fetal calf serum in an atmosphere of 5% CO_2 at 37 °C. During routinely performed subcultivation cells were seeded at a density of 20 000 cells/cm². Passages 9−11 were used for experiments.

CARS Microscopy. Chondrocytes were cultured in imaging dishes with a cover class insert in tissue culture quality. Preincubation with uptake inhibitors (5 μg/mL chlorpromazine, monensin, nystatin, ENIA) was done for 1 h prior to adding polyphenol-loaded LNC. To investigate energy dependent uptake, cells were moved to the refrigerator at 4 °C for LNC incubation. After 7 h in total the medium was replaced and dishes were moved onto the stage of the custom built CARS microscope, which is described in detail elsewhere.[25] The picosecond pulsed laser, which is coupled to the setup,

Analytical Chemistry

Table 1. Physicochemical Characteristics of Lipid-Core Nanocapsules in Aqueous Suspension and after 24 h Incubation in Cell Culture Medium (Mean Value ± SD, *n* = 3)

	in aqueous suspension			after 24 h in cell culture medium		
formulation	size (nm)	PdI	zeta potential (mV)	size (nm)	PdI	zeta potential (mV)
unloaded LNC	201.90 ± 1.95	0.077 ± 0.004	−22.43 ± 0.60	222.27 ± 1.67	0.159 ± 0.025	−4.40 ± 0.85
R-LNC	211.73 ± 1.65	0.093 ± 0.028	−21.73 ± 0.35	217.10 ± 1.65	0.140 ± 0.008	−5.73 ± 1.13
C-LNC	205.70 ± 1.04	0.077 ± 0.030	−22.17 ± 0.23	218.93 ± 1.81	0.168 ± 0.020	−4.81 ± 0.94
Co-LNC (1 mg/mL)	199.73 ± 0.93	0.115 ± 0.017	−20.97 ± 0.55	204.27 ± 0.67	0.154 ± 0.016	−3.56 ± 0.21
Co-LNC (0.5 mg/mL)	201.67 ± 1.80	0.067 ± 0.008	−22.50 ± 0.36	208.53 ± 2.82	0.143 ± 0.001	−4.49 ± 0.73

operated at a fundamental wavelength of 1032 nm (aeroPULSE-10, NKT Photonics, Birkerød, Denmark). An Olympus 60× water immersion objective was used to record the images.

Nitric Oxide Release. Chondrocytes were seeded in 96 well plates (10 000 cell per well, p10/11). Incubation times for LNC and 2 mM SNP (297.95 g/mol; 11.88 mg in 20 mL of medium) were 24 h. Cells were preincubated with LNC before exchanging for SNP solution. The Griess Reagent System (Promega Corporation, Madison, WI) was used according to provided instructions. For each assay a nitrite standard reference curve (0.1 M−0 M) was prepared in triplicate. The absorption of the formed purple colored azo compound was measured at 535 nm (Infinite M200Pro, Tecan GmbH, Crailsheim, Germany). Statistical analysis was performed using the student's *t*-test ($p < 0.05$).

Cell Viability Testing. Cell viability was investigated by the MTT assay ($n = 8$). Cells cultured in 96 well plates (10 000 cells/well) were washed with HBSS buffer prior to incubation with SNP for 24 h at 37 °C. As a positive control, 1% Triton X in medium was used. Cells were washed with HBSS and 100 μL of medium with 10% MTT reagent was added to each well. After 4 h of incubation on the shaker at 37 °C, the medium was exchanged for DMSO. After 30 min, the absorption of the formed formazan was measured at 550 nm (duration 5 s; amplitude 3 nm; Infinite M200Pro).

Atomic Force Microscopy. Chondrocytes were cultured in Petri dishes (10 000 cells/dish) with a growth area of 8.7 cm². The incubation time for Co-LNC and 2 mM SNP was 24 h each, where SNP was only applied after removing the medium containing nanocapsules. Subsequently, cells were fixed in 3% formaldehyde and air-dried just before AFM investigations. AFM images were recorded in air on a Dimension Fastscan Bio (Bruker-Nano, Santa Barbara, CA) operated in a dynamic force interaction control mode (Peak Force QNM) with Nanoscope 9 software. Silicon nitride tips were used (spring constants of 0.06 N/m, SNL-D tips from Bruker-Nano) as cantilevers with loading forces of approximately 1 nN. The lateral resolution of the depicted (50 μm)² AFM images is 48.8 nm/pixel. In the case of the (5 μm)² scans, the lateral resolution is 9.8 nm/pixel. Cross sectioning and bearing analyses of the images were carried out using Nanoscope Analysis software.

■ RESULTS AND DISCUSSION

The first step of this study involved a physicochemical and morphological analysis of the lipid-core nanocapsules loaded with the two polyphenols as well as their drug release kinetics. Jornada et al.[20] already proved that the granulometry profile of such lipid-core nanocapsules fabricated by interfacial deposition of PCL correlates with the concentration of raw materials in the aqueous and in the organic phase, respectively. Lipid-core nanocapsules were either loaded with curcumin or with

resveratrol (C-LNC, R-LNC, 0.5 mg polyphenol/mL) as well as with both polyphenols in combination (Co-LNC, 0.5 mg of each polyphenol/mL). For direct comparison between the effect of curcumin and resveratrol and their combination in terms of dose dependency and synergistic effects, an additional Co-LNC batch containing a total polyphenol dose of 0.5 mg/mL was included in the experiments. These Co-LNC (0.25 mg of each polyphenol/mL), which are introduced here for the first time, have a hydrodynamic diameter of 201.67 nm ±1.80 nm with a low size distribution (PdI 0.067 ± 0.008), a zeta potential of −22.50 mV ± 0.36 mV, and a pH value of 6.18 ± 0.21 in aqueous suspension. These physicochemical parameters are in good agreement with published data of C-LNC, R-LNC, and Co-LNC (0.5 mg/mL each), which have been investigated during the optimization of the LNC formulation for the encapsulation of the poorly water-soluble polyphenols.[24]

As hydrodynamic diameter, size distribution and zeta potential are important for evaluating the colloidal stability of LNC under cell culture conditions, these physicochemical characterization data for all generated nanocapsules in aqueous suspension are summarized in Table 1. As the comparison of unloaded capsules and capsules loaded with the different polyphenols proves, the fabrication process is well controlled and generates highly reproducible and physically stable nanocapsules. Drug loadings for lipid-core nanocapsules encapsulating resveratrol and/or curcumin are close to the theoretical value (R-LNC 0.49 mg/mL ± 0.01 mg/mL; C-LNC 0.49 mg/mL ± 0.02 mg/mL; Co-LNC 0.50 mg/mL ± 0.01 mg/mL (resveratrol); and 0.50 mg/mL ± 0.01 mg/mL (curcumin) as already published.[21,24,26] Consequently, the encapsulation efficiency is almost 100% for these formulations (R-LNC 98.00%; C-LNC 97.33%; Co-LNC 100.00% (resveratrol) and 99.33% (curcumin)). For this study, the physical stability of the lipid-core nanocapsules in cell culture medium is important to account for potential interactions with biomolecules in cell culture medium simulating the situation in the human body. The results of the physicochemical characterization of LNC after 24 h incubation in the medium at 37 °C are summarized in Table 1. All different LNC formulations are sized around 210 nm maintaining their narrow size range (PdI < 0.17) and a negative zeta potential. Low standard deviations suggest a homogeneous fraction of LNC despite different loadings. In comparison to LNC in aqueous suspension, the zeta potential decreases. The high values in aqueous suspension are potentially based on steric hindrances due to the presence of polysorbate 80 forming a micellar structure around the capsules.[27] In the presence of cell culture medium containing fetal calf serum among other nutritional supplements, this steric hindrance is most likely decreasing resulting in lower zeta potential values. Nevertheless, PdI values and standard deviations for investigated physicochemical characteristics remain as low as values obtained from LNC in aqueous

Article

suspension. Thus, lipid-core nanocapsules retain their physicochemical characteristics in biorelevant media without agglomeration tendency which is frequently found for other nanocarriers.[28]

An expected round shape of the nanocapsules is confirmed by transmission electron microscopy images (Figure 1).
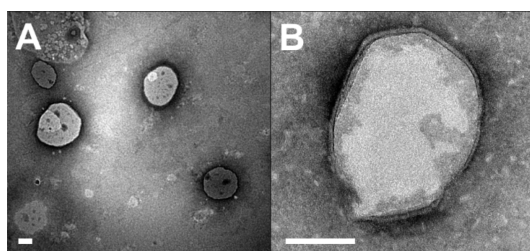
Figure 1. Representative transmission electron microscopy images showing LNC at a low magnification (10 000-fold) (A) and a close-up view showing the PCL wall (50 000-fold) (B). Scale bars denote 100 nm.

Additionally, the hydrodynamic size determined by photon correlation spectroscopy is in good agreement with the mean particle size observed during TEM analysis. The PCL wall of the nanocapsules surrounding the lipid core is homogeneous and has an estimated thickness of 8 nm.

Further, the release kinetics of the polyphenols from the nanocapsules were analyzed. The release of resveratrol (solid circle symbol) shows a steep slope which turns into a plateau phase after about 24 h, whereas curcumin (open circle symbol) release is much slower resulting in a continuous slope as depicted in Figure 2. Interestingly, neither coencapsulation of resveratrol and curcumin in the same capsules (dotted line versus straight line), nor the overall loading of the nanocapsules (0.5 mg/mL versus 1 mg/mL) does significantly change these kinetics.[24] However, a relationship between polyphenol solubility in grape seed oil, the main component of the capsule
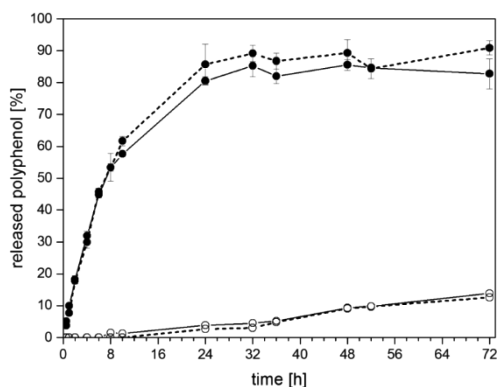
Figure 2. Drug release profiles of curcumin (○) and resveratrol (●) from lipid-core nanocapsules. Straight lines represent the capsules with one polyphenol, whereas dotted lines show the capsules loaded with both polyphenols (mean value ± SD, $n = 3$). For clarity reasons standard deviations for curcumin release which were ≤±2.64% are not shown.

core, and their different release kinetics was recently indicated. The solubility of resveratrol in grape seed oil was found to be 90 μg/mL and the solubility for curcumin in grape seed oil was determined as 475 μg/mL.[26] These solubility findings coincide well with the respective drug release, as a lower resveratrol solubility goes along with a faster release from the lipid-core nanocapsule, whereas the opposite is found for curcumin. The combination of synergistic actives like resveratrol and curcumin with different release kinetics bears a great potential for one single therapeutic system providing a fast initial therapeutic onset (resveratrol) in combination with prolonged treatment (curcumin) in one single application system.

However, physicochemical characterization of the polyphenol-loaded capsules as well as their *in vitro* release kinetics do not provide any information about the absorption into cells or the interplay of the two drugs. Osteoarthritis represents a potential therapeutic target for curcumin and resveratrol. The human joint as an application site for osteoarthritis treatment comprises a complex assembly of articular cartilage with chondrocytes as the predominant cell type. During the course of osteoarthritis, chondrocytes are severely inflamed, finally resulting into apoptosis and cartilage degeneration. It has already successfully been shown that resveratrol and curcumin have a positive effect on inflamed chondrocytes.[6,11,14,15] By encapsulating curcumin and resveratrol in lipid-core nanocapsules, we can improve their solubility circumventing the use of toxic organic solvents and at the same time avoiding precipitation. Thus, LNC facilitate the application of a higher dose delivery combined with a controlled drug release over longer therapy intervals. Further, the protective effect of nanocapsules on the polyphenols is highly beneficial.[24] In a first study, the therapeutic effect of LNC on complete Freund's adjuvant-induced arthritis in rats was tested.[21] Results were very promising especially for the formulation containing both polyphenols. Nevertheless, by using intraperitoneal injection, the administration site is far from the therapeutic target in the hind paw of the rat. Further, no experimental data were generated elucidating how the polyphenols reach the inflamed joint and their local uptake mechanism. For these investigations sophisticated analytics are necessary combining biological assays with high-end visualization techniques. In this context, we focus on cellular delivery of LNC using human chondrocytes to investigate the interplay of carrier, polyphenols, and cellular response by a multifactorial analytical approach.

The postulated pharmacological target for polyphenols in order to treat osteoarthritis is the intracellular inflammation cascade in which these substances are supposed to intervene.[6,11−13] Therefore, investigating the uptake of LNC into chondrocytes is of high interest including the potential to gain a deeper insight into their specific uptake mechanism.

For this purpose, we utilized coherent anti-Stokes Raman scattering (CARS) microscopy. This analytical method facilitates instantaneous visualization of the sample by solely detecting light scattering from an excited endogenous molecular structure The protein band at 2928 cm^{-1} is representative for the cell body. It was chosen to investigate cellular engulfment of LNC. The lipid core of the nanocapsules is the dominant structure of the carrier with the best scattering properties, thus the band for lipids located at 2845 cm^{-1} was set for LNC detection. The signal at both bands is accompanied by a nonresonant background that reveals the surrounding structure. Although cells naturally contain lipids themselves,

the local density of grape seed oil in the core provides a sufficient contrast for chemically selective imaging. In Figure 3,
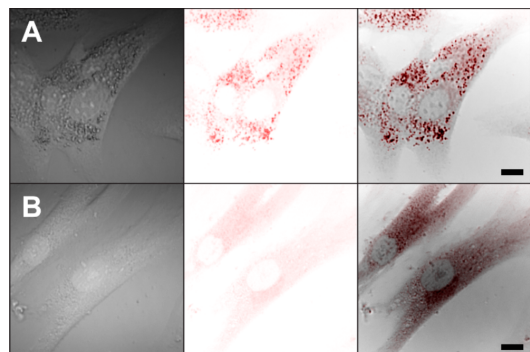
Figure 3. Coherent anti-Stokes Raman scattering microscopy images of chondrocytes engulfing lipid-core nanocapsules (A) and negative control chondrocytes (B). Left panels depict images generated by exciting the protein band. Center panels show false color background-free images of lipid location. Right panels show the overlay of left and center panels. Scale bars denote 10 μm.

the left panels depict plain cell bodies visualized by recording the protein band excitation, whereas the center panels were created by probing the lipid vibrations at 2548 cm^{-1} and using the common part of both images to remove the nonresonant background. For improved visualization and a clear differentiation in an overlap image (right panels), a MatLab algorithm was employed to create false color image based on the spectral data indication the background-free lipids in red color. The right panels depict an overlay of left and center panels.

Chondrocytes incubated with LNC are shown in Figure 3A. Cell bodies (left panel) show dark spots representing areas where molecular vibrations from proteins could not be sufficiently excited compared to the other cell parts. However, when comparing these dark spots with the false color lipid image (center panel), they colocalize with the prominent red spots. In these positions, the nanocapsules are located and their

lipid signal exceeds the intensity of the protein signal. Thus, in the presence of LNC, scattering of the proteins is barely detectable. The overlay image (right panel) underlies this spectroscopic signal contrast. A very light red hue is visible almost across the entire cell body. This observation is a logic consequence of the omnipresence of intracellular lipids especially in the cell walls. This hue is also present in the negative control chondrocytes visualized in Figure 3B. Nevertheless, the density of the grape seed oil in the nanocapsule core triggers an increased signal and its intensity is converted into a more intense color in the image, making the detection of LNC feasible even among other cellular lipids. Different incubation times were tested (6, 10, 24, and 72 h) to determine the maximum uptake. However, no obvious differences were detected, neither based on the duration of the incubation interval nor based on the different nanocapsule formulations (data not shown). Thus, all images presented here involve an exposure of chondrocytes to Co-LNC (1 mg/mL) for 6 h, as the major focus of the study is on the codelivery of both polyphenols.

There are different ways for a nanocarrier to enter a cell, mainly involving phagocytosis and nonphagocytic pathways.[17,29,30] Only a few specialized cells including macrophages and dendritic cells are able to perform phagocytosis, whereas nonphagocytic pathways occur ubiquitously.[30,31] These are categorized as micropinocytosis, clathrin-mediated endocytosis, caveolae-mediated endocytosis, and clathrin- as well as caveolae-independent endocytosis.[17,30] As chondrocytes do not belong to the group of specialized cells, most likely they do not engulf lipid-core nanocapsules by phagocytosis. Therefore, different uptake inhibitors were chosen based on the endocytic pathways for a more detailed investigation of the uptake mechanism of LNC into chondrocytes. Monensin was chosen to block clathrin- and caveolae-independent endocytosis.[32] In addition, chlorpromazine and nystatin were used to investigate if LNC uptake was driven by clathrin-mediated or caveolin-mediated endocytosis, respectively.[22,33] To examine micropinocytosis, amiloride (ENIA) was taken.[33] Chondrocytes were incubated with the respective inhibitors for 1 h before cells were exposed to LNC. CARS images were recorded to visualize potential uptake. Figure 4 depicts the CARS images with each row A−D showing experiments with another uptake
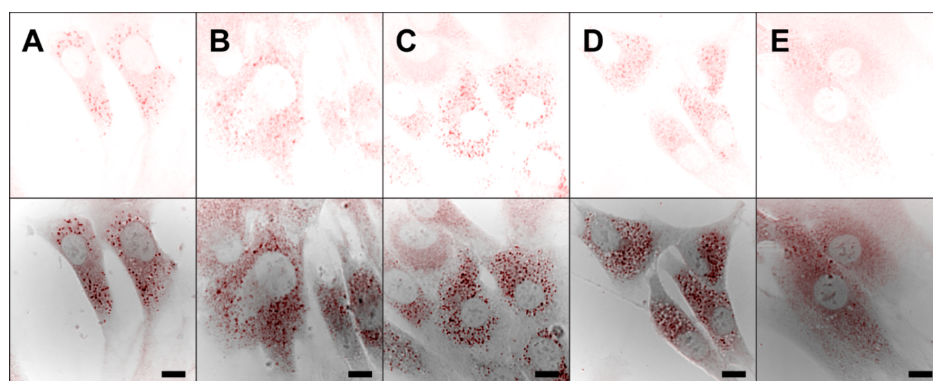
Figure 4. Coherent anti-Stokes Raman scattering microscopy images of chondrocytes exposed to lipid-core nanocapsules after preincubation with monensin (A), chlorpromazine (B), nystatin (C), ENIA (D), or at 4 °C (E). Upper panels depict CARS images generated by exciting lipid molecules. Lower panels show the overlay of cell body image and left panel. Scale bars denote 10 μm.

Analytical Chemistry

inhibitor. To discover possible effects of the inhibitors, the images were taken at fixed excitation intensities, scaled to the same size and are displayed at the same intensity scale. For all inhibitors, the upper panel depicts background-free CARS images acquired using the lipid frequency. Images in the lower panel show the overlay image of recorded lipid and protein band (Images after exciting the protein band are not depicted individually). There are no obvious differences in the uptake behavior of chondrocytes under the influence of the different inhibitors. All cells show a typical cell morphology, and LNC are visible in the cell body. LNC are located in the cytosol but could not be found in the nucleus. All images are comparable to the positive control but not to the negative control (Figure 3B). Therefore, monensin (Figure 4A), chlorpromazine (Figure 4B), nystatin (Figure 4C), and ENIA (Figure 4D), which are known to block nonendocytic pathways, do not hinder nanocasule engulfment by chondrocytes. Even switching to a higher concentration than 5 μg/mL did not lead to an uptake inhibition. Contrarily, apart from no effect for nystatin and monensin, higher concentrations had direct toxic effects on the cells (chlorpromazine, ENIA) preventing further examination (data not shown). Cytochalasin D which blocks macro-pincytosis and phagocytosis also had a toxic effect on chondrocytes even in lower contentrations. Because of morphological changes visible by light microscopy, this inhibitor was excluded from the studies. However, if cells were provided with fresh medium, they recovered which is in accordance with literature.[33] Phagocytosis is unlikely to be the engulfment mechanism due to the cell type, and the investigation of micropinocytosis was performed with amiloride. In order to examine if cellular uptake was driven by physical proximity of LNC and cell membrane, chondrocytes exposed to LNC were kept at 4 °C for the entire incubation period prior to CARS microscopy analysis to minimize energy-dependent processes like endocytosis.[22] The recorded images are depicted in Figure 4E in the same panel structure. Unlike images from inhibitor studies, CARS images in Figure 4E look similar to images of the negative control chondrocytes (Figure 3B). In both cases, the lipid-derived images consist of a red hue lacking deeply colored areas. Consequently, the local accumulation of lipid molecules represented by LNC are missing. Therefore, only lipids originating from the cell are detected and converted into images with a colored hue. The overlay image in the bottom panel visualizes the localization of the red hue over most parts of the cell body.

Thus, the uptake of LNC by human chondrocytes is most likely driven by the physical proximity of nanocapsules and cell membrane. No evidence was found that an inhibitor successfully blocked an endocytic uptake route.

As a next experimental step, the pharmacological effect of the nanocapsules is analyzed. For this a suitable readout is required. In this context, nitric oxide (NO) is a stimulus to cause apoptosis in chondrocytes and consequently progression of osteoarthritis, which has been found in high levels in osteoarthritic cartilage.[34] Sodium nitroprusside (SNP) is a NO generator which can be added to cell culture medium to investigate NO induced apoptosis mechanisms.[35−37] The increase of cellular reactive oxygen species (ROS), which are involved in many physiological cell functions, is triggered by exogenous nitrite oxide.[37,38] However, ROS becomes cytotoxic once its level exceeds a threshold marked by the cell's antioxidant ability.[37,39] To determine this threshold, we performed an MTT assay after incubating chondrocytes with

SNP at different concentrations for 24 h. After 24 h, only 19.52% $\pm$ 0.04% ($n = 8$) of the cells were viable when exposed to 2 mM SNP, while the viability remained high for incubation experiments with 1.5 mM and 1 mM SNP (93.05% $\pm$ 0.04% and 108.33% $\pm$ 0.04%, respectively; $n = 8$). Thus, 2 mM SNP was used in the subsequent experiments to investigate if polyphenol loaded LNC have a protective effect against SNP induced oxidative stress. The results are depicted in Figure 5.
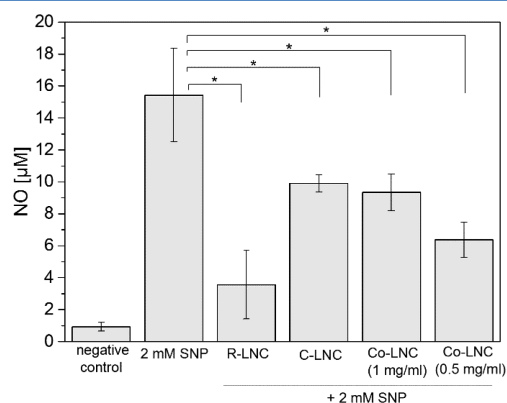
Figure 5. Nitric oxide (NO) levels expressed by chondrocytes under the influence of sodium nitroprusside (SNP) and a preincubation with different lipid-core nanocapsules ($n \geq 3$). Calculations are based on a standard calibration curve ($n = 3$). Statistical significance ($p < 0.05$) is indicated by *.

Chondrocytes express nitrite oxide (NO), as the molecule is a physiological messenger. Under the influence of 2 mM SNP, the NO level significantly increases. Similar to cell viability measurements, the level of NO depends on the SNP concentration. Incubation with 1 mM SNP resulted in 8.8 μM $\pm$ 1.5 μM of nitric oxide, whereas application of 1.5 mM SNP resulted in a readout of 11.2 μM $\pm$ 0.6 μM NO ($n = 10$). After preincubation with LNC, the amount of expressed NO significantly decreases ($p < 0.05$). The lowest value was found for R-LNC followed by Co-LNC (0.5 mg/mL), Co-LNC (1 mg/mL), and C-LNC. The contrary findings for R-LNC and C-LNC are very plausible as they correlate with the drug release profiles (Figure 2). Resveratrol shows the fastest release and is thus immediately available to scavenge ROS, consequently protecting chondrocytes, which is represented by the expression of low nitric oxide values (Figure 5, R-LNC). In contrast, a highly protective effect of curcumin is hardly expectable as only 3.9% $\pm$ 0.3% of the polyphenol are released after 24 h. Consequently, the expression of NO levels is rather high (Figure 5, C-LNC). Interestingly, the effect of coencapsulated polyphenols is in-between the results for R-LNC and C-LNC, respectively. Although the release profiles of the individual polyphenols from the combined formulation are coinciding with their counterparts R-LNC and C-LNC, resveratrol does not perform accordingly as the NO values at least for Co-LNC containing 0.5 mg/mL of resveratrol would be expected to be similar to R-LNC results. A study by Liang et al.[40] showed that resveratrol applied in solution prevented the SNP induced production of reactive oxygen species in rabbit chondrocytes as the polyphenol scavenged ROS. The authors proposed a signaling pathway which is invaded by resveratrol
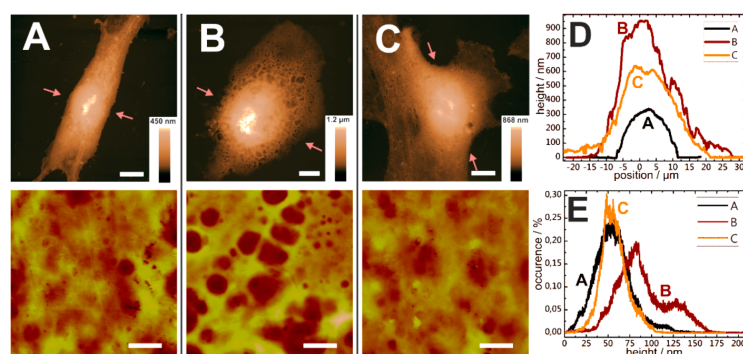
Figure 6. Atomic force microscopy analysis of chondrocytes as control (A), exposed to 2 mM SNP (B), and preincubation with Co-LNC prior to SNP exposure (C). Panels in the upper row show the entire cell bodies acquired in tapping mode (scale bars are 10 μm). Panels in the lower row show a close up of the cell surfaces with a z-scale of 200 nm (scale bars are 1 μm). Panel D shows cross sections of all cells through their highest point (indicated by the small arrows in parts A−C, upper panels). Panel E displays the results of bearing analysis from all closeup scans.

before ROS reaches the mitochondria. Curcumin was not included in this study. However, multiple studies employing curcumin and/or resveratrol are published where IL-1β was used to trigger inflammation in chondrocytes.[6,13,15,41,42]

Csaki et al.[6] studied synergistic effects of dissolved curcumin and resveratrol on chondrocytes upon exposure to IL-1β. The authors proposed that both polyphenols intervene in the same intracellular reaction cascade; however, curcumin interferes earlier than resveratrol. Implying a similar situation for the SNP induced mechanism, our findings lead to the following conclusions: Delivery of polyphenols by LNC and different release profiles seem to influence the protective effects of the two polyphenols and hinder a synergistic effect when codelivered in this case. Thus, the detected NO levels for nanocapsules comprising both polyphenols are higher than results for R-LNC but lower than results for C-LNC. Furthermore, the polyphenol loading of Co-LNC seems to have an impact as well. Detected NO values for Co-LNC encapsulating 0.5 mg/mL are lower than for an encapsulated polyphenol concentration of 1 mg/mL. Less curcumin is available in Co-LNC (0.5 mg/mL) to interfere with resveratrol effects, strengthening the protective effect resveratrol against SNP induced apoptotic effects by nitric oxide. While physicochemical characteristics did not show any influence on uptake behavior between capsules carrying various polyphenol loads as determined by CARS microscopy analysis, we gain a different insight from the NO-assay. Thus, this analysis is an illustrative example for the importance of research approaches using different complementary techniques to gain a "big picture" rather than relying on one single analysis. Even though the NO-assay provides interesting insight into the mechanism and interaction of the two polyphenols, the results are not suited for evaluating the overall "therapeutic effect" of the LNC codelivering the two polyphenols as the comparison with other analytical techniques shows. Further, a generally neglected factor is posed by changes of cell membrane and cytoskeleton of the cells upon induced inflammation and application of drugs.

In this context, AFM has lately been employed to detect physical differences between healthy and diseased cells, as cellular ultrastructures tend to alter in diseased or cancerous cells.[43−45] The high spatial resolution of this technique enables the investigation of cell membrane properties.[46] AFM provides

an attractive addition to conventional visualization and molecular biological assays in order to gain further information on cellular surface topography. Here, we use AFM to study the apoptotic effect of SNP and the preventive abilities of Co-LNC on cell morphology and membrane nanostructure of human chondrocytes.

AFM analysis was performed with chondrocytes without any treatment (control), after treatment with 2 mM SNP as well as after preincubation with Co-LNC prior to SNP exposure. Representative AFM images of the entire cell body as well as close-ups of the cell surface are displayed in Figure 6A−C. The control chondrocyte shows an elongated cell body with a rather homogeneous height forming lamellopodia in order to get into contact with other cells (Figure 6A). In contrast, the chondrocyte treated with 2 mM SNP presents a rather round, contracted shape with a structured surface, which is generally expected upon cell exposure with toxic substances and apoptosis (Figure 6B). These results are corroborated by results from MTT analysis showing that cell viability severely drops to 19.52% ± 0.04 after incubation with 2 mM SNP. A cell which was pretreated with Co-LNC prior to SNP exposure is shown in Figure 6C. Interestingly, in comparison to Figure 6A,B, the cell rather shows similarity to the untreated cell and defects due to SNP exposure (as seen in Figure 6B) are neglectable. Besides morphology analysis, height profiles of the cells were acquired. For all chondrocytes, the nucleus represents the highest area of the cell body, as displayed in Figure 6D. The differences in morphology revealed in Figures 6A−C are reflected in the height profiles. The control chondrocyte has a height of about 300 nm, whereas the cell treated with SNP is more than 3 times higher. When pretreated with Co-LNC prior to SNP, the cell height only increases to approximately 600 nm. Thus, the effect of SNP on cell height and morphology is significantly attenuated by polyphenol loaded LNC. To study changes in the cell membrane in more detail, close-up AFM images were recorded (Figure 6A−C, lower panel). Again, the images taken from control chondrocytes and cells pretreated with LNC depict a similar membrane structure. On the contrary, the cell membrane of SNP exposed chondrocytes exposes dents and bumps. Again, AFM analysis shows the protective effect of polyphenol-loaded LNC against SNP exposure. Nanocapsules delivering resveratrol and curcumin into the cell are likely to have a protective impact on chondrocytes against SNP. To

Analytical Chemistry

quantify the differences in surface morphology, a subsequent bearing analysis was performed (Figure 6E). The control chondrocyte and the Co-LNC pretreated cell show very similar height distributions with a maximum at approximately 50 nm. The SNP treated cell without protective pretreatment shows a different height distribution with two maxima at 75 and 140 nm, respectively. This reflects the visualized surface pattern well, as the two maxima can directly be correlated to the pitted surface structure.

Overall, the results of the AFM study are in good agreement with confocal fluorescence microscopy investigations by Liang et al. showing a remodeling of the cell's cytoskeleton upon exposure to SNP.[40] F-actin filaments shortened, microtubule structures were disrupted and thus the cell shrunk, which is observable in the AFM image in Figure 6B. A preincubation with resveratrol prevented these extreme effects on the cell, which can be substantiated by our findings. In this context, AFM investigations expanded the insight into the interplay between cells and carrier by visualizing cellular reactions and the advantage of combining different analytical procedures to create a more comprehensive picture in spite of a snapshot becomes evident. Overall, the nanocapsules have a positive effect on cellular nanobiomechanics reflected in the cell membrane morphology preventing damage leading to cell death by an externally applied nitric oxide donor.

CONCLUSIONS

In summary, we have successfully combined biological assays with sophisticated nondestructive, label-free microscopic techniques (CARS and AFM) for the an all-encompassing investigation of the therapeutic effects of advanced nanocapsules loaded with two polyphenols against induced osteoarthritic states of human chondrocytes. CARS microscopy images depict a clear uptake of the well-characterized lipid-core nanocapsules into the cellular cytosol. However, no distinct endocytotic pathway could be determined and cellular uptake was found to be energy dependent. The extent of these effects was found to be determined by the drug release kinetics from the capsules as well as by their drug loadings. Findings from these assays were underlined by AFM studies visualizing a protective effect on cell morphology and membrane surface as a result of chondrocytes treatment with the polyphenol-loaded nanocapsules. Thus, besides presenting a sophisticated carrier system for joint application, these results highlight the necessity and potential of establishing combinatorial analytical approaches to elucidate cellular uptake, the interplay of codelivered drugs, and their therapeutic effect on the subcellular level to gain a "big picture" for in-depth understanding of novel therapeutic approaches.

AUTHOR INFORMATION

Corresponding Author

*E-mail: m.windbergs@mx.uni-saarland.de. Fax: +49 681 98806 1009.

Author Contributions

The manuscript was written through contributions of all authors. All authors have given approval to the final version of the manuscript.

Notes

The authors declare no competing financial interest.

REFERENCES

(1) van der Kraan, P. M.; van den Berg, W. B. *Ageing Res. Rev.* **2008**, *7*, 106−113.
(2) Goldring, M. B. *Arthritis Rheum.* **2000**, *43*, 1916−1926.
(3) Im, H. J.; Li, X.; Chen, D.; Yan, D.; Kim, J.; Ellman, M. B.; Stein, G. S.; Cole, B.; Kc, R.; Cs-Szabo, G.; van Wijnen, A. J. *J. Cell. Physiol.* **2012**, *227*, 3488−3497.
(4) Malemud, C. J.; Islam, N.; Haqqi, T. M. *Cells Tissues Organs* **2003**, *174*, 34−48.
(5) van der Kraan, P. M.; Buma, P.; van Kuppevelt, T.; van den Berg, W. B. *Osteoarthritis Cartilage* **2002**, *10*, 631−637.
(6) Csaki, C.; Mobasheri, A.; Shakibaei, M. *Arthritis Res. Ther.* **2009**, *11*, R165.
(7) Jin, H.; Liang, Q.; Chen, T.; Wang, X. *PLoS One* **2014**, *9*, e91611.
(8) Wadsworth, T. L.; Koop, D. R. *Biochem. Pharmacol.* **1999**, *57*, 941−949.
(9) Bisht, K.; Wagner, K. H.; Bulmer, A. C. *Toxicology* **2010**, *278*, 88−100.
(10) Shen, C. L.; Smith, B. J.; Lo, D. F.; Chyu, M. C.; Dunn, D. M.; Chen, C. H.; Kwun, I. S. *J. Nutr. Biochem.* **2012**, *23*, 1367−1377.
(11) Shakibaei, M.; Schulze-Tanzil, G.; John, T.; Mobasheri, A. *Ann. Anat.* **2005**, *187*, 487−497.
(12) Shakibaei, M.; Mobasheri, A.; Buhrmann, C. *Genes Nutr.* **2011**, *6*, 171−179.
(13) Csaki, C.; Keshishzadeh, N.; Fischer, K.; Shakibaei, M. *Biochem. Pharmacol.* **2008**, *75*, 677−687.
(14) Shakibaei, M.; Csaki, C.; Nebrich, S.; Mobasheri, A. *Biochem. Pharmacol.* **2008**, *76*, 1426−1439.
(15) Shakibaei, M.; John, T.; Schulze-Tanzil, G.; Lehmann, I.; Mobasheri, A. *Biochem. Pharmacol.* **2007**, *73*, 1434−1445.
(16) Sinha, V. R.; Bansal, K.; Kaushik, R.; Kumria, R.; Trehan, A. *Int. J. Pharm.* **2004**, *278*, 1−23.
(17) Hillaireau, H.; Couvreur, P. *Cell. Mol. Life Sci.* **2009**, *66*, 2873−2896.
(18) Ourique, A. F.; Pohlmann, A. R.; Guterres, S. S.; Beck, R. C. *Int. J. Pharm.* **2008**, *352*, 1−4.
(19) Fontana, M. C.; Coradini, K.; Guterres, S. S.; Pohlmann, A. R.; Beck, R. C. *J. Biomed. Nanotechnol.* **2009**, *5*, 254−263.
(20) Jornada, D. S.; Fiel, L. A.; Bueno, K.; Gerent, J. F.; Petzhold, C. L.; Beck, R. C. R.; Guterres, S. S.; Pohlmann, A. R. *Soft Matter* **2012**, *8*, 6646−6655.
(21) Coradini, K.; Friedrich, R. B.; Fonseca, F. N.; Vencato, M. S.; Andrade, D. F.; Oliveira, C. M.; Battistel, A. P.; Guterres, S. S.; da Rocha, M. I.; Pohlmann, A. R.; Beck, R. C. *Eur. J. Pharm. Sci.* **2015**, *78*, 163−170.
(22) Herd, H.; Daum, N.; Jones, A. T.; Huwer, H.; Ghandehari, H.; Lehr, C. M. *ACS Nano* **2013**, *7*, 1961−1973.
(23) Torchilin, V. P. *Adv. Drug Delivery Rev.* **2005**, *57*, 95−109.
(24) Coradini, K.; Lima, F. O.; Oliveira, C. M.; Chaves, P. S.; Athayde, M. L.; Carvalho, L. M.; Beck, R. C. R. *Eur. J. Pharm. Biopharm.* **2014**, *88*, 178−185.
(25) Garbacik, E. T.; Herek, J. L.; Otto, C.; Offerhaus, H. L. *J. Raman Spectrosc.* **2012**, *43*, 651−655.
(26) Friedrich, R. B.; Kann, B.; Coradini, K.; Offerhaus, H. L.; Beck, R. C. R.; Windbergs, M. *Eur. J. Pharm. Sci.* **2015**, *78*, 204−213.
(27) Sabuncu, A. C.; Kalluri, B. S.; Qian, S.; Stacey, M. W.; Beskok, A. *Colloids Surf., B* **2010**, *78*, 36−43.
(28) Allouni, Z. E.; Cimpan, M. R.; Hol, P. J.; Skodvin, T.; Gjerdet, N. R. *Colloids Surf., B* **2009**, *68*, 83−87.

Analytical Chemistry

(29) Conner, S. D.; Schmid, S. L. *Nature* **2003**, *422*, 37−44.

(30) Zaki, N. M.; Tirelli, N. *Expert Opin. Drug Delivery* **2010**, *7*, 895−913.

(31) Aderem, A.; Underhill, D. M. *Annu. Rev. Immunol.* **1999**, *17*, 593−623.

(32) Pohlmann, R.; Kruger, S.; Hasilik, A.; Von Figura, K. *Biochem. J.* **1984**, *217*, 649−658.

(33) Nakase, I.; Niwa, M.; Takeuchi, T.; Sonomura, K.; Kawabata, N.; Koike, Y.; Takahashi, M.; Tanaka, S.; Ueda, K.; Simpson, J. C.; Jones, A. T.; Sugiura, Y.; Futaki, S. *Mol. Ther.* **2004**, *10*, 1011−1022.

(34) Diaz-Gallego, L.; Prieto, J. G.; Coronel, P.; Gamazo, L. E.; Gimeno, M.; Alvarez, A. I. *J. Orthop. Res.* **2005**, *23*, 1370−1376.

(35) Blanco, F. J.; Ochs, R. L.; Schwarz, H.; Lotz, M. *Am. J. Pathol.* **1995**, *146*, 75−85.

(36) Tonomura, H.; Takahashi, K. A.; Mazda, O.; Arai, Y.; Inoue, A.; Terauchi, R.; Shin-Ya, M.; Kishida, T.; Imanishi, J.; Kubo, T. *Osteoarthritis Cartilage* **2006**, *14*, 545−553.

(37) Wu, G. J.; Chen, T. G.; Chang, H. C.; Chiu, W. T.; Chang, C. C.; Chen, R. M. *J. Cell. Biochem.* **2007**, *101*, 1520−1531.

(38) Lo, Y. Y.; Conquer, J. A.; Grinstein, S.; Cruz, T. F. *J. Cell. Biochem.* **1998**, *69*, 19−29.

(39) Stoop, R.; Buma, P.; van der Kraan, P. M.; Hollander, A. P.; Billinghurst, R. C.; Poole, A. R.; van den Berg, W. B. *Arthritis Rheum.* **2000**, *43*, 2121−2131.

(40) Liang, Q.; Wang, X.-p.; Chen, T.-s. *Apoptosis* **2014**, *19*, 1354−1363.

(41) Mathy-Hartert, M.; Jacquemond-Collet, I.; Priem, F.; Sanchez, C.; Lambert, C.; Henrotin, Y. *Inflammation Res.* **2009**, *58*, 899−908.

(42) Lei, M.; Wang, J.-g.; Xiao, D.-m.; Fan, M.; Wang, D.-p.; Xiong, J.-y.; Chen, Y.; Ding, Y.; Liu, S.-l. *Eur. J. Pharmacol.* **2012**, *674*, 73−79.

(43) Cross, S. E.; Jin, Y. S.; Tondre, J.; Wong, R.; Rao, J.; Gimzewski, J. K. *Nanotechnology* **2008**, *19*, 384003.

(44) Iyer, S.; Gaikwad, R. M.; Subba-Rao, V.; Woodworth, C. D.; Sokolov, I. *Nat. Nanotechnol.* **2009**, *4*, 389−393.

(45) Lee, G. Y.; Lim, C. T. *Trends Biotechnol.* **2007**, *25*, 111−118.

(46) Lesniewska, E.; Emmanuel Milhiet, P.; Giocondi, M.-C.; Le Grimellec, C. In *Methods in Cell Biology*, Bhanu, P. J., Hörber, J. K. H., Eds.; Academic Press: New York, 2002; pp 51−65.

Addendum III – Adhesion of *Staphylococcus aureus* and its Mutants to Abiotic Surfaces of Different Surface Energies

Authors: C. Spengler[1], N. Thewes[1], F. Nolle[1], M. Bischoff[2] and K. Jacobs[1]

[1] Department of Experimental Physics, Saarland University, 66041 Saarbrücken, Germany.
[2] Institute of Medical Microbiology and Hygiene, Saarland University, Homburg, Germany.

Author contributions:
*Experiments were designed by **C. Spengler** and N. Thewes. Experimental results were achieved by **C. Spengler**, N. Thewes and F. Nolle. The article was written by **C. Spengler**, N. Thewes, M. Bischoff and K. Jacobs. Scientific work was directed by M. Bischoff and K. Jacobs.*

Abstract - The adhesion of *Staphylococcus aureus* to abiotic surfaces is crucial for the spreading of infectious diseases. By combining a high number of single cell force spectroscopy measurements with genetically modified *S. aureus* cells, this study provides unique insights into the adhesion process of this pathogen to abiotic surfaces of different wettability. Our results show that *S. aureus* utilizes different mechanisms and interactions when binding to hydrophobic and hydrophilic surfaces. This results in a much higher adhesive strength on the hydrophobic surfaces. We found that covalently bound cell wall proteins strongly interact with hydrophobic substrates, while their contribution to the overall adhesion force is smaller on hydrophilic substrates. Teichoic acids promote the adhesion to hydrophilic as well as hydrophobic surfaces, however, to different extents. A comparison of the binding properties of *S. aureus* with that of the apathogenic *Staphylococcus carnosus* revealed that the pathogen adheres much stronger to abiotic substrates than cells of the apathogenic relative. Additionally, our studies demonstrate that different bacterial cells of one and the same culture may exhibit strongly varying adhesion properties ('cell individuality'). Our results can help to design new models of bacterial adhesion and may also be used to interpret adhesion of other microorganisms with similar surface properties to abiotic surfaces.

Adhesion of *Staphylococcus aureus* and its Mutants to Abiotic Surfaces of Different Surface Energies

Christian Spengler,[†,¶] Nicolas Thewes,[†,¶] Friederike Nolle,[†] Markus Bischoff,[‡] and Karin Jacobs*[,†]

†*Department of Experimental Physics, Saarland University, 66041 Saarbrücken, Germany*
‡*Institute of Medical Microbiology and Hygiene, Saarland University, 66421 Homburg/Saar, Germany*
¶*These authors contributed equally to this work.*

E-mail: k.jacobs@physik.uni-saarland.de
Phone: +49 (0)681 302 71777. Fax: +49 (0)681 302 71700

Abstract

The adhesion of *Staphylococcus aureus* to abiotic surfaces is crucial for establishing device related infections. By combining a high number of single cell force spectroscopy measurements with genetically modified *S. aureus* cells, this study provides unique insights into the adhesion process of these pathogens to abiotic surfaces of different wettability. Our results show that *S. aureus* utilizes different mechanisms and interactions when binding to hydrophobic and hydrophilic surfaces. This results in a much higher adhesive strength on the hydrophobic surfaces. We found that covalently bound cell wall proteins strongly interact with hydrophobic substrates, while their contribution to the overall adhesion force is smaller on hydrophilic substrates. Teichoic acids promote the adhesion to hydrophilic as well as hydrophobic surfaces, however, to different extents. A comparison of the binding properties of *S. aureus* with that of the apathogenic *Staphylococcus carnosus* revealed that the pathogen adheres much stronger to abiotic substrates than cells of the apathogenic relative. Additionally, our studies demonstrate that different bacterial cells of one and the same culture may exhibit strongly varying adhesion properties ('cell individuality'). Our results can help to design new models of bacterial adhesion and may be used to interpret adhesion of other microorganisms with similar surface properties to abiotic surfaces.

Introduction

Staphylococcus aureus is an opportunistic pathogen associated with different community and hospital acquired infections.[1] One reason for its high infectivity is the cells' ability to strongly adhere to various surfaces, including a large number of abiotic materials,[2–4] and subsequently form mechanically and chemically robust biofilms.[5,6] Thereby, the adhesion of cells and biofilm formation can take place on natural surfaces as well as on abiotic surfaces, such as implanted medical devices.

Because of the latter, the organism is a major cause of implant related infections with severe consequences for the patients' health.[7–11] Furthermore, due to its environmental robustness and ability to adhere to many different types of surfaces, the bacterium spreads quickly to formerly non-inhabited space, for example in clinical buildings.[12] Hence, understanding and controlling the adhesive behaviour of *S. aureus* is

of fundamental importance for health care and engineering. [13,14]

The state-of-the-art method in quantitative bacterial adhesion research is AFM-based force spectroscopy with single bacterial probes ('single cell force spectroscopy', SCFS). [15–19] This method allows the investigation of many different mechanisms on a single-cell or even molecular level. For instance, it can be performed on bare abiotic surfaces, on conditioned surfaces and on natural near surfaces (e.g. hydroxyapatite) with pretreated cells. [20–24]

Using SCFS, a previous study demonstrated that, bacterial adhesion to hydrophobic surfaces is governed by cell wall macromolecules tethering to the surface. [4] As a consequence, the adhesive strength of a single cell is determined by the number of contact-forming macromolecules and by the strength of each individual binding site whereby one macromolecule could also have more than one of these binding sites. Of note, important adhesion parameters, such as the bacterial contact area to solid surfaces, are a highly cell-individual property. [25] Thus, general statements concerning the adhesion of certain cell types can only be derived with good statistics obtained from a sufficiently large number of cells.

Nevertheless, all former studies have in common that the adhesive strength strongly depends on surface wettability: Adhesion to hydrophobic surfaces is markedly stronger than to hydrophilic surfaces. [16,26,27] However, to date, it remains unclear which bacterial cell wall macromolecules, respectively which groups of macromolecules, are mainly responsible for the adhesion to these two types of abiotic surfaces with highly different surface energies.

To find important adhesion factors, previous studies used mutant cells deficient in some types of surface macromolecules to investigate the role of these specific macromolecules for adhesion to natural environments. [28,29] For instance, it was found that *S. aureus* cells lacking cell wall teichoic acids adhere weaker to human endothelial cells than wild-type cells and that surface anchored proteins are important for nasal colonization. [28,29] Other work demonstrated that individual adhesion factors such as fibronectin

binding protein A and clumping factor B are important for the ability of *S. aureus* to adhere to endothelial cells and to human desquamated nasal epithelial cells, respectively. [30,31]

Nevertheless, a quantitative analysis of the role of different types of bacterial macromolecules for adhesion to abiotic surfaces on a single cell level was not conducted yet.

In this paper, we present a detailed characterization of the adhesion of *S. aureus* cells to abiotic surfaces (i.e. substrates without any surface conditioning layer) by evaluating differences in adhesion behaviour of wild-type cells to hydrophilic and hydrophobic surfaces and consecutively analyzing the role of different types of surface macromolecules in the adhesion process. Our research is based on SCFS of *S. aureus* 113 wild-type nd mutant cells exhibiting changes in cell wall macromolecular properties. Adhesion properties were investigated on very hydrophilic and strongly hydrophobic Si wafer-based substrates with an as yet unprecedented large sample size of over 250 single bacterial cells.

Considering that the investigated groups of surface molecules are quite common in the microbial world and do have several general properties (e.g. hydrophobic domains on proteins, sugar containing backbone in teichoic acids), the outcome of this study may also be of relevance to understand the adhesive behaviour of many other species of bacteria. Even for other microorganisms, such as fungi or eucaryotic cells, our results may help the elucidate the process of adhesion to abiotic surfaces and the role of the surface hydrophobicity of various substrates.

Experimental

Substrate Preparation

Si wafers (Siltronic AG, Burghausen, Germany) are the basis of the hydrophilic as well as the hydrophobic substrates used in this study. The Si substrates feature a native silicon oxide layer of 1.7(2) nm (the number in parentheses denotes the error of the last digit) and an RMS (root mean square) surface rough-

ness of $0.09(2)$ nm.[32] Cleaning the Si wafers thoroughly results in a hydrophilic substrate with an advancing water contact angle of $5(2)°$, a surface energy $64(1)$ mJ/m^2 and a zeta-potential of $-104.4(1)$ mV at pH 7.3.[32] The hydrophobic substrate is prepared by covering a Si wafer with a self-assembled monolayer of octadecyltrichlorosilane (OTS) according to a standard protocol.[33] The result is a CH$_3$-terminated substrate with an advancing (receding) water contact angle of $111(1)°$ $(107(2)°)$, a surface energy of $24(1)$ mJ/m^2[33] and a zeta-potential of $-80.0(1)$ mV.[32] For force spectroscopy experiments substrates were immersed into phosphate-buffered saline (PBS, pH 7.3, ionic strength 0.1728 mol/l at 20 °C).

Bacterial Strains and Growth Conditions

Adhesion studies were performed with *Staphylococcus aureus* strain SA113. This biofilm-positive laboratory strain is a common platform to study cell wall macromolecules of *S. aureus*.[28,34–36] For an in-depth analysis of the cell wall macromolecule contribution to the staphylococcal adhesion process, the adhesion of SA113 wild-type cells (SA113 WT) on abiotic substrates was compared to mutant cells of the same strain featuring the following changes in cell wall properties:

- SA113 $\Delta srtA$: deficient in covalently bound cell wall proteins due to a deletion of the gene *srtA* encoding the enzyme sortase that catalyzes the covalent linkage of proteins into the cell wall.[29,37]

- SA113 $\Delta tagO$: lacking the gene *tagO* encoding a glycosyltransferase that catalyzes the first committed step of wall teichoic acid synthesis (but having lipoteichoic acids).[28]

- SA113 $\Delta dltA$: lacking the d-alanine-d-alanyl carrier protein ligase ΔltA catalyzing the first step in the d-alanylation of lipoteichoic acids (LTAs). As a consequence, the wall- and lipoteichoic acids of this mutant lack d-alanine, leading to an increased negative surface charge of the cell wall.[35]

As an additional comparison, adhesion measurements with apathogenic *Staphylococcus carnosus* cells (strain TM300) were performed.[16,38,39]

All bacterial cultures were prepared the same way, starting the day before the force spectroscopy experiments: An overnight culture was prepared in 5 ml tryptic soy broth (TSB) medium and incubated at 37 °C and 150 rpm for 16 h. The next day, 40 μl of the overnight culture were transferred into 4 ml of fresh TSB medium and incubated for another 2.5 h to obtain exponential phase cells. Subsequently, 0.5 ml of this culture were diluted 1:1 with PBS and washed three times, using 1 ml PBS each, to remove extracellular material.

Single-Cell Force Spectroscopy

Single bacterial probes were prepared according to a standard protocol:[19] Tipless cantilevers (MLCT-O, Bruker-Nano, Santa Barbara, USA) were covered with a thin layer of polydopamine by polymerization of dopamine hydrochloride (99%, Sigma-Aldrich, St. Louis, USA) in TRIS buffer (pH 4.8). Afterwards, single bacterial cells were attached to the polydopamine coated cantilever using a micromanipulator; care was taken that cells never dry out during probe preparation or force measurements. The cantilevers were calibrated before each measurement.

Force spectroscopy measurements with single bacterial probes were conducted under ambient conditions in phosphate buffered saline (PBS, pH 7.3) using a Bioscope Catalyst (Bruker-Nano, Santa Barbara, USA). Force-distance curves were performed using parameter values that correspond to similar studies.[16,40–42] The ramp size was 800 nm, the force trigger (denoting the maximal force with which the cell is pressed onto the substrate) was 300 pN and retraction speed was 800 nm/s. Approach speed was 800 nm/s for force-distance measurements without surface delay and 100 nm/s when a surface delay of 5 s was applied. Surface delay

3

times of a few seconds are a common choice to study the influence of the contact time on bacterial adhesion processes.[18,26,41–43] Measurements without surface delay yield a contact time below 0.5 s.[16,40]

We performed force-distance measurements with single bacterial cells of different species (*S. aureus*113 wild-type and mutants, *S. carnosus*) on either a hydrophobic or a hydrophilic substrate. Thereby, for each bacterial probe and parameter set at least 50 force-distance curves were recorded. The retraction part of each force-distance curve was evaluated to characterize the strength of adhesion, see Figure 1. Hence, the maximum force between a surface and an individual cell ('adhesion force') as well as the work necessary to completely separate cell and surface ('adhesion energy') were calculated. In addition, the so called 'rupture length' depicting the distance at which bacterium and surface lose contact was measured. On hydrophobic surfaces, bacterial cells are object to a long-ranging attractive force mediated by surface macromolecules ('snap-in event').[4] We evaluated this mechanism with respect to the distance at which attraction starts ('snap-in separation') in order to detect differences between wild-type and mutant cells. In contrast, on hydrophilic surfaces, force-distance measurements with single bacterial cells show no significant snap-in process, see inset to Figure 1.

Histograms

All collected data of the same type (e.g. adhesion force or rupture length) of all tested cells of one kind (WT or mutant) are visualized in one histogram each. Thereby, the bin size is determined as follows: The number of bins n_B is calculated based on the dataset in the histogram with the smallest number of individual values N by Rice's rule: $n_B = \lfloor 2 \cdot \sqrt[3]{N} \rfloor$.[44] Then, the bin size is determined by equidistant fragmentation of the maximal range of this data set.
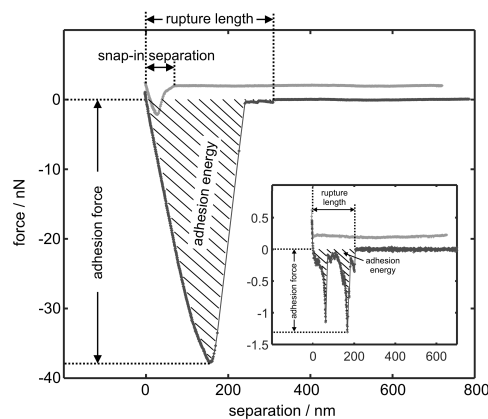
Figure 1: Exemplary force-distance curves and the measures used to quantify adhesion of a single bacterial cell. The large curve depicts the adhesion of a *S. aureus* wild type cell to a hydrophobic surface. The small curve in the inset shows a single *S. aureus* wild type cell adhering to a hydrophilic surface with an additional contact time of five seconds. (Note that in both curves, for better visibility, the approach part (light grey) has a small offset compared to the retraction part (dark grey).)

Results and Discussion

In the first part of the paper, the adhesion behaviour of SA113 WT cells is demonstrated and discussed in detail on hydrophilic and hydrophobized Si wafers. Then, to identify different contributions of bacterial surface molecules to the adhesion on both types of surfaces, the adhesion of apathogenic *S. carnosus* cells and of *S. aureus* mutant cells exhibiting changes in cell wall macromolecular properties is compared to the data of the SA113 WT cells.

Adhesion of SA113 WT to Hydrophobic and Hydrophilic Surfaces

Shape of Force-Distance Curves on Different Surfaces
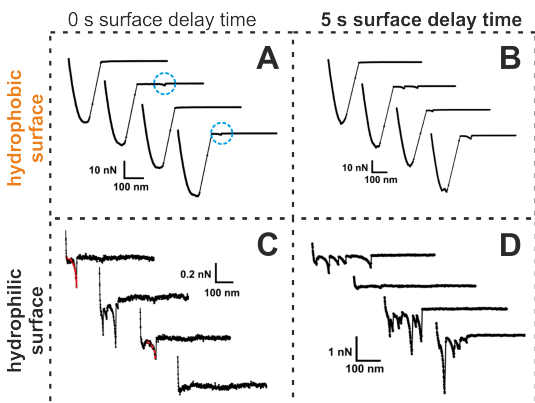
Figure 2: Exemplary retraction parts of force-distance curves for one and the same SA113 WT cell on hydrophobic (upper panel) and hydrophilic (lower panel) surfaces with surface delay times of 0 s (left side) and of 5 s (right side). The blue circles in panel A and the red curve in panel C highlight specific features of the curve that are discussed in detail in the main text.

To understand general differences between adhesion on hydrophobic and hydrophilic surfaces, force-distance measurements with one and the same bacterial cell were performed on both substrates consecutively. We used the same probe without additional surface contact time (0 s) and with 5 s of surface delay time on both surfaces. Figure 2 shows exemplary retraction parts of force-distance curves on both substrates for both surface contact times used.

Most strikingly, the shapes of the force-distance curves exhibit strong differences between hydrophobic and hydrophilic substrates: All individual curves of one bacterial cell on the hydrophobic substrate look nearly the same, see Figure 2 A: The curves are very 'smooth' and have a reproducible, characteristic shape in depth and width. They feature an almost linear increase in (negative) force upon retracting the bacterium from the surface. Close to the maximal absolute force value, the gradient of the force-distance curves decreases and around the maximal absolute force, a small plateau can be observed. At larger distances from the surface, rarely single polymer stretching signals are observed (see. Figure 2 A, blue circles). Additionally, the cells are subject to a cell wall macromolecule-induced long ranging attraction ('snap-in event' in the approach part of the curve, not shown) that has been investigated in detail in a previous study.[4]

In contrast, on the hydrophilic substrate, force-distance curves have a 'spiky' shape, i. e. they often show several distinct 'adhesion peaks' that remind of stretching and rupturing of surface polymers.[45,46] These peaks can be fitted by the worm-like chain (WLC) model,[47,48] see Figure 2 B, first and third curve. Of note, on hydrophilic substrates, the shapes of the force-distance curves for one and the same cell are not reproducible and consecutive curves exhibit strong fluctuations in number and depth of individual peaks.

Using the curves of this single bacterial cell, it is also possible to make first statements about the adhesive strength on both surfaces: Without additional surface contact time, mean values of adhesion forces F_{adh} differ by two orders of magnitude between hydrophobic (F_{adh}=35.2(9) nN[1]) and hydrophilic (F_{adh}=0.23(30) nN) substrates, Fig-

---

[1]The number in brackets gives the standard deviation of the calculated mean value.

ure 2 A and C.

After a surface delay time of 5 s compared to 0 s, the relative increase in adhesion force is much more pronounced on the hydrophilic compared to the hydrophobic substrate, see Figure 2: The mean adhesion force on the hydrophilic substrate increased, by a factor of 5.5 to 1.26(66) nN, while on the hydrophobic substrate, the mean adhesion force remained more or less identical (47.4(16) nN). Interestingly, the basic characteristics of the force-distance curves did not change: The shapes of the curves on hydrophobic and hydrophilic substrates described for zero seconds of surface delay basically resembled those seen with a surface delay of 5 s. Only, on the hydrophilic substrate, for prolonged surface contact time, more characteristic adhesion peaks emerged in the retraction curve.

From the above mentioned findings, it can be concluded that for one and the same cell the shapes of the retraction part of force-distance curves on hydrophobic compared to hydrophilic surfaces are clearly distinguishable and very characteristic for each type of surface. Additionally, these data confirm previous findings reporting that adhesion forces of *S. aureus* cells differ strongly between the two substrates.[2] To substantiate these findings, a high number of single cells was tested and characteristic measures of the adhesion are discussed in the next paragraph.

Statistical Analysis of SA113 WT Adhesion to Surfaces of Different Wettability

In order to identify potential cell-to-cell variations, we investigated the adhesion of *S. aureus* 113 wild-type cells to abiotic substrates by recording a variety of force-distance curves for a large number of single cells. The obtained measures – adhesion force, adhesion energy, rupture length and snap-in separation (the latter characteristic was determined on hydrophobic surfaces only) – of every single curve were combined and visualized in histograms. On both substrates, we used a surface delay time of 0 s and additionally, 5 s of surface de-

lay time on hydrophilic substrates due to the strong dependence of adhesion forces to hydrophilic substrates on the contact time.[26,41,42] Additionally, the mean values and standard deviation (as error bars) of adhesion force and adhesion energy (for the hydrophobic surface only) for every tested cell are shown separately.

On the hydrophobic surfaces (see Fig. 3), adhesion forces of single SA113 WT cells were in the range of 5–50 nN and adhesion energies in the range of 10^2–2.2×10^6 k_BT. The distributions exhibit two maxima containing roughly half of the data points and being more pronounced in adhesion force data (at values of approx. 10 nN and 35 nN) compared to adhesion energy data. Interestingly, the values of each individual cell revealed only small standard deviations but varied strongly between different cells (see insets in Fig. 3). Rupture lengths of SA113 WT cells were in the range of 100–750 nm with most values located at 100–400 nm, but also including a second maximum at values of approximately 600 nm. The snap-in event is characterized by the maximal range of the attractive force, called the 'snap-in separation' with values of 10–100 nm.

Figure 4 shows histograms of adhesion forces, adhesion energies and rupture length of SA113 WT cells adhering to hydrophilic silicon. The histograms condense data of 20 single cells with a surface delay time of 0 s as well as of 53 single cells with a surface delay time of 5 s. We found adhesion forces of 0–1.5 nN and adhesion energies of 0–200,000 k_BT for a surface delay time of 0 s. Both magnitudes strongly increased when applying a surface delay time of 5 s, which is in accordance with another study on bacterial adhesion:[16] By increasing the surface delay time, the maximum values as well as the relative occurrences shifted towards larger values. The rupture lengths were in the range of around 0–500 nm. Notably, for the rupture lengths, a larger surface delay time did only slightly increase the maximum value here, rather the relative occurrence of larger values increased. For 5 s of surface delay time most rupture lengths were located at 50–250 nm. Confirming our findings presented in Figure 2 C, and in contrast to measurements on

---

[2]Here, we have only shown data of one cell, but these results also hold true for all other individuals.
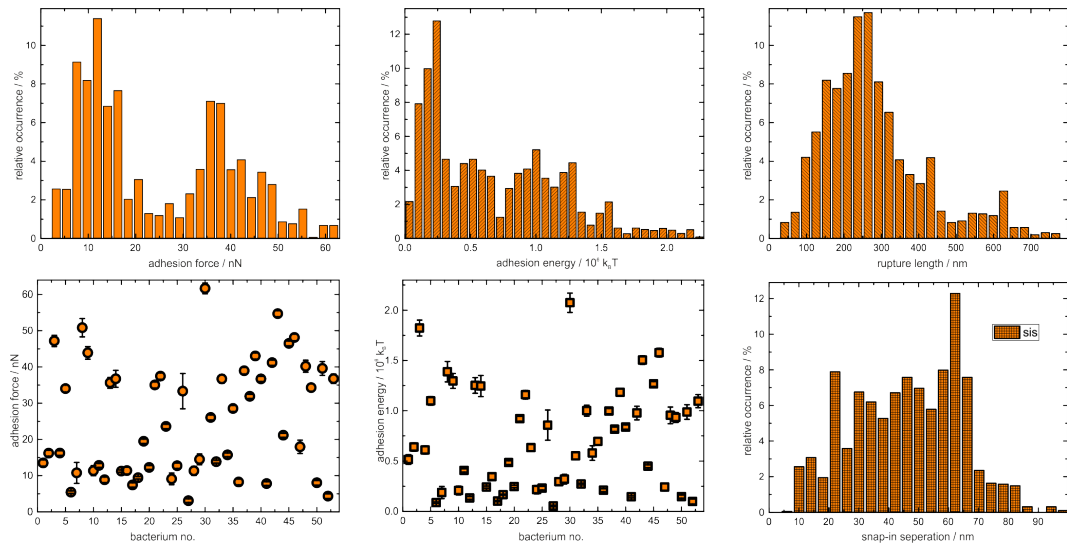
Figure 3: Histograms of adhesion forces, adhesion energies, rupture lengths and snap-in separations for all tested SA113 WT cells (53 individuals in total) on hydrophobized silicon surfaces. Additionally, the values of adhesion force and energy – including their standard deviations – for each individual cell are depicted separately.
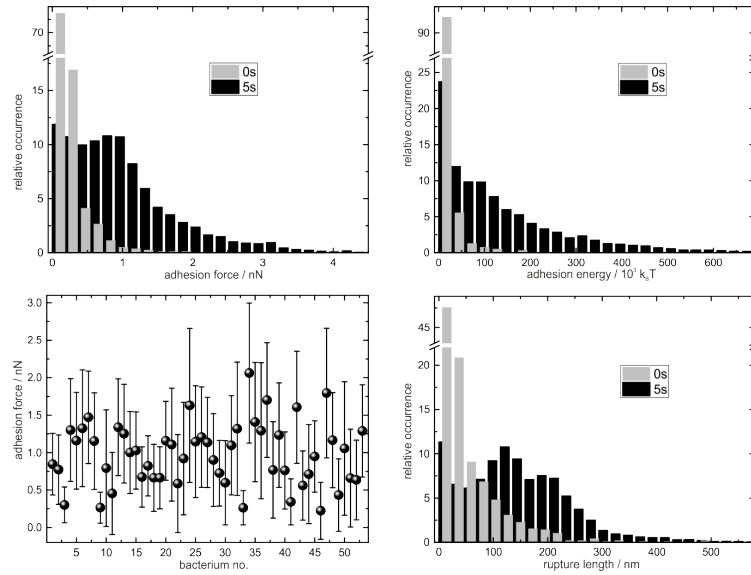
Figure 4: Histograms of adhesion forces, adhesion energies and rupture lengths for all tested SA113 WT cells (73 individuals in total) on hydrophilic silicon surfaces for surface delay times of 0 s and 5 s. Additionally, the values of adhesion force – and their standard deviations – for each individual cell (that was tested with 5 s of surface delay time) are depicted separately.

7

the hydrophobic surface, each individual cell showed quite large variations in the adhesive strength in the course of several force-distance curves. Additionally, the mean value for different cells were all in the very same force and energy range which is also in contrast to the hydrophobic case where the adhesive strength was a very cell-individual property.

Discussion of SA113 Wild-Type Adhesion

Although the shape of the force-distance curves and the histograms from many measurements were very different for surfaces with different surface energies, the adhesion process seemed to rely on the same concept: On both substrates, the retraction curves indicated the consecutive stretching and rupturing of tethered macromolecules,[49,50] suggesting that bacterial adhesion relies on the binding of bacterial cell wall macromolecules. For hydrophobic surfaces, the correctness of this assumption has been shown in previous studies by combining experimental results and Monte Carlo simulations;[4,16] on the hydrophilic surface, however, it also seems to be true because characteristic features of the retraction curves can be fitted by the WLC model suggesting stretching of single polymers (see Figure 2 B, first and third curve).

That way, the obtained experimental results may be explained by different numbers of tethering bacterial surface macromolecules: On the hydrophobic surface, the smooth curve shape and the high adhesion forces correspond to large amounts of tethered surface molecules. This decreases the load on each macromolecule, thus reduces the probability for each molecule to detach from the surface which results in a high adhesion force upon retraction. At the same time, a high number of tethering surface molecules suppresses stochastic fluctuations and causes very reproducible and smooth curve shapes without visible characteristic single molecule stretching signals. Therefore, the mean values of every cell (adhesion force and energy) show only small standard deviations. Also, because of the high reproducibility of curves for every individual cell, adhesion force and ad-

hesion energy are directly connected, namely by the rupture length. As a consequence on the hydrophobic surface, histograms of adhesion force and adhesion energy show almost the same characteristics, especially the bimodal distribution of measured values. This bimodality is slightly less pronounced in adhesion energy data because some curves exhibit an additional adhesion peak just before the cell loses contact to the surface (see Figure 2 A, second and fourth curve). This may be the result of some long and soft molecules that only occasionally tether to the surface and also make the last contact to it. Their presence manifests in the second small maximum in the histogram of rupture lengths at approximately 600 nm.

The bimodal distribution in adhesive strength could have one of the following reasons: i) *S. aureus* cells can form capsules of polysaccharides that could reduce or improve the adhesion capability of the respective cell. However, this explanation seems rather unrealistic because all used cells in this study are taken from exponential growth phase when capsule formation should not happen regularly.[51] Especially because both distributions contain almost equally half of the data, the following explanation seems to be more reasonable: ii) Depending on the region of the cell envelope (newly formed or already several generations old) the occurrence of some adhesins could be reduced or vice versa enhanced. Because the cells divide basically in their equatorial plane, on average, for approximately half of the cells a 'new' region was pressed onto the surface while for the other half of the cells an 'older' cell wall region was tested. This hypothesis is corroborated by the fact that with very good accuracy the two distribution cover half of the cells tested. Additionally, previous scanning electron microscopy studies demonstrated that the cell surface morphology of individual *S. aureus* cells may differ substantially in a cell division based manner.[52,53]

For the rupture length of one adhesion event, only few – or in the extreme case only one – tethering macromolecules are needed that make the last contact to the surface. Our results show, that these molecules have in average a

length of around 250 nm when stretched immediately before detaching from the surface. In contrast, for the snap-in event many molecules are needed in order to exhibit a force strong enough to 'pull' the cell to the surface.[4] These thermally fluctuating molecules have on average exhibited enough binding sites when the cell body is in a distance of around 50 nm from the surface. Therefore, it is hardly possible to decide if the same molecules are responsible for the snap-in event and the last contact to the surface.

In contrast to the large number of tethering macromolecules on the hydrophobic surface, spiky curves and rather weak adhesion forces on the hydrophilic surface correspond to small numbers of tethered macromolecules. A small number of tethering macromolecules produces force-distance curves where individual polymer stretching is visible. Curves with strongly fluctuating shapes, in number as well as in depths of individual peaks, imply that in each adhesion event, different numbers or types of molecules bind to the substrate. As seen in Figure 4, on the hydrophilic surface no cell individuality occurs: All forces are in the same range with very high standard deviations for each individual. (This holds also true for adhesion energy and rupture length, not shown). As a consequence, in contrast to the scenario on hydrophobic surfaces, adhesion force and energy do not necessarily show the same distribution.

For a surface delay time of 0 s, all histograms show distributions with maxima very close to zero (see Figure 4), meaning that SA113 WT cells are almost non-adherent to hydrophilic substrates if no additional surface contact time is applied. For 5 s of surface delay time, adhesion force and energy feature a strong increase. This increase is most likely due to additional surface macromolecules tethering to the surface within the 5 s of surface delay time. Alternatively, bound proteins might rearrange (i.e. change their topology) to better adhere to the surface. But still the number of tethering macromolecules seems low compared to the hydrophobic case because curves show individual peaks and highly fluctuating shapes. It is also possible that quite a large number of adhesion

molecules might get into contact with the hydrophilic surface, however, only a small proportion of specific proteins can bind firmly enough to this type of surface to hold the cell back, once the retraction of the probe starts. The macromolecules responsible for adhesion on the hydrophilic part have on average a length of around 100 nm when stretched.

So far, we have shown that the main difference between adhesion on the two substrates is a large number of tethering macromolecules on the hydrophobic and a small number on the hydrophilic surface. This difference can have two reasons (or a combination of them): i) The bacterial surface macromolecules mediating adhesion to hydrophilic substrates and to hydrophobic substrates are not the same and the molecules that cause adhesion to hydrophilic substrates are less numerous, i.e. their density is low on the bacterial surface. ii) The macromolecules tethering to both surfaces are the same but the binding probability is much lower on the hydrophilic surface. The large increase of adhesion forces on hydrophilic substrates with prolonged contact time is a clear hint towards reason ii).

With the above discussed results, the forces that cause the different amounts of tethering cell wall macromolecules on both substrates may be identified. Van der Waals and electrostatic forces may be excluded because they differ only slightly between both substrates. Hence, the hydrophobic interaction strongly influences the adhesion of SA113 WT cell; a fact that has been shown for different bacterial species.[16,26,27] This way, the strong adhesion to hydrophobic substrates is caused by the extensive binding of bacterial surface proteins via hydrophobic residues.[16,26] The binding of these groups to the surface is non-directional and occurs immediately as soon as the group is close enough to the surface. This also explains why an additional surface contact time has almost no effect of the adhesion on the hydrophobic surface. In contrast, on hydrophilic substrates, where the number of tethering macromolecules is much lower, adhesion seems to rely on directional hydrogen-bonds.[54,55] In this case, bond formation is a stochastic process and does

9

not happen instantaneously. This hypothesis is supported by the fact that an additional surface contact time of 5 s strongly increases the adhesive strength due to an increased number binding sites.

Conclusion – On hydrophobic surfaces, many bacterial macromolecules tether to the substrate by hydrophobic interactions and therefore the adhesive strength is mainly determined by the individual bacterial cell and its cell wall composition (the number and properties of cell wall macromolecules). In contrast, on hydrophilic surfaces, much fewer molecules take part in the adhesion process and apparently not the properties of the individual cell, but rather the characteristics of each single adhesion event (probability to exhibit a binding site for every cell wall macromolecule) determine the adhesive strength.

Overview for the rest of the paper – Regarding the large number of cells in the adhesion statistics, we assume that the force-distance curves and distributions in Figures 2, 3 and 4 elaborately characterize the adhesion of SA113 WT cells to hydrophobic and hydrophilic substrates.

Based on this detailed characterization, it is now possible to investigate the contribution of different groups of cell wall molecules to the adhesion of *S. aureus* further by comparing the adhesion of the SA113 WT cells to the adhesion of a set of isogenic SA113 mutants lacking certain groups of cell wall macromolecules, and of the apathogenic relative *S. carnosus* TM300. First, the adhesion to hydrophobic and afterwards to hydrophilic surfaces is characterized. For this purpose, all data of the mutants are shown in histograms compared to the histograms of the wild-type depicted above. For reasons of clarity, the number of histograms is slightly reduced as compared to SA113 WT cells as follows: Because of the high reproducibility of force-distance curves for each individual cell on the hydrophilic surface and the direct connection between adhesion force and adhesion energy, only one of these measures is depicted, namely the adhesion force. The mean values of the adhesion force for every individual cell are depicted as insets in the force histograms.

On the hydrophilic surface, because of the high variance between single adhesion events even for one and the same cell, data from individual cells are not shown. Because of the very poor adhesion for 0 s of surface delay time, we only performed force-distance measurements with additional surface contact time of 5 s for the mutants.

Adhesion of Mutant Cells on Hydrophobic Substrates
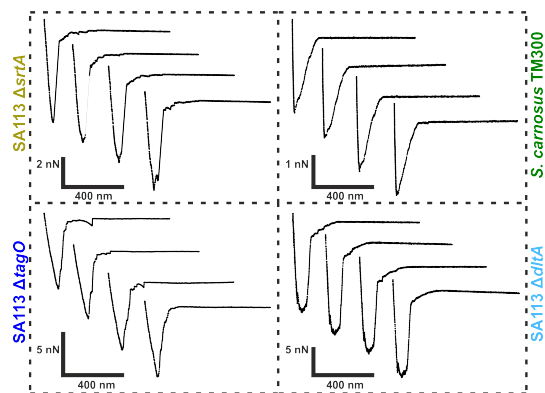
Figure 5: Retraction parts of exemplary force-distance curves of mutants and *S. carnosus* cells on hydrophobic surfaces.

Results – Figure 5 shows four typical retraction parts of force-distance curves on hydrophobic surfaces from one representative cell of *S. carnosus* and each mutant strain. As for the SA133 WT cells (see Fig. 1), all curves show large 'adhesion peak' at the beginning of the retraction and non, or only few, 'spiky' features. Furthermore, the curves from one and the same cell are very reproducible – again, in line with the observations for SA113 WT cells. The strength of adhesion, given by the depth of the adhesion peak, is for *S. carnosus* and the mutants clearly reduced compared to the SA113 WT cells. The extent of this reduction can be investigated in more detail by the investigation of a higher number of individual cells.

Figure 6 shows the statistical analysis of mutant and *S. carnosus* TM300 cells adhering to
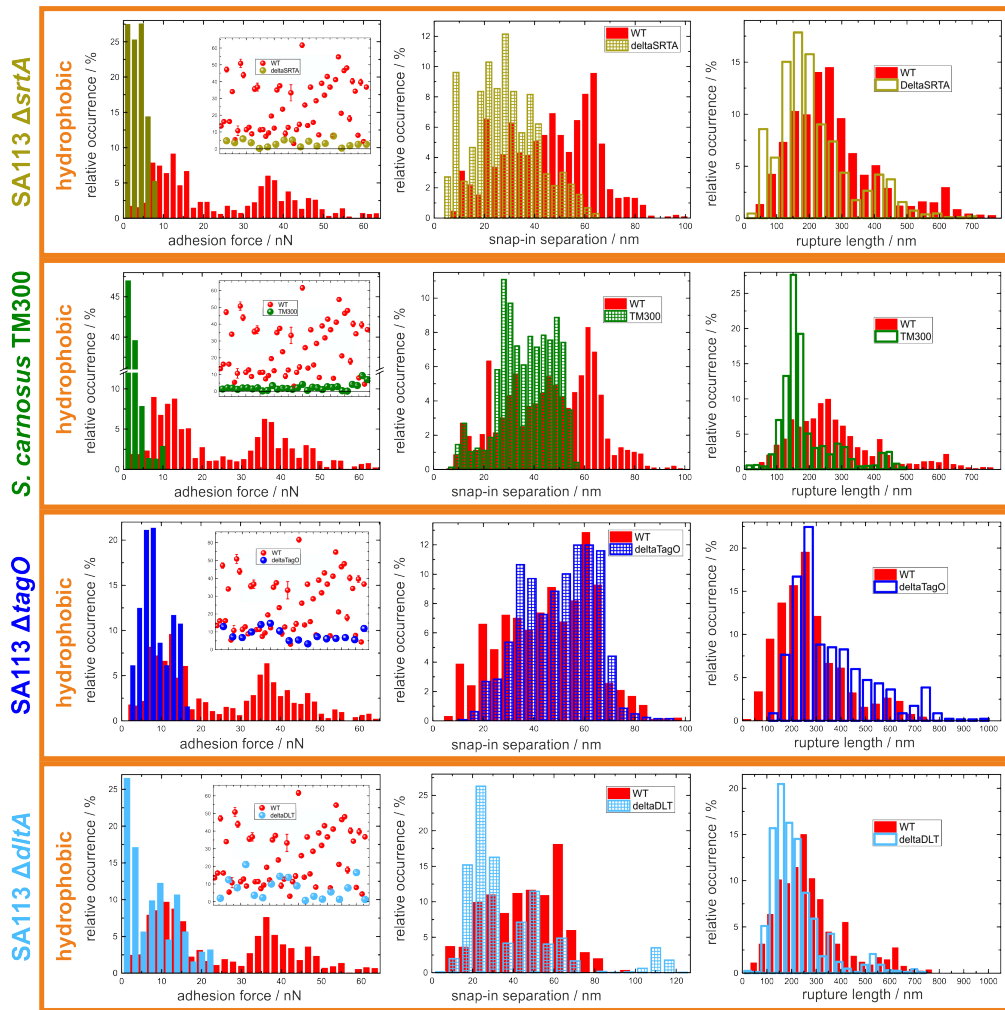
Figure 6: Histograms of adhesion forces, rupture lengths and snap-in separations for all tested mutant cells on hydrophobized silicon surfaces. For comparison, each histogram is plotted together with the corresponding histogram of SA113 WT cells. (Bin widths can vary, but are calculated each according to the description in the experimental chapter.)

11

hydrophobic surfaces: 17 single SA113 $\Delta srtA$, 28 single *S. carnosus*, 16 single SA113 $\Delta tagO$ and 18 single SA113 $\Delta dltA$ cells were compared to the SA113 WT cells (53 individuals in total) each.

In line with our recent observations indicating a major impact of cell wall proteins on the adhesion force of *S. aureus* to attach to hydrophobic surfaces,[4] we observed markedly reduced adhesion forces of the SA113 $\Delta srtA$ mutant that lacks the majority of covalently bound proteins on the bacterial cell wall. Interestingly, the adhesion strength of SA113 cells to bind to the hydrophobic surface was also markedly affected, when the teichoic acid composition of the bacterial cell wall was altered. Thereby, the 'teichoic acid mutants' showed slightlyhigher adhesion forces than the SA113 $\Delta srtA$ mutant that are mainly located close to the first maximum (approx. 10 nN) of the bimodal distribution of the SA113 WT cells. Just like in the wild-type, the adhesion forces for one single cell were very reproducible and displayed only small variations for all mutants (see insets in Figure 6). Histograms of *S. carnosus* TM300 cells displayed the lowest adhesion forces of all tested strains with a maximum about 1–2 nN, thereby confirming recent findings showing that the adhesion forces of cells of this apathogenic staphylococcal species are about one order of magnitude smaller than the ones seen with cells of the pathogenic species.[25]

Of note, all mutant cells showed a distinct snap-in event in the approach part of every force-distance curve so that a snap-in separation could be determined. For SA113 $\Delta srtA$ cells, the snap-in separations were in the range of 10–40 nm. For SA113 $\Delta tagO$ cells, a distribution of snap-in separation very similar to that seen for SA113 WT cells was observed. Inactivation of *dltA* elicited the strongest effect on the snap-in behaviour. The histogram of snap-in separations of SA113 $\Delta dltA$ cells seems to have several maxima: The first at around 25 nm, the second at around 50 nm and a third at especially large values of about 110 nm which was even larger than the snap-in separation values observed with SA113 WT cells. Cells of *S. carnosus* TM300 displayed slightly smaller

snap-in separation values than the ones seen with SA113 WT cell, which were in the range of 30–70 nm. This suggests that TM300 produces macromolecules on the bacterial cell surface that interact strong enough with the hydrophobic substratum to pull the bacterium to this type of surface.

Again similar to the SA113 WT, the histograms of the rupture lengths for all mutants and for *S. carnosus* TM300 cells showed in the widest sense bimodal distributions where the first maximum (at lower values) contained the majority of data. For *S. carnosus* TM300, SA113 $\Delta srtA$, and SA113 $\Delta dltA$ cells, first maxima were located at rupture lengths of about 100–200 nm, and thus smaller as the ones seen with SA113 WT cells (200–300 nm). In contrast, for the SA113 $\Delta tagO$ cells, the position of the first maximum was shifted towards higher values of almost 300 nm. Similar to the situation seen for the first maxima, the second maxima of *S. carnosus* TM300, SA113 $\Delta srtA$, and SA113 $\Delta dltA$ cells were again smaller as the one seen with SA113 WT cells. These second maxima were located between 400–500 nm for SA113 $\Delta srtA$ and *S. carnosus* TM300 cells. For SA113 $\Delta dltA$ cells, the second maximum was slightly shifted to about 550 nm, but still below the one seen with the parental strain (650 nm). The SA113 $\Delta tagO$ cells again showed the highest values for the second maximum at around 750 nm. This means the rupture lengths of *S. carnosus* TM300, SA113 $\Delta srtA$ and SA113 $\Delta dltA$ were slightly reduced compared to SA113 WT cells while SA113 $\Delta tagO$ cells displayed on average slightly increased rupture lengths.

Discussion – The most striking observation on the hydrophobic surface is the markedly reduced adhesive strength of all mutants compared to the wild-type cells. This suggests that covalently bound cell wall proteins as well as wall teichoic acids and the properties of d-alanine groups in teichoic acids have a strong – direct or indirect – influence on the strength of adhesion to this type of surface. The lower adhesion forces observed for *S. carnosus* TM300 cells on hydrophobic surfaces suggest furthermore that the type and/or

composition of macromolecules relevant for adhesion differ markedly between *S. aureus* and *S. carnosus*.

Considering relevant forces, we can again (same as in the discussion about the wild-type cells adhering to substrates of different wettability) state that electrostatic interactions seem to play a minor – or rather indirect – role in adhesion to hydrophobic surfaces which feature a negative surface potential.[32] This observation gets peculiarly evident by analyzing the adhesion of both 'teichoic acid mutants': In general, teichoic acids are a major factor for the overall negative surface charge of bacterial cells. Therefore SA113 $\Delta tagO$ cells lacking cell wall teichoic acids[28,35] have the lowest negative surface charge of all investigated cells (especially lower than SA113 WT cell), whereas SA113 $\Delta dltA$ cells lacking the positively charged d-alanine groups linked to teichoic acids[28,35] carry a higher negative surface charge as the other cell types, including wild-type cells. Nonetheless, the adhesion forces of these two mutants do not show big differences and are both clearly lower than adhesion forces of the wild-type cells meaning that electrostatic interaction does not dominate bacterial adhesion to hydrophobic surfaces.

SA113 $\Delta srtA$ cells lack the cell wall anchored proteins of this species, thus they most likely feature a reduced overall protein density in their cell wall. By assuming that a decreased protein density in the bacterial cell wall results directly in a decreased number of tethering macromolecules during the adhesion process, the smaller adhesion force of SA113 $\Delta srtA$ cells nicely fits our hypothesis that proteins are important for adhesion. Although the strongly reduced adhesive strength hints to a markedly reduced density of bacterial cell wall molecules, the very small variations between single force-distance curves (and the small standard deviations of adhesion force data of one and the same cell) imply that there is still a quite large number of tethering surface proteins.

The lack of d-alanine groups in wall teichoic acids in SA113 $\Delta dltA$ cells leads to a decrease in adhesion strength similar to SA113 $\Delta tagO$ cells that lack the complete wall teichoic acids (including d-alanine groups) on hydrophobic substrates. Alanin is a hydrophobic amino acid, hence a possible explanation for the lower adhesion strength of 'teichoic acid mutants' may be that teichoic acids tether to hydrophobic substrates via d-alanine residues, thus adhesive strength lowers for SA113 $\Delta dltA$ as well as SA113 $\Delta tagO$ cells as both lack a substantial part of the alanine groups present in the cell wall of wild-type cells.

Very interestingly, no matter what type of surface macromolecules was knocked-out, the adhesion capability was reduced to a quite high extent: The SA$\Delta srtA$ cells exhibited only one eighth of the adhesion force of the SA113 WT cells while both 'teichoic acid mutants' exhibit only one third of the force of the wild-type cells. The only explanation for this observation is the fact that knocked-out macromolecules influence each other so that they magnify their individual adhesion capability. Nevertheless, covalently bound surface proteins seems to have the biggest influence on adhesion strength.[56–58]

However, apparently, the lack of cell wall teichoic acids or even of the alanin-groups of teichoic acids seems to change the protein composition of the cell wall. This assumption is corroborated by several studies: For example, the translocation of proteins from their building site to the cell wall is a highly complex process involving many mechanisms and needing a specific interplay of charges, enzymes and ions.[59,60] Furthermore, cations, charge and gradients in pH value inside the cell envelope influence protein folding, structure and function.[61] The microenvironment of the cell wall is strongly influenced by the presence (or absence) of teichoic acids and e. g. their d-alanine groups.[62,63] Even more, it has been shown that d-alanisation directly influences protein expression.[64–66]

After having elucidated the rather complex interplay of surfaces macromolecules defining adhesive strength on hydrophobic surfaces, we can now speculated about their influence on snap-in separations and rupture lengths. Most notably, the snap-in event is still observable for all mutants whereas it was not in previous studies where surface proteins of *S. aureus*113 wild-type cells were cut by proteases or cross-linked

by glutaraldehyde.[4] Therefore, for all investigated cells, the number of surface proteins can still be considered as being sufficient to induce this process. Also, the very reproducible and rather smooth shapes of the retraction curves (see Fig. 5) corroborates the assumption of a rather high number of surface macromolecules participating in adhesion to hydrophobic surfaces.

Results of SA113 $\Delta srtA$ cells show that covalently bound cell wall proteins have a bigger influence on the snap-in event, the first contact to the surface, than on the rupture length, the last contact to the surface. This observation might be explained by the pure reduction in the density of surface proteins: The snap-in event occurs as soon as enough thermally fluctuating surface proteins reach the surface and bind to it. If the overall density is reduced – as it can be safely assumed for SA113 $\Delta srtA$ cells – this number will be reached 'later' meaning at shorter distances to the surface, resulting in a decreased snap-in separation. The exact same argumentation holds true for the decreased rupture length: The cells loses contact at a distance where not enough proteins bind to the substrate anymore which is slightly earlier when the proteins density is reduced because then also less long proteins are present on the bacterial cell wall. Also, for fewer proteins the force on each protein is increased which can lead to a earlier (at smaller distance) detachment from the surface. However, the influence of covalently bound surface proteins on the rupture length is rather small. For hydrophobic surfaces, this means, while the strength of adhesion as well as the first contact (indicated by the snap-in separation) to a surface is significantly determined by the presence of covalently bound surface proteins, those are not necessarily the molecules that make the last contact to the surface.

The slightly increased rupture length for SA113 $\Delta tagO$ cells may without further experiments only be explained by indirect secondary effects: For example, it is possible that due to the reduced electrostatic repulsion some rather long molecules of the bacterial surface are able to bind to the surface resulting in some force-distance curves with an increased rupture length. This reduced repulsion may not have an influence on the snap-in separation because in this case, anyways very many surface proteins tether to the surface.

The small maximum in the histogram of snap-in separations of SA113 $\Delta dltA$ cells at values clearly higher than for the SA113 WT cells is much harder to interpret. In general, electrostatic interactions between this mutant and the surface should be more repulsive than for the wild-type cells and not leading to increased snap-in separations. It could be possible that the change in the cell wall microenvironment leads occasionally to the expression of a high number of quite long or fast fluctuating surface proteins that can exhibit extraordinary large snap-in separations. It may also happen that a reduced *dlt* content correlates with a thinned cell wall. If this is the case, it could be that *SrtA* anchored proteins (which happens at membrane-cell wall interface as *SrtA* is anchored within the membrane) expose a higher proportion of their protein content to the extracellular space than the ones with a thicker cell wall in which a larger proportion of the protein is buried within the peptidoglycan.

Two reason may explain the weaker adhesion of apathogenic *S. carnosus* compared to SA113 WT cells. It could be a result of either a lower density of surface adhesins, or of the fact that the surface macromolecules of *S. carnosus* are not specialized to adhere to hydrophobic substrates. However, as hydrophobic residues are a found in almost all proteins, the smaller adhesion capability of *S. carnosus* cells is most likely a result of a smaller protein surface density. A hint in this direction is the fact that at least for specific adhesins that bind to human host factors, it has been shown that their production is strongly reduced in *S. carnosus* compared to *S. aureus* cells.[39] However, it is completely unknown whether *S. carnosus* in general expresses other cell wall anchored ashesins. The used strain TM300 at least produces SrtA and the genome encodes a number of LPXTG containing motifs, strongly suggesting that TM300 produces at least some MSCRAMMS.

Adhesion of Mutant Cells on Hydrophilic Substrates

Results – Figure 7 shows the statistical analysis of mutant cells adhering to hydrophilic surfaces: 11 single SA113 $\Delta srtA$, 19 single *S. carnosus*, 15 single SA113 $\Delta tagO$ and 18 single SA113 $\Delta dltA$ cells were compared to the SA113 WT cells each.

The principle shape of the adhesion forces histograms of SA113 $\Delta srtA$, *S. carnosus* and SA113 $\Delta dltA$ cells are very similar to each other and to the histograms of the wild-type cells: Most values were located at forces near 0 nN and a smooth decay of the distribution towards higher forces was observed. Thereby, the values of SA113 $\Delta srtA$ cells are almost the same as the values of the SA113 WT cells (about 25 % of the values are close to 0 nN and the distribution ends at around 4 nN). SA113 $\Delta dltA$ cells adhered slightly less strongly to the substrate: More values (about 45 %) were located close to 0 nN and the decay of the distribution was steeper than for the wild-type. The adhesion of *S. carnosus* cells was even weaker: Here, about 65 % of data were located close to 0 nN and the decay of the distribution was even stronger than for the other cells. In contrast, SA113 Δtag0 cells adhered stronger than SA113 WT cells and the adhesion forces displayed a very different distribution: It showed a maximum at 3 nN and maximal values went up to 12 nN.

Adhesion energy histograms featured in principle the same shape as described for the adhesion forces. Furthermore, the same trend as for the adhesion forces of all mutants could be observed: *S. carnosus* cells showed the lowest adhesion energies (up to 50,000 k_bT), SA113 $\Delta dltA$ cells slightly enhanced and SA113 $\Delta srtA$ cells even higher values, but still in contrast to the adhesion forces, lower values than the SA113 WT cells. SA113 $\Delta tagO$ cells again, by contrast, generated adhesion energies up to 350,000 k_BT and thus much higher values than SA113 WT cells.

As for the rupture lengths, SA113 $\Delta tagO$ cells showed slightly larger values (up to 600 nm) than the SA113 WT cells. However, SA113 $\Delta dltA$ yielded almost the same shape of the distribution as SA113 WT cells but tended to produce smaller values with about twice as many values at very low rupture lengths. SA113 $\Delta srtA$ and *S. carnosus* cells exhibited mainly the same distribution with maxima below 50 nm, whereas *S. carnosus* cells generated occasionally higher maximal rupture lengths: 650 nm as compared to about 400 nm for the SA113 $\Delta srtA$ cells.

Discussion – First, the influence of covalently bound surface proteins on the adhesion to hydrophilic surfaces is discussed: Adhesion forces were almost not affected by the absence of covalently bound surface proteins whereas rupture lengths markedly decreased. The latter implies that cell wall anchored proteins do bind to hydrophilic surfaces and are on average longer than other tethering macromolecules. The more minor effect of lacking covalently bound cell wall proteins on the adhesive strength to hydrophilic surfaces may be interpreted in the light of the first part of the paper: Either the covalently bound proteins have only few hydrophilic residues able to interact with this type of surface (most likely through hydrogen bonds), or there are anyways – even without covalently bound proteins – so many surface molecules/proteins that they occupy all possible binding sites whose number may be limited due to interaction between different surface macromolecules.

The mutant cells without wall teichoic acids (SA113 $\Delta tagO$), respectively without d-alanine residues on teichoic acids (SA113 $\Delta dltA$), allowed investigating the influence of charges on the adhesion of *S. aureus* cells. On hydrophilic substrates, we found an increased adhesive strength for SA113 $\Delta tagO$ cells that feature a lower negative surface charge. For SA113 $\Delta dltA$ cells featuring a higher negative surface charge we measured a decreased adhesion strength. Together, both findings point towards a charge effect on bacterial adhesion to hydrophilic surfaces. However, as we attribute bacterial adhesion solely to the binding of cell wall macromolecules,[16,26,67] the rising adhesive strength seen with SA113 $\Delta tagO$ cells may rather be caused by a higher binding affinity of the remaining cell wall macromolecules after removal
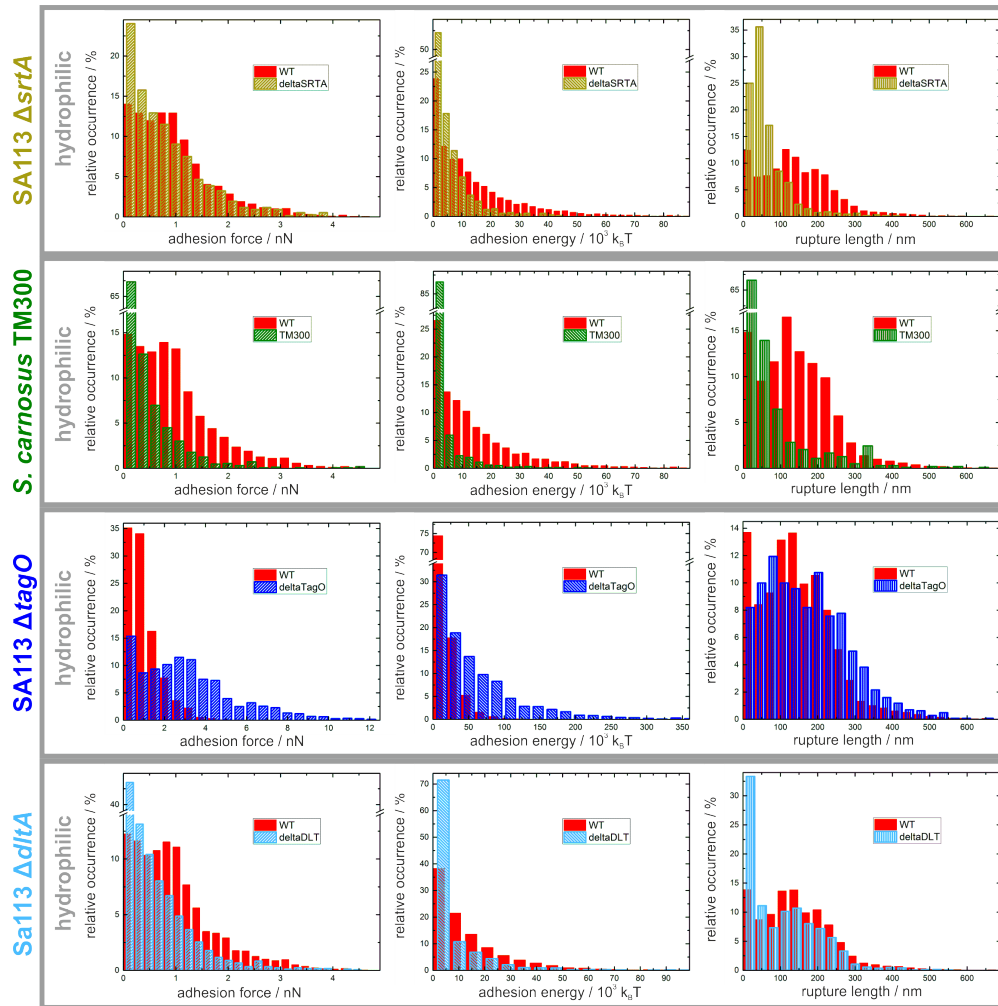
Figure 7: Histograms of adhesion forces, adhesion energies and rupture lengths for all tested mutant cells on hydrophilic silicon surfaces. For comparison, each histogram is plotted together with the corresponding histogram of SA113 WT cells. (Bin widths can vary, but are calculated each according to the description in the experimental chapter.)

16   119

of the wall teichoic acids. At the moment, we are not able to explain the molecular origin of this result in detail. The reason may be that especially the formation of hydrogen bonds, that seem to dominate the adhesion to hydrophilic substrates, is influenced by changed electrostatic interactions. Furthermore, these results indicate that wall teichoic acids do not contribute directly to the adhesive potential of *S. aureus* to abiotic hydrophilic substrates or that their contribution is small compared to the adhesive strength exerted by other surface molecules.

Another explanation neglecting charge variations might be that the pure lack of teichoic acids, which contribute to up to 40 % of the cell wall biomass, allow additional proteins to bind to the peptidoglycan and/or to adhere to the cell wall at places that are usually occupied by the teichoic acids.

In contrast to SA113 $\Delta srtA$ cells, rupture lengths of SA113 $\Delta tagO$ and SA113 $\Delta dltA$ cells were , if at all, only slightly reduced. This suggests that most likely – as described above – the on average rather long covalently bound surface proteins contribute to the adhesion of 'teichoic acid mutants' to hydrophilic substrates and seem to make the last contact to the surface. If teichoic acids themselves bind to the surface, they usually do not contribute to the rupture lengths. This might be due to the natures of both macromolecules. Teichoic acids, being composed of glycerol phosphate or ribitol phosphate and carbohydrates linked via phosphodiester bonds, most likely do not form a complex tertiary structure that is usually seen with proteins. As a consequence, teichoic acids most likely exhibit only small stretching capabilities. Proteinaceous adhesion molecules, in contrast, are usually folded to yield a complex tertiary structure important for their functionality. Under tension, these structures may unfold – at least in part – and stretch without loosing contact to the surface, thereby causing the characteristic 'spiky' structures in the force-distance curves displayed in Figure 1 c and d.

Differences in adhesion energies for the mutant cells compared to the wild-type cells are in any case the direct result of the combination of reduced (or enhanced) adhesion force combined with the decrease or increase in rupture lengths. SA113 $\Delta srtA$ cells generated similar adhesion forces as SA113 WT cells but markedly decreased rupture lengths supporting the hypothesis that the latter effect is mainly driven by proteins. As a consequence, adhesion energies are reduced as well. In contrast, SA113 $\Delta tagO$ cells have similar rupture lengths as SA113 WT cells but clearly enhanced adhesion forces which also results in distinctly larger adhesion energies than SA113 WT cells.

The reduced adhesive strength (adhesion force and energy) and rupture length of *S. carnosus* cells if compared to the values seen with SA113 WT cells, may be again interpreted in light of the results of the first part of the study. It is known that *S. carnosus* does not produce a lot of surface adhesins found in *S. aureus*113 wild-type cells.[39] When comparing adhesion forces of pathogenic SA113 WT cells and apathogenic *S. carnosus* cells on hydrophilic surfaces, the large difference may, again, be attributed to a smaller macromolecular density in general or at least a smaller density of polymers specialized to attach to abiotic substrates in the case of *S. carnosus*.[39]

Summary and Discussion of Mutant Adhesion

All experimental results obtained from mutant cells can be explained by the hypothesis that the adhesion to hydrophobic surfaces is mediated by the hydrophobic interaction between the substrate and hydrophobic residues of a large number of surface macromolecules. On hydrophilic surfaces, however, we hypothesize (see first part of the paper) that a quite small number of macromolecules tethers to the surface, probably by formation of directional hydrogen bonds. Hence, bond formation is slower as it can be seen by the drastically enhanced adhesive strength when applying an additional surface contact time. Due to the hypothetically small number of binding macromolecules, they exhibit in total rather low adhesion forces. This may also explain why electrostatic interactions seem to play an important role in adhe-

sion to hydrophilic surfaces whilst this effect is not present or suppressed by the high number of tethering proteins on non-wettable surfaces due to the hydrophobic interactions.

Not only the adhesive strength and the retraction part of force-distance curves is strongly different for surfaces of different wettability, but also the process of contact formation is governed by hydrophobic interaction between thermally fluctuating surface proteins and the substrate: They attach consecutively to the surface and pull the bacterium into close contact, as has been shown in a preceding study.[4] Therefore, the snap-in separation increases the higher the substrate's hydrophobicity is, nicely fitting our experimental results where snap-in events never occur on hydrophilic substrates, regardless of the type of staphylococcal cell probed.

The experimental results of SA113 $\Delta srtA$ cells indicate that the presence of covalently bound cell wall proteins is more important for the adhesion to hydrophobic than to hydrophilic surfaces. Teichoic acids and their d-alanine residues, in contrast, seem to influence adhesion on hydrophilic surfaces mainly through electrostatic interactions. However, this effect may be of indirect nature by enhancing or reducing the probability of hydrogen bond formation. On hydrophobic surfaces, however, they may contribute more directly by tethering of hydrophobic d-alanine residues presented by teichoic acid regions that poke out of the cell wall.

Very interestingly, we found that adhesive strength is reduced to a very high extent by the knock-out of certain types of surface macromolecules, no matter which specific type this might be (see Figure 6). Thus, bacterial adhesion – at least on hydrophobic surfaces – relies on a very efficient interplay of the different investigated types of surface macromolecules.

Furthermore, our study may explain the individuality of bacterial cells and their properties, also seen in another study:[25] As experiments have shown, number and nature of bacterial surface molecules define the adhesion capability of an individual bacterial cell. Hence, variations in the surface macromolecular composition cause bacterial cell individuality. Especially the bimodal distribution of adhesion

forces, gives rise to the assumption that the age of the respective cell wall region might be the major property responsible for differences in its macromolecular composition.

Concerning adhesion-relevant surface proteins, we can not state which proteins exactly contribute to which extent. Of note, different studies identified over 400 different proteins in or attached to the cell wall of *S. aureus*.[68–73] By the use of SA113 $\Delta srtA$ cells we can at least state that covalently bound proteins, although representing only a minor part of the cell wall proteome of this pathogen, have a major influence. However, other cell wall associated proteins (e. g. SERAMs, secretable expanded repertoire adhesive molecules) which might be quite high in number likely contribute to the adhesion properties of *S. aureus* as well.

Conclusions

We investigated the adhesion process of *S. aureus* to abiotic substrates by combining AFM-based single cell force spectroscopy with a set of isogenic mutants. As substrates, we chose a smooth silicon wafer in its natural very hydrophilic oxidized state, as well as covered with a self-assembling monolayer of strongly hydrophobic silanes. On both surfaces, bacterial adhesion can be described by the binding of thermally fluctuating bacterial cell wall macromolecules.

In line with previous findings, on the hydrophobic surface, adhesion is mediated by a large number of fast tethering cell wall macromolecules driven by the hydrophobic interaction.[4] This results in very reproducible shapes of force-distance curves and small fluctuations in adhesive strength exerted by each individual. With the restriction that only a small area of the bacterial cell surface is probed, the adhesion force is a very cell-individual property. Covalently bound cell wall proteins are mostly responsible for the adhesive strength. But also teichoic acids seem to have an influence on adhesion. The latter effect may be rather indirect by affecting protein composition on the cell wall as well as more direct through the tethering of

their hydrophobic residues.

In contrast, much fewer macromolecules tether to the hydrophilic surface. This process seems to be rather slow and is probably driven by hydrogen bond formation. Thus, force-distance curves of one and the same cell exhibit varying shapes and adhesion forces and energies show big fluctuations between different adhesion events. The influence of covalently bound cell wall proteins is rather small whereas teichoic acids have a bigger influence and affect bond formation most likely by their charges. Especially, this impact of electrostatic interactions through surface charges on hydrophilic substrates may be an important aspect for material engineering.

By the presented experiments it is not possible to determine which specific proteins in detail are relevant for adhesion to abiotic surfaces and how numerous they are each. This could be the subject of future studies using more sophisticated mutant cells, in which for example only one specific protein is knocked-out, combined with qualitative simulations of the bacterial cell wall in different surface potentials. In these studies, it should be considered that the number of binding sites on hydrophobic surfaces is quite high and therefore, the binding strength of each individual 'bond' is rather weak. In contrast, on the hydrophilic surface, the binding strength of individual binding sites should be quite strong, corroborating the assumption that these are hydrogen bonds.

Finally, the fundamental mechanisms of *S. aureus* adhesion to abiotic surfaces revealed in this study, may be transferred to other bacterial species as microbial adhesion might in general rely on the binding of surface macromolecules.

References

(1) Lowy, F. D. Staphylococcus aureus infections. *New England Journal of Medicine* **1998**, *339*, 520.

(2) Yongsunthon, R.; Fowler, V. G.; Lower, B. H. Correlation between fundamental binding forces and clinical prognosis of Staphylococcus aureus infections of medical implants. *Langmuir* **2007**, *23*, 2289.

(3) Linke, D.; Goldman, A. *Bacterial adhesion: chemistry, biology and physics*; 2011.

(4) Thewes, N.; Thewes, A.; Loskill, P.; Peisker, H.; Bischoff, M.; Herrmann, M.; Santen, L.; Jacobs, K. Stochastic binding of Staphylococcus aureus to hydrophobic surfaces. *Soft Matter* **2015**, *11*, 8913–9046.

(5) Hall-Stoodley, L.; Costerton, J. W.; Stoodley, P. Bacterial biofilms: from the Natural environment to infectious diseases. *Nature Reviews Microbiology* **2004**, *2*, 95–108.

(6) Flemming, H.-C.; Wingender, J. The biofilm matrix. *Nature Reviews Microbiology* **2010**, *8*, 623–633.

(7) Christensen, G. D.; Baldassarri, L.; Simpson, W. A. *Colonization of medical devices by coagulase-negative staphylococci*; 1994.

(8) Chamis, A. L.; Peterson, G. E.; Cabell, C. H.; Corey, G. R. Staphylococcus aureus bacteremia in patients with permanent pacemakers or implantable cardioverter-defibrillators. *Circulation* **2001**, *104*, 1029.

(9) Mylonakis, E.; Calderwood, S. B. Infective endocarditis in adults. *New England Journal of Medicine* **2001**, *345*, 1318.

(10) Olsen, M. A.; Mayfield, J.; Lauryssen, C.; Polish, L. B. Risk factors for surgical site infection in spinal surgery. *Journal of Neurosurgery: Spine* **2003**, *98*, 149.

(11) Darouiche, R. O. Treatment of infections associated with surgical implants. *New England Journal of Medicine* **2004**, *350*, 1422.

(12) Lax, S.; Sangwan, N.; Smith, D.; Larsen, P. Bacterial colonization and succession in a newly opened hospital. *Science Translational Medicine* **2017**, *9*, eaah6500.

(13) Arciola, C. R.; Campoccia, D.; Speziale, P.; Montanaro, L. Biofilm formation in Staphylococcus implant infections. A review of molecular mechanisms and implications for biofilm-resistant materials. *Biomaterials* **2012**,

(14) Razavi, M.; Shepard, D. S.; Suaya, J. A.; Stason, W. B. Postoperative Staphylococcus aureus Infections in Medicare Beneficiaries. *PLoS ONE* **2014**, *9*, e110133.

(15) Kang, S.; Elimelech, M. Bioinspired single bacterial cell force spectroscopy. *Langmuir* **2009**, *25*, 9656.

(16) Thewes, N.; Loskill, P.; Jung, P.; Peisker, H.; Bischoff, M.; Herrmann, M.; Jacobs, K. Hydrophobic interaction governs unspecific adhesion of staphylococci: a single cell force spectroscopy study. *Beilstein Journal of Nanotechnology* **2014**, *5*, 1501–1512.

(17) Dufrene, Y. F. Sticky microbes: forces in microbial cell adhesion. *Trends in microbiology* **2015**,

(18) Aguayo, S.; Donos, N.; Spratt, D.; Bozec, L. Single-bacterium nanomechanics in biomedicine: unravelling the dynamics of bacterial cells. *Nanotechnology* **2015**, *26*, 062001.

(19) Thewes, N.; Loskill, P.; Spengler, C.; Hümbert, S.; Bischoff, M.; Jacobs, K. A detailed guideline for the fabrication of single bacterial probes used for atomic force spectroscopy. *The European Physical Journal E* **2015**,

(20) Mitchell, G.; Lamontagne, C. A.; Brouillette, E. Staphylococcus aureus SigB activity promotes a strong fibronectin–bacterium interaction which may sustain host tissue colonization by smallâĂŘcolony variants .... *Molecular Microbiology* **2008**, *70*, 1540.

(21) Ovchinnikova, E. S.; Krom, B. P. Evaluation of adhesion forces of Staphylococcus aureus along the length of Candida albicans hyphae. *F1000 - Post-publication peer review of the biomedical literature* **2012**,

(22) Herman-Bausier, P.; El-Kirat-Chatel, S.; Foster, T. J.; Geoghegan, J. A.; Dufrêne, Y. F. Staphylococcus aureus Fibronectin-Binding Protein A Mediates Cell-Cell Adhesion through Low-Affinity Homophilic Bonds . *mBio* **2015**, *6*, e00413–15.

(23) Vanzieleghem, T.; Herman, P. Staphylococcus epidermidis affinity for fibrinogen-coated surfaces correlates with the abundance of the SdrG adhesin on the cell surface. *Langmuir* **2015**, *31*, 4713.

(24) Spengler, C.; Thewes, N.; Nolle, F.; Faidt, T. Enhanced adhesion of Streptococcus mutans to hydroxyapatite after exposure to saliva. *Journal of Molecular Recognition* **2017**, e2615.

(25) Spengler, C.; Thewes, N.; Jung, P.; Bischoff, M.; Jacobs, K. Determination of the nano-scaled contact area of staphylococcal cells. *Nanoscale* **2017**,

(26) Beaussart, A.; El, S. Single-cell force spectroscopy of probiotic bacteria. *Biophysical journal* **2013**,

(27) Sullan, R. M. A.; Li, J. K.; Crowley, P. J.; Brady, L. J.; Dufrêne, Y. F. Binding Forces of Streptococcus mutans P1 Adhesin. **2015**,

(28) Weidenmaier, C.; Peschel, A.; Xiong, Y. Q. Lack of wall teichoic acids in Staphylococcus aureus leads to

reduced interactions with endothelial cells and to attenuated virulence in a rabbit model of endocarditis. *The Journal of Infectious Diseases* **2005**, *191*, 1771.

(29) Weidenmaier, C.; Kokai, J. F. Differential roles of sortase-anchored surface proteins and wall teichoic acid in Staphylococcus aureus nasal colonization. *International Journal of . . .* **2008**,

(30) Kerdudou, S.; Laschke, M. W.; Sinha, B.; Preissner, K. T.; Menger, M. D.; Herrmann, M. Fibronectin binding proteins contribute to the adherence of Staphylococcus aureus to intact endothelium in vivo. *Thrombosis and Haemostasis* **2006**, *96*, 183–189.

(31) Corrigan, R. M.; Miajlovic, H.; Foster, T. J. Surface proteins that promote adherence of Staphylococcus aureus to human desquamated nasal epithelial cells. *BMC Microbiology* **2009**, *9*, 22.

(32) Bellion, M.; Santen, L.; Mantz, H.; Hähl, H. Protein adsorption on tailored substrates: long-range forces and conformational changes. *Journal of Physics: Condensed Matter* **2008**, *20*, 404226.

(33) Lessel, M. et al. Self-assembled silane monolayers: an efficient step-by-step recipe for high-quality, low energy surfaces. *Surface and Interface Analysis* **2015**, *47*, 557–564.

(34) Maxe, I.; Ryden, C.; Wadström, T.; Rubin, K. Specific attachment of Staphylococcus aureus to immobilized fibronectin. *Infection and Immunity* **1986**, *54*, 695–704.

(35) Peschel, A.; Otto, M.; Jack, R. W.; Kalbacher, H. Inactivation of the dlt Operon inStaphylococcus aureus Confers Sensitivity to Defensins, Protegrins, and Other Antimicrobial Peptides. *Journal of Biological Chemistry* **1999**, *274*, 8405.

(36) Bur, S.; Preissner, K. T.; Herrmann, M.; Bischoff, M. The Staphylococcus aureus extracellular adherence protein promotes bacterial internalization by keratinocytes independent of fibronectin-binding proteins. *Journal of Investigative . . .* **2013**,

(37) Dramsi, S.; Magnet, S.; Davison, S. Covalent attachment of proteins to peptidoglycan. *FEMS Microbiology Reviews* **2008**, *32*, 307.

(38) Schleifer, K. H.; Fischer, U. Description of a new species of the genus Staphylococcus: Staphylococcus carnosus. *International Journal of Systematic* **1982**,

(39) Götz, F. Staphylococcus carnosus: a new host organism for gene cloning and protein production. *Journal of Applied Bacteriology* **1990**, *69*, 49S.

(40) Beaussart, A.; Herman, P.; El, S. Single-cell force spectroscopy of the medically important Staphylococcus epidermidis–Candida albicans interaction. *Nanoscale* **2013**, *5*, 10894.

(41) Zeng, G.; Muller, T.; Meyer, R. L. Single-cell force spectroscopy of bacteria enabled by naturally derived proteins. *Langmuir* **2014**, *30*, 4019.

(42) Herman, P.; El-Kirat-Chatel, S.; Beaussart, A. The binding force of the staphylococcal adhesin SdrG is remarkably strong. *Molecular Microbiology* **2014**, *93*, 356.

(43) El, S. Forces driving the attachment of Staphylococcus epidermidis to fibrinogen-coated surfaces. *Langmuir* **2013**, *29*, 13018.

(44) Scott, D. W.; Terrell, G. R. Biased and unbiased cross-validation in density estimation. *Journal of the American Statistical Association* **1987**,

(45) Lower, S. K.; Hochella, M. F.; Beveridge, T. J. Bacterial recognition of mineral surfaces: nanoscale interactions between Shewanella and α-FeOOH. *Science* **2001**, *292*, 1360.

21

(46) El, S. Single-molecule analysis of Pseudomonas fluorescens footprints. *ACS Nano* **2014**, *8*, 1690.

(47) Marko, J. F.; Siggia, E. D. Stretching dna. *Macromolecules* **1995**,

(48) Rubinstein, M. *RH Colby Polymer Physics Oxford University Press*; 2003; Vol. 53.

(49) Helenius, J.; Heisenberg, C. P.; Gaub, H. E. Single-cell force spectroscopy. *Journal of Cell Science* **2008**, *121*, 1785.

(50) Hori, K.; Matsumoto, S. Bacterial adhesion: from mechanism to control. *Biochemical Engineering Journal* **2010**,

(51) Meier, S.; Goerke, C.; Wolz, C.; Seidl, K.; Homerova, D.; Schulthess, B.; Kormanec, J.; Berger-Bachi, B.; Bischoff, M. ÂăB and the ÂăB-Dependent arlRS and yabJ-spoVG Loci Affect Capsule Formation in Staphylococcus aureus. *Infection and Immunity* **2007**, *75*, 4562.

(52) Amako, K.; Umeda, A. Scanning electron microscopy of Staphylococcus. *Journal of Ultrastructure Research* **1977**, *58*, 34–40.

(53) Amako, K.; Umeda, A. Mode of cell separation and arrangement of Staphylococcus. *Microbiology and Immunology* **1979**, *23*, 329–338.

(54) Jucker, B. A.; Harms, H.; Hug, S. J.; Zehnder, A. Adsorption of bacterial surface polysaccharides on mineral oxides is mediated by hydrogen bonds. *Colloids and Surfaces B: Biointerfaces* **1997**, *9*, 331.

(55) Leckband, D.; Israelachvili, J. Intermolecular forces in biology. *Intermolecular Forces* **2001**, 1.

(56) Schlag, M.; Biswas, R.; Krismer, B.; Kohler, T. Role of staphylococcal wall teichoic acid in targeting the major autolysin Atl. *Molecular Microbiology* **2010**, *75*, 864.

(57) Becker, S.; Frankel, M. B.; Schneewind, O.; Missiakas, D. Release of protein A from the cell wall of Staphylococcus aureus. *Proceedings of the National Academy of Sciences* **2014**, *111*, 1574–1579.

(58) Bertsche, U.; Yang, S.-J.; Kuehner, D.; Wanner, S.; Mishra, N. N.; Roth, T.; Nega, M.; Schneider, A.; Mayer, C.; Grau, T.; Bayer, A. S.; Weidenmaier, C. Increased cell wall teichoic acid production and D-alanylation are common phenotypes among daptomycin-resistant methicillin-resistant Staphylococcus aureus (MRSA) clinical isolates. *PLoS One* **2013**, *8*, e67398.

(59) van Wely, K.; Swaving, J.; Freudl, R. Translocation of proteins across the cell envelope of Gram-positive bacteria. *FEMS Microbiology Reviews* **2001**, *25*, 437.

(60) Sarvas, M.; Harwood, C. R.; Bron, S.; van Dijl, J. M. Post-translocational folding of secretory proteins in Gram-positive bacteria. *Biochimica et Biophysica . . .* **2004**,

(61) Forster, B. M.; Marquis, H. Protein transport across the cell wall of monoderm GramâĂŘpositive bacteria. *Molecular Microbiology* **2012**, *84*, 405.

(62) Hyyryläinen, H. L.; Vitikainen, M.; Thwaite, J.; Wu, H. D-Alanine substitution of teichoic acids as a modulator of protein folding and stability at the cytoplasmic membrane/cell wall interface of Bacillus subtilis. *Journal of Biological Chemistry* **2000**, *275*, 26696–26703.

(63) Neuhaus, F. C.; Baddiley, J. A continuum of anionic charge: structures and functions of D-alanyl-teichoic acids in gram-positive bacteria. *Microbiology and Molecular Biology Reviews* **2003**, *67*, 686.

(64) Nouaille, S.; Commissaire, J.; Gratadoux, J. J. Influence of lipoteichoic acid D-alanylation on protein secretion in Lactococcus lactis as revealed by random mutagenesis. *Applied and . . .* **2004**,

Addendum IV – Determination of the Nano-scaled Contact Area of Staphylococcal Cells

Authors: C. Spengler[1], N. Thewes[1], P. Jung[2], M. Bischoff[2] and K. Jacobs[1]

[1] Department of Experimental Physics, Saarland University, 66041 Saarbrücken, Germany.
[2] Institute of Medical Microbiology and Hygiene, Saarland University, Homburg, Germany.

Author contributions:
*Experiments were designed by **C. Spengler** and N. Thewes. Experimental results were achieved by **C. Spengler** and P. Jung. The article was written by **C. Spengler**, N. Thewes, M. Bischoff and K. Jacobs. Scientific work was directed by M. Bischoff and K. Jacobs.*

Abstract - Bacterial adhesion is a crucial step during the development of infections as well as the formation of biofilms. Hence, fundamental research of bacterial adhesion mechanisms is of utmost importance. So far, less is known about the size of the contact area between bacterial cells and a surface. This gap will be filled by this study using a single-cell force spectroscopy-based method to investigate the contact area between a single bacterial cell of *Staphylococcus aureus* and a solid substrate. The technique relies on the strong influence of the hydrophobic interaction on bacterial adhesion: by incrementally crossing a very sharp hydrophobic/hydrophilic interface while performing force–distance curves with a single bacterial probe, the bacterial contact area can be determined. Assuming circular contact areas, their radii – determined in our experiments – are in the range from tens of nanometers to a few hundred nanometers. The contact area can be slightly enlarged by a larger load force, yet does not resemble a Hertzian contact, rather, the enlargement is a property of the individual bacterial cell. Additionally, *Staphylococcus carnosus* has been probed, which is less adherent than S. aureus, yet both bacteria exhibit a similar contact area size. This corroborates the notion that the adhesive strength of bacteria is not a matter of contact area, but rather a matter of which and how many molecules of the bacterial species' cell wall form the contact. Moreover, our method of determining the contact area can be applied to other microorganisms and the results might also be useful for studies using nanoparticles covered with soft, macromolecular coatings.

Nanoscale

ROYAL SOCIETY OF CHEMISTRY

PAPER

Determination of the nano-scaled contact area of staphylococcal cells†

Christian Spengler, ‡[a] Nicolas Thewes,‡[a] Philipp Jung,[b] Markus Bischoff [b] and Karin Jacobs *[a]

Bacterial adhesion is a crucial step during the development of infections as well as the formation of biofilms. Hence, fundamental research of bacterial adhesion mechanisms is of utmost importance. So far, less is known about the size of the contact area between bacterial cells and a surface. This gap will be filled by this study using a single-cell force spectroscopy-based method to investigate the contact area between a single bacterial cell of *Staphylococcus aureus* and a solid substrate. The technique relies on the strong influence of the hydrophobic interaction on bacterial adhesion: by incrementally crossing a very sharp hydrophobic/hydrophilic interface while performing force–distance curves with a single bacterial probe, the bacterial contact area can be determined. Assuming circular contact areas, their radii – determined in our experiments – are in the range from tens of nanometers to a few hundred nanometers. The contact area can be slightly enlarged by a larger load force, yet does not resemble a Hertzian contact, rather, the enlargement is a property of the individual bacterial cell. Additionally, *Staphylococcus carnosus* has been probed, which is less adherent than *S. aureus*, yet both bacteria exhibit a similar contact area size. This corroborates the notion that the adhesive strength of bacteria is not a matter of contact area, but rather a matter of which and how many molecules of the bacterial species' cell wall form the contact. Moreover, our method of determining the contact area can be applied to other microorganisms and the results might also be useful for studies using nanoparticles covered with soft, macromolecular coatings.

Introduction

Bacterial adhesion to solid substrates is of high relevance concerning the formation of biofilms.[1–3] A fundamental understanding of the bacterial adhesion process can help to control or prevent the attachment of bacterial cells.[4] An established method to characterize the interactions relevant in this process on a molecular scale is atomic force microscopy (AFM)-based force spectroscopy.[5,6] With the help of this technique, many properties of the bacterial cell wall could be determined by using functionalized tips[7–10] or well-conceived modes of measurement.[11] By using bacterial probes for force spectroscopy, an unprecedented expansion of the knowledge

about bacterial adhesion mechanisms was achieved[12–14] by measuring bacterial adhesion properties like adhesion forces, rupture lengths or protein mechanics.[15–17]

This way, it was found that most bacteria, including the Gram-positive pathogen *Staphylococcus aureus* and its apathogenic relative *Staphylococcus carnosus*, bind much more strongly to hydrophobic than to hydrophilic substrates irrespective of their individual adherence strength that may differ up to one order of magnitude due to differing amounts of adhesion factors on the bacterial cell surface.[18] This is a consequence of the excessive binding of bacterial surface proteins on hydrophobic substrates *via* the hydrophobic interaction.[19–23] In contrast, on hydrophilic substrates, macromolecular tethering is much less likely.

However, as of today, studies characterizing bacterial adhesive strength under various conditions lack the exact information about the size of the contact area. Investigating this contact area by means of classical optical microscopy is challenging because typical cocci species such as *S. aureus* and *S. carnosus* exhibit a cell diameter of only roughly 1 μm. Therefore, contact mechanical modeling has been the only way to investigate the contact area of bacterial cells so far. A promising modeling approach was developed by Chen *et al.* considering the bond between cell and substrate of viscous

[a]Department of Experimental Physics, Saarland University, 66041 Saarbrücken, Germany. E-mail: k.jacobs@physik.uni-saarland.de; Fax: +49 681 302 717 00; Tel: +49 681 302 717 77

[b]Institute of Medical Microbiology and Hygiene, Saarland University, 66421 Homburg/Saar, Germany

‡ These authors contributed equally to this work.

nature. However, also this model does not include the full complexity of the bacterial adhesion process such as macromolecular tethering to the substrate.[24]

With this study, we intend to fill this gap by the size of the contact area of *Staphylococci* to solid surfaces with the help of a new AFM-based technique on tailored surfaces. Thereby, differing loading forces were also used to probe their influence on the contact area. Additionally, the correlation of contact area and adhesive strength was investigated.

We prepared a substrate with a sharp transition between a strongly hydrophobic (functionalized silicon) and very hydrophilic (bare silicon) surface and performed single-cell force spectroscopy experiments with consecutive force–distance curves on gradually varying positions while crossing the hydrophobic/hydrophilic interface. The experimental procedure causes the behavior sketched in Fig. 1: on the hydrophobic surface, a large number of bacterial cell wall macromolecules tether to the substrate, resulting in high adhesion energies and forces, as shown before.[18] By approaching the hydrophobic/hydrophilic interface, first macromolecules will reach the hydrophilic part of the surface where macromolecular tethering is much less likely, which consequently will lead to a decrease in adhesion energy and force. Reaching farther into the hydrophilic part of the sample with the single bacterial force probe, fewer and fewer macromolecules tether to the substrate and the adhesion strength decreases further until a plateau value is reached. This is the case as soon as the entire contact area is located on the hydrophilic part of the sample. By evaluating the behavior of adhesion energy (or force) as a function of the position of the bacterial probe relative to the interface, the radius of the contact area (or rather, of the 'interaction area') can be evaluated.

Apart from the direct quantification of the contact area, our study gives new insights into the macromolecular processes involved in bacterial adhesion as well as the macromolecular state of the bacterial cell wall (*e.g.* properties, density, homogeneity of surface adhesins).

Our method of determining the contact area can also be applied to bacterial cells of different shapes and/or other microorganisms, such as for example *Escherichia coli* and *Candida albicans*. This way, our technique could help to gain new knowledge about adhesive and pathogenic properties of these species. Moreover, our study suggests that nanoparticles covered with soft, macromolecular coatings should not always be considered as simple spheres in terms of adhesion processes because our results may also hold true for these particles, especially when the coating has structural and compositional heterogeneities similar to the bacterial cell wall.[25–28]

Materials and methods

Bacteria and bacterial probes

For the experiments, freshly prepared *Staphylococcus aureus* (strain SA113) and *Staphylococcus carnosus* (strain TM300) cells in exponential growth phase were used to yield a high proportion of viable, undamaged cells.[29–31] The bacteria were cultured on blood agar plates. The day before each experiment, one colony was transferred into 5 ml of sterile TSB medium and cultured at 37 °C overnight under agitation (150 rpm). Before the experiments, 40 µl of the overnight culture were transferred into 4 ml of fresh TSB medium and cultured for another 2.5 hours. Then, bacteria were washed three times using phosphate buffered saline (PBS, pH 7.3, ionic strength 0.1728 mol L^{-1} at 20 °C) to remove extracellular material. Subsequently, a single bacterial cell was attached to a polydopamine coated tipless AFM cantilever (MLCT-0 from Bruker-Nano, Santa Barbara, USA, nominal spring constants of 0.03 N m^{-1} and 0.6 N m^{-1}) using a micromanipulator (Narishige Group, Tokyo, Japan) according to a protocol published elsewhere.[32] SEM micrographs of both bacterial species and their typical size distributions are given in the ESI.†

Substrate preparation

Silicon (Si) wafers (Siltronic AG, Burghausen, Germany) with a native oxide layer (d = 1.7(2) nm) were partially covered with a self-assembling monolayer of CH_3-terminated octadecyltrichlorosilane molecules (OTS, Sigma-Aldrich, St Louis, USA) in the following way: an area of the wafer was masked with a thin polymer film (PMMA, M_w = 14.3 kg mol^{-1}) exhibiting a very distinct edge. Then, the uncovered area of the wafer was silanized following a standard protocol.[33] Subsequently, the polymer film was completely removed by thoroughly rinsing the wafer with chloroform.

Measuring procedure and data fitting

To investigate the quality of the hydrophobic/hydrophilic interface, the wafer surfaces were scanned with an atomic force microscope (Bioscope Catalyst, Bruker-Nano, Santa Barbara, USA) operating in tapping mode© using different scan sizes.

Fig. 1 Illustration of the experimental setup to determine the contact area (indicated by black ellipses) of a spherical bacterial cell to a surface. Consecutive force–distance measurements at gradually increasing *s*-positions with single bacterial probes on a substrate with an extremely sharp interface between a hydrophobic and a hydrophilic surface are expected to show the sketched trend for adhesion energy and adhesion force. The width of the degression zone in the data is a function of the bacterial 'interaction area'. Thickness of the coating not to scale, for details see text and for dimensions see Fig. 3.

IV. Addendum IV – Determination of the Nano-scaled Contact Area of Staphylococcal Cells

The surface hydrophobicities were studied by dynamic water contact angle measurements of a sessile ultrapure water drop, using a custom-made setup.

Afterwards, to reveal the contact radius of single bacterial cells, force–distance curves were recorded in PBS§ at room temperature using a Bioscope Catalyst and single bacterial probes of *S. aureus* and *S. carnosus* cells. In the first step, the surface was covered with approx. 8 ml of PBS and placed under the AFM scan head in such a way that the interface between OTS and bare silicon was in the middle of the scan area. Then, the cantilever holder for measurements in liquid was mounted on the AFM and the cantilever carrying a single bacterial probe was approached towards the surface. Next, consecutive force–distance curves were recorded starting on the hydrophobic surface. The *s*-position (direction perpendicular to the hydrophobic/hydrophilic interface) of the cantilever (*i.e.* the bacterium) was changed by 10 nm in between each two force–distance curves and force measurements were carried out until the whole bacterium was placed above the hydrophilic substrate. At every position, one force–distance curve with a ramp size of 800 nm and a ramp velocity of 800 nm s^{-1} was recorded. The maximum force with which the bacterial cell was pressed on the surface – called force trigger – was 0.3 nN and 3 nN for *S. carnosus* and 0.3 nN, 3 nN and 30 nN for *S. aureus* cells for one set of measurements each. In one passage, 200–300 force–distance curves were recorded, hence, the total movement in *s*-direction was 2–3 µm. To guarantee high lateral precision, the cantilever was not withdrawn during this procedure.

For each force–distance curve, adhesion energy (integral over the adhesion part of the retraction curve) as well as adhesion force (maximum absolute value of the recorded force during retraction) were calculated as described before.[32] These values were plotted against the *s*-position of the bacterial probe on the surface and fitted using eqn (1). The fitting procedure was carried out by the curve fitting tool of the software Matlab (MathWorks, Natick, USA) using a non-linear least square fit with a trust-region algorithm.

the area before crossing the line is weighted with ξ_{max}, whereas the fraction after crossing the line is weighted with ξ_{min}.

The fitting parameters are a quantity of the maximum adhesion strength ξ_{max} (which can be the maximum adhesion energy E_{max} or maximum adhesion force F_{max} present on the hydrophobic OTS surface), a quantity of the minimum adhesion strength ξ_{min} (minimal adhesion energy E_{min} or minimal adhesion force F_{min} present on the hydrophilic Si surface), and the radius r of the contact area (that is assumed to be circular). During the fitting procedure, also s_0 is a free parameter. It indicates the *s*-position of the interface which was set to zero in eqn (1) for convenience.

The fitting parameter m accounts for systematic changes (*i.e.* linear increase or decrease) in the adhesion energy (or force) on the hydrophobic surface for *S. aureus* cells (for details, see ESI†).[34] For the fitting of data obtained with *S. carnosus* cells, m was set to zero.

In the setup employed, it is not possible to place the hydrophobic/hydrophilic interface exactly perpendicular to the *x*-direction of the AFM piezo and also the exact angle between interface and *x*-direction of the piezo is not known. To account for this fact, the interface was positioned at an angle of approx. 45° to the *x*-direction (as precisely as possible) and the above described procedure was performed twice (*i.e.* the hydrophobic/hydrophilic interface was crossed twice), while the pathways of both series were precisely perpendicular to each other (in *x*- and *y*-direction of the piezo) as shown in Fig. 2. If the bacterial cell crosses the interface by an angle θ, the measured contact radius is larger than the 'real' radius. Using the values of two series, r_1 and r_2 (with $\theta_1 + \theta_2 = 90°$), it is tan $(\theta_1) = r_1/r_2$ and the 'real' radius r of the bacterial contact area then reads to $r = r_1/\sin(\theta_1)$. In our analysis, the data from both pathways were fitted simultaneously (with θ_1 and θ_2 as additional fitting parameters) and we defined the uncertainty of the determined contact radius as the 95% confidence interval of the respective fitting parameter r. In the following, these uncertainty intervals are visualized as error bars.

$$\xi_{\text{fit}}(s) = \begin{cases} \xi_{max} + m \cdot s & \text{for } s \leq -r \\ \left(\pi \cdot r^2 - \left(r^2 \cdot \arccos \left(1 - \frac{r+s}{r} \right) - s \cdot \sqrt{2 \cdot r \cdot (r+s) - (r+s)^2} \right) \right) \cdot \frac{\xi_{max} - \xi_{min}}{r^2} + \xi_{min} & \text{for } -r < s \leq 0 \\ \left(r^2 \cdot \arccos \left(1 - \frac{r-s}{r} \right) + s \cdot \sqrt{2 \cdot r \cdot (r-s) - (r-s)^2} \right) \cdot \frac{\xi_{max} - \xi_{min}}{r^2} + \xi_{min} & \text{for } 0 < s \leq +r \\ \xi_{min} & \text{for } s > +r \end{cases} \quad (1)$$

The idea of eqn (1) is a circle of radius r crossing a straight line (in the experiment represented by the interface of OTS and bare silicon) at position $s_0 = 0$ in positive *s*-direction. The equation gives the fraction of the circular area that has crossed the line as a function of the movement s. Thereby, the fraction of

Note that these calculations are based on an assumed circular-shaped contact area. If adhesion energies or forces differed significantly between the first and the second pathway for unknown reasons, the corresponding bacterial probe and data were discarded. For this study, we measured the radius of the contact area of eight cells of *S. aureus* and eight cells of *S. carnosus*. For half of the investigated individuals, cell viability after force spectroscopy was checked by live/dead staining.[32] Thereby, all tested cells were marked as viable.

§A different buffer, *e.g.* TBS, does neither alter the adhesion force nor the adhesion energy within the error.
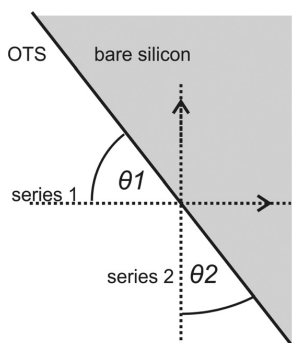
Fig. 2 Sketch of the experimental procedure. Two series of measurements are performed perpendicular to each other. θ_1 and θ_2 depict the angles between each pathway and the hydrophobic/hydrophilic interface.

Additionally, all other cells of this study were inspected after measurement by optical microscopy and did not show any conspicuity.

Results and discussion

The hydrophobic/hydrophilic interface

Fig. 3 shows AFM data of the hydrophobic/hydrophilic interface on the silicon(Si)-based substrate obtained with a very sharp tip. The interface is straight on a length scale of at least 10 μm. A zoom-in at the interface reveals a transition zone of 30(3) nm between the hydrophobic and the hydrophilic part of the substrate (see Fig. 3c). This value was determined as follows: ten cross-sections perpendicular to the interface were recorded in high resolution and the given width is the mean value (and standard deviation) of the horizontal distance between the 'last' local maximum on the higher part and the 'first' local minimum on the lower part of the wafer. By taking into account that the AFM tip used to scan the surface (scana-
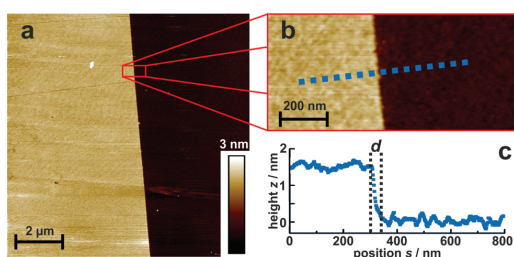
Fig. 3 AFM images of the hydrophobic/hydrophilic transition zone. Images were recorded in tapping mode© (a) at a scan rate of 0.33 Hz and (b) at 0.65 Hz. (c) Scan line perpendicular to the hydrophobic/hydrophilic interface indicating the width of the transition zone as d = 30 nm. In all images, the hydrophobic part is displayed on the left side.

syst-air, Bruker-Nano, Santa Barbara, CA) has a nominal radius of 2 nm and a maximum radius of 12 nm, the transition zone features a 'real' width d of less than 26(3) nm. The difference in height between the lower hydrophilic and the higher hydrophobic part in Fig. 3 is 1.8 nm.¶ Compared to the size of a bacterial cell and cell wall macromolecules, this height difference is negligible. Water contact angle measurements revealed an advancing water contact angle of 112(3)° with a hysteresis of 7° on the hydrophobic part of the substrate and 8(2)° with a hysteresis of 8° on the hydrophilic part. Surface roughness (rms) was determined by AFM on a scan area of 1 μm² to 0.12(2) nm on the OTS surface and 0.09(2) nm on the bare Si surface, thus the 'half and half'-wafer features the same surface characteristics as a native Si wafer and accordingly a fully covered OTS wafer.[33]

In the transition zone, the surface hydrophobicity may not decrease to its minimum instantaneously. Rather, intermediate hydrophobicities might be present. Therefore, the width of the transition zone may lead to an overestimation of the bacterial contact radius as explained in Fig. 4: the adhesion force of a bacterium with a contact radius r that crosses the hydrophobic/hydrophilic transition zone starts to decline as soon as its contact area reaches the transition zone (circle 1). After the contact area (or rather the bacterium) was moved by a distance of $2r$, the bacterium does not touch the hydrophobic part of the substrate anymore (circle 2). However, because the surface hydrophobicity may not have reached its minimum yet (due to the width of the transition zone), further movement of the bacterium in s-direction may result in a further decrease in adhesive strength. The adhesion energy and force reach their
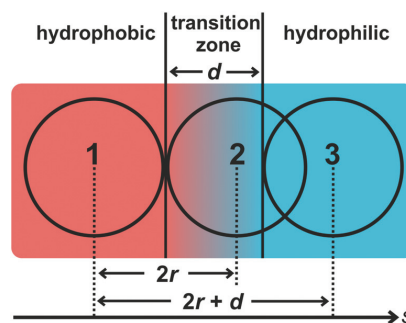
Fig. 4 Sketch to illustrate the influence of the width d of the transition zone on the measurement of the bacterial contact radius r. The circles denote different positions of the bacterial contact area while crossing the hydrophobic/hydrophilic transition zone. (Transition zone and bacterial contact area are not to scale.)

¶This is slightly smaller than expected for a SAM layer of octadecyltrichlorosilane (OTS) and may be the result of the AFM tip penetrating the silanes (tip radius ≈2 nm). When scanning the interface with a distinctly less sharp tip and averaging over 10 μm², we recorded a height difference of 2.4(5) nm which nicely corresponds to the length of an OTS molecules.

minimum first as soon as the entire bacterial contact area probes only the hydrophilic part of the substrate (circle 3), *i.e.* after a traveled distance of $2r + d$ (circle 3 relative to circle 1). This distance reflects the diameter of the bacterial contact area measured according to the presented method. Hence, the radius of the contact area may be overestimated by half of the width of the transition zone, up to 13 nm for the surface used in this study.

Determination of the bacterial contact area

Experimental curves and raw data. Fig. 5 shows force–distance curves and corresponding values of adhesion force obtained with a single *S. aureus* cell when crossing the hydrophobic/hydrophilic interface. Fig. 5a shows typical force–distance curves on the hydrophobic (red) and hydrophilic (blue) surface area as well as curves on the transition zone (intermediate colors). Already in these curves, a continuous decrease in adhesive strength is visible when the cell is moved from the hydrophobic to the hydrophilic surface. Fig. 5b shows the measured values of the adhesion force in dependence of the *s*-position while crossing the hydrophobic/hydrophilic interface (located at $s \approx 0$). Adhesion forces show the expected trend: strongest adhesion occurs on the hydrophobic part of the substrate, then adhesion forces decline while the bacterial cell crosses the interface and reach a minimum as soon as the cell exclusively probes the hydrophilic part of the surface. Notably, changing the direction (*i.e.* moving from the hydrophilic to the hydrophobic surface area) does not alter the experimental outcome: on the hydrophobic substrate area, adhesion forces of *S. aureus* cells are more than an order of magnitude higher than on the hydrophilic substrate area (in line with previous findings[18,20,35]).

A closer look at the raw data reveals that the adhesion force of *S. aureus* cells already decreases slightly on the hydrophobic surface area before reaching the interface. This is a specific behaviour of *S. aureus* cells on hydrophobic substrates that was taken into account for all measurements (for details see Experimental section and ESI†).[18]

To investigate the influence of the radius of the contact area on the adhesive strength, we also used *S. carnosus* cells that show distinctively weaker adhesion as compared to *S. aureus* cells.

Quantification of the bacterial contact area

Fig. 6 displays exemplary values of adhesion energy and force in dependence of the *s*-position while crossing the hydrophobic/hydrophilic interface (see Fig. 5b) as well as the corresponding fit functions used to determine the radius of the contact area for a single *S. aureus* cell (Fig. 6a and c) and a single *S. carnosus* cell (Fig. 6b and d), for details see Experimental section. The fit function used (eqn (1)) describes the experimental data for both bacterial species well.

Fig. 7 a depicts the determined radii of the contact area of eight different *S. aureus* and *S. carnosus* cells each. The displayed values were calculated using the adhesion energy values in dependence of the position at the surface near the hydrophobic/hydrophilic interface. Note that all radii might be overestimated by up to 13 nm as described above.

With an exception of a large value for one *S. aureus* cell and a small value for one *S. carnosus* cell, we found radii of the contact areas for both species in a range of about 150–350 nm. Thus, the radii of the contact area determined with our method are twice as large as values according to the 'elastic deformation model',[24] and much larger than obtained with colloidal probes of similar sizes (see ESI†), which seems reasonable since in both scenarios, a macromolecular tethering is absent (as will be discussed later in more detail). It is striking at first sight that the adhesion strength for *S. aureus* cells is in general about one order of magnitude higher than
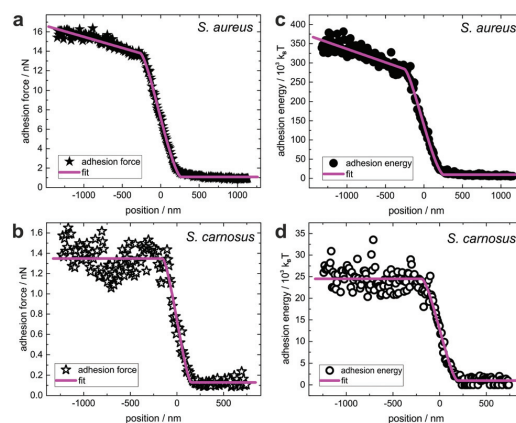
Fig. 6 (a, b) Measured adhesion force *versus* position for one bacterial probe together with the fitted function according to eqn (1) while crossing the hydrophobic/hydrophilic interface (at position 0 nm) for *S. aureus* (a) and *S. carnosus* (b). (c, d) Measured adhesion energy *versus* position for one bacterial probe together with the fit function according to eqn (1) while crossing the hydrophobic/hydrophilic interface (at position 0 nm) for *S. aureus* (c) and exist *S. carnosus* (d).

Fig. 5 (a) Exemplary force–distance curves during the transition from the hydrophobic (red) to the hydrophilic (blue) part of the surface for a single *S. aureus* cell. (b) Measured adhesion force against position for one bacterial probe while crossing the hydrophobic/hydrophilic interface (at $x \approx 0$). Each data point reflects the result of a single force–distance curve at a certain position. Data of the exemplary curves shown in (a) are colored.

Fig. 7 (a) Radii of the contact area between bacterial cell and surface for eight individuals of *S. aureus* (left) and *S. carnosus* (right). The error bars denote the 95% confidence interval of the respective fitting parameter (see 'Materials and methods'). (The radii were measured with force triggers of 0.3 nN.) (b) Illustration of the fact that contact radii of $r = 150–320$ nm originate from surface macromolecules with a length of $l = 20–120$ nm.

for *S. carnosus* cells, yet the calculated radii of the contact areas (as well as their scatter) are in the same range for both species.

To exclude an influence of the cell wall elasticity (E_{cw}) or turgor-dependent cell elasticity (E_t) on the contact area experiments, we performed elasticity mapping in peak force tapping mode© as described in a previous study.[36] Values for individual cells of *S. carnosus* and *S. aureus* differed, but average values showed no distinct differences between the two staphylococcal species (*S. carnosus*: $E_{cw} = 5.4 \pm 2.6$ MPa, $E_t = 4.2 \pm 3.0$ MPa; *S. aureus*: $E_{cw} = 7.4 \pm 1.6$ MPa, $E_t = 3.9 \pm 1.1$ MPa).

In the following, the origin of the scatter in the radii of the contact area for both species shall be elucidated. Are slightly different cell diameters responsible for this or can the scatter be attributed to individual properties of each bacterial cell such as differences in the amount and distribution of bacterial surface macromolecules? However, the different adhesive strength of both tested bacterial species must be attributed to differences in density and nature of surface macromolecules.[18,37,38]

From the measured sizes of the contact radii, the length of these tethering macromolecules can be estimated using simple geometric arguments. If we consider the bacterial cell as a totally inelastic sphere (radius $R = 500$ nm) decorated with elastic macromolecules,[23] the measured contact radii of 150–320 nm are the result of surface macromolecules with a length of 20–120 nm when tethering (as depicted in Fig. 7b). These lengths are in good accordance with previous studies, where the lengths of the macromolecules were estimated to 50–100 nm by analyzing force–distance curves upon approach.[23]

Comparison of contact radii determined by adhesion energy and adhesion force

As shown in Fig. 6, adhesion force as well as adhesion energy can be fitted with eqn (1) and both can be used independently

to calculate the radius of the contact area. A comparison between the two methods (see Fig. 8) reveals two different scenarios: (i) the radius of the contact area determined by the adhesion energy data exceeds the one determined by the adhesion force (cells A1 and C7 in Fig. 8, indicated by red arrows), (ii) both radii of the contact area are equal (cells A6 and C8 in Fig. 8, indicated by green arrows). Both cases may be understood in terms of the macromolecular nature of bacterial adhesion (see Fig. 9): in the first case, bacterial surface macromolecules exist that contribute to the adhesion energy, but not to the adhesion force. This can be some very long macromolecules (green springs in Fig. 9) which start contributing to the overall force between bacterium and surface during retraction only after the maximum force value (taken as
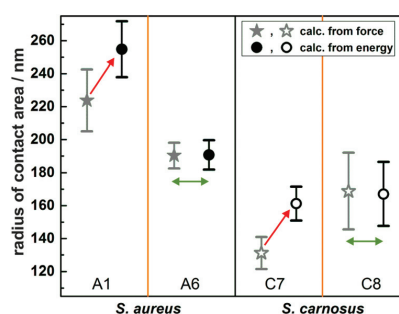
Fig. 8 Radii of the contact area calculated from adhesion force (gray stars) and adhesion energy (black circles) for two exemplary individuals of *S. aureus* (left) and *S. carnosus* (right). The error bars denote the 95% confidence interval of the respective fitting parameter (see 'Materials and methods'). (The radii obtained from energy values are also shown in Fig. 7, the nomenclature corresponds to Fig. 7.)
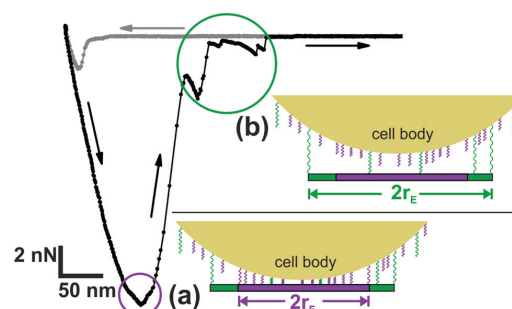
Fig. 9 Sketch to illustrate the origin of the difference in contact radius, depending on the calculation method, namely *via* adhesion energy (r_E) or *via* adhesion force (r_F). The cell is considered as an inelastic sphere decorated with – for reasons of simplification – two different types of springs. (a) Maximum adhesion force is reached by the impact of many short and/or stiff macromolecules (represented by violet springs). (b) Long macromolecules (green springs) do not markedly contribute to the maximum adhesion force, but to the adhesion energy.
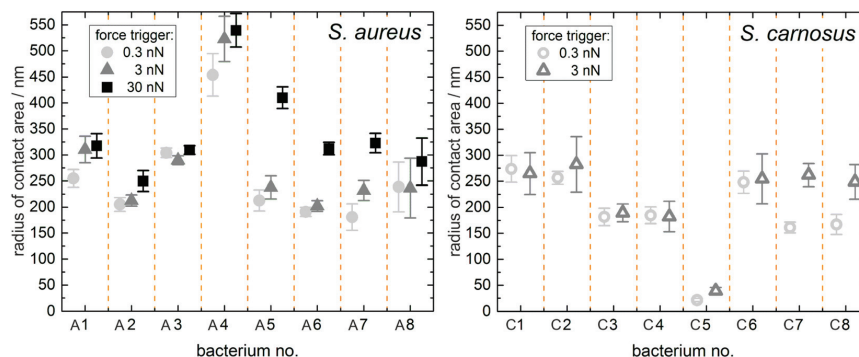
Fig. 10   Radii of the contact area between bacterial cell and surface for eight individuals of *S. aureus* (left) and *S. carnosus* (right). The radii were achieved with force triggers of 0.3 nN (light grey circles), 3 nN (dark grey triangles) and (for *S. aureus* only) 30 nN (black squares). The error bars denote the 95% confidence interval of the respective fitting parameter (see 'Materials and methods').

adhesion force) has already been reached by the impact of many other macromolecules with different properties (violet springs in Fig. 9). In the second case, if both calculated radii are equal, the bacterial surface may lack such long macromolecules (green springs in Fig. 9) or they do not tether to the surface.

Influence of different force triggers

If the adhesion process of a spherical bacterial cell is described with the Hertzian model of a sphere interacting with a flat solid surface, the radius of the contact area is proportional to $\sqrt[3]{F}$, where F is the applied force, in our case the force trigger describing the maximal force that is used to press the bacterial cell onto the surface.[39] This means a tenfold increase in the force trigger leads to an approximately 2.2 times larger radius of the contact area.

To evaluate this hypothesis, cells were next tested with different force triggers: first, one complete set of measurements was done with a force trigger of 0.3 nN, and the contact area was calculated. Then, the next set was performed with the exact same cell using a force trigger of 3 nN and the contact area was calculated again. For *S. aureus* cells only, also a third set of measurements and following contact area calculation was done with a force trigger of 30 nN. (For *S. carnosus* cells, softer cantilevers were used and loading them with 30 nN was not feasible.) For Fig. 10, radii of the contact areas were calculated from adhesion energies, but using adhesion force data lead to equal conclusions (see ESI†). When comparing data obtained with force triggers of 0.3 nN and 3 nN, the change of the contact radii is in the range of the error bar for all *S. aureus* and the majority of *S. carnosus* cells. Only cells C7 and C8 show a distinct increase from approximately 175 nm to 250 nm. When increasing the force trigger to 30 nN, half of the *S. aureus* cells (A2, A5, A6, A7) show a distinctly enlarged radius of the contact area, whereas for the other half of the cells, the change is in the range of the error bar. In other words, an increase of the radius of the contact area by a factor

of 2.2 for a tenfold larger load – as predicted by the Hertzian model – is only very rarely observed. Therefore, these data clearly show that the contact between a spherical bacterial cell and a flat surface is not purely Hertzian as assumed in other studies.[24,40,41] ‖

Rather, this observation can be explained by the fact that by applying a higher force, the bacterial cell wall macromolecules are compressed stronger, allowing the whole cell body to come closer to the substrate which leads to more macromolecules tethering to the surface. At variance with data reported for vesicles,[45] here, a deformation of the whole cell body is unlikely, as the pressure is still low.[36]

The fact that with a higher force trigger, the increase in the radius of the contact area was for some cells stronger than for others might be explained by a heterogeneous nature and distribution of surface macromolecules over the bacterial cell wall. Also, the very small contact radius of cell C5 might be explained that way: such a small area is a strong indicator of a narrow cluster with a high density of macromolecules mediating adhesion in the case of this cell.

Correlation between adhesive strength and contact area

Fig. 11 shows that there is no direct correlation between the size of the contact area and the corresponding adhesion energy or adhesion force for neither *S. aureus* nor *S. carnosus* cells. This observation is irrespective of the force trigger used, see ESI.†

This observation becomes in particular evident when looking at the pink circle (and the pink star, see arrow 1) in the right diagram of Fig. 11: this individual cell of *S. carnosus* (cell C5 in Fig. 7) has an almost two orders of magnitude

---

‖ Here we have chosen the Hertz model because of its simplicity and its common use in other studies.[24,40,41] However, also more complex classic models of adhesion between solids, such as, for example, the model of Johnson, Kendall and Roberts,[42–44] apparently cannot predict the individual responses of different cells under varying external loads.
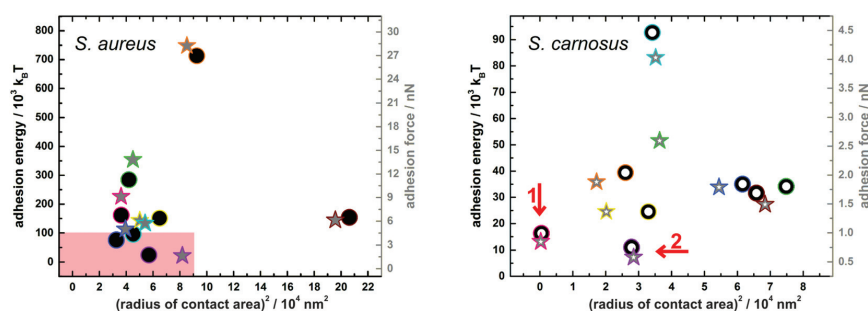
Fig. 11 Adhesion energy (black circles) and force (grey stars) in dependence of the contact area for eight different bacterial cells each (different edge colors), *S. aureus* (left) and *S. carnosus* (right) cells (exemplary for a force trigger of 0.3 nN; for other force triggers, see ESI†). To place emphasis on the lower adhesive strength of *S. carnosus* cells, the colored rectangle in the left diagram represents the scale of the right diagram. (The red arrows indicate distinct data points discussed in the text.)

smaller contact area ($A \approx \pi \cdot (18 \text{ nm})^2$) than all other cells of this species. The reason for this fact might be left-overs of the septum of former divisions of the cell as seen in SEM studies.[46,47] Nevertheless, its adhesive strength is in the same range as the adhesive strengths of the other cells, and even stronger than the adhesive strength of the cell corresponding to the violet circle (and the violet star, see arrow 2). This phenomenon may be attributed to an accumulation of macromolecules that mediate exceptional strong adhesion.**

Summary and explanation of the experimental findings

We found radii of the contact area between tens and some few hundred of nanometers with significant differences between individual bacterial cells. The radius of the contact area of a single cell differed depending on whether adhesion force or adhesion energy data were used for its calculation. Increasing the load did either not affect the radius of the contact area or enlarged it slightly, yet not to the extent predicted in the Hertzian model. The measured extent is individual to the bacterial cells; for some cells, even a tenfold higher loading force hardly increased the contact area. No correlation was found between the size of the contact area and the adhesive strength, neither for adhesion energy nor for adhesion force. This also explains that between *S. aureus* and *S. carnosus* cells no distinct differences in contact area size were found although *S. aureus* cells exhibited a significantly larger adhesive strength.

Our observations lead to several conclusions concerning adhesion mechanics of bacterial cells: since the contact between a bacterial cell and a surface is not Hertzian, classic contact mechanical models fail. Rather, the contact between a bacterium and a solid substrate can be described by multiple small contacts between bacterial cell wall macromolecules and the substrate.

The spatial distribution and nature of these macromolecules determine the cell's individual contact area, as well as the difference between contact areas calculated from adhesion energies and adhesion forces. The individual mechanical properties of a cell's surface macromolecules determine the cell's response to different external loads: a soft macromolecular layer allows for a larger increase in the surface contact area upon higher external loads as compared to a stiffer macromolecular layer. Since contact area and adhesive strength are not correlated, we conclude that bacterial surface adhesins form clusters rather than being uniformly distributed over the surface and the adhesive strength is mainly defined by the density of surface adhesins and their individual binding properties.

The reason for the heterogeneity of the properties and distribution of surface macromolecules and of mechanical cell wall properties may be variations in history and/or age of different cell wall parts: other studies have shown that – depending on the location of previous division planes – some proteins show different local prevalences.[48] Furthermore, also the surface shape of the cell, *i.e.* the peptidoglycan structure, and its mechanical properties, vary depending on previous division planes.[49,50] Also, the stiffness of the cell wall is different directly after cell division, allowing the cell for rapid enlargement.[51,52] Scanning electron micrographs show different 'roughnesses' for different parts of the cell wall. These topological features can as well be attributed to different macromolecular compositions of the cell wall.[46,47]

Conclusions

In this study, we describe a method that enables a direct evaluation of the size of the contact area between a single bacterial cell and a solid substrate using single-cell force spectroscopy on a partially silanized silicon surface. A general finding of our study is that the contact between a bacterial cell and surface is a highly individual property of bacterial cells. Hence, this

---

**Of note, the viability of this cell was not checked after force spectroscopy. Therefore, cell death or (partial) rupture of the cell wall cannot be fully excluded.

contact may not be described as the contact between a sphere and a surface, rather, the contact formation should be mainly attributed to bacterial cell wall macromolecules. The nature and distribution of these macromolecules define the contact formation properties of the respective cell.

Consequently, general quantitative modelling approaches describing bacterial surface contact will only be successful if the individual properties of a bacterium's cell wall macromolecular state is experimentally accessible.

Our results may also be important for describing adhesion and adsorption phenomena of nanoparticles that are covered with a soft, macromolecular layer comparable to the bacterial cell wall.

Acknowledgements

References

1 J. W. Costerton, P. S. Stewart and E. P. Greenberg, *Science*, 1999, **284**, 1318–1322.

2 L. Hall-Stoodley, J. W. Costerton and P. Stoodley, *Nat. Rev. Microbiol.*, 2004, **2**, 95–108.

3 X. Shi and X. Zhu, *Trends Food Sci. Technol.*, 2009, **20**, 407–413.

4 K. Hori and S. Matsumoto, *Biochem. Eng. J.*, 2010, **48**, 424–434.

5 D. J. Müller and Y. F. Dufrêne, *Trends Cell Biol.*, 2011, **8**, 461–469.

6 C. A. Bippes and D. J. Müller, *Rep. Prog. Phys.*, 2011, **74**, 086601.

7 J. Liu, X. Zhang, H. Yang, J. Yuan, H. Wei, J. Yu and X. Fang, *Nanoscale*, 2015, **7**, 15245.

8 L. Arnal, G. Longo, P. Stupar, M. F. Castez, N. Cattelan, R. C. Salvarezza, O. M. Yantorno, S. Kasas and M. E. Vela, *Nanoscale*, 2015, **7**, 17563.

9 Q. Li, T. Zhang, Y. Pan, L. C. Ciacchi, B. Xu and G. Wei, *RSC Adv.*, 2016, **6**, 12893–12912.

10 P. Stock, J. I. Monroe, T. Utzig, D. J. Smith, M. S. Shell and M. Valtiner, *ACS Nano*, 2017, **11**(3), 2586–2597.

11 C. Marlière and S. Dhahri, *Nanoscale*, 2015, **7**, 8843.

12 R. M. A. Sullan, A. Beaussart, P. Tripathi, S. Derclaye, S. El-Kirat-Chatel, J. K. Li, Y. Schneider, J. Vanderleyden, S. Lebeer and Y. F. Dufrêne, *Nanoscale*, 2014, **6**, 1134.

13 S. Aguayo, N. Donos, D. Spratt and L. Bozec, *Nanotechnology*, 2015, **26**, 062001.

14 Y. F. Dufrêne, *Trends Microbiol.*, 2015, **23**, 376–382.

15 E. S. Ovchinnikova, B. P. Krom, H. J. Busscher and H. C. van der Mei, *BMC Microbiol.*, 2012, **12**, 281.

16 G. Zeng, R. Ogaki and R. L. Meyer, *Acta Biomater.*, 2015, **24**, 64–73.

17 K. P. Heim, R. M. A. Sullan, P. J. Crowley, S. El-Kirat-Chatel, A. Beaussart, W. Tang, R. Besingi, Y. F. Dufrêne and L. J. Brady, *J. Biol. Chem.*, 2015, **290**, 9002–9019.

18 N. Thewes, P. Loskill, P. Jung, H. Peisker, M. Bischoff, M. Herrmann and K. Jacobs, *Beilstein J. Nanotechnol.*, 2014, **5**, 1501–1512.

19 C. J. Van Oss, *Interfacial forces in aqueous media*, CRC Press, 2006.

20 A. Beaussart, S. El-Kirat-Chatel, P. Herman, D. Alsteens, J. Mahillon, P. Hols and Y. F. Dufrêne, *Biophys. J.*, 2013, **104**, 1886–1892.

21 A. Beaussart, A. E. Baker, S. L. Kuchma, S. El-Kirat-Chatel, G. A. O'Toole and Y. F. Dufrêne, *ACS Nano*, 2014, **8**, 10723–10733.

22 P. Herman-Bausier, S. El-Kirat-Chatel, T. J. Foster, J. A. Geoghegan and Y. F. Dufrêne, *mBio*, 2015, **6**, e00413–e00415.

23 N. Thewes, A. Thewes, P. Loskill, H. Peisker, M. Bischoff, M. Herrmann, L. Santen and K. Jacobs, *Soft Matter*, 2015, **11**, 8913–8919.

24 Y. Chen, W. Norde, H. C. van der Mei and H. J. Busscher, *mBio*, 2012, **3**, 00378–00312.

25 M. Lai, N. E. Clay, D. H. Kimb and H. Kong, *Nanoscale*, 2015, **7**, 6737.

26 Z. Wang, C. Wang, S. Liu, W. He, L. Wang and J. J. Gan, *ACS Nano*, 2017, **11**, 1659–1672.

27 V. Sayevich, C. Guhrenz, V. M. Dzhagan and M. Sin, *ACS Nano*, 2017, **11**, 1559–1571.

28 X. Zhang, J. Zhang, F. Zhang and S. Yu, *Nanoscale*, 2017, **9**, 4787–4792.

29 K. H. Schleifer and U. Fischer, *Int. J. Syst. Bacteriol.*, 1982, **32**, 153–156.

30 F. Goetz, *J. Appl. Microbiol.*, 1990, **69**, 49–53.

31 M. Rüger, G. Bensch, R. Tüngler and U. Reichl, *Cytometry, Part A*, 2012, **81**, 1055–1066.

32 N. Thewes, P. Loskill, C. Spengler, S. Hümbert, M. Bischoff and K. Jacobs, *Eur. Phys. J. E: Soft Matter Biol. Phys.*, 2015, **38**, 1–9.

33 M. Lessel, O. Bäumchen, M. Klos, H. Hähl, R. Fetzer, M. Paulus, R. Seemann and K. Jacobs, *Surf. Interface Anal.*, 2015, **47**, 557–564.

34 S. El-Kirat-Chatel, C. D. Boyd, G. A. O'Toole and Y. F. Dufrêne, *ACS Nano*, 2014, **8**, 1690–1698.

35 S. El-Kirat-Chatel, A. Beaussart, S. Derclaye, D. Alsteens, S. Kucharikova, P. Van Dijck and Y. F. Dufrêne, *ACS Nano*, 2015, **9**, 1648–1655.

36 P. Loskill, P. M. Pereira, P. Jung, M. Bischoff, M. Herrmann, M. G. Pinho and K. Jacobs, *Biophys. J.*, 2014, **107**, 1082–1089.

37 A. Beaussart, P. Herman, S. El-Kirat-Chatel, P. N. Lipke, S. Kucharíková, P. Van Dijck and Y. F. Dufrêne, *Nanoscale*, 2013, **5**, 10894–10900.

38 T. Vanzieleghem, P. Herman-Bausier, Y. F. Dufrêne and J. Mahillon, *Langmuir*, 2015, **31**, 4713–4721.

39 H. Hertz, *J. Reine Angew. Math*, 1882, **92**, 156–171.

40 M. Benoit and H. E. Gaub, *Cells Tissues Organs*, 2002, **172**, 174–189.

41 Y. J. Oh, M. Hubauer-Brenner, H. J. Gruber, Y. Cui, L. Traxler, C. Siligan and P. Hinterdorfer, *Sci. Rep.*, 2016, **6**, 33909.

42 K. L. Johnson, K. Kendall and A. D. Roberts, *Proc. R. Soc. A*, 1971, **324**(1558), 301–313.

43 D. Maugis, *J. Colloid Interface Sci.*, 1992, **150**, 243–269.

44 E. Barthel, *J. Phys. D: Appl. Phys.*, 2008, **41**, 163001.

45 D. Vorselen, F. C. MacKintosh, W. H. Roos and G. J. L. Wuite, *ACS Nano*, 2017, **11**(3), 2628–2636.

46 K. Amako and A. Umeda, *J. Ultrastruct. Res.*, 1977, **58**, 34–40.

47 J. M. Monteiro, P. B. Fernandes, F. Vaz, A. R. Pereira, A. C. Tavares, M. T. Ferreira, P. M. Pereira, H. Veiga, M. S. VanNieuwenzhe, Y. V. Brun, S. R. Filipe and M. G. Pinho, *Nat. Commun.*, 2015, **6**, 8055.

48 H. Rosado, R. Turner, S. Foster and P. Taylor, *Int. J. Mol. Sci.*, 2015, **16**, 16710–16727.

49 R. D. Turner, E. C. Ratcliffe, R. Wheeler, R. Golestanian, J. K. Hobbs and J. F. Foster, *Nat. Commun.*, 2010, **1**, 26.

50 R. Bailey, R. Turner, N. Mullin, N. Clarke, S. Foster and J. Hobbs, *Biophys. J.*, 2014, **107**, 2538–2545.

51 A. M. Jorge, E. Hoiczyk, J. P. Gomes and M. G. Pinho, *PLoS One*, 2011, **6**, e27542.

52 R. Wheeler, R. Turner, R. Bailey, B. Salamaga, S. Mesnage, S. Mohamad, E. Hayhurst, M. Horsburgh, J. Hobbs and S. Foster, *mBio*, 2015, **6**, e00660-15.

137

Nanoscale

ELECTRONIC SUPPLEMENTARY MATERIAL

Determination of the nano-scaled contact area of Staphylococcal cells[†]

Christian Spengler,[a] Nicolas Thewes,[a] Philipp Jung,[b] Markus Bischoff,[b] and Karin Jacobs[*a]

Supporting information

S. aureus adhesion on hydrophobic surfaces

S. aureus cells showed a slowly decreasing adhesive strength on strongly hydrophobic surfaces: Adhesion force and energy decreased linearly with an increasing number of force-distance curves on random positions on an OTS surface (see Figure 1). Notably, this effect was pronounced to a different extent for different individual cells (different slopes of the fits in Figure 1). This phenomenon may be due to the loss of cell wall attached macromolecules that mediate adhesion in course of repeated force-distance curves[1]. Crossing the hydrophobic/hydrophilic interface, we therefore expect a similar effect on the hydrophobic part of the sample. To characterize that linear decrease, the negative slope *m* of the best-fit lines in Figure 1 is used to interpret the force-distance curves gained while crossing the hydrophobic/hydrophilic interface shown in Figure 6 a and 6 c in the full article.

In contrast to *S. aureus* cells, *S. carnosus* cells featured robust adhesion mechanisms (yet a lower adhesion strength than *S. aureus*) that withstand multiple adhesion events when probed by AFM force spectroscopy, meaning that within the experimental error, adhesion energy and force remained constant when probing only the hydrophobic or hydrophilic surface area. Therefore, the slope of the best-fit line is set to zero for the experiments with *S. carnosus*, see Figure 6 b and 6 d in the full article.

[a] *Department of Experimental Physics, Saarland University, 66041 Saarbrücken, Germany. Fax: +49 681 302 717 00; Tel: +49 681 302 717 77; E-mail: k.jacobs@physik.uni-saarland.de*
[b] *Institute of Medical Microbiology and Hygiene, Saarland University, 66421 Homburg/Saar, Germany.*

Size of *S. carnosus* and *S. aureus*

On average, the cell diameters of *S. aureus* and *S. carnosus* cells are very similar, as can be seen in Figure 2, with diameters matching literature values.[2,3] The mean radii of both species differ by less than 6 % and the standard deviation for both species less is than 7 %. However, the radii measured in SEM micrographs characterize the size of the bacteria in the dry state (in vacuum), therefore, the absolute size may not be the one that is relevant for our experiments, yet it can be expected that the size distribution is similar. However, the variation in bacterial cell radius is much smaller than the variation of the radius of the contact area (Figure. 7 in the main paper), which can be over 30 %.

Application of the method to rigid spheres

To illustrate the strength of the experimental setup, we performed the same type of experiments with a polystyrene bead (purchased as colloidal AFM-probe from Sqube, Bickenbach, Germany) with a diameter of 2 µm to determine its contact area. The sphere features an RMS surface roughness of 1.2 nm as determined by AFM. We obtained a radius of the contact area of 94 *pm*4 nm (see Figure 3, left). For comparison, the experiments were also performed with a hydrophobized silica sphere of 4 µm radius (sphere from Polyscience, Warrington, USA, glued to an MLCT-0-E cantilever from Bruker Nano, Santa Barbara, USA). Here, we find a contact area radius of 190 ± 8 nm (see Figure 3, right). For both relatively rigid spheres, the ratio of the radius of the contact area to the radius of the sphere is substantially smaller than for the bacterial cells. However, for the rigid spheres, the contact mechanics is very different to the one for the soft, macromolecule-covered bacterial cell wall since its interaction forces to the surface is mainly dominated by single asperities of
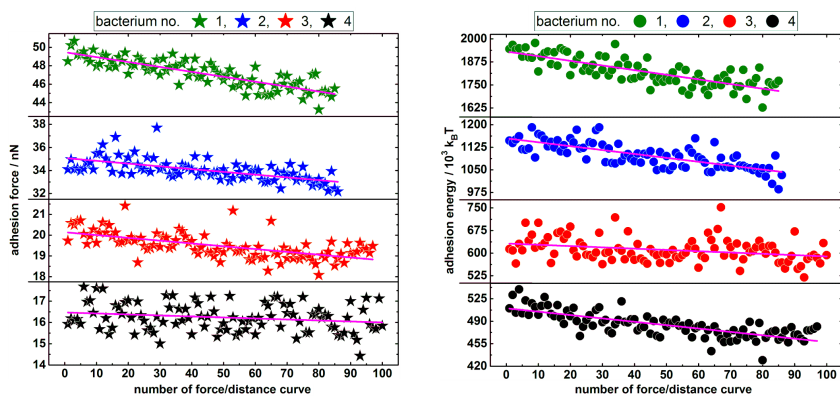
Fig. 1 Adhesion force (left) and energy (right) of four *S. aureus* cells in dependence of the number of recorded force-distance curves on random positions on a strongly hydrophobic OTS-surface. A linear fit of each set of values revealed a systematic decrease in adhesive strength in all cases. The extent of this decrease (slope of the linear fit) is a cell-individual property.
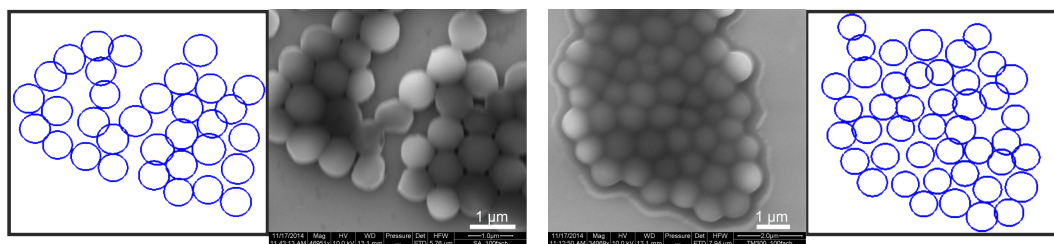
Fig. 2 Scanning electron micrographs of dried *S. aureus* (left) and *S. carnosus* (right) cells. (Note that the scales are not the same.) Cells and their size were automatically recognized with Matlab.
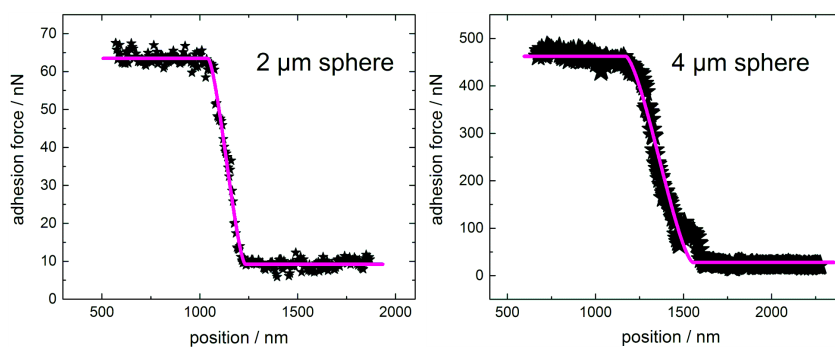
Fig. 3 Adhesion force as a function of the position near the hydrophobic/hydrophilic interface for a 2 μm-polystyrene bead (left) and 4 μm-hydrophobized silica sphere (right).

the colloidal probe.[4] Therefore, a deeper study of colloidal contact will not pave the way to interpreting our results for bacteria in more detail. However, the colloidal probe experiments show the versatility of our method, which is not restricted to bacterial cells. It moreover corroborates the notion that the size of the bacterial contact area is mainly determined by tethering surface macromolecules which are obviously not present on the colloidal probes.

Influence of the force trigger of radii calculated from force data

The radii calculated from adhesion force data for different force triggers displayed in Figure 4 show a similar trend as already shown in Figure 10 in the full article: Radii determined from experiments with a higher force trigger are in the same range or larger than radii recorded with a lower force trigger. This is especially visible when comparing data for *S. aureus* cells calculated from force triggers of 3 nN and 30 nN. Nevertheless, in all cases - and for both tested species - the increase of the contact area does not behave like predicted by the Hertzian model.

Correlation between adhesive strength and contact area – all data

Figure 5 shows adhesion forces and adhesion energies of all tested cells (*S. aureus* as well as *S. carnosus*) in dependence of their contact area for all force triggers used. In all cases, no correlation betweeen adhesive strength and size of the contact area is observed.

References

1 S. El-Kirat-Chatel, C. D. Boyd, G. A. OToole and Y. F. Dufrêne, *ACS Nano*, 2014, **8**, 1690–1698.

2 K. H. Schleifer and U. Fischer, *International Journal of Systematic Bacteriology*, 1982, **32**, 153–156.

3 J. M. Monteiro, P. B. Fernandes, F. Vaz, A. R. Pereira, A. C. Tavares, M. T. Ferreira, P. M. Pereira, H. Veiga, M. S. Van-Nieuwenzhe, Y. V. Brun, S. R. Filipe and M. G. Pinho, *Nature Communications*, 2015, **6**, 8055.

4 H.-J. Butt and M. Kappl, *Advances in Colloid and Interface Science*, 2009, **146**, 48–60.
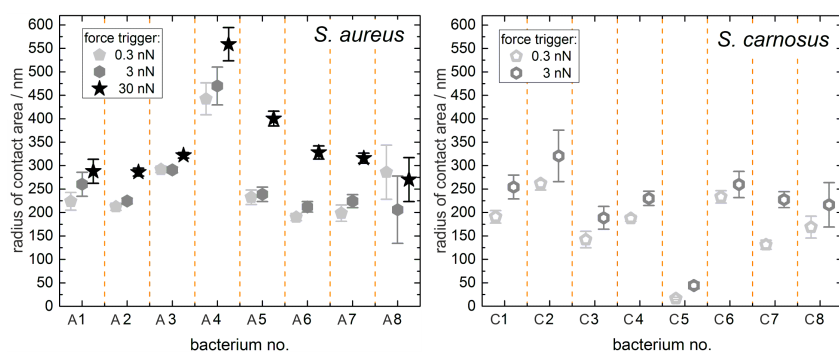
Fig. 4 Radii of the contact area between bacterial cell and surface for eight individuals of *S. aureus* (left) and *S. carnosus* (right). The radii were calculated from adhesion force data that were obtained with force triggers of 0.3 nN (light grey pentagons), 3 nN (dark grey hexagons) and (for *S. aureus* only) 30 nN (black stars).
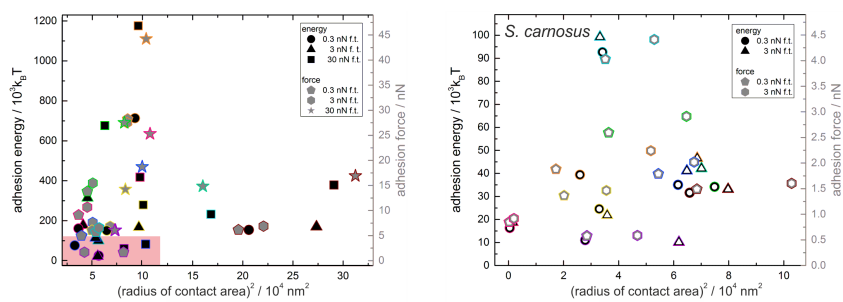
Fig. 5 Adhesion energy (black symbols) and force (grey symbols) in dependence of the contact area for eight different bacterial cells (different edge colors) and all used force triggers (f. t.); *S. aureus* (left) and *S. carnosus* (right). To place emphasis on the lower adhesive strength of *S. carnosus* cells, the colored rectangle in the left diagram represents the scale of the right diagram.

Addendum V – Morphometric Quantification of the Influence of Substrate Nano-Roughness on Bacterial Adhesion and Viability

Authors: C. Spengler[1], F. Nolle[1], J. Mischo[1], S. Grandthyll[1] N. Thewes[1], M. Koch[2], F. Müller1, M. Bischoff[3], M. A. Klatt[4] and K. Jacobs[1]

[1] Department of Experimental Physics, Saarland University, 66041 Saarbrücken, Germany.
[2] Leibniz Institute for New Materials, 66041 Saarbrücken, Germany.
[3] Institute of Medical Microbiology and Hygiene, Saarland University, 66421 Homburg, Germany.
[4] Institute of Stochastics, Karlsruhe Institute of Technology, 76131 Karlsruhe, Germany

Author contributions:
*Experiments were designed by C. Spengler and N. Thewes. Experimental results were achieved by **C. Spengler**, F. Nolle (SCFS), J. Mischo (flow chamber), S. Grandthyll, F. Müller (XPS), and M Koch (SEM). Data analysis was performed by **C. Spengler**, F. Nolle, M. Mischo, and M. Klatt (Minkowski functionals). The article was mainly written by **C. Spengler**, M. A. Klatt, M. Bischoff, and K. Jacobs. Scientific work was directed by M. Bischoff and K. Jacobs.*

Abstract - The adhesion of bacterial cells and the subsequent formation of resilient biofilms at solid/liquid interfaces is of great importance in industry and medicine. The process of bacterial adhesion is decisively influenced by substrate properties, e. g. the topography. For this paper, the influence of nanoscaled surface roughness on the adhesion and viability of *S. aureus* cells was investigated by AFM-based single cell force spectroscopy and flow chamber experiments. Adhesion was studied on hydrophilic and hydrophobic silicon-based surfaces that featured surface structures in the same size range as the bacterial cell wall molecules ($7\,\text{nm} \leq \text{RMS} \leq 35\,\text{nm}$). The morphology of these structures was analyzed in great detail by Minkowski functionals. We demonstrate that an increased surface roughness reduces the adhesive strength of the cells, regardless of the substrate's hydrophobicity. On hydrophobic surfaces, the adhesive force of the cells can be quantified by the size of the surface that is available for cell wall molecule attachment. In addition, a bactericidal effect is observed on the rough surfaces, which is more pronounced at higher roughness values. The results can be transferred to the specific development of new materials for industrial as well as medical applications.

Morphometric Quantification of the Influence of Substrate Nano-Roughness on Bacterial Adhesion and Viability

Christian Spengler,[†] Friederike Nolle,[†] Johannes Mischo,[†] Samuel Grandthyll,[†] Nicolas Thewes,[†] Marcus Koch,[‡] Frank Müller,[†] Markus Bischoff,[¶] Michael A. Klatt,[§] and Karin Jacobs*,[†]

†*Department of Experimental Physics, Saarland University, 66041 Saarbrücken, Germany*
‡*Leibniz Institute for New Materials, 66041 Saarbrücken, Germany*
¶*Institute of Medical Microbiology and Hygiene, Saarland University, 66421 Homburg/Saar, Germany*
§*Institute of Stochastics, Karlsruhe Institute of Technology, 76131 Karlsruhe, Germany*

E-mail: k.jacobs@physik.uni-saarland.de
Phone: +49 (0)681 302 71777. Fax: +49 (0)681 302 71700

Abstract

The adhesion of bacterial cells and the subsequent formation of resilient biofilms at solid/liquid interfaces is of great importance in industry and medicine. The process of bacterial adhesion is decisively influenced by substrate properties, e. g. the topography. For this paper, the influence of nanoscaled surface roughness on the adhesion and viability of *S. aureus* cells was investigated by AFM-based single cell force spectroscopy and flow chamber experiments. Adhesion was studied on hydrophilic and hydrophobic silicon-based surfaces that featured surface structures in the same size range as the bacterial cell wall molecules ($7\,\mathrm{nm} \leq \mathrm{RMS} \leq 35\,\mathrm{nm}$). The morphology of these structures was analyzed in great detail by Minkowski functionals. We demonstrate that an increased surface roughness reduces the adhesive strength of the cells, regardless of the substrate's hydrophobicity. On hydrophobic surfaces, the adhesive force of the cells can be quantified by the size of the surface that is available for cell wall molecule attachment. In addition, a bactericidal effect is observed on the rough surfaces, which is more pronounced at higher roughness values. The results can be transferred to the specific development of new materials for industrial as well as medical applications.

Introduction

Besides their beneficial effects, for example in waste water cleaning,[1] bacterial biofilms can cause serious problems in many medical, biological and industrial applications.[2–6] Once formed, they are chemically and me-chanically robust and consequently very hard to remove.[7–9] Hence, a promising approach in biofilm prevention should be to inhibit the first step of its formation, namely the adhesion of bacterial cells to surfaces. Besides the nature of the bacterial cells themselves, the properties of the underlying surfaces play a crucial role in

the attachment process and the final strength of adhesion: with respect to the material, its chemical composition (of the surface and up to 100 nm beneath into the bulk[10,11]) and its charge are of major relevance since they determine the surface energy.[12,13] It was shown that a lower surface energy fosters the adhesion of different types of bacterial cells.[12,14] Additionally, mechanical properties, such as substratum stiffness, can have an impact on the bacterial adhesion capability.[15]

Another surface property of particular importance for the adhesion of bacterial cells is the surface topography. This topic was often addressed by the use of regularly structured or patterned surfaces (e. g. grooves and trenches of different geometries and aspect ratios) of microscale dimensions (and therefore in the range of or larger than typical bacterial cell diameters).[16–22] For example, it was shown that bacteria – under flow or under static conditions – adsorb with respect to such patterns and that rod-shaped cells even re-orient themselves according to the surface structures.[16,18,19]

Other studies were conducted on more irregularly or randomly structured surfaces – often metals, such as titanium and steel – that displayed surface structures on the nano- or microscale.[23–30]

For such irregularly structured surfaces, there are a number of parameters to describe their roughness and morphology.[29,31,32] The average roughness or the root means square (RMS) roughness are very descriptive parameters and are, therefore, often used in bacterial adhesion studies. Other measures, such as the skewness or the kurtosis of the surface, are less intuitive, but give additional information about the surface morphology.[28,33]

However, these measures are still local shape descriptors that are insensitive to global features because they do not distinguish between arbitrary permutations of the positions of different heights. This is in contrast to a morphological description via the so-called Minkowski functionals.[34] These more sensitive global structural characteristics allow for a better comparison of results from different experiments. They are comprehensive

and efficient shape descriptors from integral geometry[35] that contain the complete additive – and hence robust – shape information (according to Hadwiger's theorem).[36] Since they are versatile geometric measures, they have already been widely used in statistical physics and pattern analysis; for example, see Refs.[34,37–42] and references therein. A rough surface can be analyzed either directly by the three-dimensional Minkowski functionals or by the two-dimensional Minkowski functionals of the level sets at different heights. In 2D, the Minkowski functionals of a compact body can be intuitively interpreted as its area, perimeter, and Euler characteristic. The latter is a topological constant, which is given by the number of components minus the number of holes. For a visualization of the Minkowski functionals of level sets, see Figure S2 in the Supporting Information.

Moreover, most other studies examined adhesion mainly by counting the number of cells that adhered to the surfaces under different conditions. This technique resembles the natural situation of bacterial colonization quite closely. Consequently, the 'adhesion probability' (how likely are the cells to adhere to the surface) of cells is measured which may not be the same as their adhesive strength (energy or force needed to separate the cell from the surface). Of note, previous studies used quantitative force sensors on rough surfaces, however, these works focused on different aspects of bacterial removal,[43,44] or multi-cellular effects in adhesion.[45] It should be mentioned that such cell counting-based approaches are more qualitative than quantitative. Many different causes can lead to systematic errors that make it very difficult to compare the results of different labs: Depending on the process to gain the number of adhering cells, even the same systems will lead to different results. Rarely, the exact flow geometry and the shear rate of the bacterial solution are given, which also determine the initial number of adsorbed cells, as well as washing of non-adsorbed cells; in some cases, the sample is first dried and then coated with gold in order to be able to count the bacteria later in SEM images; also the removal of the cells in order to plate them

2

out and then count them is difficult to describe in all parameters.[20,24,25]

In summary, it seems that literature is lacking quantitative bacterial adhesion force measurements at a single-cell level on nano-rough surfaces that are characterized in great detail. We attend to fill this gap with our study. Therefore, we used single-cell force spectroscopy (SCFS), a well-established method for quantitative adhesion force measurements of living bacterial cells.[46–51] We investigate the influence of surface nano-roughness on the adhesion of *S. aureus* cells to two types of silicon-based substrates with strongly different hydrophobicity. These surfaces were fully characterized by Minkowski functionals. Their topography can be – on a nanoscopic scale – described as rough: with RMS roughnesses of the surfaces ranging from 7 nm to 35 nm, the structural features are one to two orders of magnitude smaller than the bacterial cell diameter and comparable to dimensions of cell wall macromolecules.[46,52] Bacterial adhesion to these surfaces was compared to the adhesion to very smooth silicon wafers that were chemically identical to the rough ones. Besides the adhesion force, other characteristic measures such as the rupture lengths and snap-in separations were determined.[46]

Of note, if adhesion cannot be completely inhibited, a promising approach to prevent the formation of biofilms could include surfaces that are capable of 'killing' adsorbed bacteria. In this context, it was found that nano-structured natural surfaces (e. g. wings of flies and cicadas[53–56]) as well as manufactured surfaces with small spikes (such as the so-called 'black silicon'[57,58]) or sharp structures (i. e. graphene sheets[59]) exhibit such bactericidal properties. Therefore, we also investigated the influence of the nano-rough surfaces on bacterial viability after the SCFS and the flow chamber experiments.

Our results can spur the production and/or modification of high-tech materials that prevent bacterial adhesion and/or kill already adsorbed cells. On a more general level, our results could help to improve the understanding of bacterial adhesion mechanisms on surfaces with different topographies.

Materials and methods

Silicon wafers Silicon wafers in (100) orientation with a resistivity of 10–20 Ωcm were purchased from Siltronic (Burghausen, Germany). They feature a native silicon oxide layer with a thickness of 1.7(2) nm as determined by ellipsometry.[60] The wafers are by default polished to an RMS roughness of 0.09(2) nm as determined by AFM.[60]

Preparation of the rough surfaces In a first step, silicon surfaces were covered with a gold layer of a nominal film thickness of 2 nm* by physical vapor deposition. As known, this procedure does not result in a continuous gold film, but in gold clusters of sub-micron size.[61] Subsequently, following a recipe by Koynov *et al.*,[62] the gold covered silicon was etched by immersing the wafers in a mixture of fluoric acid (HF, 40 %), hydrogen peroxide (H_2O_2, 35 %) and water for 90 s, 180 s and 360 s, respectively. Residues from the etching solution were removed by extensively rinsing the etched wafers in ultra-pure water. After etching, the gold clusters were removed by immersing the wafers in aqua regia (1:3 mixture of HNO_3 (65 %) and HCl (37 %)) for 25 min. Afterwards, the wafers were rinsed again with ultra-pure water to remove possible leftovers of the acid. X-ray photoelectron spectroscopy (XPS) confirmed that no gold was present on the surface after this treatment (an XPS overview spectrum is given in Figure S1 a in the Supporting Information).

To render some of the wafers hydrophobic, they were covered with a self-assembling monolayer of silanes according to a standard recipe.[63]

Right before every set of experiments with bacteria, all surfaces were cleaned as follows: hydrophilic surfaces were cleaned for 30 min in peroxymonosulfuric acid (1:1 mixture of H_2SO_4 (conc.) and H_2O_2 (30 %)) to remove any organic contamination followed by three rinsing steps with hot ultra-pure water to remove residues of the cleaning solution. Hydrophobic surfaces were consecutively cleaned in ultrasonic baths of ethanol and acetone for 3 min

---

*The film thickness was determined with a quartz crystal microbalance during gold evaporation.

each. After cleaning, hydrophilic as well as hydrophobic surfaces were dried under a stream of pure nitrogen.

Bacteria   For this study, cells of the *S. aureus* strain SA 113 were used. Bacteria from a deep-frozen stock solution were grown on a blood agar plate for three days at 37 °C. Such a plate was used for two weeks at the maximum. For the experiments, one colony from the plate was transferred into 5 ml of sterile tryptic soy broth (TSB) and cultured for 16 h at 37 °C under agitation (150 rpm). From this culture, 40 µl were transferred into 4 ml of fresh TSB and cultured once more for 2.5 h at 37 °C and 150 rpm. Finally, 1 ml was taken from this culture and washed three times by centrifuging for 3 min at 17,000 g, replacing the supernatant by 1 ml of fresh phosphate buffered saline (PBS, pH 7.3) and thoroughly vortexing. This procedure results in a bacterial suspension with an optical density at 600 nm (OD_{600}) of 0.2–0.3.

Viability measurements   To check the viability of the cells, the BacLight assay purchased from Molecular Probes, Eugene, USA was used. It consists of Syto 9 and propidium iodide. After excitation, the Syto 9 stain emits green light when bound to RNA of bacteria. In contrast, propidium iodide, which can only enter the porous cell wall of dead bacterial cells, emits red light and causes a reduction of the binding between the Syto 9 stain and the bacterial RNA. Hence, after staining a bacterial solution with the BacLight mixture and illuminating it with white light, viable cells glow green and dead cells red. To achieve best results, the stain is left to act on the cells for 10 min in the dark and thereafter its residues are removed by carefully washing the cells with PBS.

Force-distance measurements   Force-distance measurements were performed on a Bioscope Catalyst (Bruker-Nano, Santa Barbara, USA) with a single viable bacterial cell immobilized on a tipless cantilever (MLCT-0, Bruker-Nano) with nominal spring constants of

$0.01 \frac{N}{m}$ and $0.3 \frac{N}{m}$.[46] The cantilevers were calibrated before each set of measurements. For every force-distance curve, the approach and retraction distance was 800 nm with an retraction velocity of $800 \frac{nm}{s}$. The force trigger (i. e. the force with which the cell is pressed onto the substrate) was set to 300 pN. Since adhesion of *S. aureus* is very low for short contact times on hydrophilic surfaces,[52,64] all measurements on hydrophilic substrates were performed with a contact time (also called surface delay time) of 5 s. On hydrophobic surfaces, curves were recorded without surface delay time which corresponds to a 'real' contact time below 0.5 s.[64,65]

For each individual cell, 100 single force-distance curves were recorded on the smooth as well as on a rough surface in a rectangular pattern with a distance of 1 µm between each curve. To exclude that probing the smooth/rough surfaces might alter the adhesive behaviour of the bacterial cell, the first 50 curves were recorded on the smooth surface and the next 50 were recorded on the rough surface. Then, again, the smooth surface and afterwards the rough surface was probed by 50 curves each. By comparing the adhesion of each set of curves on the smooth/rough surface, it was ensured that the adhesion behaviour was not changed during the recording of several force-distance curves on the different surfaces (as it was also seen before on smooth silicon[64]).

Flow chamber measurements   The flow chamber used in the viability experiments consists of polymethyl methacrylate and has an area of $8 \times 8 \, mm^2$ and a height of 2.8 mm. Together with a low flow rate of maximum 250 µl/min, these dimensions guarantee a laminar flow profile in the center of the chamber where the investigated surfaces were attached using bio-compatible casting material as glue (Reprorubber by Flexbar, Islandia, USA).[66,67] Inlet and outlet of the cell were connected to a syringe pump system with high precision control of tube pressure and flow rates.

In a first step, the chamber was filled with PBS. Afterwards, a bacterial suspension in PBS with $OD_{600} \approx 0.01$ was flushed through the chamber of a flow rate of 250 µl/min allowing

4

the bacteria to adsorb to the surface. After 8 min of flushing with the bacterial suspension, the setup was rinsed with pure PBS to remove non-adsorbed cells from the system. Then, the flow was stopped[†] for 60 min[‡]. Subsequently, the flow chamber was filled with viability stain at a flow rate of 150 µl/min and after this, the flow was stopped and the stain acted on the cells for 10 min in darkness. Afterwards, the stain was washed out by flushing the chamber with pure PBS at a flow rate of 150µl/min and the viability was observed by optical microscopy.

AFM surface topography measurements
The surface topography was measured in tapping mode with an Icon FastscanBio (Bruker-Nano, Santa Barbara, USA) in air using high aspect ratio tips (HAR1-200-10, Bruker-Nano) with a nominal spring constant of $42 \frac{N}{m}$ in soft tapping mode. The scan area was $1 \, \mu m \times 1 \, \mu m$ for the 90 s and 180 s etched substrates and $3 \, \mu m \times 3 \, \mu m$ for the 360 s etched substrates with a lateral resolution of 1024×1024 pixels. The resolution in z-direction was below 0.5 nm. From the obtained images, the AFM tip shape was determined and the real surface was reconstructed by deconvoluting the recorded image and the tip geometry using the freely available software *Gwyddion*.

Minkowski analysis Both the level sets of the AFM images and their three-dimensional triangulations were analyzed using Minkowski functionals. In the latter case, the triangulation was constructed using the 'Advancing Front Surface Reconstruction' from CGAL.[68] Using the 3D Minkowski software *Karambola*,[41] the surface area was computed as a function of the height. More precisely, as a function of the difference in height to the maximal peak within the observation window, the surface area was

computed for all those triangles whose lowest vertex was above this threshold.

In the first case, the AFM images were converted into pixelated gray scale maps and then into black-and-white images via thresholding. A pixel whose height is above a threshold h turns white, all others become black. The three two-dimensional Minkowski functionals of the white domains were then computed as a function of the threshold height h using the software *Papaya*.[40] To reduce the pixelization errors, a standard marching square algorithm was applied.[39] Edge effects from the observation window were avoided by using minus-sampling boundary conditions (the outermost pixels were used for the boundary conditions).

Electronmicroscopy measurements For the scanning electron microscopy (SEM) measurements a FEI (Hilsboro, OR, USA) Quanta 400 FEG SEM in high vacuum mode was used. Secondary electron images were collected at 10 kV and 15 kV accelerating voltage under different tilting angles.

[†]Instead of completely stopping the flow (flow rate 0 µl/min) the flow rate was reduced to 2 µl/min so that the pressure in the system is preserved.

[‡]60 min was used because this is the time it takes to perform a complete force spectroscopy experiment with one cell.

Results and discussion

Morphological analysis of rough silicon surfaces

After repeated etching, the formerly highly reflective silicon surfaces changed to less reflecting ones, and this property became more pronounced for longer etching times. Such highly light absorbing silicon surfaces are often termed 'black silicon' and are frequently used for the production of solar cells.[62,69,70]
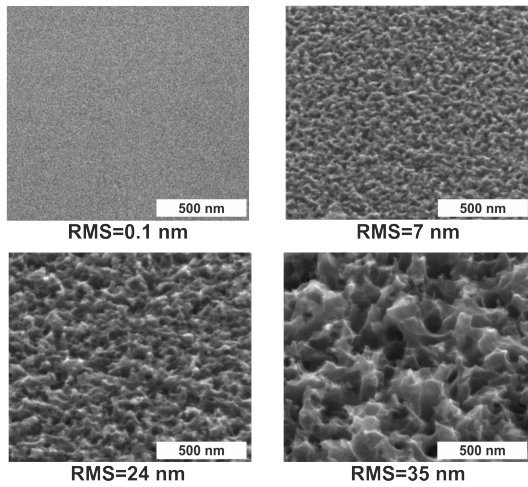
Figure 1: SEM images of the surfaces before etching and after etching for 90 s, 180 s and 360 s (from top left to bottom right). The RMS values have been gained on the same samples by AFM.

SEM images of the three differently long etched surfaces indicate the reason for their non-reflectivity (see Figure 1): on the formerly smooth surfaces, characteristic structures were created by etching, whose lateral and vertical dimensions increased with increasing etching time. Nevertheless, the structures feature sharp edges on all surfaces and their morphology seems similar in general.

Since SEM images do not provide quantitative height information, the surfaces were imaged by AFM to characterize their morphology in a quantitative way. The images were acquired with high aspect ratio AFM tips and the real surface was reconstructed by unfolding the recorded image and the tip geometry

before further analysis. As a simple parameter – and for comparison to other studies – the RMS roughness of all surfaces was determined. Its value increases with increasing etching time: 7(1) nm for the 90 s etched surface, 24(1) nm for the 180 s etched surface, and 35(1) nm for the 360 s etched surface. Since the RMS roughness is a common and descriptive parameter, the surfaces will be labeled by their RMS value for the rest of the paper. To compare the different substrates in greater detail, the Minkowski functionals for all surfaces were determined from the AFM images. Since the maximum height range of the samples varies, the functionals were normalized to their respective maximum height value. In Figure 2, the Euler characteristic density and the specific perimeter are shown in dependence of this normalized threshold height (absolute values and data of surface area are given in Figure S3 in the Supporting Information).
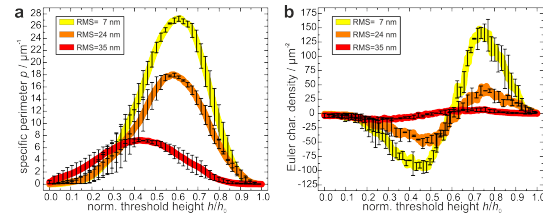
Figure 2: Specific perimeter (a) and Euler characteristic density (b) of the roughened substrates as a function of the normalized threshold height (for clarity, only for every 20th data point, an error bar is shown).

Both quantities have similar shapes with only a variation in extension for all surfaces: the specific perimeter features a very smooth shape with a single maximum for all substrates. The position of the maximum slightly changes on different substrates (for an explanation, see the discussion section). The Euler characteristic density has, in every case, for low threshold heights, a minimum featuring negative values and at larger heights, a maximum with positive values. The differences of the surfaces concern the absolute values of the specific perimeter and Euler characteristic density: both quantities have the highest values for the surface with 7 nm RMS roughness, lower values for the surface with 24 nm RMS roughness and the lowest

values for the surface with 35 nm RMS roughness. This means that the lateral dimensions of the etched structures are smaller for the surfaces that were etched shorter times.

Therefore, in summary, the Minkowski analysis, together with the RMS values and different height scales, confirms the first impression from SEM data indicating that the morphologies of the surfaces are equivalent, but their dimensions – in all spatial directions – increased with increasing etching times. On top of that, the analysis shows that all etched surfaces feature a sub-micron roughness with dimensions in the range as the radius of the bacterial contact area, which is about 150–300 nm.[52]

As bacterial adhesion strongly depends on surface wettability,[52] the water contact angles of all surfaces – both natural and hydrophobized silicon wafers – were determined before and after roughening. On the hydrophilic surfaces, in both cases, complete wetting (with no measurable hysteresis) of the surface can be observed. Results for the hydrophobic surfaces are depicted in Table 1. On all rough hydrophobic

Table 1: Advancing water contact angles (CA) and hysteresis of the hydrophobized surfaces.

RMS roughness	0.1 nm	7 nm	24 nm	35 nm
Advancing CA	111(1)°	154(2)°	153(3)°	158(2)°
Hysteresis	4(2)°	43(3)°	32(1)°	21(2)°

[a] Numbers in brackets depict the standard deviation of values obtained at different sample positions.

surfaces, the advancing water contact angles are in a comparable range of about 155° and hence approximately 45° larger than on the smooth hydrophobic surface. Also, the contact angle hysteresis for all rough surfaces is larger than for the smooth surface but decreased with increasing roughness.

These results match with theoretical expectations stating that with increasing roughness, hydrophobic surfaces become more hydrophobic and hydrophilic ones become more hydrophilic.[71] In our case, the latter was not observed because the hydrophilicity was already at its maximum before. Because of this correlation between roughness and hydrophobic-

ity, we can assume that the apparent superhydrophobicity (water contact angles above 150°) of our surfaces is not an effect of different surface chemistry, but, the effect of an increased roughness. This means the microscopic surface energy (as 'seen' by bacteria and especially their cell wall molecules) remains unchanged in comparison to the smooth surface.

Of note, bacterial adhesion is known to be affected not only by surface chemistry but also by the subsurface of a material through long-ranging van der Waals forces.[10] Therefore, to exclude potential influences originating from differences in surface and subsurface composition, XPS measurements were performed showing that the roughened surfaces oxidize immediately after etching. Since this surface oxide layer has the same thickness as the oxide layers of the non-etched substrates, all used surfaces can be assumed to be chemically identical (XPS spectra are given in Figure S1 in the Supporting Information).

Bacterial adhesion on rough silicon surfaces

Figure 3 displays the results of single cell force spectroscopy measurements on hydrophilic (Figure 3 a) and hydrophobic (Figure 3 b) surfaces with variable roughness. On the hydrophilic surfaces, the determined adhesion forces vary greatly between different force-distance curves of one and the same cell.[14] Therefore, the mean values of individual cells are not very informative; instead, the adhesion forces of all tested cells on each set of surfaces are condensed in a histogram (Figure 3 a). On hydrophobic surfaces, adhesion forces of each tested cell show a quite low scattering, which allows each cell to be assigned a mean adhesion force. Nevertheless, these mean adhesion forces are very cell-individual, i. e. they can differ markedly between different individuals.[14] Therefore, for each cell, its mean adhesion force determined on the smooth surface was normalized to 1.0 and its mean adhesion force on the roughened surface was adjusted accordingly (not normalized values are given in Figure S4 in the Supporting Information).
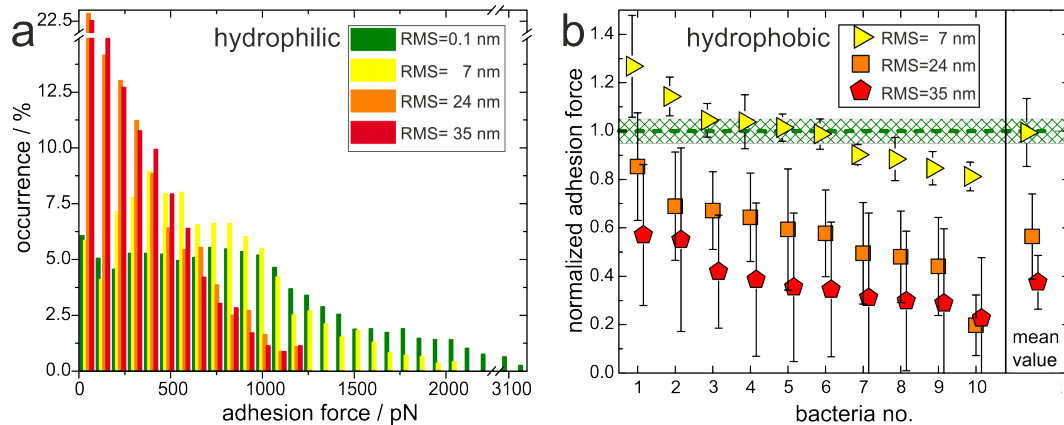
Figure 3: a) Histogram of all measured adhesion forces of in total 42 individual *S. aureus* cells determined on hydrophilic surfaces of different roughnesses. b) Adhesion forces of in total 30 *S. aureus* cells determined on the three types of roughened surfaces. Data are normalized to their individual adhesion force on the smooth silicon surface (marked in green). Error bars depict the standard deviation of the adhesion force distribution for every individual cell and – in the case of the mean value – the standard deviation of the arithmetic mean of the mean adhesion forces of every cell. (For reasons of clarity, cells are sorted in order of decreasing reduction of adhesion force.)

On the hydrophilic sample sets, the strongest adhesion forces (from 0 nN to over 3 nN with almost one third of data points above 1.25 nN) were observed on the smooth, polished silicon surface (green bars in Figure 3 a). On the surface with 7 nm RMS roughness (yellow bars in Figure 3 a), the distribution of adhesion forces is already shifted towards smaller values (varying between 0 nN and 2 nN, with a small maximum at about 0.4 nN). The distributions of adhesion forces determined on the two roughest surfaces (orange and red bars in Figure 3 a) are almost identical and show maxima at around 1.2 nN and most values located close to 0 nN.

On the hydrophobic sample sets, adhesion forces on the surface with 7 nm RMS roughness (yellow triangles in Figure 3 b) range from 80-130 % of the forces recorded on the smooth sample. Their mean value exactly matches the mean adhesion force on the smooth surface. On the surface with 24 nm RMS roughness (orange squares in Figure 3 b), cells feature adhesion forces between 30 % and 90 % of the ones observed on the smooth surface with a mean value of 56(18) %. Adhesion forces on the roughest surface (red pentagons in Figure 3 b) vary between 25 % and 60 % of the forces seen on the smooth surface. The mean value on the rough-

est surface is 38(11) % of the value determined on the smooth surface. Notably, while the adhesive strength decreases on rougher surfaces, the standard deviation of the force distributions increases: while, on the smooth surface, the standard deviation is approximately 10 % of the mean adhesion force (width of the green shaded area in Figure 3 b), it increases to about 20 % on the surface with 7 nm RMS roughness and over 60 % on the roughest surface.

Regardless of the surface roughness, the bacterial adhesion force on all tested substrates is stronger on hydrophobic surfaces than on hydrophilic ones. This difference has also been observed in other studies on smooth surfaces and was attributed to different numbers of tethered cell wall macromolecules. [14,64] However, the scatter in the adhesion forces is much larger for values recorded on hydrophilic surfaces than on hydrophobic surfaces. This low scattering on hydrophobic surfaces was also observed for other measured quantities, such as the rupture lengths and the snap-in separations. Therefore, on the hydrophobic surfaces, it is possible to analyze the correlation between these values determined on smooth and rough surfaces as well as the relative change in adhesion force. As shown in Figure 4 a and b, rupture
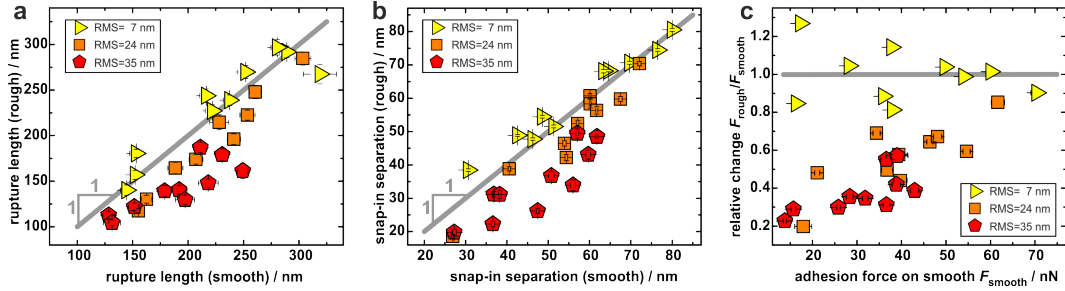
Figure 4: a)/b) Mean rupture length (a) and snap-in separation (b) of every tested cell on the rough hydrophobic surfaces in dependence of their value on the smooth hydrophobic surface. c) Relative change of the adhesion force on the rough hydrophobic surfaces in dependence of the adhesion force on the smooth hydrophobic surface.

lengths as well as snap-in separations decrease with increasing surface roughness. Additionally, rupture lengths and snap-in separations on the rough surfaces are positively correlated with the respective values recorded on the smooth surface. This means that cells with high rupture lengths and/or high snap-in separations on the smooth surface also have rather high respective values on the rough surfaces (see Figure 4 a and b). From the average snap-in separation, the average extension length of the molecules (caused by random thermal fluctuations) can be deduced, which for *S. aureus* lies in the range of 50 nm (see Figure 4 b and the study of Thewes et al.[46]).

Furthermore, as shown in Figure 4 c, for the two roughest surfaces, high adhesion forces on the smooth hydrophobic surface are reduced to a smaller extent on the rough surfaces than weak adhesion forces. This means, that cells with a high adhesion force on the smooth surface 'lose' little of their adhesive strength on the rough surfaces. In contrast, cells that only weakly adhered on the smooth surface forfeit a rather high fraction of their adhesive strength when probed on the rough surfaces. However, this is not the case for the surface with the lowest roughness where no correlation between adhesive strength on the smooth surface and its decrease on the rough surface is observed.

In general, also on the hydrophilic surfaces, it should be worth investigating if a similar relationship between the initial adhesion force and its change on the rough surfaces as well as between the rupture lengths on the different substrates exists. However, in contrast to the scenario on hydrophobic surfaces, on hydrophilic surfaces, measured data of one and the same cell scatter so much that no dependencies of rupture lengths on different surfaces or adhesion forces and their decrease are observable (data in Figure S5 in the Supporting Information).

The results of adhesion measurements on smooth and differently roughened silicon surfaces can be interpreted by the macromolecular nature of bacterial adhesion stating that the contact between cell and surface is primarily mediated by cell wall macromolecules that tether to the substrate.[46,64] Consequently, the adhesive strength of an individual cell is mainly determined by the total number of such macromolecules in contact to the substrate.[14] For *S. aureus*, it was shown that these macromolecules can extend about 50 nm due to thermal fluctuations and can be stretched to a length of several hundred nanometers when firmly attached to a surface.[14,46] Using this knowledge, Figure 5 sketches the proposed molecular picture on increasingly rough surfaces.

On the smooth silicon surface, a high number or even all surface macromolecules within a certain area, called the contact area,[52] tether to the surface and, thus, adhesion is the strongest. Then, with increasing roughness, an increasing number of cell wall macromolecules cannot reach the surface which results in a reduced adhesion.

As already mentioned above, on the hydrophilic surfaces, it is hardly possible to quan-
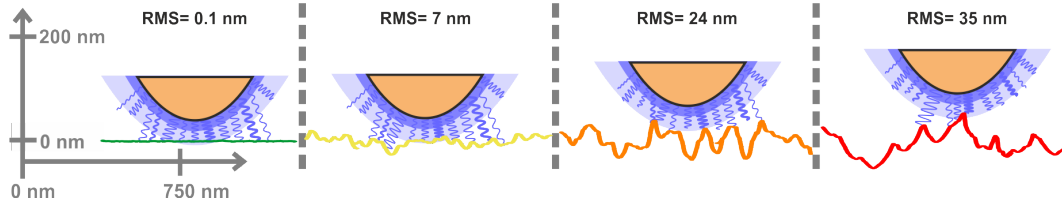
Figure 5: Sketch to illustrate the adhesion of *S. aureus* mediated by macromolecular tethering on the different rough surfaces (for details, see text). On the cell wall, only few proteins are shown, their density is in reality much higher (as symbolized by the blue shaded layer). All surfaces are represented by real AFM scan lines.

tify the consequences of this hypothesis on the adhesive strength of cells because the adhesion forces for single cells differ largely. This may indicate that the number of tethering molecules varies in every adhesion event and, thus, that their number may therefore not necessarily be reduced on a rougher substrate.

For the hydrophobic surfaces, in contrast, the hypothesis can be quantified using data from the Minkowski analysis. To do so, in Figure 6, the real surface area of the substrates is plotted in dependence of the distance from the top of the surface (defined by the highest surface structures). Data were normalized to the projected surface area[§].

Under the assumption that the reason for reduced adhesion is only the reduced accessible surface area, we can now quantitatively understand the reduced adhesion on rough hydrophobic surfaces (see Figure 3 b): on the surface with 7 nm RMS roughness, after about 30 nm from top, the accessible surface area is already at 100 % and and all cell wall macromolecules (with an average extension of 50 nm) responsible for adhesion can reach the surface and, therefore, the same adhesive strength is recorded as for the smooth wafer. Some cells even show a stronger adhesion than to the smooth surface. This observation can be explained by the fact that total surface area on the rough substrate is – for heights from top greater than 30 nm – larger than on the smooth wafer. Hence, cell wall macromolecules with an thermal extension of 50 nm can 'find' even more binding sites resulting in stronger adhesion. [43,44] For the surface with 24 nm RMS roughness,
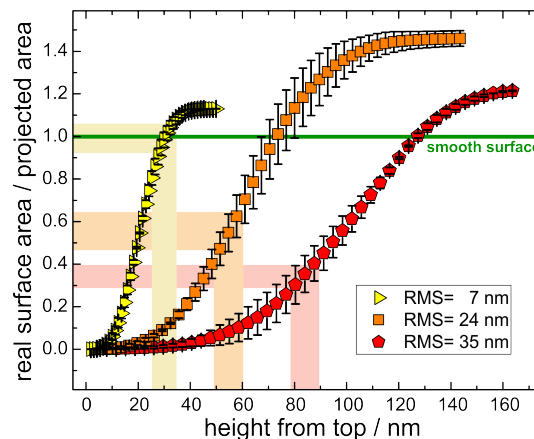
Figure 6: Averaged real surface area of the three roughened substrates normalized to the projected surface area. The light-colored horizontal rectangles are located at values corresponding to the relative decrease of adhesion forces on the rough hydrophobic surfaces (The middle of each rectangle indicates the mean value and the width corresponds the standard deviation of the adhesion force from Figure 3 b.) The vertical rectangles approximately indicate the corresponding distances from the overall maximum height of the surface.

[§]For a smooth wafer real surface area and projected surface area differ less than 1 % (as determined by AFM)

it shows that molecules with an extension of about 50 nm can access approximately 50 % of the projected surface area. Thus, these data nicely match the reduced adhesion force which is 56(18) % on this surface.

On the roughest surface, the accessible surface area and reduced adhesion force data cannot be connected that directly: Here, 38(11) % of the adhesion force measured on the flat surface was recorded, however, a matching percentage of the projected surface area is only reached at around 85 nm from the top of the sample. At first sight, 50 nm thermally extended proteins have, therefore, only access to a too small fraction of the projected surface area. Yet, analyzing the rough surface in more detail, it shows that the top 30 nm of surface consist of a very low number of fine peaks (3 peaks/μm^2 for the surface with 35 nm RMS roughness, for comparison: 57 peaks/μm^2 for the surface with 35 nm RMS roughness). For two reasons, these peaks can be neglected: i) due to their small number, the probability of the cell to come into contact with one of the peaks is low and if, then ii) a single peak will not deform the bacterium as a whole to prevent a further approach of the cell to the surface; rather, it will intrude into the outer proteinaceous cell wall layer,[72] which is reported to be in the range of 30 nm[46] for *S. aureus*.

In other words: on the roughest surface, the very few single peaks can be neglected since they are – if in contact to the cell at all – embedded in the 30 nm thick proteinaceous layer. Hence, from there, the proteins can extend additional 50 nm by thermal fluctuations to make contact to the surface. This matches well with the fact that at 80 nm from the top of the sample surface, around 35 % of the projected surface area are exposed.

This geometric interpretation of the results caused by tethering molecules of certain numbers and lengths is corroborated by our measurements showing a correlation between adhesive strength on the smooth surface and drop in adhesive strength on the two roughest surfaces (see Figure 4 c): stronger adhesion means that more molecules bind to the surface as compared to lower adhesion. Consequently, the more molecules bind, the higher is the probability that there are rather long molecules amongst them. According to the sketch in Figure 5, a higher surface roughness will not prevent the binding of these long molecules. This is exactly what the data in Figure 4 c show on the two roughest surfaces: the higher the adhesion force on the smooth surface (more molecules and, therefore, also more long molecules) the weaker is the drop in adhesive strength on the rough surfaces (because long molecules can 'overcome' this roughness). For the surface with 7 nm RMS roughness, this effect may not play a role because surface structures have a size that is already distinctly smaller than the average thermal extension of the macromolecules.

The geometric explanation becomes even clearer considering the data shown in Figure 4 a and b: cells that have high rupture lengths or snap-in separations on the smooth surface, also show rather high values on the roughened surfaces with a linear dependence between the respective values. This means that on average the same long molecules take part in adhesion on all surfaces.

The assumption of adhesion forces being determined by the number of tethering molecules can also help to explain the error bars in Figure 3 b). For hydrophobic surfaces, the standard deviation of adhesion forces increases with increasing surface roughness. This observation might be caused by two effects: i) the randomly roughed surfaces exhibit small differences in the exact surface topography for different positions on the sample. Therefore, also adhesion forces vary only slightly for different positions. ii) Thermal fluctuations and tethering of cell wall macromolecules are stochastic processes. Consequently, the numbers of individual binding sites scatter more strongly on rough surfaces compared to smooth surfaces because – in contrast to the smooth surface – on the rough surfaces, not every molecule is close to the surface at the same time.

Of note, the second effect seems to be especially relevant on the hydrophobic surfaces, where plenty of molecules participate in the adhesion process. On the hydrophilic surfaces, in contrast, this effect might be not very pro-

nounced because anyway only few molecules are involved in adhesion. This hypothesis might also explain that, on hydrophilic surfaces, as soon as a certain 'roughness threshold' ($R_q \approx$ 24 nm) is exceeded, a further increase in roughness does not change the adhesion force of the cells (see Figure 3 a).

Moreover, the effect that a certain roughness parameter has varying effects on adhesive strength for different cells can be explained assuming that different individual cells have a different macromolecular cell wall composition with differences in (average) extension lengths of the macromolecules: on the roughest hydrophobic surface, for example, the decrease in adhesion force for one cell is only 40 % while it is around 70 % percent for another individual (see Figure 3 b, cells no. 1 and no. 10). It could be speculated that a cell with the smaller decrease in adhesive strength possesses, on average, longer cell wall macromolecules than the other cell.

Viability on rough silicon surfaces

Table 2 shows the viability of bacterial cells after they were used in SCFS measurements (100 force-distance curves on the smooth and on the rough surface each) or in flow chamber experiments. On the hydrophilic surface, after SCFS, the percentage of killed cells increases with increasing surface roughness: it is zero on the smooth and least roughened surface and raises up to 100 % (6 out of 6 tested cells) dead cells on the roughest surface. In contrast, in the flow chamber experiments on the hydrophilic surface, the cells' viability is not influenced at all by the roughest surface.

On the hydrophobic surfaces, after SCFS measurements, the fraction of dead cells also increases with increasing surface roughness but to only a maximum of about 67 % on the roughest surface (4 out of 6 tested cells were found to be dead after measurement). In the flow chamber experiments with the hydrophobic surface, about 28 % of cells were killed by the roughest surface.

Interestingly, no correlation between the adhesion force (or the change in adhesion force)

and the viability of the corresponding cell can be observed in SCFS measurements (see Fig. 7 a). Accordingly, the characteristic shape of the force-distance curves on the hydrophobic surfaces did not change in the course of several measurements with cells that were found to be dead at the end of the experiment (see Fig. 7 b). In summary, it seems that the viability of a cell does not influence its adhesive strength on time scales up to one hour.
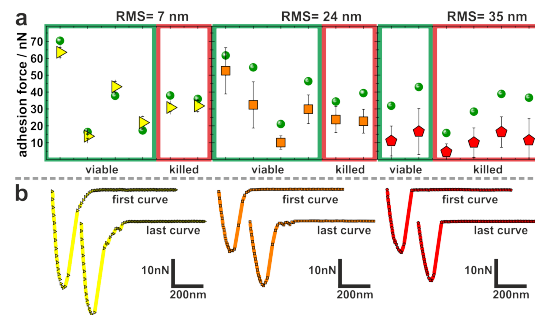
Figure 7: a) Adhesion forces of cells that were found to be viable/killed after SCFS measurements. b) First and last force-distance curves recorded on each rough surfaces with an exemplary cell that was found to be killed afterwards. To indicate measurements on surfaces of different roughnesses, the same color code as in Figure 3 is used.

In literature, the bactericidal property of rough surfaces is usually attributed to the penetration of the bacterial cell wall by 'spiky' structures on the substratum.[53,55,58,73] Hence, since the structures are the same in all experiments, viability data from SCFS and flow chamber measurements seem contradictory, on first sight (see Table 2): on the roughest hydrophilic surface, for instance, all tested cells were killed in the course of SCFS measurements whereas their viability was completely unaffected in flow chamber experiments.

However, it is important to note that – although the surfaces were the same in both types of experiments – there is at least one vital difference between SCFS and flow chamber measurements: in SCFS experiments, the cells are pressed to the surface by an external force (in our case, 300 pN), while in the flow chamber, the cells freely adsorb to the surface and the force with which they are 'pressed' to the sub-

Table 2: Fraction of killed cells by different types of experiments on hydrophilic and hydrophobic surfaces.

wettability	experiment	RMS			
		0.1 nm	7 nm	24 nm	35 nm
hydrophilic	SCFS	0 %	0 % (0/6) [b]	14 % (1/7) [b]	100 % (6/6) [b]
	flow chamber	0 %	—	—	0 %
hydrophobic	SCFS	0 %	33 % (2/6) [b]	33 % (2/6) [b]	67 % (4/6) [b]
	flow chamber	0 %	—	—	28(10) %

[a] The fraction of dead cells initially present in the bacterial solutions used ($\approx 5\,\%$) is already subtracted from the presented flow chamber values.

[b] The numerator of the fraction in brackets gives the number of dead cells and the denominator the total number of tested cells.

stratum is established by the cell itself through macromolecules that pull the cell in contact to the surface. This 'pulling force' is not necessarily related to the 'adhesion force', which is defined as the force needed to separate the cell from the surface.

Having this difference in mind, it is possible to explain the responses of the cells in terms of their viability as depicted in Figure 8: on the hydrophilic surface, the external force in the SCFS measurements seems sufficient for the spiky surface structures to penetrate the cell wall resulting in the death of the cell (as also seen in other studies [55,58,73]). In the flow chamber, in contrast, the 'pulling force' seems not strong enough to penetrate the cell wall by the surface structures and therefore cell death was not observed. On the hydrophobic sur-

Figure 8: Depiction to illustrate the influence of surface roughness on the viability of bacterial cells after SCFS and flow chamber measurements.

faces, the situation is different: the external force of the SCFS measurements and the cell-originated 'pulling force' in the flow chamber experiments seem to be in the same order of magnitude and cell death seems to be influenced only by the bacterial cell's individual cell wall properties (see Figure 8): on the hydrophobic surfaces, where many cell wall macromolecules participate in adhesion, the restoring force and stiffness of this macromolecular layer may be so 'strong' that it hinders the spiky surface structures to penetrate the cell wall (as also shown in another study using gram-positive cells [73]). Other cells, in contrast, may have a rather 'weak' and/or less dense cell wall macromolecular layer and can, therefore, be penetrated by the spiky structures. Since the adhesion force of an individual cell is not correlated to its viability after SCFS measurement (see Figure 7), it seems that a hypothetically more 'robust' cell wall macromolecular layer is not necessarily a more 'adhesive' layer.

Conclusions

In this study, we investigated the influence of nanoscaled surface roughness ($7(1)\,\text{nm} \leq \text{RMS} \leq 35(1)\,\text{nm}$) on the adhesive strength and viability of *S. aureus* cells. Thereto, we used two sets of silicon-based substrates with very different surface energies whose surfaces were roughened to different extents by etching for varying times. Using Minkowski functionals, it was shown that the surface structures were – besides their spatial dimensions – morphological identical. Adhesion

13

forces were determined by SCFS and viability by live/dead staining after SCFS and in a flow chamber setup.

Our results show that for both surface energies, the adhesive strength of bacterial cells decreases with increasing surface roughness as compared to their adhesion on smooth surfaces. Interestingly, this increase is less pronounced for individual cells with high adhesion on smooth surfaces. These results can be nicely explained by the macromolecular picture of bacterial adhesion: the adhesive strength is determined by the number of cell wall macromolecules that are able to tether to the surface. With increasing roughness, less of the molecules can reach the actual surface due to their finite length resulting in lower adhesive strength.

Furthermore, the influence of the roughness on the viability of bacteria in contact with these surfaces (freely 'self-adsorbed' or pressed onto the surface by AFM) was investigated. Similar to the adhesive strength, the percentage of viable bacterial cells on the surface decreases with increasing surface roughness.

For industrial and medical applications, where bacterial adhesion is to be prevented, our results can provide suggestions regarding surface roughness: while molecularly smooth surfaces or those with structures larger than the cells show relatively high adhesion, it is minimized on surface that feature structures in the same size range as the cell wall molecules of the bacteria. In addition, this size range also seems to be most effective for killing cells by contact with the structures. It should be mentioned that the observed influence of surface roughness on the adhesion of *S. aureus* cells can probably be transferred to other (gram-positive) bacteria. However, the exact range of surface roughness that best prevents adhesion depends on the length of the cell wall macromolecules and may, therefore, vary for different species.

Acknowledgements

References

(1) Nicolella, C.; Van Loosdrecht, M.; Heijnen, J. "Wastewater treatment with particulate biofilm reactors". *Journal of Biotechnology* **2000**, *80*, 1–33.

(2) Costerton, J. W.; Montanaro, L. "Bacterial Communications in Implant Infections: A Target for an Intelligence War". *The International Journal of Artificial Organs* **2007**, *30*, 757–763.

(3) Neut, D.; van der Mei, H. C.; Bulstra, S. K.; Busscher, H. J. "The role of small-colony variants in failure to diagnose and treat biofilm infections in orthopedics". *Acta Orthopaedica* **2007**, *78*, 299–308.

(4) Chew, B. H.; Lange, D. "Ureteral stent symptoms and associated infections: a biomaterials perspective". *Nature Reviews Urology* **2009**, *6*, 440.

(5) Callow, J. A.; Callow, M. E. "Trends in the development of environmentally friendly fouling-resistant marine coatings". *Nature Communications* **2011**, *2*, 244.

(6) Scardino, A. J.; de Nys, R. "Mini review: Biomimetic models and bioinspired surfaces for fouling control". *Biofouling* **2011**, *27*, 73–86.

(7) Simões, M.; Simões, L. C.; Vieira, M. J. "Species association increases biofilm resistance to chemical and mechanical treatments". *Water Research* **2009**, *43*, 229–237.

(8) Lieleg, O.; Caldara, M.; Baumgärtel, R.; Ribbeck, K. "Mechanical robustness of Pseudomonas aeruginosa biofilms". *Soft Matter* **2011**, *7*, 3307–3314.

(9) Laspidou, C. S.; Spyrou, L. A.; Aravas, N. "Material modeling of biofilm mechanical properties". *Mathematical Biosciences* **2014**, *251*, 11–15.

(10) Loskill, P.; Hähl, H.; Thewes, N.; Kreis, C. T.; Bischoff, M. "Influence of the Subsurface Composition of a Material on the Adhesion of Staphylococci". *Langmuir* **2012**, *28*, 7242–7248.

(11) Loskill, P.; Hähl, H.; Faidt, T.; Grandthyll, S.; Müller, F.; Jacobs, K. "Is adhesion superficial? Silicon wafers as a model system to study van der Waals interactions". *Advances in Colloid and Interface Science* **2012**, *179*, 107–113.

(12) Li, B.; Logan, B. E. "Bacterial adhesion to glass and metal-oxide surfaces". *Colloids and Surfaces B: Biointerfaces* **2004**, *36*, 81–90.

(13) Kao, W. K.; Gagnon, P. M.; Vogel, J. P.; Chole, R. A. "Surface charge modification decreases Pseudomonas aeruginosa adherence in vitro and bacterial persistence in an in vivo implant model". *The Laryngoscope* **2017**, *127*, 1655–1661.

(14) Spengler, C.; Thewes, N.; Nolle, F.; Bischoff, M.; Jacobs, K. "Adhesion of Staphylococcus aureus and its Mutants to Abiotic Surfaces of Different Surface Energies". *In preparation* **2018**,

(15) Lichter, J. A.; Thompson, M. T.; Delgadillo, M.; Nishikawa, T.; Rubner, M. F.; Van Vliet, K. J. "Substrata Mechanical Stiffness Can Regulate Adhesion of Viable Bacteria". *Biomacromolecules* **2008**, *9*, 1571–1578.

(16) Perera, D. "Studying the Influence of Surface Topography on Bacterial Adhesion using Spatially Organized Microtopographic Surface Patterns". *Langmuir* **2014**, *30*, 4633–4641.

(17) Hsu, L. C.; Fang, J.; Borca, D. A. "Effect of Micro- and Nanoscale Topography on the Adhesion of Bacterial Cells to Solid Surfaces". *Applied and Environmental Microbiology* **2013**, *79*, 2703.

(18) Lu, N.; Zhang, W.; Weng, Y.; Chen, X.; Cheng, Y.; Zhou, P. "Fabrication of PDMS surfaces with micro patterns and the effect of pattern sizes on bacteria adhesion". *Food Control* **2016**, *68*, 344–351.

(19) Hochbaum, A. I.; Aizenberg, J. "Bacteria Pattern Spontaneously on Periodic Nanostructure arrays". *Nano Letters* **2010**, *10*, 3717–3721.

(20) Scheuerman, T. R.; Camper, A. K.; Hamilton, M. A. "Effects of Substratum Topography on Bacterial Adhesion". *Journal of Colloid and Interface Science* **1998**, *208*, 23–33.

(21) Díaz, C.; Schilardi, P. L.; Salvarezza, R. C. "Nano/Microscale Order Affects the Early Stages of Biofilm Formation on Metal Surfaces". *Langmuir* **2007**, *23*, 11206–11210.

(22) Díaz, C.; Cortizo, M. C.; Schilardi, P. L.; Saravia, S. "Influence of the Nano-micro structure of the surface on bacterial adhesion". *Materials Research* **2007**, *10*, 11–14.

(23) Flint, S. H.; Brooks, J. D.; Bremer, P. J. "Properties of the stainless steel substrate, influencing the adhesion of thermo-resistant streptococci". *Journal of Food Engineering* **2000**, *43*, 235–242.

(24) Ivanova, E. P.; Truong, V. K.; Wang, J. Y.; Berndt, C. C. "Impact of Nanoscale Roughness of Titanium Thin Film Surfaces on Bacterial Retention". *Langmuir* **2009**, *26*, 1973–1982.

(25) Truong, V. K.; Rundell, S.; Lapovok, R.; Estrin, Y. "Effect of ultrafine-grained titanium surfaces on adhesion of bacteria". *Applied Microbiology and Biotechnology* **2009**, *83*, 925–937.

(26) Puckett, S. D.; Taylor, E.; Raimondo, T.; Webster, T. J. "The relationship between the nanostructure of titanium surfaces and bacterial attachment". *Biomaterials* **2010**, *31*, 706–713.

(27) Rizzello, L.; Sorce, B.; Sabella, S.; Vecchio, G.; Galeone, A.; Brunetti, V.; Cingolani, R.; Pompa, P. P. "Impact of Nanoscale Topography on Genomics and Proteomics of Adherent Bacteria". *ACS Nano* **2011**, *5*, 1865–1876.

(28) Ivanova, E. P.; Truong, V. K.; Webb, H. K.; Baulin, V. A. "Differential attraction and repulsion of Staphylococcus aureus and Pseudomonas aeruginosa on molecularly smooth

titanium films". *Scientific Reports* **2011**, *1*, 165.

(29) Wu, Y.; Zitelli, J. P.; TenHuisen, K. S.; Yu, X.; Libera, M. R. "Differential response of Staphylococci and osteoblasts to varying titanium surface roughness". *Biomaterials* **2011**, *32*, 951–960.

(30) Truong, V. K.; Pham, V.; Medvedev, A. "Self-organised nanoarchitecture of titanium surfaces influences the attachment of Staphylococcus aureus and Pseudomonas aeruginosa bacteria". *Applied Microbiology and Biotechnology* **2015**, *99*, 6831–6840.

(31) Gadelmawla, E.; Koura, M.; Maksoud, T.; Elewa, I.; Soliman, H. Roughness parameters. *Journal of Materials Processing Technology"* **2002**, *123*, 133–145.

(32) Crawford, R. J.; Webb, H. K.; Truong, V. K.; Hasan, J.; Ivanova, E. P. "Surface topographical factors influencing bacterial attachment". *Advances in Colloid and Interface Science* **2012**, *179*, 142–149.

(33) Singh, A. V.; Vyas, V.; Patil, R.; Sharma, V.; Scopelliti, P. E. "Quantitative Characterization of the Influence of the Nanoscale Morphology of Nanostructured Surfaces on Bacterial Adhesion and Biofilm Formation". *PLoS One* **2011**, *6*, e25029.

(34) Schröder-Turk, G. E.; Mickel, W.; Kapfer, S. C.; Klatt, M. A.; Schaller, F. M.; Hoffmann, M. J. F.; Kleppmann, N.; Armstrong, P.; Inayat, A.; Hug, D.; Reichelsdorfer, M.; Peukert, W.; Schwieger, W.; Mecke, K. "Minkowski Tensor Shape Analysis of Cellular, Granular and Porous Structures". *Advanced Materials* **2011**, *23*, 2535–2553.

(35) Schneider, R.; Weil, W. *"Stochastic and Integral Geometry (Probability and Its Applications)"*; Springer: Berlin, 2008.

(36) Hadwiger, H. *"Vorlesungen über Inhalt, Oberfläche und Isoperimetrie"*; Springer, Berlin, 1957.

(37) Mecke, K. "Integral Geometry and Statistical Physics". *International Journal of Modern Physics B* **1998**, *12*, 861–899.

(38) Jacobs, K.; Seemann, R.; Mecke, K. *Statistical Physics and Spatial Statistics*; Springer, 2000; pp 72–91.

(39) Mantz, H.; Jacobs, K.; Mecke, K. "Utilising Minkowski Functionals for Image Analysis". *Journal of Statistical Mechanics* **2008**, *12*, P12015.

(40) Schröder-Turk, G. E.; Kapfer, S.; Breidenbach, B.; Beisbart, C.; Mecke, K. "Tensorial Minkowski functionals and anisotropy measures for planar patterns". *Journal of Microscopy* **2010**, *238*, 57–74.

(41) Schröder-Turk, G. E.; Mickel, W.; Kapfer, S. C.; Schaller, F. M.; Breidenbach, B.; Hug, D.; Mecke, K. "Minkowski tensors of anisotropic spatial structure". *New Journal of Physics* **2013**, *15*, 083028.

(42) Göring, D.; Klatt, M. A.; Stegmann, C.; Mecke, K. "Morphometric analysis in gamma-ray astronomy using Minkowski functionals: Source detection via structure quantification". *Astrononmy & Astrophysics* **2013**, *555*, A38.

(43) Boyd, R. D.; Verran, J.; Jones, M. V.; Bhakoo, M. "Use of the atomic force microscope to determine the effect of substratum surface topography on bacterial adhesion". *Langmuir* **2002**, *18*, 2343–2346.

(44) Whitehead, K. A.; Rogers, D.; Colligon, J.; Wright, C.; Verran, J. "Use of the atomic force microscope to determine the effect of substratum surface topography on the ease of bacterial removal". *Colloids and Surfaces B: Biointerfaces* **2006**, *51*, 44–53.

(45) Preedy, E.; Perni, S.; Nipic, D.; Bohinc, K.; Prokopovich, P. "Surface Roughness Mediated Adhesion Forces between Borosilicate Glass and Gram-Positive Bacteria". *Langmuir* **2014**, *30*, 9466–9476.

(46) Thewes, N.; Thewes, A.; Loskill, P.; Peisker, H.; Bischoff, M.; Herrmann, M.; Santen, L.; Jacobs, K. "Stochastic binding of Staphylococcus aureus to hydrophobic surfaces". *Soft Matter* **2015**, *11*, 8913–9046.

(47) El-Kirat-Chatel, S.; Beaussart, A.; Derclaye, S.; Alsteens, D.; Kucharikova, S.; Van Dijck, P.; Dufrêne, Y. F. "Force

Nanoscopy of Hydrophobic Interactions in the Fungal Pathogen Candida glabrata". *ACS Nano* **2015**, *9*, 1648–1655.

(48) Formosa-Dague, C.; Fu, Z.-H.; Feuillie, C.; Derclaye, S.; Foster, T. J.; Geoghegan, J. A.; Dufrêne, Y. F. "Forces between Staphylococcus aureus and human skin". *Nanoscale Horizons* **2016**, *1*, 298–303.

(49) Aguayo, S.; Donos, N.; Spratt, D.; Bozec, L. "Single-bacterium nanomechanics in biomedicine: unravelling the dynamics of bacterial cells". *Nanotechnology* **2015**, *26*, 062001.

(50) Spengler, C.; Thewes, N.; Nolle, F.; Faidt, T. "Enhanced adhesion of Streptococcus mutans to hydroxyapatite after exposure to saliva". *Journal of Molecular Recognition* **2017**, e2615.

(51) Dufrêne, Y. F. "Microbial Nanoscopy: Breakthroughs, Challenges, and Opportunities". *ACS Nano* **2017**, *11*, 19–22.

(52) Spengler, C.; Thewes, N.; Jung, P.; Bischoff, M.; Jacobs, K. "Determination of the nano-scaled contact area of staphylococcal cells". *Nanoscale* **2017**, *9*, 10084–10093.

(53) Bhadra, C. M.; Truong, V. K.; Pham, V.; Al Kobaisi, M. "Antibacterial titanium nano-patterned arrays inspired by dragonfly wings". *Scientific Reports* **2015**, *5*, 16817.

(54) Hasan, J.; Webb, H. K.; Truong, V. K.; Pogodin, S. "Selective bactericidal activity of nanopatterned superhydrophobic cicada Psaltoda claripennis wing surfaces". *Applied Microbiology and Biotechnology* **2013**, *97*, 9257–9262.

(55) Ivanova, E. P.; Hasan, J.; Webb, H. K.; Truong, V. K. "Natural Bactericidal Surfaces: Mechanical Rupture of Pseudomonas aeruginosa Cells by Cicada Wings". *Small* **2012**, *8*, 2489–2494.

(56) Linklater, D. P.; De Volder, M.; Baulin, V. A.; Werner, M.; Jessl, S.; Golozar, M.; Maggini, L.; Rubanov, S.; Hanssen, E.; Juodkazis, S.; Ivanova, E. P. "High Aspect Ratio Nanostructures Kill Bacteria via Storage and

Release of Mechanical Energy". *ACS Nano* **2018**,

(57) Wang, X.; Bhadra, C. M.; Dang, T.; Buividas, R.; Wang, J. "A bactericidal microfluidic device constructed using nano-textured black silicon". *RSC Advances* **2016**, *6*, 26300–20306.

(58) Ivanova, E. P.; Hasan, J.; Webb, H. K.; Gervinskas, G.; Juodkazis, S.; Truong, V. K.; Wu, A. H.; Lamb, R. N.; Baulin, V. A.; Watson, G. S.; Watson, J. A.; Mainwaring, D. E.; Crawford, R. J. "Bactericidal activity of black silicon". *Nature Communications* **2013**, *4*, 2838.

(59) Pham, V.; Truong, V. K.; Quinn, M.; Notley, S. M.; Guo, Y. "Graphene Induces Formation of Pores That Kill Spherical and Rod-Shaped Bacteria". *ACS Nano* **2015**, *9*, 8458–8467.

(60) Bellion, M.; Santen, L.; Mantz, H.; Quinn, A.; Nagel, A.; Gilow, C.; Weitenberg, C.; Schmitt, Y. "Protein adsorption on tailored substrates: long-range forces and conformational changes". *Journal of Physics: Condensed Matter* **2008**, *20*, 404226.

(61) Doron-Mor, I.; Barkay, Z.; Filip-Granit, N.; Vaskevich, A.; Rubinstein, I. "Ultrathin Gold Island Films on Silanized Glass. Morphology and Optical Properties". *Chemistry of Materials* **2004**, *16*, 3476–3483.

(62) Koynov, S.; Brandt, M. S.; Stutzmann, M. "Black nonreflecting silicon surfaces for solar cells". *Applied Physics Letters* **2006**, *88*, 203107.

(63) Lessel, M.; Bäumchen, O.; Klos, M.; Hähl, H.; Fetzer, R.; Paulus, M.; Seemann, R.; Jacobs, K. "Self-assembled silane monolayers: an efficient step-by-step recipe for high-quality, low energy surfaces". *Surface and Interface Analysis* **2015**, *47*, 557–564.

(64) Thewes, N.; Loskill, P.; Jung, P.; Peisker, H.; Bischoff, M.; Herrmann, M.; Jacobs, K. "Hydrophobic interaction governs unspecific adhesion of staphylococci: a single cell force spectroscopy study". *Beilstein Journal of Nanotechnology* **2014**, *5*, 1501–1512.

(65) Beaussart, A.; Herman, P.; El, S. "Single-cell force spectroscopy of the medically important Staphylococcus epidermidis–Candida albicans interaction". *Nanoscale* **2013**, *5*, 10894–10900.

(66) Van Wagenen, R.; Andrade, J. "Flat plate streaming potential investigations: hydrodynamics and electrokinetic equivalency". *Journal of Colloid and Interface Science, volume=76, number=2, pages=305–314, year=1980, publisher=Elsevier*

(67) Streaming potential in the hydrodynamic entrance region of cylindrical and rectangular capillaries".

(68) Da, T. K. F.; Cohen-Steiner, D. *"CGAL User and Reference Manual*, 4.12 ed.; CGAL Editorial Board, 2018.

(69) Oh, J.; Yuan, H.-C.; Branz, H. M. "An 18.2%-efficient black-silicon solar cell achieved through control of carrier recombination in nanostructures". *Nature Nanotechnology* **2012**, *7*, 743–748.

(70) Ma, L. L.; Zhou, Y. C.; Jiang, N.; Lu, X.; Shao, J.; Lu, W. "Wide-band "black silicon" based on porous silicon". *Applied Physics Letters* **2006**, *88*, 171907.

(71) Quéré, D. "Rough ideas on wetting. *Physica A: Statistical Mechanics and its Applications"* **2002**, *313*, 32–46.

(72) Halperin, A.; Zhulina, E. "Atomic Force Microscopy of Polymer Brushes: Colloidal Versus Sharp Tips". *Langmuir* **2010**, *26*, 8933–8940.

(73) Pogodin, S.; Hasan, J.; Baulin, V. A.; Webb, H. K.; Truong, V. K. "Biophysical model of bacterial cell interactions with nanopatterned cicada wing surfaces". *Biophysical Journal* **2013**, *104*, 835–840.

SUPPORTING INFORMATION FOR

'Morphometric Quantification of the Influence of Substrate Nano-Roughness on Bacterial Adhesion and Viability'

Christian Spengler,[†] Friederike Nolle,[†] Johannes Mischo,[†] Samuel Grandthyll,[†] Nicolas Thewes,[†] Marcus Koch,[‡] Frank Müller,[†] Markus Bischoff,[¶] Michael A. Klatt,[§] and Karin Jacobs[*,†]

†*Department of Experimental Physics, Saarland University, 66041 Saarbrücken, Germany*
‡*Leibniz Institute for New Materials, 66041 Saarbrücken, Germany*
¶*Institute of Medical Microbiology and Hygiene, Saarland University, 66421 Homburg/Saar, Germany*
§*Institute of Stochastics, Karlsruhe Institute of Technology, 76131 Karlsruhe, Germany*

E-mail: k.jacobs@physik.uni-saarland.de
Phone: +49 (0)681 302 71777. Fax: +49 (0)681 302 71700

1

XPS spectrum of a roughened silicon surface
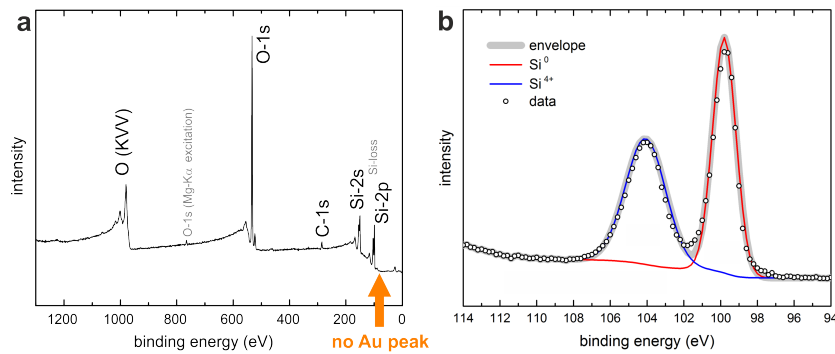
Figure S1: a): Overview spectrum of a roughened surface after cleaning with aqua regia: since there is no Au peak detectable at an energy of 84 eV, the gold layer was completely removed by the acid. b): XPS data (open circles) of a roughened surface (270 s in fluoric acid). The natural Si^0 line is shown in red and the natural Si^{4+} line is shown in blue. The ratio of their intensities is used to calculate the oxide layer thickness.[1]

Figure S1 shows the XPS data of the Si-2p core level of a (exemplary) roughened substrate with both peaks assigned to Si^0 contributions from the bulk and Si^{4+} contributions from the oxide layer. Comparing the intensities of both contributions it is straightforward to estimate the thickness of the oxide layer to be 3.2–4.0 nm. However, it has to be noted that these values have to be considered as an upper limit, since the Si^{4+} contribution is overestimated in the experiment on a rough surface.

Due to the high surface sensitivity in XPS, only a thickness of about 1–2 nm is probed and the surface sensitivity increases with increasing the polar angle (i. e. the angle between the surface normal and the direction of the emission of the photoelectrons). For a rough surface, the surface normals of local surface areas are distributed over a wide range (if compared to a smooth Si wafer) and, therefore, a large part of the overall surface is probe with enhanced surface sensitivity, causing an increased Si^{4+} contribution.

As a consequence, the thickness of the oxide layer of about 3.2–4.0 nm, as probed in experiments on a rough surface, does not really differ from the thickness of about 1.7 nm,[1] as probed in experiments on a smooth Si wafer and it is not expected that bacterial adhesion is much affected by the difference in the thickness of the oxide layer.[2]

2

Exemplary Visualization of the Minkowski functionals
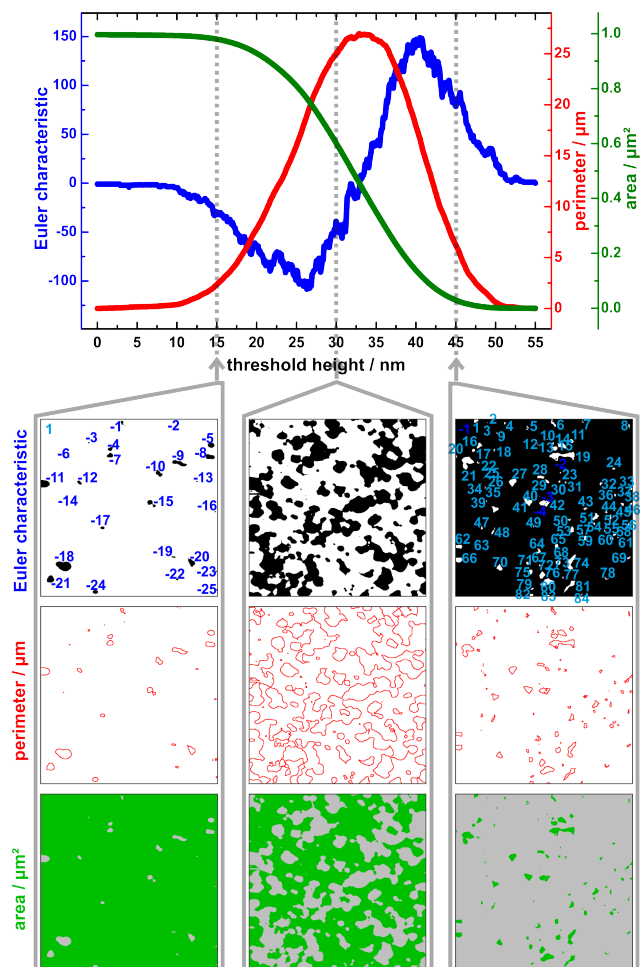
Figure S2: Visualization of the Minkowski functionals for an AFM topography scan of an etched Si wafer (7 nm RMS roughness) for three different threshold heights (15 nm, 30 nm, 45 nm). (In the middle panel of the Euler characteristic, no numbers are given for reasons of clarity.)

3

Not normalized Minkowski functionals of the roughened surfaces
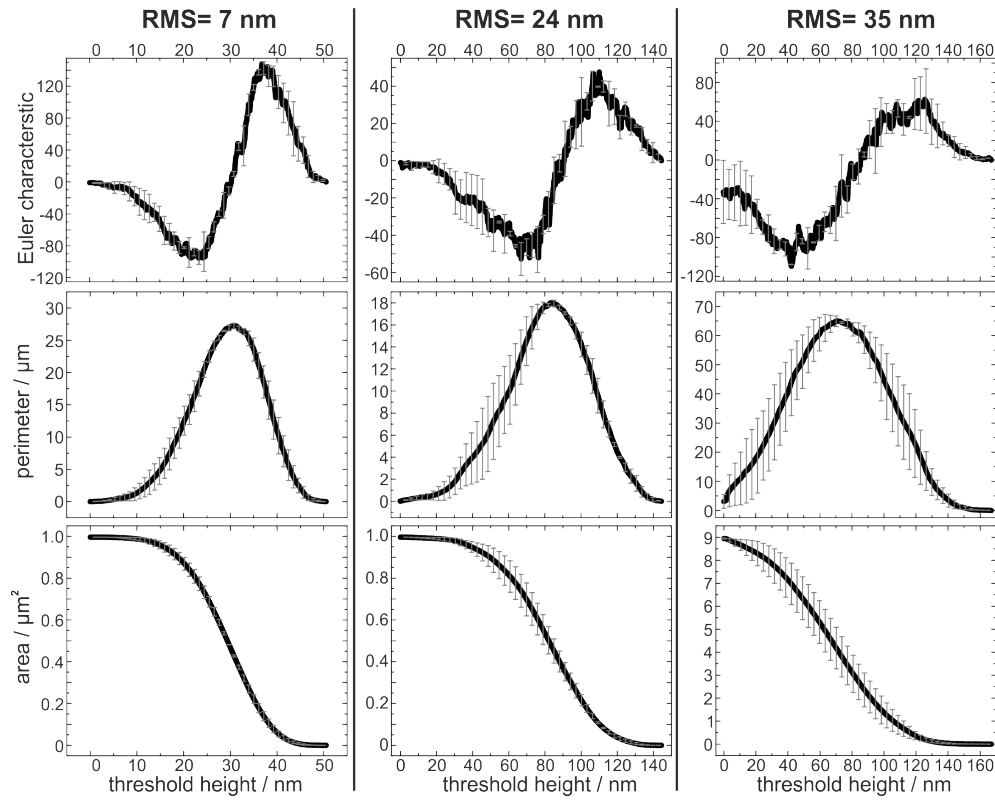
Figure S3: Minkowski functionals in dependence of the threshold height for all surfaces (averaged over different surfaces of the same etching time).

4

Not normalized adhesion forces on rough hydrophobic silicon
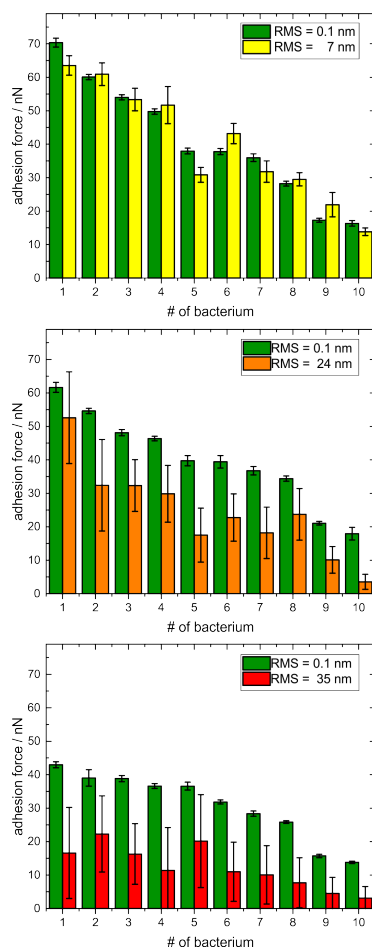
Figure S4: Adhesion forces of 3×10 *S. aureus* cells to hydrophobic silicon of different roughness. With each cell, 200 force-distance curves were taken: first 50 force-distance curves on the smoothest surface, then 50 on one of the rough surface, then again 50 curves on the smooth surface, and again 50 curve on the rough surfaces. The forces on the smooth and rough surfaces are shown as green and yellow/orange/red bars, respectively

5

Force-dependencies on hydrophilic surfaces
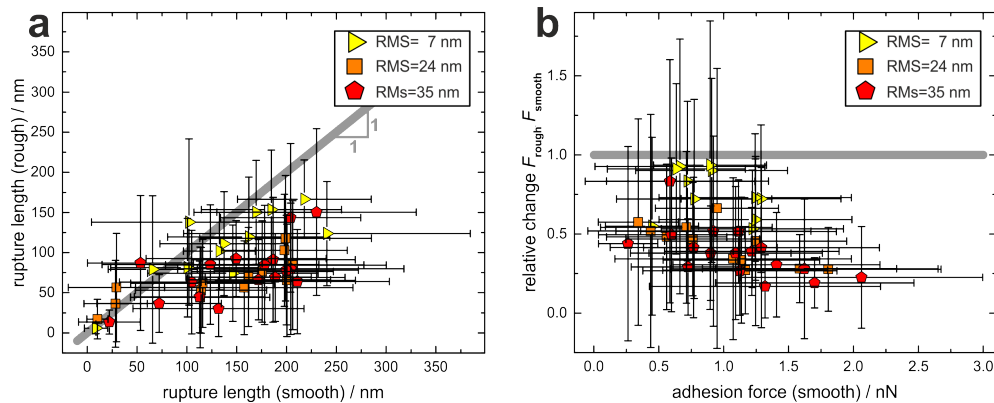
Figure S5: a) Mean rupture length of every tested cell on the rough hydrophilic surfaces in dependence of their value on the smooth hydrophilic surface. b) Relative change of the adhesion force on the rough hydrophilic surfaces in dependence of the adhesion force on the smooth hydrophilic surface.

References

(1) Loskill, P.; Hähl, H.; Faidt, T.; Grandthyll, S.; Müller, F.; Jacobs, K. "Is adhesion superficial? Silicon wafers as a model system to study van der Waals interactions". *Advances in Colloid and Interface Science* **2012**, *179*, 107–113.

(2) Loskill, P.; Hähl, H.; Thewes, N.; Kreis, C. T.; Bischoff, M. "Influence of the Subsurface Composition of a Material on the Adhesion of Staphylococci". *Langmuir* **2012**, *28*, 7242–7248.

6

Addendum VI – Engineered 2D and 3D Spider Silk Materials With Intrinsic Bacteriostatic and Fungistatic Properties

Authors: G. Lang[1,2,3], S. Kumari[1], E. Desimone[1], C. Spengler[4], S. Lücker[5], M. Hudel[5], K. Jacobs[4], N. Krämer[5] and T. Scheibel[1,3,6,7,8,9]

[1] Chair of Biomaterials, Faculty of Engineering Science, University of Bayreuth, 95447 Bayreuth, Germany.
[2] Biopolymer Processing Group, Faculty of Engineering Science, University of Bayreuth, 95447 Bayreuth, Germany.
[3] Bayreuth Center for Material Science and Engineering (BayMAT).
[4] Department of Experimental Physics, Saarland University, 66041 Saarbrücken, Germany
[5] Medical Center for Dentistry, Department of Paediatric Dentistry, Medical Center Gießen and Marburg, Justus-Liebig University Gießen, 35392 Gießen, Germany
[6] Institute of Medical Microbiology, Justus-Liebig University Gießen, 35392 Gießen, Germany
[7] Bayreuth Center for Colloids and Interfaces (BZKG)
[8] Bayreuth Center for Molecular Biosciences (BZMB)
[9] Research Center for Bio-Macromolecules (BIOmac), 95440 Bayreuth, Germany

Author contributions:
*G. L. and S. K. contributed equally to this work. G. L. prepared films (smooth and patterned), prepared protein coated silanized glass slides, performed SEM and analyzed the data. S. K. performed the in vitro bacteriostatic/fungistatic experiments and coculture experiments with E. coli and P. pastoris. E.D. assisted in the designing of coculture experiments. S. L., M. H. & N. K. carried out in vitro experiments of S. mutans and C. albicans. **C. S.** & K. J. prepared bacterial probes and performed force distance measurements. T. S. designed the experiments and supervised the project. S. K. and G. L. wrote the manuscript. E .D., **C. S.**, K. J. and T. S. contributed to writing and editing of the manuscript.*

Abstract - Antimicrobiotics resistant strains are a major problem in health care and are increasing at an alarming rate due to the overuse of antimicrobial agents. Advanced materials are within the focus that selectively inhibit microbial growth but not actively kill microbes, while simultaneously being non-toxic to and biocompatible with mammalian cells. 2D-films and 3D-hydrogels made of recombinantly produced spider silk proteins enable selectively mammalian cell attachment and proliferation but inhibit pathogenic bacteria as well as fungi adhesion without the need of further additives. Together with their mechanical features, lack of immunogenicity and adjustable biodegradability, recombinant spider silk-based materials provide an excellent prospect for the development of a new generation of bio-selective microbial-resistant materials, used as a coating material in biomedical but also technical applications.

Engineered 2D and 3D spider silk materials with intrinsic bacteriostatic and fungistatic properties

1

2

3   *Gregor Lang[1,2,3,4], Sushma Kumari[1,4], Elise Desimone[1], Christian Spengler[5], Susanne Lücker[6],*

4   *Martina Hudel[7], Karin Jacobs[5], Norbert Krämer[6] and Thomas Scheibel[1,3, 8, 9, 10, 11, *]*

5   [1]Chair of Biomaterials, Faculty of Engineering Science, University of Bayreuth, [3]Bayreuth

6   Center for Material Science and Engineering (BayMAT), [8]Bavarian Polymer Institute (BPI),

7   [9]Bayreuth Center for Colloids and Interfaces (BZKG), [10]Bayreuth Center for Molecular

8   Biosciences   (BZMB),   and   [11]Research   Center   for   Bio-Macromolecules   (BIOmac),

9   Universitätsstraße 30, 95440 Bayreuth, Germany

10   [2]Biopolymer Processing Group, Faculty of Engineering Science, University of Bayreuth,

11   Ludwig-Thoma-Straße 36A, 95447 Bayreuth, Germany

12   [5]Department of Experimental Physics, Saarland University, 66041 Saarbrücken, Germany

13   [6]Medical Center for Dentistry, Department of Paediatric Dentistry, Medical Center Gießen and

14   Marburg, Justus-Liebig University Gießen, Schlagenzahl 14, 35392 Gießen, Germany

15   [7]Institute of Medical Microbiology, Justus-Liebig University Gießen, Schubertstraße 81, 35392

16   Gießen, Germany

17   [4]Gregor Lang and Sushma Kumari contributed equally to this work.

18

19

Abstract

Antimicrobiotics resistant strains are a major problem in health care and are increasing in number at an alarming rate due to the overuse of antimicrobial agents. Advanced materials are within the focus that selectively inhibit microbial growth but not actively kill microbes, while simultaneously being non-toxic to and biocompatible with mammalian cells. 2D-films and 3D-hydrogels made of recombinantly produced engineered spider silk proteins enable selectively mammalian cell attachment and proliferation but inhibit pathogenic bacteria as well as fungi adhesion without the need of further additives. Together with their mechanical features, lack of immunogenicity and adjustable biodegradability, recombinant spider silk-based materials provide an excellent prospect for the development of a new generation of bio-selective microbial-resistant materials, used as a coating material in biomedical but also technical applications.

33 **Introduction**

34   Pathogenic microbial contaminations on any kind of surface and the associated risk of

35 infection are severe problems, especially in the public health care sector.[1, 2] Infections are also

36 induced by food contamination and biofouling of material's surfaces in contact with water

37 supply systems.[3] Microbial colonization and subsequent biofilm formation are highly

38 problematic, as biofilms are much more difficult to eradicate than isolated microbes.[4]

39 Consequently, microbial biofilm generation and nosocomial infection during conventional

40 medical therapy have significantly increased mortality as well as healthcare costs worldwide. For

41 example, surface microbial infestation on biomedical devices such as prosthetics devices,

42 medical implants, contact lenses, and catheters limits their functionality and lifetime and can

43 cause life-threatening infections.[5, 6] New multidrug-resistant microorganisms, which have

44 adapted to the over-use of antimicrobial agents, further complicate the problem.[7, 8] Therefore,

45 biomaterials, which have inherent non-fouling features to prevent the growth of pathogenic

46 microorganisms would provide new opportunities of long-term protection, especially when they

47 can be used as surface coating materials for already existing products.

48   Since one critical step in biofilm formation is the initial adherence of pathogenic

49 microbes onto a material's surface,[9, 4] inhibiting microbial attachment is a favorable approach to

50 develop material surfaces resistant to biofilm formation.[10, 11] There are two main approaches for

51 inhibiting surface attachment, referred to as either active or passive resistance. While passively

52 resistant surfaces utilize super hydrophilic or hydrophobic polymers, zwitterionic and other

53 synthetic polymers,[12, 13] actively resistant ones include "contact killing" materials such as

54 cationic polymers, amphiphilic polymers, antimicrobial peptides and polymeric/composite

55 materials loaded with antimicrobial agents.[14 - 17]

56   Although these approaches can combat microbial infection by inhibiting mechanisms of

57   persistence and adaptation, several drawbacks exist such as instability under physiological

58   conditions, cytotoxicity to mammalian cells, inflammatory responses, a narrow antimicrobial

59   spectrum, and implication for transmitting multidrug resistance.[18] Furthermore, antimicrobial

60   activity has been mostly investigated in terms of its effectiveness against bacteria, although

61   fungal infections also contribute significantly to patient morbidity and mortality. Moreover,

62   fungal infections can readily form polymicrobial biofilms with enhanced resistance to antifungal

63   drugs, further limiting therapeutic options.[19] Therefore, efficient mitigation of microbial

64   infection associated with both bacteria and fungi is required for the future development of broad-

65   range multifunctional material coatings.

66   Exhibiting extraordinary mechanical properties surpassing the toughness of synthetic

67   polymer fibers and simultaneously displaying excellent biocompatibility, spider silk is known to

68   be a biomaterial for miscellaneous applications.[20, 21] Remarkably, most spider silk webs

69   withstand microbial omnipresence and remain resistant to microbial decomposition for years,

70   irrespective of environmental impacts such as humidity, temperature, and location, though being

71   composed of proteins and therefore of amino acids, which would be a valuable source of

72   nutrition for microbes. Only few studies have been published examining antimicrobial effects of

73   natural spider silk,[22] but the underlying mechanism remained ambiguous, owing to the composite

74   characteristics of silk fiber surfaces i.e., consisting of different spidroins, glycoproteins and

75   lipids.[23]

76   In this study, 2D and 3D materials based on well-established recombinant spider silk

77   proteins were found to withstand microbial infestation. The engineered *Araneus diadematus*

78   fibroins 3 and 4 (eADF3 and eADF4), based on the consensus sequence of the core domains of

79   fibroin 3 or 4, respectively, originating from the dragline silk of the European garden spider

80   *Araneus diadematus.*[24, 25] Biotechnological production enables the design of different spider silk

81   protein variants with adjustable molecular weight by simply varying the number of motive

82   repeats within the core sequence or by the addition of naturally occurring non-repetitive termini.

83   Henceforth, molecular weight and chemical properties of the proteins can be efficiently tailored,

84   e.g., eADF4(C16) with 47.7 kDa, eADF4(C32NR4) with 104 kDa (containing a C-terminal

85   assembly domain) , and eADF3((AQ)12) with 48 kDa, which have all been used in this study for

86   comparison.

87   Materials made of eADF4(C16) display interesting properties such as biocompatibility,

88   mechanical toughness, absence of toxicity, lack of immune reactivity and slow biodegradation.[26]

89   [- 28] Since eADF4(C16) like most spider silk proteins lack cell binding motifs, eADF4(C16)

90   coated implants and catheters display a significantly reduced adhesion and proliferation of

91   fibroblasts.[29, 30] When transplanted *in vivo* in rabbits, eADF4(C16) coated silicone implants

92   displayed a significant reduction in capsular fibrosis.[29] However, cell attachment can be

93   promoted by generating defined surface topographies such as in surface-structured silk films.[31]

94   Non-woven mats generated from eADF4(C16) showed also good cell adhesion and proliferation

95   due to the increased surface area and rougher topography.[32] Alternatively, genetically modifying

96   eADF4(C16) with the cell binding motif RGD promoted also mammalian cell adhesion and

97   proliferation with good cell viability.[33, 34] Strikingly, we detected that even without sterilization

98   surfaces of materials based on these recombinant spider silk proteins were free of microbes.[33, 34]

99   **Bacteriostatic and fungistatic properties of eADF spider silk films**

100   To systematically investigate the absence of microbes and the putative bacteriostatic and

101   fungistatic properties of spider silk surfaces, films of the recombinant spider silk proteins with

102 negatively charged eADF4(C16) and eADF4(C32NR4), and uncharged eADF3((AQ)12) were

103 fabricated to test the influence of molecular weight, net charge and the presence of a terminal

104 assembly domain (**Table. 1**). All recombinant spider silk proteins were cast into flat as well as

105 micro-patterned (2 µm wide grooves, 1 µm wide and 4 µm high ridges) films to simultaneously

106 investigate the influence of surface topography, which has previously been shown to influence

107 mammalian cell attachment and proliferation on such spider silk surfaces.[31] Regenerated *Bombyx*

108 *mori* (*B. mori*) fibroin, representing a silk produced by insects, and poly(caprolactone) (PCL), as

109 a synthetic polymer used in biomaterials applications, were used as controls. Suspended

110 cariogenic *S. mutans* as well as pathogenic *C. albicans* were seeded on top of all smooth and

111 patterned films for 12 h at 37 °C. After washing to remove non-adherent pathogens, films were

112 air dried for microscopic analysis of microbial growth. SEM images clearly showed that both,

113 smooth and patterned eADF films significantly restricted the attachment, growth and microbial

114 colonization of *S. mutans* as well as *C. albicans* independent of the molecular weight, charge or

115 presence of the terminal domain of the recombinant spider silk proteins (**Fig. 1 (A-i) – (A-iv),**

116 **(B-i) - (B-iv)** and **(C-i) - (C-iv)**). This finding can have far-reaching impact on future

117 applications, since *C. albicans* is an opportunistic common fungal pathogen found in hospitals

118 and is known to be highly infectious and life threatening. In addition, our results clearly

119 demonstrated that surface topography does not influence microbial attachment in case of spider

120 silk materials since they couldn't attach to the patterned surface. The finding was surprising

121 since the grooves were expected to provide optimal niches for bacterial and fungal attachment. *E.*

122 *coli* and *P. pastoris* as additional examples were also tested and could not attach to both smooth

123 and patterned eADF4(C16) films (**Fig. SI 1-2**). As expected, films made of regenerated *B. mori*

124 fibroin and PCL displayed severe microbial infestation (**Fig. 1 (D-i) - (D-iv)** and **(E-i) – (E-iv)**).

125   The results are interesting, since both *B. mori* fibroin and recombinant spider silk proteins

126   comprise similar repetitive amino acid sequences yielding comparable structural features.

127   However, the microbe-repellent properties of these different silks seem to be as distinct as their

128   mechanical features and their surface characteristics.
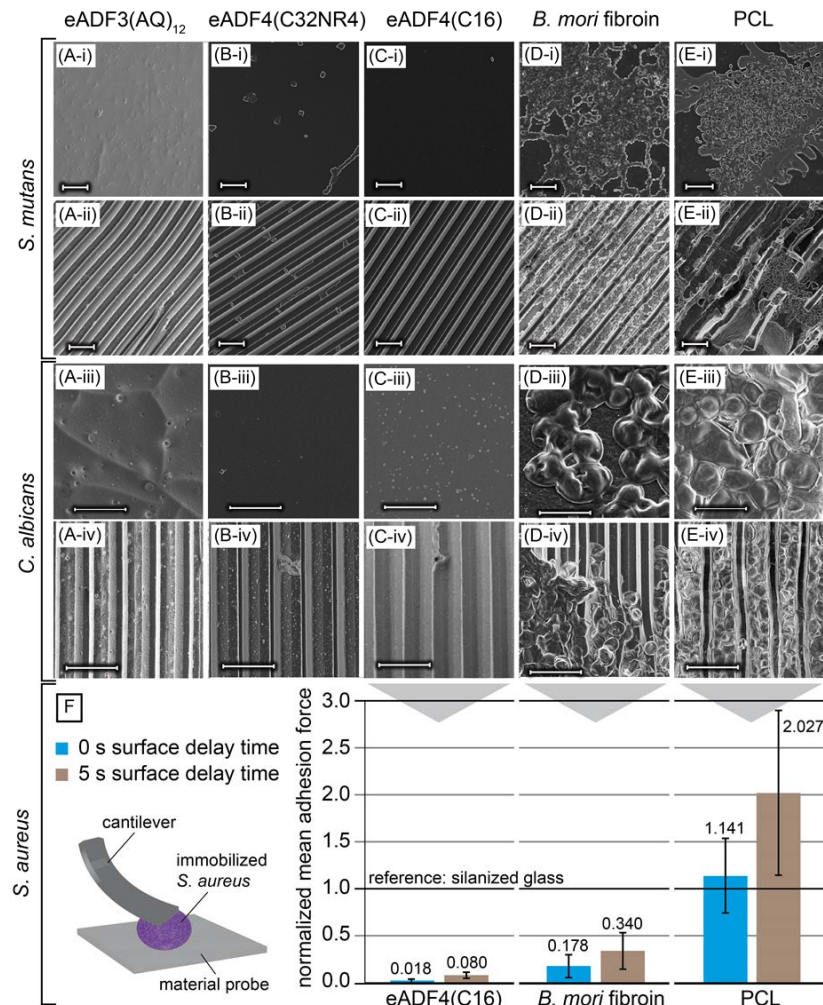
129

130   **Fig. 1: Bacteriostatic and fungistatic properties of films made of recombinant spider silk**
131   **proteins.** SEM images showing (i & iii) plane and (ii & iv) micro patterned surfaces of (A)
132   eADF3((AQ)12); (B) eADF4(C32NR4); (C) eADF4(C16); (D) *B. mori* fibroin; and (E) PCL
133   after 12 h of incubation with (i & ii) *S. mutans* and (iii & iv) *C. albicans* at 37 °C. Growth and

134   microbial colonization on smooth and patterned films of recombinant spider silk proteins is
135   significantly restricted. Scale bars = 5 μm. Adhesion force measurements using single *S. aureus*
136   probes on silanized glass coated with eADF4(C16), *B. mori* fibroin and PCL; (F) Representative
137   normalized mean adhesion forces were obtained from 25 force-distance curves performed on
138   each surface for 0 s (blue) as well as 5 s (brown) surface delay time using one and the same cell
139   immobilized on a cantilever with a nominal spring constant of 0.03 N m^{-1}. Forces were referred
140   to the values measured on uncoated silanized glass (4.8 ± 2.4 nN). It was found that all
141   distributions of adhesion forces were significantly different with p values below 0.001.

142   To elucidate whether bacterial adhesion is inhibited at contact or if bacteria can adhere

143   but subsequently dissociate due to insufficient growth conditions, the forces involved in bacterial

144   adhesion were quantified by atomic force microscopy (AFM) in force spectroscopy mode using

145   single cell bacterial probes.[35, 36] Methicillin-resistant *Staphylococcus aureus* strain (MRSA) is a

146   widespread problem in hospitals and is a highly infectious pathogen responsible for numerous

147   fatalities worldwide. A single *S. aureus* cell was immobilized on a tipless AFM cantilever and

148   pressed with a maximum force of 300 pN onto silanized glass slides coated with eADF4(C16)

149   which was used for all the following studies, since it is the best characterized recombinant spider

150   silk variant with already used for biomedical application[29, 30] and was compared to surfaces of *B.*

151   *mori* fibroin and PCL. Direct contact was allowed for some microseconds (termed 0 s in the

152   following) or 5 s of additional surface delay time before the single bacterium was lifted and the

153   adhesion force F_{ad} measured. Then, the normalized mean adhesion force was determined (F_{ad}

154    $_{(bacteria)}$ / adhesion force on uncoated silanized glass $F_{ad\ (glass)}$). Therein, the microbe-repellent

155   property of eADF4(C16) spider silk films could be confirmed as an extremely low bacterial

156   adhesion force was measured (**Fig. 1 F**). The initial adhesive force at 0 s was significantly higher

157   for *B. mori* fibroin (factor ~10) and dramatically higher for PCL (factor ~63) in comparison to

158   that of eADF4(C16). At a surface delay time of 5 s, the adhesive forces increased in all cases, but

159   still adhesion forces on eADF4(C16) films were significantly lower than on the other materials.

160   These results clearly indicate, that eADF4(C16) materials surfaces do not allow efficient

161 adhesion of *S. aureus*, an observation that is complementary to the qualitative results of the

162 growth study using *S. mutans* and *C. albicans*.

163 A possible explanation for the low attachment of microbial cells is the inherent property

164 of spider silk surfaces to inhibit unspecific protein adhesion, a phenomenon that was already

165 shown in context of silicone implant coatings.[29, 30] Further, negative charge and increased surface

166 hydrophilicity are also known to repel bacteria and fungi.[37, 38] However, ADF3((AQ)12) has no

167 surface charge indicating it is probably an intrinsic structural feature of the surface providing

168 bacteriostatic and fungistatic properties. The results obtained for eADF4 films and coatings show

169 that microbial repellants can be directly attributed to the physicochemical properties of the

170 underlying spider silk protein, and interestingly no additional components such as glycoproteins

171 or lipids or antimicrobial agents (often found in natural spider silk) are necessary. To the best of

172 our knowledge, this is a completely new finding that will open the door for novel applications of

173 spider silk materials e.g. as coatings in various biomedical applications.

174 Then it was investigated whether these bacteriostatic and fungistatic properties are restricted to

175 the surface of spider silk films or if they are generic, i.e. a feature that can also been found on

176 surfaces of other spider silk morphologies such as hydrogels. eADF4 spider silk proteins can be

177 processed into shear thinning hydrogels[34] that can be 3D printed, and one possible application is

178 their use in tissue regeneration. Therefore, bacteriostatic and fungistatic properties would

179 complement the recently observed biocompatibility, non-toxicity and biodegradability properties

180 of recombinant spider silk hydrogels[26 – 28] and would boost their applicability in different

181 biomedical applications.

182 **Bacteriostatic and fungistatic properties of eADF4 spider silk hydrogels**

183   To monitor their bacteriostatic and fungistatic properties, eADF4(C16) hydrogels were

184   incubated with *E. coli* and *P. pastoris* for 12 h at 37 °C. As a control, hydrogels of regenerated *B.*

185   *mori* fibroin[39] and gelatin[40] as a further control of a commonly used biomaterial were incubated in

186   an identical manner.
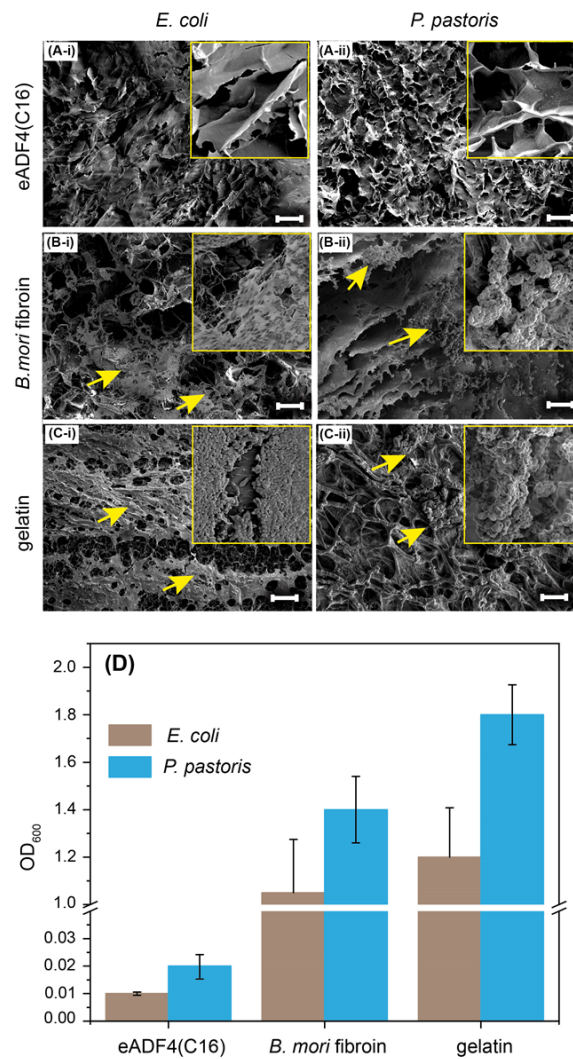
187

188 **Fig. 2: Bacteriostatic and fungistatic properties of hydrogels made of eADF4(C16) protein.**
189 SEM images of hydrogels prepared from (A) eADF4(C16), (B) *B. mori* fibroin and (C) gelatin
190 after 24 h of incubation with (i) *E. coli* and (ii) *P. pastoris,* magnification 500X. Scale bars = 20

191 μm. The insets are images with higher magnification 1500X. (A) eADF4(C16) hydrogels showed
192 no biofilm formation and growth of *E. coli* and *P. pastoris*; (B) *B. mori* fibroin and (C) gelatin
193 hydrogels were loaded with bacteria and fungi cells on the surfaces and within the pores. The
194 arrows indicate microbial colonization on hydrogels of *B. mori* fibroin and gelatin. (D) Optical
195 density of *E. coli* and *P. pastoris* in liquid cultures at 600 nm (OD$_{600}$) after 12 h incubation with
196 microbial inoculated hydrogels of eADF4(C16), *B. mori* fibroin and gelatin at 37 °C. Each result
197 is an average of three experiments, and the error bars designate the standard deviation.
198

199   Subsequently, all hydrogels were washed carefully to remove non-adherent bacteria.

200 SEM images of lyophilized hydrogels clearly indicated that bacteria and fungi were incapable of

201 adhering and growing on and within recombinant spider silk hydrogels (**Fig. 2 A**). In contrast, *B.*

202 *mori* fibroin and gelatin hydrogels enabled *E. coli* and *P. pastoris* cells to adhere and colonize, as

203 visualized by SEM images (**Fig. 2 B – C**). In both materials superficial microbial biofilms could

204 clearly be detected. Next, microbial inoculated hydrogels were incubated in fresh media and

205 microbial growth was measured therein after 12 h. No microbial growth was observed in liquid

206 cultures incubated with eADF4(C16) hydrogels (**Fig. 2 D**).

207 **Bio-selective properties of spider silk films and hydrogels**

208   The identified bacteriostatic and fungistatic properties of the spider silk materials are

209 obviously different to the previously determined controllable adhesion of mammalian cell lines.

210 Therefore, we wanted to elucidate whether it is possible to trigger a bio-selective behavior,

211 which represses the growth of microbes but enforces mammalian cell attachment and

212 proliferation. It was necessary to use a genetically modified variant of eADF4(C16) containing

213 the cell binding motif RGD, which interacts with integrin receptors of mammalian cells

214 promoting mammalian cell attachment on spider silk films.[33] Importantly, all other

215 physicochemical characteristics of this variant are indistinguishable to that of eADF4(C16)

216 including significant bacteriostatic and fungistatic properties to resist biofilm formation.

217 BALB/3T3 fibroblast cells were seeded on eADF4(C16)-RGD films prepared in cell culture

218 plates and allowed to adhere overnight, followed by incubation with *E. coli* and *P. pastoris* cells

219 for 6 h to mimic a situation similar to that of a post-operative infection (**Fig. 3 A**).
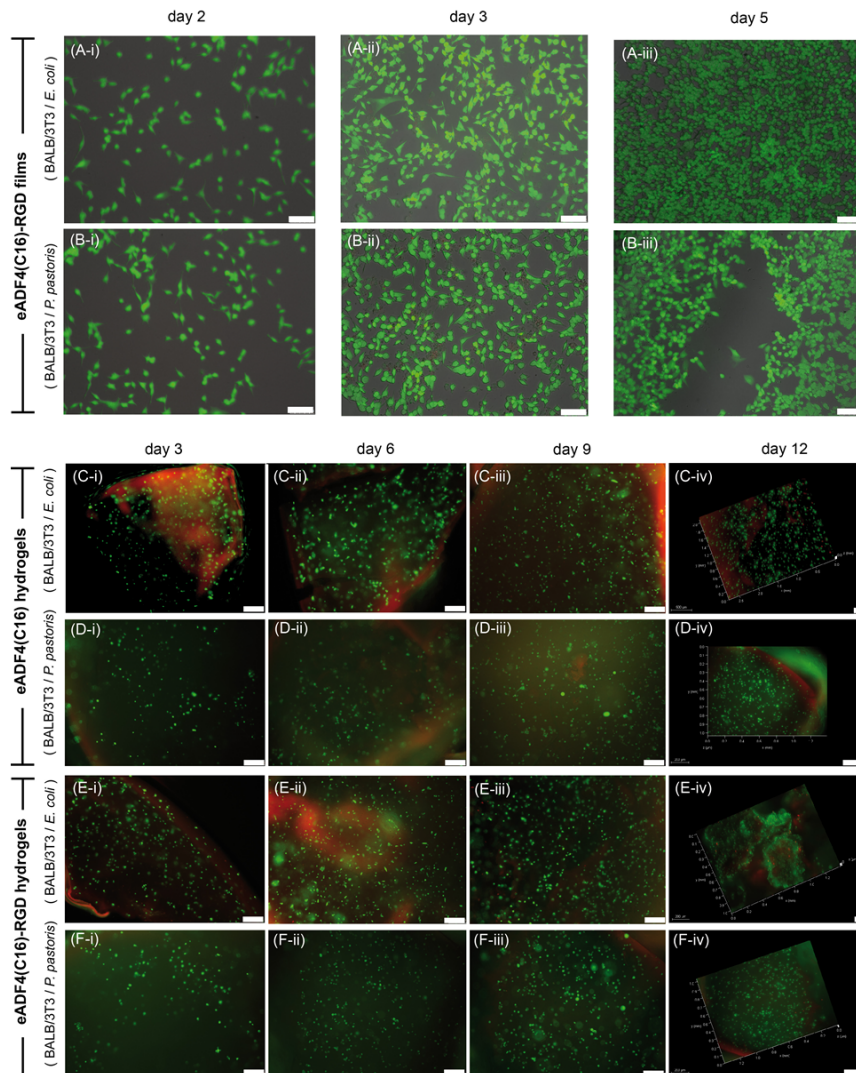
220

221 **Fig. 3: Bacteriostatic and fungistatic properties of spider silk scaffolds in co-culture of**
222 **microbes and mammalian cells.** eADF4(C16)-RGD films were incubated with BALB/3T3
223 fibroblasts for 12 h and then seeded with bacteria/fungi for 6 h. Fluorescence images of co-
224 cultures on eADF4(C16)-RGD films with (A) *E. coli* and (B) *P. pastoris* after (i) 2 days, (ii) 3
225 days and (iii) 5 days. Scale bars = 250 μm. Fluorescence images of (C and D) eADF4(C16) and

226 (E and F) eADF4(C16)-RGD hydrogels encapsulated with BALB/3T3 fibroblast cells and co-
227 culturing with (C and E) *E. coli* and (D and F) *P. pastoris* (on top of hydrogels) for (i) 3 days, (ii)
228 6 days, (iii) 9 days and (iv) 12 days. Scale bars = 250 µm. The cells were stained with calcein
229 A/M (live cells: green) and ethidium homo dimer (dead cells: red). Fluorescence microscopy
230 images showing cell viability (live: green, dead: red) of BALB/3T3 fibroblast cells co-cultured
231 with *E. coli* and *P. pastoris*.
232

233   Co-cultures on eADF4(C16)-RGD films were washed to remove non-adherent cells, and

234 the viabilities of both fibroblasts and bacteria/fungi were evaluated by microscopy and live/dead

235 staining, (**Fig. 3 (A-i) – (B-i)**) as well as proliferation during the following period of 5 days of

236 culture (**Fig. 3 (A-ii) – (A-iii) and (B-ii) – (B-iii)**). This showed that the introduction of the

237 RGD-sequence allowed the generation of a bio-selective spider silk surface, displaying selective

238 attachment of mammalian BALB/3T3 fibroblasts but only little/no adhesion of bacteria and

239 fungi.

240   Next, this effect was also investigated in hydrogels. eADF4(C16) and eADF4(C16)-RGD

241 hydrogels were successfully utilized as a cell-encapsulating bioink.[34, 41] However, eADF4(C16)

242 hydrogels without the cell binding motif RGD does not provide sites for focal adhesion and

243 proliferation of encapsulated BALB/3T3 fibroblasts. To observe the bacteriostatic and fungistatic

244 properties of the spider silk bioinks, co-culture experiments were performed with BALB/3T3

245 fibroblasts encapsulated in eADF4(C16) and eADF4(C16)-RGD hydrogels and seeded with *E.*

246 *coli* and *P. pastoris*. After 12 h of incubation, hydrogels were washed carefully to remove non-

247 adherent cells and the hydrogels were further incubated with fresh cell culture media. Viability

248 of microbes and fibroblasts was determined after 3, 6, 9 and 12 days of incubation (**Fig. SI 3,**

249 **Fig. 3 (C-i) – (C-iv), (D-i) – (D-iv), (E-i) – (E-iv), and (F-i) – (F-iv)**). Encapsulated fibroblasts

250 maintained a high cell viability within the hydrogels of eADF4(C16) and eADF4(C16)-RGD

251 over a culture period of 12 days, while no bacterial and fungi growth/contamination could be

252 detected during the entire cultivation period (**Fig. SI 3**).

253 **Conclusion**

254   2D- and 3D-materials based on engineered recombinant spider silk proteins show

255 bacteriostatic and fungistatic properties with a range of tested microbial organisms, i.e., bacteria

256 such as *S. mutans, S. aureus,* and *E. coli,* and fungi such as *C. albicans,* and *P. pastoris*, and

257 none of them are able to form biofilms thereon or therein. Such microbial pathogens are often

258 found in nosocomial infections in humans, and their strong ability to produce biofilms and

259 aggressive infections can be a severe health threat. The obtained novel results complement the

260 previously shown biocompatibility, non-toxicity, biodegradability and mechanical stability of

261 recombinant spider silk materials boosting the potential for various biomedical (e.g. tissue

262 engineering, wound coverage devices, implant coatings) or technical (e.g. coatings of textiles,

263 water tubes) applications. To specifically demonstrate the aptness of these properties of

264 recombinant spider silk in the field of tissue engineering, we performed co-culture experiments

265 of bacteria and fungi with mammalian cells using films and hydrogels made of an RGD-modified

266 spider silk variant. The results clearly indicated a designable bio-selective behavior of the spider

267 silk material, as mammalian cells were able to adhere and proliferated while no biofilm

268 formation occurred over several days.

269   To our knowledge, the bacteriostatic and fungistatic properties of materials made of

270 recombinant spider silk are unique, and intriguingly materials made of regenerated fibroin from

271 *B. mori,* which closely resembles the composition and properties of spider silk proteins, do not

272 show such behavior.

273 **Methods**

274 **Production of recombinant spider silk proteins.** eADF4(C16) was purchased from AMSilk

275 GmbH (Planegg, Germany). The recombinant spider silk proteins eADF4(C16)-RGD,

276 eADF4(C32NR4) and eADF3(AQ)12 were produced and purified as described previously.[24, 33]

277 ***Bombyx mori* (*B. mori*) fibroin protein.** Regenerated fibroin solutions were prepared as

278 described previously,[39] by dissolving degummed silk fibres in 9.3 M LiBr solution, dialyzed

279 against ultrapure water (Milli-Q) for 2 d at 4 °C, centrifuged at 8500 rpm for 45 min at 4 °C, and

280 the supernatant was collected. The *B. mori* fibroin solution had a final concentration of 5 -6%

281 w/v and were stored at 4 °C until use.

282 **Production of flat and patterned films.** All flat and patterned films of proteins and

283 Polycaprolactone (PCL; Perstorp AB) were produced by film casting onto patterned

284 polydimethylsiloxane (PDMS; Sylgard 184 Silicone Elastomer, Dow Corning) substrates. PDMS

285 stamps were produced by casting of a 10:1 mixture of PDMS pre-polymer and curing agent

286 (degassed for 20 min) on a photo-lithographically patterned waver to generate the desired

287 geometry (12 x 12 mm area with grooves of 2 μm in width, ridges with a width of 1 μm, and a

288 height of 4 μm). After curing at 80 °C for 90 min, the stamps were solidified and could be easily

289 peeled off. To produce patterned films, proteins and polymers were dissolved in 1,1,1,3,3,3,-

290 hexafluoro-2-propanol (HFIP; Alpha Aesar) at a concentration of 10 mg/mL (room temperature,

291 overnight). To generate films with a thickness of 10-15 μm, 250 μL of solution was poured into

292 the stamp, and the solvent subsequently evaporated at room temperature. The dried patterned

293 films were removed and post-treated with 100% ethanol for 1 h to render the silk protein water

294 insoluble by induction of β–sheet structures. To ensure, that only material properties determined

295   the results of microbial growth experiments, all samples (including PCL films) were treated the

296   same way. After post-treatment, the samples were stored sterile in 70% ethanol at 4 °C.

297   For co-culture experiments, films were cast from a 25 mg/mL solution of eADF4(C16)-RGD

298   dissolved in 1,1,1,3,3,3-hexafluoro-2-propanol (HFIP) into polystyrene 24 well plates. For each

299   film 0.25 mg of eADF4(C16)-RGD was used per cm^2. Films were allowed to dry and were post-

300   treated with 100% ethanol to induce β-sheet formation in order to render silk films water

301   insoluble.[3]

302   **Bacteria and yeast culture on films.**

303   (**a**) *Streptococcus mutans* (DSMZ 20523, Braunschweig) and *Candida albicans* (patient isolate),

304   stored at -80 °C, were thawed at RT, fractionally spread on Columbia blood agar (PB 5039A,

305   oxoid, Wesel) and incubated for 48 h at 37 °C and 5% CO_2. Afterwards, an overnight culture

306   was prepared in BBLTM Schaedler Broth medium (Becton Dickinson, Sparks MD, USA), and

307   then the culture was diluted (1:10) with Schaedler Broth medium.

308   (**b**) *Escherichia coli* BL21(DE3)-gold (Novagen, Merck, Darmstadt, Germany) stored at -80 °C,

309   was thawed at RT, and inoculated in Luria–Bertani medium (LB), at 37 °C with constant shaking

310   at 150 rpm, until an optical density (OD_{600}) between 0.8 and 1 was reached (corresponding to a

311   viable count of approx. 10^7 –10^8 CFU mL^{-1}). The *E. coli* culture was diluted (1:10) with LB

312   medium.

313   (**c**) *Pichia pastoris* X33 (wild type, Invitrogen, Germany) was inoculated in YPD-media and

314   allowed to grow for 24 h at 30 °C with constant shaking at 150 rpm. The *P. pastoris* culture was

315   diluted (1:10) with YPD medium.

316   Silk and polymer films were taken out of 70% ethanol, subsequently washed with PBS (8.18 g

317   NaCl, 0.2 g KCl, 0.24 g anhydrous KH_2PO_4, 1.78 g Na_2HPO_4 x $2H_2O$, 1 L distilled water, pH

318   7.4, Sigma Aldrich, St. Louis, Missouri, USA), and incubated in 5 mL of diluted microbial

319   solution (as described above: a-c) in petri dishes (Ø 5 cm) for 60 h (5% CO_2, 37 °C). Then, the

320   films were removed and carefully washed with PBS to remove non-adherent bacteria and yeast

321   cells, and dried at room temperature for subsequent SEM imaging.

322   (**d**) For adhesion force measurements, *Staphylococcus aureus* (strain SA113), stored at -20 °C,

323   was thawed and cultured for three days at 37 °C on blood agar plates. Then, a colony from a

324   plate was transferred into 5 mL of sterile tryptic soy broth (TSB) and cultured overnight at 37

325   °C, 150 rpm agitation. For each experiment, 40 µL of the culture were transferred into 4 mL

326   fresh TSB and cultured for another 2.5 h at 37 °C. The bacterial culture was washed three times

327   with sterile phosphate buffered saline (PBS). The final suspension of bacteria in PBS was stored

328   at 4°C and used no longer than 6 hours.

329   **Adhesion force measurements.** Single *S. aureus* cells were attached to a tipless AFM cantilever

330   (MLCT-0 with a nominal spring constant of 0.03 N/m from Bruker Nano, Santa Barbara, Ca,

331   USA) coated with polydopamine.[35, 36] Force-distance measurements were performed with a

332   Bioscope Catalyst from Bruker-Nano in PBS at room temperature.[15] The maximum force with

333   which the cells were pressed onto the surfaces was set to 300 pN. On each surface, 25 force-

334   distance curves were performed for 0 s and 5 s of additional surface delay time with one and the

335   same cell, the total number of individual cells being 13. Approaching speed towards the surfaces

336   was set to 800 nm/s for 0 s of surface delay time and 100 nm/s for 5 s of surface delay time.

337   Retraction speed was 800 nm/s. To test the results of adhesion measurements for statistical

338   significance, all adhesion force distributions were analyzed in pairs by a Man-Whitney-U-test

339   with the software Matlab.

340   **Bacterial and yeast cell viability.** Adhesion of *E. coli* and *P. pastoris* cells to silk and polymer

341   films after culturing for 24 h at 37 °C was measured by analysis of cell vitality using the

342   CellTiter-Blue assay. Samples incubated with bacterial and yeast cells were washed with

343   phosphate buffered saline (PBS; Sigma-Aldrich) three times, and then incubated with 10%

344   CellTiter-Blue (Promega) in PBS for 3 h at 37 °C. Transformation of the blue fluorescent dye

345   resazurin into red fluorescent resorufin (λ_{ex} = 530 nm; λ_{em} = 590 nm) was measured using a plate

346   reader (Mithras LB 940, Berthold, Bad Wildbad) with counting time of 0.5 s.

347   **Preparation of eADF4(C16) and eADF4(C16)-RGD hydrogels.** Lyophilized eADF4(C16) and

348   eADF4(C16)-RGD were dissolved in 6 M guanidinium thiocyanate (GdmSCN) at 5 mg/mL and

349   dialyzed against 10 mM Tris/HCl, pH 7.5 overnight at room temperature using dialysis

350   membranes with a molecular weight cutoff of 6–8 kDa. Subsequent dialysis against 20% w/v

351   poly (ethylene glycol) (PEG, 20,000 g/mol) at a volume ratio of PEG/eADF4(C16) solution of

352   100:1 was used to remove water by osmotic pressure and to adjust 30 mg/mL (3% w/v) spider

353   silk solutions. Hydrogels self-assembled after an overnight incubation at 37 °C.

354   For co-culture experiments, 1×10^6 BALB/3T3 fibroblasts cells were added to 3% w/v

355   eADF4(C16) and eADF4(C16)-RGD spider silk solutions before gelation in an incubator at 37

356   °C.

357   **Preparation of *B. mori* fibroin hydrogels.** *B. mori* fibroin hydrogels were prepared using

358   sonication induced gelation, as previously reported.[39] In brief, 4 % (w/v) aqueous silk fibroin

359   solution in a 15 mL conical tube was ultra-sonicated (Ultrasonic Homogenizers HD 3100,

360   BANDELIN) at 50 % amplitude (21 W) for 30 s, and overnight incubation at 37 °C allowed

361   gelation.

362   **Preparation of gelatin hydrogels.** GelMA was produced by the reaction of gelatin solutions

363   (gelatin from bovine skin, Type B, ~225g Bloom, Sigma-Aldrich) and methacrylic anhydride

364   (Sigma-Aldrich), following previously described protocols.[40] After the dissolution of 10% (w/v)

365   gelatin in 0.1M CB buffer (3.18 g sodium carbonate and 5.86 g sodium bicarbonate in 1L

366   distilled water) at 60 °C, one sixth of 1% (v/v) methacrylic anhydride was added dropwise every

367   30 min for 3 h. The solution was vigorously stirred for another 1 h, diluted with 0.1M CB, and

368   dialyzed for 2 days against ultrapure (Milli-Q) water at 37 °C. The solution was then freeze-dried

369   in a lyophilizer to obtain methacrylamide-modified gelatin as a dry white powder.

370   Methacrylamide-modified gelatin hydrogel was obtained by UV exposure of 5% (w/v) GelMA

371   solution in 24 well cell culture vessels at 365 nm using ultraviolet lamp (Benda, type NU -4 KL)

372   for 15 min in the presence of 0.5 mg/mL of the photoinitiator 2-hydroxy-4′-(2-hydroxyethoxy)-

373   2-methylpropiophenone (Irgacure- 2959, Sigma-Aldrich).

374   **Bacteria and yeast culture on hydrogels.** Hydrogels were incubated with 1 mL of diluted

375   liquid cultures of *E. coli* and *P. pastoris* for 12 h at 37 °C. Hydrogels were washed with

376   phosphate buffered saline (PBS; Sigma-Aldrich) three times to remove non-adherent bacteria

377   and yeast cells, and then lyophilized to examine by SEM.

378   **Microbial adhesion**. The anti-adherence activity of eADF4(C16) and eADF4(C16)-RGD

379   hydrogels for *E. coli* and *P. pastoris* was measured by inoculating the supernatant (100 μL) of

380   the microbe-treated hydrogels (after washing), into fresh media and culturing for 12 h at 37 °C.

381   Optical density at 600 nm (OD_{600}; OD600 DiluPhotometer™, IMPLEN) was measured to

382   monitor microbial growth/infection.

383   **BALB/3T3 cultivation.** BALB/3T3 mouse fibroblasts (European Collection of Cell Cultures)

384   were cultured in Dulbecco's Modified Eagle Medium (DMEM, Biochrom) supplemented with

385   10% fetal bovine serum (Biochrom) and 1 % (v/v) GlutaMAX (Gibco) in a controlled

386   atmosphere of 5 % CO_2, 95 % humidity and at 37 °C. Viability and number of cells were

387   analyzed using trypan blue (Sigma-Aldrich) in a Neubauer chamber (Laboroptik, UK).

388   **Co-culture experiments on films.** Films prepared on polystyrene plates were sterilized by UV

389   treatment at 254 nm for 1 h prior to cell seeding. BALB/3T3 mouse fibroblasts cells were seeded

390   at 5000 cells/well and incubated in a controlled atmosphere overnight (12 h, 5% CO_2, 95%

391   humidity at 37 °C). After washing with PBS twice, samples were incubated with *E. coli* or *P.*

392   *pastoris* prepared in DMEM and incubated for 6 h at 37 °C, 80 % humidity. Non-adherent

393   microbes were removed by washing three times with PBS. Cell culture medium was changed

394   after every 24 h and cultivated up to 5 days. Samples were analyzed for cell viability after 2, 3,

395   and 5 days using a Live/Dead assay.

396   **Co-culture experiments with hydrogels.** eADF4(C16) and eADF4(C16)-RGD hydrogels with

397   encapsulated BALB/3T3 mouse fibroblasts (i.e. bioinks) were prepared in hanging cell culture

398   inserts for 24-well plates (Merck Millipore) and then exposed to diluted bacterial and yeast cells

399   prepared in DMEM for 6 h at 37 °C with 80 % humidity under static conditions. Hydrogels were

400   washed three times to remove non-adherent microbes and incubated with fresh DMEM media

401   and cultivated for 12 days under the same conditions. Cell culture medium was changed after

402 every 24 h. The cell viability of BALB/3T3 mouse fibroblasts was analyzed using Live/Dead

403 assay after 3, 6, 9 and 12 days.

404 **Live/Dead assay.** Films and hydrogels of eADF4(C16) and eADF4(C16)-RGD were washed

405 with PBS and stained with Calcein acetoxymethylester (Calcein A/M, Invitrogen) and Ethidium

406 Homodimer-1 (EthD-1, Invitrogen) in cell culture medium for the detection of live and dead

407 cells, respectively. Calcein A/M was added to the medium at a final concentration of 0.3 µM,

408 Ethidium Homodimer-1 was added to the medium at a final concentration of 0.1 µM and

409 incubated for 30 min. After staining, the solution was removed and fresh PBS was added for

410 imaging. Live and dead cells were visualized and analyzed using a fluorescence microscopy

411 (Leica DMi8, Wetzlar) and processed using either Leica Application Suite or Image J.

412 **Scanning electron microscopy (SEM).** To analyze the morphological structure via SEM,

413 hydrogels were lyophilized and fixed to SEM stubs using conductive carbon cement solution

414 (Leit-C, PLANO GmbH). Samples were sputter coated with 2 nm platinum (Sputter Coater 208

415 HR with 268 MTM 20, Cressington, Watford, U.K.) and then imaged at an 269 accelerating

416 voltage of 2.5 kV, using a scanning electron microscope 270 Zeiss Sigma VP 300 (Zeiss,

417 Oberkochen, Germany).

418 **Acknowledgements**

421 **Author contributions**

422 G.L. and S.K. contributed equally to this work. G.L. prepared films (smooth and patterned),

423 prepared protein coated silanized glass slides, performed SEM and analyzed the data. S.K.

424 performed the in vitro bacteriostatic/fungistatic experiments and coculture experiments with *E.*

425 *coli* and *P. pastoris*. E.D. assisted in the designing of coculture experiments. S.L., M.H. & N.K.

426 carried out in vitro experiments of *S. mutans* and *C. albicans*. C.S. & K.J. prepared bacterial

427 probes and performed force distance measurements. T.S. designed the experiments and

428 supervised the project. S.K. and G.L wrote the manuscript. E.D., C.S., K.J. and T.S. contributed

429 to writing and editing of the manuscript.

430

Additional information

431

432 Supplementary information is available in the online version of the paper.

Competing financial interests

433

434 T.S. is co-founder and shareholder of AMSilk GmbH. All other authors declare no competing

435 financial interests.

References:

436

437 1. Wright, G. D. The antibiotic resistome: the nexus of chemical and genetic diversity. *Nat.*

438 *Rev. Microbiol.* **5**, 175-186, (2007).

439 2. Davies, D. Understanding biofilm resistance to antibacterial agents. *Nat. Rev. Drug*

440 *Discov.* **2**, 114-122, (2003).

441   3.   Carpentier, B. & Cerf, O. Biofilms and their consequences, with particular reference to

442   hygiene in the food industry. *J. Appl. Bacteriol.* **75**, 499-511, (1993).

443   4.   Costerton, J. W., Stewart, P. S. & Greenberg, E. P. Bacterial Biofilms: A Common

444   Cause of Persistent Infections. *Science* **284**, 1318-1322, (1999).

445   5.   Barth, E., Myrvik, Q. M., Wagner, W. & Gristina, A. G. In vitro and in vivo

446   comparative colonization of Staphylococcus aureus and Staphylococcus epidermidis on

447   orthopaedic implant materials. *Biomaterials* **10**, 325-328, (1989).

448   6.   Raad, I. I. *et al.* Vancomycin-Resistant Enterococcus faecium: Catheter Colonization,

449   esp Gene, and Decreased Susceptibility to Antibiotics in Biofilm. *Antimicrob. Agents*

450   *Chemother.* **49**, 5046-5050, (2005).

451   7.   Stewart, P. S. & William Costerton, J. Antibiotic resistance of bacteria in biofilms. *The*

452   *Lancet* **358**, 135-138, (2001).

453   8.   Levy, S. B. & Marshall, B. Antibacterial resistance worldwide: causes, challenges and

454   responses. *Nat. Med.* **10**, 122–129, (2004).

455   9.   Chandra, J. *et al.* Biofilm Formation by the Fungal Pathogen Candida albicans:

456   Development, Architecture, and Drug Resistance. *J. Bacteriol.* **183**, 5385-5394, (2001).

457   10. Campoccia, D., Montanaro, L. & Arciola, C. R. A review of the biomaterials

458   technologies for infection-resistant surfaces. *Biomaterials* **34**, 8533-8554, (2013).

459   11. Campoccia, D., Montanaro, L. & Arciola, C. R. A review of the clinical implications of

460   anti-infective biomaterials and infection-resistant surfaces. *Biomaterials* **34**, 8018-8029,

461   (2013).

462   12. Cheng, G., Zhang, Z., Chen, S., Bryers, J. D. & Jiang, S. Inhibition of bacterial adhesion

463   and biofilm formation on zwitterionic surfaces. *Biomaterials* **28**, 4192-4199, (2007).

464   13. Kenawy, E.-R., Worley, S. D. & Broughton, R. The Chemistry and Applications of

465   Antimicrobial Polymers: A State-of-the-Art Review. *Biomacromolecules* **8**, 1359-1384,

466   (2007).

467   14. Zasloff, M. Antimicrobial peptides of multicellular organisms. *Nature* **415**, 389-395,

468   (2002).

469   15. Tiller, J. C. In *Bioactive surfaces* 193-217 (Springer, 2010).

470   16. Miller, K. P., Wang, L., Benicewicz, B. C. & Decho, A. W. Inorganic nanoparticles

471   engineered to attack bacteria. *Chem. Soc. Rev.* **44**, 7787-7807, (2015).

472   17. Hetrick, E. M. & Schoenfisch, M. H. Reducing implant-related infections: active release

473   strategies. *Chem. Soc. Rev.* **35**, 780-789, (2006).

474   18. Campoccia, D., Montanaro, L., Speziale, P. & Arciola, C. R. Antibiotic-loaded

475   biomaterials and the risks for the spread of antibiotic resistance following their

476   prophylactic and therapeutic clinical use. *Biomaterials* **31**, 6363-6377, (2010).

477   19. Harriott, M. M. & Noverr, M. C. Candida albicans and Staphylococcus aureus form

478   polymicrobial biofilms: effects on antimicrobial resistance. *Antimicrob. Agents*

479   *Chemother.* **53**, 3914-3922, (2009).

480   20. Eisoldt, L., Smith, A. & Scheibel, T. Decoding the secrets of spider silk. *Mater. Today*

481   **14**, 80-86, (2011).

482   21. Kluge, J. A., Rabotyagova, O., Leisk, G. G. & Kaplan, D. L. Spider silks and their

483   applications. *Trends Biotechnol.* **26**, 244-251, (2008).

484   22. Wright, S. & Goodacre, S. L. Evidence for antimicrobial activity associated with

485   common house spider silk. *BMC Research Notes* **5**, 326-326, (2012).

486   23. Sponner, A. *et al.* Composition and Hierarchical Organisation of a Spider Silk. *PLoS*
487   *ONE* **2**, e998, (2007).

488   24. Huemmerich, D. *et al.* Primary Structure Elements of Spider Dragline Silks and Their
489   Contribution to Protein Solubility. *Biochemistry* **43**, 13604-13612, (2004).

490   25. Vendrely, C. & Scheibel, T. Biotechnological Production of Spider-Silk Proteins
491   Enables New Applications. *Macromol. Biosci.* **7**, 401-409, (2007).

492   26. Spiess, K., Lammel, A. & Scheibel, T. Recombinant Spider Silk Proteins for
493   Applications in Biomaterials. *Macromol. Biosci.* **10**, 998-1007, (2010).

494   27. Leal-Egaña, A. & Scheibel, T. Silk-based materials for biomedical applications.
495   *Biotechnol. Appl. Biochem.* **55**, 155-167, (2010).

496   28. Müller-Herrmann, S. & Scheibel, T. Enzymatic degradation of films, particles, and
497   nonwoven meshes made of a recombinant spider silk protein. *ACS Biomater. Sci. Eng.* **1**,
498   247-259, (2015).

499   29. Zeplin, P. H. *et al.* Spider Silk Coatings as a Bioshield to Reduce Periprosthetic Fibrous
500   Capsule Formation. *Adv. Funct. Mater.* **24**, 2658-2666, (2014).

501   30. Borkner, C. B., Wohlrab, S., Möller, E., Lang, G. & Scheibel, T. Surface Modification
502   of Polymeric Biomaterials Using Recombinant Spider Silk Proteins. *ACS Biomater. Sci.*
503   *Eng.*, **3**, 767–775, (2016).

504   31. Bauer, F., Wohlrab, S. & Scheibel, T. Controllable cell adhesion, growth and orientation
505   on layered silk protein films. *Biomater. Sci.* **1**, 1244-1249, (2013).

506   32. Leal-Egaña, A. *et al.* Interactions of Fibroblasts with Different Morphologies Made of
507   an Engineered Spider Silk Protein. *Adv. Eng. Mater.* **14**, 67-75, (2012).

25

508   33. Wohlrab, S. *et al.* Cell adhesion and proliferation on RGD-modified recombinant spider

509   silk proteins. *Biomaterials* **33**, 6650-6659, (2012).

510   34. Schacht, K. *et al.* Biofabrication of Cell-Loaded 3D Spider Silk Constructs. *Angew.*

511   *Chem., Int. Ed.* **54**, 2816-2820, (2015).

512   35. Thewes, N. *et al.* A detailed guideline for the fabrication of single bacterial probes used

513   for atomic force spectroscopy. *Eur. Phys. J. E* **38**, 140, (2015).

514   36. Thewes, N. *et al.* Stochastic binding of Staphylococcus aureus to hydrophobic surfaces.

515   *Soft Matter* **11**, 8913-8919, (2015).

516   37. Garrett, T. R., Bhakoo, M. & Zhang, Z. Bacterial adhesion and biofilms on surfaces.

517   *Prog. Nat. Sci.* **18**, 1049-1056, (2008).

518   38. Tuson, H. H. & Weibel, D. B. Bacteria-surface interactions. *Soft matter* **9**, 4368-4380,

519   (2013).

520   39. Rockwood, D. N. *et al.* Materials fabrication from Bombyx mori silk fibroin. *Nat.*

521   *Protoc.* **6**, 1612-1631, (2011).

522   40. Shirahama, H., Lee, B. H., Tan, L. P. & Cho, N.-J. Precise Tuning of Facile One-Pot

523   Gelatin Methacryloyl (GelMA) Synthesis. *Sci. Rep.* **6**, 31036, (2016).

524   41. DeSimone, E., Schacht, K., Pellert, A. & Scheibel, T. Recombinant spider silk-based

525   bioinks. *Biofabrication* **9**, 044104, (2017).

526

1 Supporting Information

2 Engineered 2D and 3D spider silk materials with intrinsic

3 bacteriostatic and fungistatic properties

4 *Gregor Lang[1,2,3,4], Sushma Kumari[1,4], Elise Desimone[1], Christian Spengler[5], Susanne Lücker[6],*

5 *Martina Hudel[6], Karin Jacobs[5], Norbert Krämer[6] and Thomas Scheibel[1,3, 7, 8, 9, 10, *]*

6 [1]Chair of Biomaterials, Faculty of Engineering Science, University of Bayreuth, [3]Bayreuth

7 Center for Material Science and Engineering (BayMAT), [7]Bavarian Polymer Institute (BPI),

8 [8]Bayreuth Center for Colloids and Interfaces (BZKG), [9]Bayreuth Center for Molecular

9 Biosciences (BZMB), and [10]Research Center for Bio-Macromolecules (BIOmac),

10 Universitätsstraße 30, 95440 Bayreuth, Germany

11 [2]Biopolymer Processing Group, Faculty of Engineering Science, University of Bayreuth,

12 Ludwig-Thoma-Straße 36A, 95447 Bayreuth, Germany

13 [5]Department of Experimental Physics, Saarland University, 66041 Saarbrücken, Germany

14 [6]Medical Center for Dentistry, Department of Paediatric Dentistry, Medical Center Gießen and

15 Marburg, Justus-Liebig University Gießen, Schlagenzahl 14, 35392 Gießen, Germany

16 [7]Institute of Medical Microbiology, Justus-Liebig University Gießen, Schubertstraße 81, 35392

17 Gießen, Germany

18 [4]Gregor Lang and Sushma Kumari contributed equally to this work.

19

20

21   **Table. 1:** Properties of recombinant spider silk proteins:

Recombinant spider silk protein	M_w (kDa)	No. of charged amino acid residues at neutral pH (positive/negative)	pI
eADF4(C16)	47.7	0/16	3.5
eADF4(C16)-RGD	48.45	1/17	3.6
eADF4(C32NR4)	104.1	2/34	3.5
eADF3(AQ)12	48	0/0	5.5

22   Charged amino acid residues refer to silk sequences only; T7 tags comprise an additional
23   arginine residue.
24
25
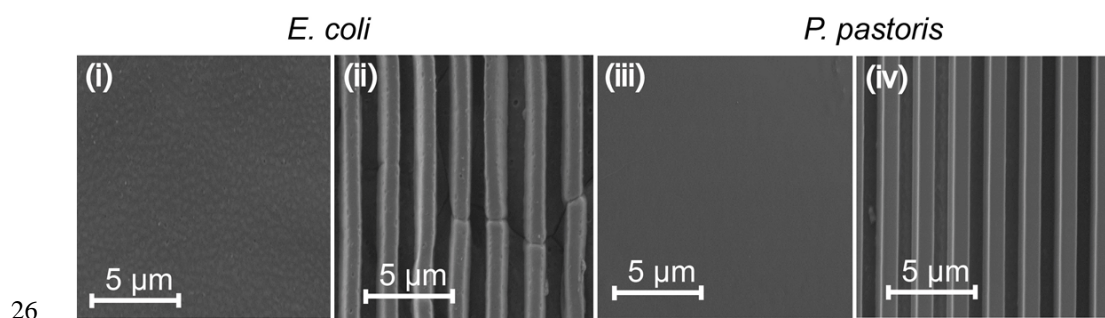
Fig. SI 1: Bacteriostatic and fungistatic properties of films made of eADF4(C16). SEM images showing (i & iii) plane and (ii & iv) micro structured surfaces of eADF4(C16); after 12 h of incubation with (i & ii) *E. coli* and (iii & iv) *P. pastoris* at 37 °C. Growth and microbial colonization on smooth and patterned films of eADF4(C16) is significantly restricted. Scale bars = 5 µm.
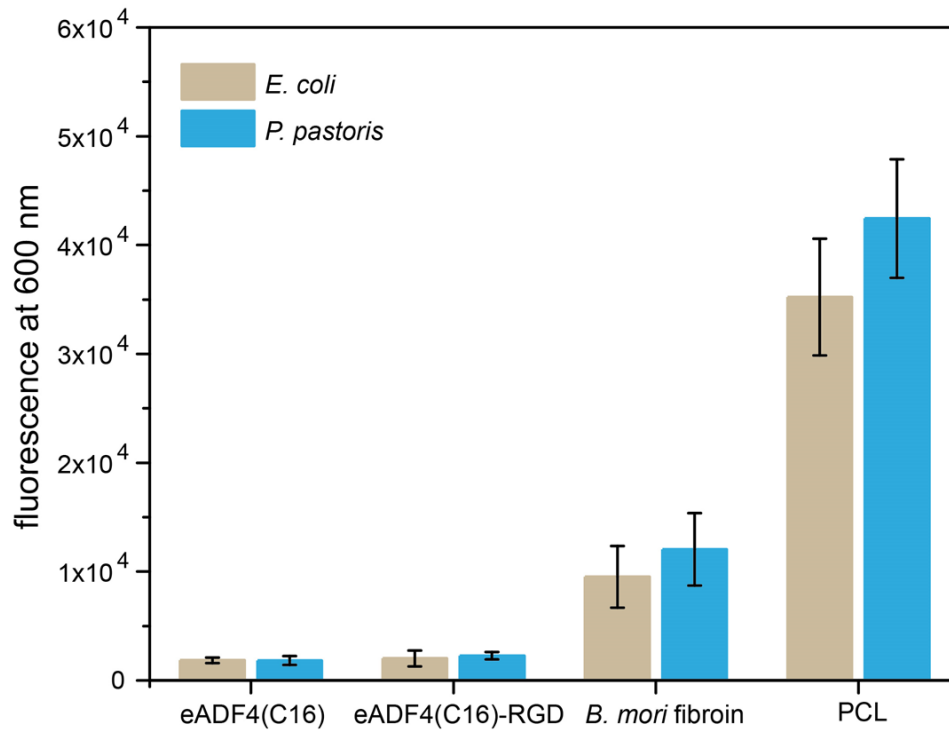
Fig. SI 2: Bacterial and yeast cells viability. Films of eADF4(C16), eADF4(C16)-RGD, *B. mori* fibroin and PCL were incubated with *E. coli* and *P. pastoris* for 24 h at 37 °C. Microbial viabilty was quantified using CellTiter-Blue assay by measuring the transformation of the blue fluorescent dye resazurin into red fluorescent resorufin with 530 nm excitation and 600 nm emission filters in a microplate reader. Minimal adhesion of *E. coli* and *P. pastoris* on eADF4(C16) and eADF4(C16)-RGD films results in very low fluorescence intensity comparatively to *B. mori* fibroin and PCL films with higher microbial viability. Each result is an average of five experiments, and the error bars designate the standard deviations.
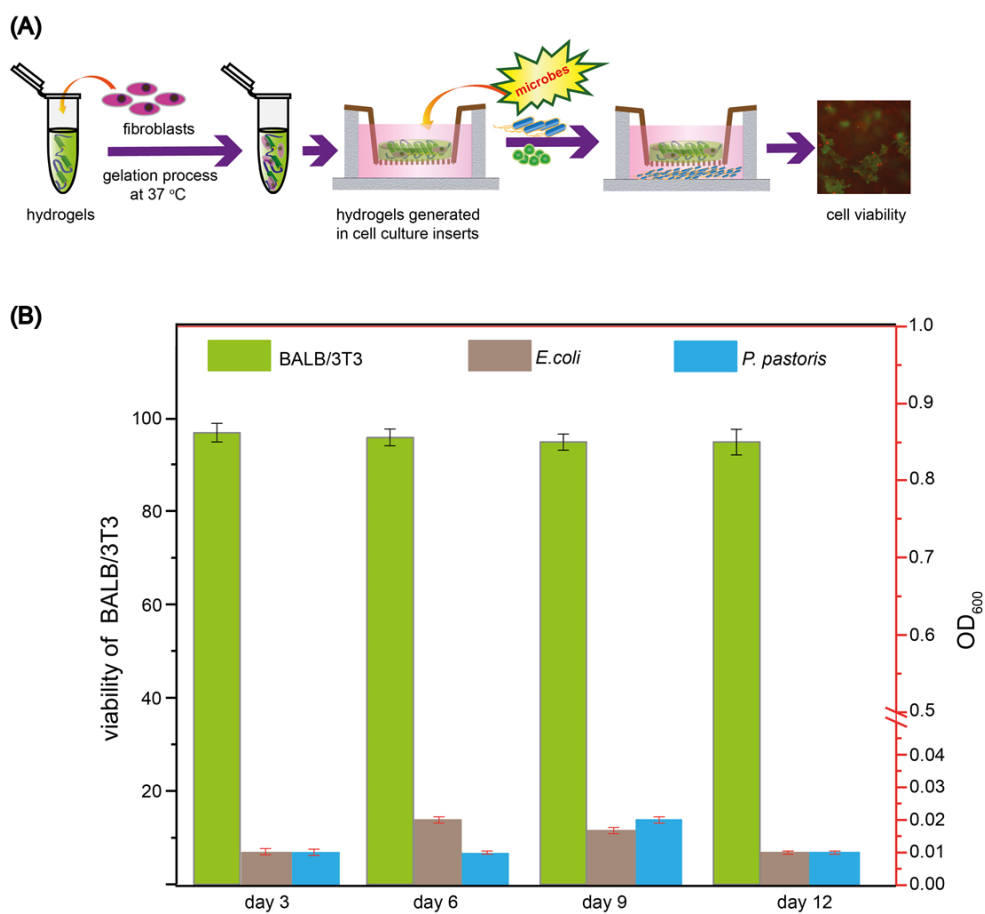
Fig. SI 3: (A) Schematic illustration demonstrating the coculture of microbes (*E.coli and P. pastoris*) and mammalian cells (BALB/3T3) with hydrogels of eADF4(C16) and eADF4(C16)-RGD. (B) The cell viability (left side scale) of mouse fibroblasts (BALB/3T3) encapsulated in eADF4(C16)-RGD hydrogels in co-culture with microbes was evaluated by cell staining with calcein A/M (live cells: green) and ethidium homodimer I (dead cells: red) after 3, 6, 9, and 12 days. Each result is an average of three experiments, and the error bars designate the standard deviations. Microbial growth (right side scale) of *E.coli* and *P. pastoris* in fresh media was measured by optical density at 600 nm (OD$_{600}$) with microbial inoculated hydrogels (after washing), and incubating for 12 h at 37 °C.

Addendum VII – Synthesis of Hydroxyapatite Substrates: Bridging the Gap Between Model Surfaces and Enamel

Authors: C. Zeitz[1], T. Faidt[1], S. Grandthyll[1], H. Hähl[1], N. Thewes[1], C. Spengler[1], J. Schmauch[1], M. J. Deckarm[1], C. Garchot[2] H. Natter[3], M. Hannig[4], F. Müller[1] and K. Jacobs[1]

[1] Experimental Physics, Saarland University, 66123 Saarbrücken, Germany.
[2] Department of Materials Science, Saarland University, 66123 Saarbrücken, Germany.
[3] Physical Chemistry, Saarland University, 66123 Saarbrücken, Germany.
[4] Clinic of Operative Dentistry, Periodontology and Preventive Dentistry, Saarland University, 66421 Homburg/Saar, Germany.

Author contributions:
*Experimental results were achieved by T. Faidt, C. Zeitz (production of samples and AFM measurements), J. Schmauch, (TEM, SEM, EBSD measurements), M. J. Deckarm (XRD measurements), C. Gachot (micro-indentation measurements), S. Grandthyll and F. Müller (XPS measurements). Data were analyzed by C. Zeitz, T. Faidt, S. Grandthyll, H. Natter and F. Müller. The manuscript was written by C. Zeitz, T. Faidt, **C. Spengler**, H. Hähl. N. Thewes, M. Hannig, F. Müller and K. Jacobs. Scientific work was directed by F. Müller and K. Jacobs.*

Abstract - Hydroxyapatite substrates are common biomaterials, yet samples of natural teeth do not meet the demands for well-defined, highly reproducible properties. Pellets of hydroxyapatite were produced via the field assisted sintering technology (FAST) as well as via pressureless sintering (PLS). The applied synthesis routes provide samples of very high density (95 % − 99 % of the crystallographic density) and of very low surface roughness (lower than 1 nm when averaged per $1\,\mu m^2$). The chemical composition of the raw material (commercial HAP powder) as well as the crystalline structure is maintained by the sintering processes. These specimens can therefore be considered as promising model surfaces for studies on the interactions of biomaterial with surfaces of biological relevance, as demonstrated for the adsorption of BSA proteins.

Synthesis of Hydroxyapatite Substrates: Bridging the Gap between Model Surfaces and Enamel

Christian Zeitz,[†] Thomas Faidt,[†] Samuel Grandthyll,[†] Hendrik Hähl,[†] Nicolas Thewes,[†] Christian Spengler,[†] Jörg Schmauch,[†] Michael Johannes Deckarm,[†] Carsten Gachot,[‡] Harald Natter,[§] Matthias Hannig,[‖] Frank Müller,*[,†] and Karin Jacobs*[,†]

[†]Experimental Physics, [‡]Department of Materials Science, and [§]Physical Chemistry, Saarland University, 66123 Saarbrücken, Germany

[‖]Clinic of Operative Dentistry, Periodontology and Preventive Dentistry, Saarland University, 66421 Homburg, Germany

Ⓢ *Supporting Information*

ABSTRACT: Hydroxyapatite substrates are common biomaterials, yet samples of natural teeth do not meet the demands for well-defined, highly reproducible properties. Pellets of hydroxyapatite were produced via the field assisted sintering technology (FAST) as well as via pressureless sintering (PLS). The applied synthesis routes provide samples of very high density (95%−99% of the crystallographic density) and of very low surface roughness (lower than 1 nm when averaged per 1 μm^2). The chemical composition of the raw material (commercial HAP powder) as well as the crystalline structure is maintained by the sintering processes. These specimens can therefore be considered as promising model surfaces for studies on the interactions of biomaterial with surfaces of biological relevance, as demonstrated for the adsorption of BSA proteins.

KEYWORDS: *atomic force microscopy (AFM), electron backscattering diffraction (EBSD), hydroxyapatite (HAP), field assisted sintering technology (FAST), pressureless sintering (PLS), transmission/scanning electron microscopy (TEM, SEM), protein adsorption, X-ray diffraction (XRD), X-ray photoelectron spectroscopy (XPS)*
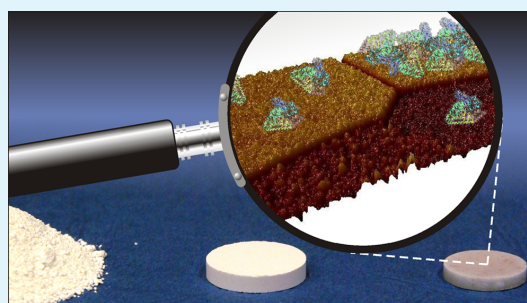
1. INTRODUCTION

During the past decade, interfaces between soft and hard matter became a dynamic topic in the life sciences.[1−3] Many physiological processes are influenced by the properties of interfaces, e.g., the growth of biofilms or the adsorption of proteins or bacteria.[4−9] The specific interaction between an adhering particle and a surface causes a particular behavior of adhering objects on different surfaces.[10,11] This interaction highly depends on the physicochemical properties of both, particle and surface. Therefore, if a quantitative description of the interaction is intended, the exact chemical composition and the precise structure of the surface and the bulk of the interacting objects have to be considered.[4−7,12,13] In the case of biomaterials, such as teeth, bones, or any other kind of tissue, the demand for "precise knowledge" typically asks, however, for the impossible, since structure and chemical composition of individual specimens are often subject to large variations. For example, the fluoride content of human teeth—as a parameter that strongly affects the adhesion force between bacteria and enamel[7]—differs for each individual. Therefore, probing the interaction of biomacromolecules, cells, proteins, or bacteria to biomaterials is often restricted to well-defined model surfaces, such as silicon wafers or glass slides. At first sight, investigations

using such substrates resemble pure academic playgrounds under no realistic conditions. Yet, even from these simple model systems, valuable information concerning the impact of surface and subsurface properties on adsorption properties was obtained.[6] In a second step, it is of course of high interest to consider substrates that combine both the significance of a real-life material and the warranty of well-defined material properties, like surface topography and chemical composition.

Human enamel is a hierarchically organized bioceramic consisting mainly of calcium-deficient hydroxyapatite (HAP: $Ca_{10}(PO_4)_6(OH)_2$).[14,15] On the nanoscale, enamel is composed of apatite crystallites measuring 40−60 nm in diameter and 100−1000 nm in length.[15] On the microscale, the crystallites are arranged in prisms that have a diameter of several micrometers and a length of millimeters.[15] Besides the dominant inorganic components (97%), enamel also contains matrix proteins (1 wt %). The variation of the chemical composition[16] and the structure can be influenced by extrinsic factors, e.g., by physiological processes in the mouth, by the

application of fluoride-containing agents, or simply by genetics. Thus, variations in structure and composition of enamel are not unusual, and a quantitative description therefore requires a characterization of each individual specimen.

In terms of the need of standardized tooth-like model surfaces, the present study describes the synthesis and properties of sintered hydroxyapatite samples as approximately representing a single crystallite of enamel.[14] In contrast to previous studies where nano-HAP samples were prepared rather in the light of their application as a biomaterial,[17,18] the aim of the present study was the synthesis of HAP samples with well-defined, highly reproducible properties to get new enamel-like model samples of biorelevance.

These samples were prepared by the field assisted sintering technology (FAST) of HAP powder and by pressureless sintering (PLS) of precompacted HAP powder. In contrast to previous studies where the preparation of sintered HAP samples also included the synthesis of the HAP powder itself,[19,20] commercial HAP powder (with follow-up treatment) was used in the present case to make the overall synthesis route as simple as possible.

The application of both sintering techniques aims at potential differences in sample properties such as density, grain size, hardness, chemical composition, or crystal structure. The utility of these types of samples has already been proven in previous works concerning depth distribution of fluoridation on HAP[12] and fluoride-induced bacterial adhesion on HAP surfaces.[7]

2. MATERIALS AND METHODS

2.1. Materials. Nanoscaled HAP powder (Sigma-Aldrich Chemie GmbH, Munich, Germany) was used as a raw material for the synthesis of HAP pellets. Before sintering, 10 g of the powder was dispersed and rinsed three times in 1 L of freshly demineralized water (Thermo Fisher, resistivity ∼18.2 MΩ·cm) in order to remove any water-soluble impurities, as e.g., byproducts from the HAP synthesis such as Na^+ or Cl^-.[12] After filtration, the powder was dried in a drying cabinet at 110 °C for at least 15 h, followed by mincing of the clotted powder in a mortar for further preparation or analysis.

2.2. Synthesis of FAST Samples. For the FAST method, 3 g of HAP powder was filled into a carbon compression mold (diameter 22 mm) which was mounted into a FAST furnace (HP D 25 by FCT Systems). After evacuation of the setup below 1 mbar, the mold has been heated electrically by a pulsed current (pulse duration 10 ms). Up to a temperature of 700 °C, the heating was carried out with a temperature ramping of 150 °C/min. At 700 °C the mold was instantly loaded with a uniaxial force of 19 kN (resulting in a pressure of 50 MPa), and the heating rate was reduced to 10 °C/min. At the maximum temperature of 1000 °C the pressure was kept constant for 5 min, and afterward, the force was released instantly and the heating power was switched off. Down to 500 °C, the cooling rate was approximately −50 °C/min. At 500 °C, the setup was flooded with N_2. Reaching room temperature, the sample was removed from the mold. It finally featured a cylindrical shape of 22 mm in diameter and about 5 mm in height. The mass-to-volume ratio revealed a density of ∼3.00 g/cm³, which is larger than 95% of the crystallographic density of ∼3.156 g/cm³.[19]

2.3. Synthesis of PLS Samples. In the case of the PLS method, 1 g of HAP powder was filled into a 15 ton compression tool of stainless steel (MsScientific, Berlin, Germany) with a diameter of 16 mm. For compacting the powder, a compressing force of 20 kN was applied uniaxially (resulting in a pressure of ∼100 MPa). The green body with a density of 66% of the crystallographic density was placed into a high temperature sinter furnace on a corundum ceramic disk and was sintered according to the temperature profile in Figure 1a with a heating rate of 1 °C/min, as proposed in ref 19. To reduce strain and
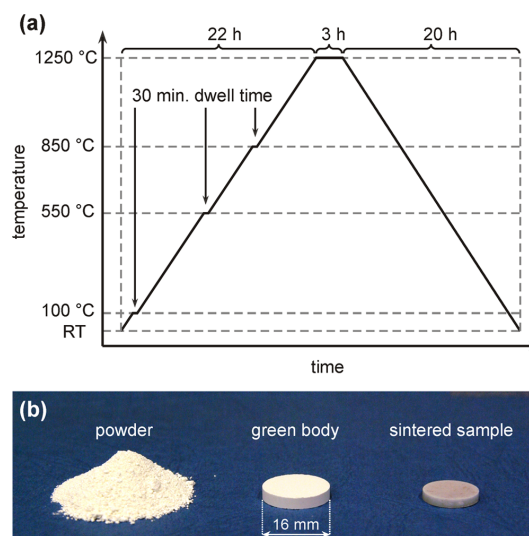
Figure 1. (a) Temperature profile used for the pressureless sintered (PLS) samples. (b) 1 g of HAP in different stages of sample preparation: powder, green body after compression, and sintered sample.

to degas the samples, heating was paused at 100 °C, 550 °C, and 850 °C for 30 min.[19] The final temperature of 1250 °C was held for 3 h. Cooling was performed with −1 °C/min. The samples finally featured a density (as determined by an Archimedes balance) between 97% and 99% of the crystallographic density.[19] The thickness of the disc-shaped samples was in the range of 2.0–2.5 mm (cf. Figure 1b).

After sintering, both types of samples were treated with abrasive paper (SiC, Struers, Willich, Germany) and polishing suspensions (MDAC, Struers, Willich, Germany: 1 μm diamond polishing suspension; MSY 0-0.03, Microdiamant, Lengwil, Switzerland: 30 nm diamond polishing suspension). Since the application of the diamond suspension results in a dilute distribution of some nanodiamonds on the surface (cf. Figure S1b), a final etching step was applied by exposing the surface to a 0.01 mol/L acetate buffer solution of pH 4.5 for 10 s in order to remove the residues of the polishing suspension.

2.4. Methods. X-ray photoelectron spectroscopy (XPS) was performed with an ESCA MKII spectrometer by Vacuum Generators (base pressure ∼10⁻¹⁰ mbar) using nonmonochromatized Al Kα excitation ($\hbar\omega$ = 1486.6 eV). For quantitative analysis of the stoichiometry, spectra of Ca-2p, Ca-2s, P-2p, P-2s, O-1s, and C-1s were taken at a pass energy of 20 eV in normal emission mode (i.e., emission angle = 0° with respect to the surface normal). To get the relative amount of each element, the intensities (i.e., peak areas) of the particular core levels were scaled with the photoemission cross sections by Yeh and Lindau[21] after Shirley background subtraction.[22] For Ca and P, the elemental contributions were averaged using the 2p and 2s peaks.

For atomic force microscopy (AFM) a Bruker Bioscope Catalyst (Santa Barbara, CA) was used with Olympus OMCL-AC160TS tips (Tokyo, Japan) in tapping mode. The AFM probed root-mean-square (RMS) roughness of a surface is given by

$$\sigma_{RMS} = \sum_n \sqrt{(z_i - z)^2 / n}$$

with z_i, z, and n describing the height coordinates of a particular pixel, the mean height, and the number of pixels, respectively.

Prior to the calculation of the RMS roughness, plane fit and flattening procedures were applied to the AFM images. In case of the
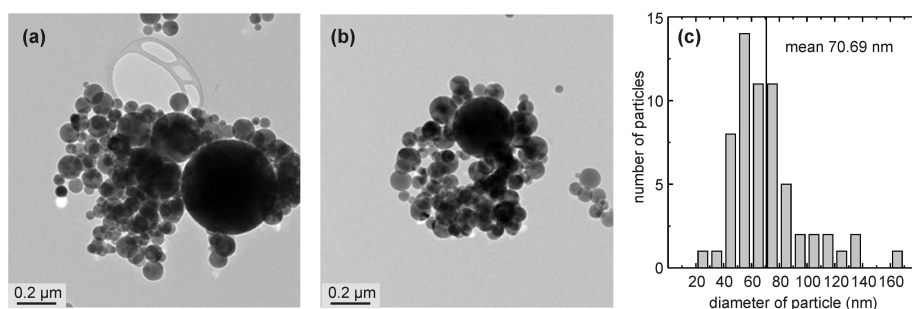
Figure 2. (a, b) TEM micrographs of washed HAP powder dispersed in propanol. (c) Distribution of particle diameters as extracted from TEM data (as based on the analysis of 61 particles).

plane fit, a first-order polynomial equation was used to fit the scanned surface and remove tilt in both x and y directions:

$$z_{\text{fit}} = a + bx + cy$$

Flattening (zeroth order) was used to center data along each line and thereby remove offsets between scan lines.

Scanning electron microscopy (SEM) was performed with a JSM-7000 F by JEOL Ltd., Tokyo, Japan, using 20 keV electrons. For electron backscattering diffraction (EBSD), the same setup was operated with an electron acceleration voltage of 15 kV and a Digiview 3 detector by EDAX Inc., Mahwah, NJ. The identification of different grains was achieved by comparing the diffraction patterns with the Kikuchi patterns[23] from the database provided by the manufacturer. For transmission electron microscopy, a JEM 2011 by JEOL Ltd., Tokyo, Japan, working with 200 keV electrons was used.

X-ray diffraction (XRD) was carried out using an X'Pert Pro diffractometer with PIXcel 1D detector by PANalytical, Almelo, Netherlands, with Cu $K\alpha_{1/2}$ radiation ($\lambda = 0.154$ nm).

Microindentation tests were done by a Struers DuraScan facility according to HV0.1 with a 60× objective. Nine indents were performed for each sample and finally averaged.

3. RESULTS AND DISCUSSION

3.1. Powder Characterization. To probe the particle size distribution, HAP powder was dispersed in propanol and placed on a TEM grid. After evaporation of the solvent, the grid was mounted into a TEM. Figure 2 displays the typical size distribution of HAP particles after dispersion in propanol with the size of the clusters ranging from some hundreds of nanometers to about 1 μm. The diameters of the particles range from some tens to some hundreds of nanometers with a mean value of about 70 nm.

To reveal the chemical composition, small amounts of the powder were pressed to a pellet and probed by XPS.

Table 1 compares the stoichiometry of HAP (i.e., $Ca_{10}(PO_4)_6(OH)_2 \rightarrow$ Ca:P:O = 5:3:13) with the composition of washed HAP powder. The deviation between the nominal HAP composition and the XPS derived HAP stoichiometry is similar to that observed in other studies.[24−26] The observation

Table 1. Relative Amount of Elements for Washed HAP Powder[a]

	Ca	P	O	C	Ca:P	Ca:O
washed HAP	4.6	3	14.0	3.2	1.52	0.33
nominal formula unit	5	3	13	0	1.67	0.38

[a]For better comparison values are scaled to the nominal phosphorus content in the HAP sum formula.

of carbon (as a ubiquitous impurity for *ex situ* prepared samples) as well as the excess of oxygen can be simply related to the presence of adsorbates. Such impurities have a strong impact on the measurement due to the surface sensitivity of XPS and the nanoscale (i.e., surface dominated) structure of the powder.

Concerning the crystal structure of the powder, the XRD data in Figure 3 are in good agreement with the diffraction
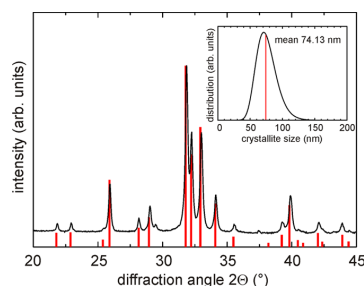
Figure 3. XRD pattern of washed HAP powder. The red bars denote the pattern of the $P6_3/m$ space group for stoichiometric HAP according to the PDF card 98-004-7182. The additional peaks at diffraction angles of ∼29° and ∼37° probably result from small amounts of impurities such as $CaCO_3$ and CaO. The inset shows the crystallite size distribution obtained from a Warren−Averbach analysis resulting in a mean value of 74.13 nm.

pattern of the $P6_3/m$ space group[27] for stoichiometric HAP (PDF card 98-004-7182). Additional peaks at diffraction angles of about 29° and 37° can be assigned to small amounts of impurities such as calcite, $CaCO_3$, or quicklime, CaO. Together, chemical composition and structural data imply that the HAP powder represents a nearly phase-pure raw material. The crystallite size distribution was determined by a Warren−Averbach analysis. Using a self-developed software package,[28,29] the measured data were corrected for instrumental resolution. The correction was done by deconvolution in Fourier space. Assuming a log-normal distribution[30,31] the Fourier coefficients were used for the calculation of the corresponding parameters μ and σ, representing the mean value and the asymmetry, respectively. The resulting crystallite size distribution (Figure 2c, inset) with a μ value of 74.13 nm and a σ value of 1.23 is in accordance with the values obtained from the TEM data in Figure 2c (for details, see Table S1 in the Supporting Information).
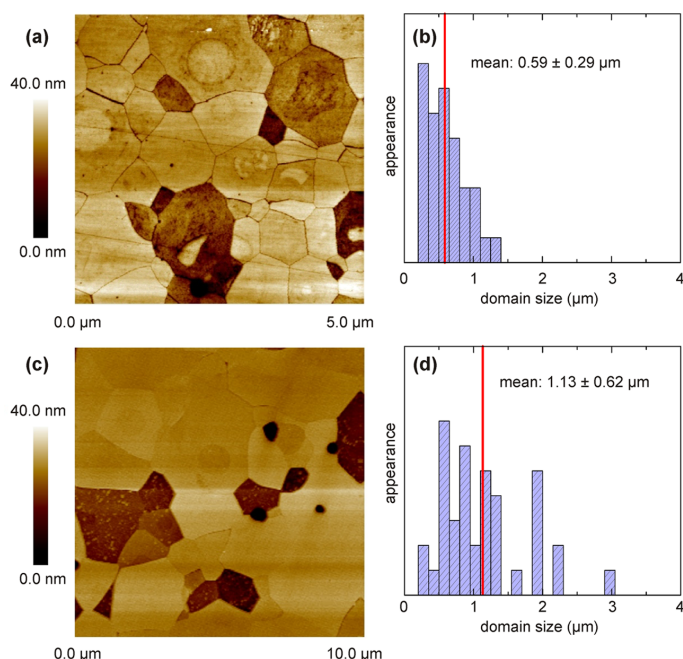
Figure 4. Atomic force microscopy on HAP pellets after polishing and final etching. (a) Topography of a $5 \times 5 \ \mu m^2$ surface area of a FAST sample. (b) Distribution of domain sizes for FAST sample, as based on the analysis of 36 domains from (a). (c) Topography of a $10 \times 10 \ \mu m^2$ surface area of a PLS sample. (d) Distribution of domain sizes for PLS sample as based on the analysis of 39 domains from (c). For analysis of domain sizes, domain perimeters were marked by closed polygons, and the areas were related to the area of the whole AFM image.
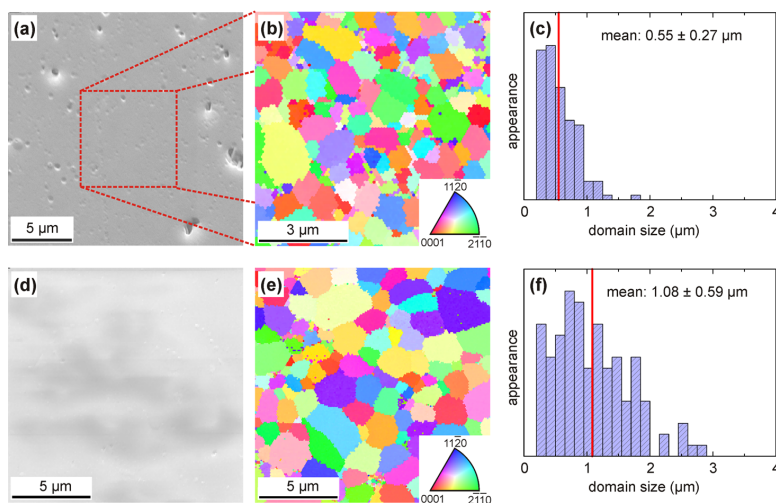
Figure 5. (a) SEM micrograph of a FAST sintered sample after the final polishing step using 30 nm diamond suspension followed by etching. (b) ESBD map taken from the marked area (red box) with colors representing crystallographic orientations (cf. inset). (c) Distribution of domain sizes taken from the ESBD map (as based on ~130 grains with size larger than 200 nm to exclude single pixels). (d–f) Same experiments on the surface of a pressureless sintered sample. For Image-Quality maps of the EBSD data, cf. Figure S2.

3.2. Characterization of Sintered Samples. Figure 4 compares the AFM-probed surface topography of a FAST sample and a PLS sample after polishing and final etching. In both cases, distinct domains exhibiting different heights could be identified. This kind of topography results from the final etching of the polished samples since domains of very different heights are not observed before the etching procedure (see Figure S1 in the Supporting Information). When restricting the RMS-probing area to $\sim 1 \times 1 \ \mu m^2$, the roughness strongly depends on the particular domains. For deep grains (dark areas

205
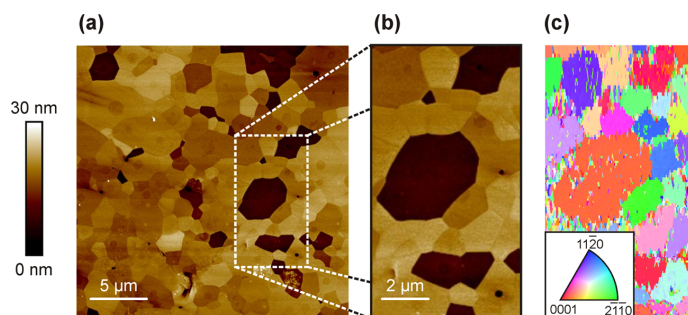
Figure 6. (a) AFM picture of a PLS sintered sample with domain distribution similar to Figure 4. (b) Selected area for EBSD mapping. (c) EBSD map of selected area. Because of a drift of the sample during the EBSD scan, the EBSD map had to be slightly stretched to fit the selected AFM area.

in Figure 4) typical RMS values range around 1 nm, whereas for high grains (i.e., bright areas in Figure 4) the RMS values clearly drop to the angstrom range. For both samples, only a small amount of pores is visible in accordance with the high density of both samples. The most prominent difference between the FAST and PLS prepared samples concerns the size distribution of the domains. For the FAST sintered sample, the average domain size is 0.59 ± 0.29 μm while it is nearly twice as large for the PLS sintered sample, i.e., 1.13 ± 0.62 μm (these values represent the square roots of the average domain areas to have characteristic lengths for comparison with the average particle diameter of the powder).

In Figure 5, SEM micrographs, EBSD maps, and the distribution of grain sizes are compared for FAST and PLS prepared samples. Apart from pores also seen in AFM, a homogeneous surface is found in SEM images (Figures 5a and 5d). Only with the help of EBSD, the domains found in AFM (Figure 4) can be revealed. The EBSD technique allows, however, to identify these domains as individual single-crystalline grains that are terminated by different crystal planes.

In terms of crystallographic orientation, no texture (i.e., preferred orientation) can be observed in the EBSD maps (Figures 5b and 5e). The orientation of the grains is distributed nearly randomly; i.e., there is no distinct impact of mechanical anisotropy due to the uniaxial compression. With respect to the grain size, the FAST sample provides the most homogeneous distribution with an average grain size of 0.55 ± 0.27 μm (cf. AFM data 0.59 ± 0.29 μm). For the PLS sample, the average grain size amounts to 1.08 ± 0.59 μm (cf. AFM data 1.13 ± 0.62 μm); i.e., the average grain area of the PLS sample is nearly 4 times as large as in the case of the FAST sample (at least for the preparation parameters used here).

Although the AFM data in Figure 4 and the EBSD data in Figure 5 were taken from different samples, the distributions of AFM-probed domain sizes (Figures 4b and 4d) compare well with the distributions of the EBSD-probed domain sizes (Figures 5c and 5f). Therefore, domains of constant height seem to represent single-crystalline grains. To prove this assumption unambiguously, AFM data are compared with EBSD data for the very same surface area, as depicted in Figure 6. The direct comparison of the topography in Figure 6b with the scattering distribution in Figure 6c gives evidence that the height distribution in AFM strongly matches with the crystallographic orientation in EBSD. Since the etching rate for a crystallite is affected by the crystallographic orientation of its surface,[32] the height of each domain is a direct measure for

the etching rate of different crystallite's facets (note that the topographic characteristics in Figures 4 and 6 are not observed for samples without the final etching procedure; cf. Figure S1). The domains with strongest etching (dark areas in Figure 6b) correspond to the facets close to the (0001) basal plane (reddish coloring in Figure 6c; cf. also inset).

The chemical compositions of the samples as probed by XPS are compared in Table 2. At first sight, the composition of the

Table 2. Relative Amounts of Elements in Sintered HAP Samples, As Probed on the Initial Surface and after Ablation of Several nanometers by Ar Ion Etching[a]

		Ca	P	O	C	Ca:P	Ca:O
PLS sample	as sintered	4.0	3	12.8	2.0	1.33	0.31
	after Ar ion etching	4.6	3	11.4	0.8	1.70	0.44
FAST sample	as sintered	4.1	3	13.2	9.2	1.36	0.31
	after Ar ion etching	4.5	3	12.1	2.1	1.50	0.37
formula unit		5	3	13	0	1.67	0.38

[a]For better comparison values are scaled to the nominal phosphorus content in the HAP sum formula.

samples seems to deviate from the nominal composition of the HAP sum formula. Especially in the case of the as-sintered samples, there is a strong depletion of Ca resulting in a Ca:P ratio that meets only 82% of the nominal value. This is probably caused by element-specific preferred wet chemical etching in acetate buffer solution performed in the last preparation step of the samples. However, after ablation of several nanometers by Ar ion etching, the Ca:P ratio approaches the nominal value (at least in the range of 10% error which is not unusual in XPS).

According to the increase in average particle size upon sintering as observed by the TEM data in Figure 2 (average particle size ~70 nm) and by the EBSD data in Figure 5 (average domain size ~550−1100 nm), the XRD data in Figure 7 display a strong decrease in peak widths. More importantly, no contributions from crystalline material other than HAP and the initial impurities (e.g., $CaCO_3$ and CaO) can be observed, indicating that there is no distinct transformation of material during the sintering processes. In contrast to the XRD data analysis of the HAP raw powder by a Warren−Averbach evaluation, a corresponding analysis of the sintered HAP samples was not possible because of a too small difference in
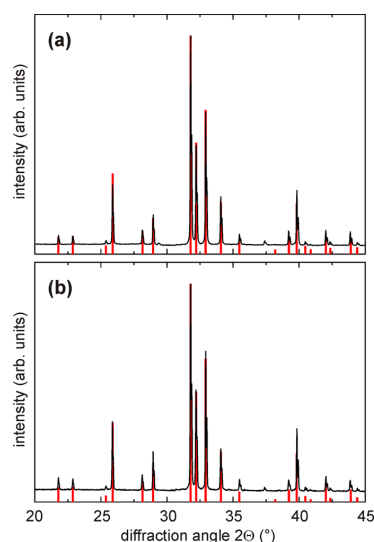
Figure 7. Typical XRD patterns of (a) a FAST prepared HAP sample and (b) of a PLS prepared HAP sample. The red bars denote the pattern of the $P6_3/m$ space group for stoichiometric HAP according to the PDF card 98-004-7182.

peak width between the measured data and the resolution of the instrument (0.04°). For this reason, only the crystallite size and the microstrain content were determined by nonprofile evaluating methods, i.e., Scherrer[33] and Williamson Hall analysis.[34] The results confirm the observations from the AFM and EBSD data, namely, a larger mean crystallite size for the PLS prepared sample (for details, see Table S1).

Microindentation experiments reveal also no distinct differences for pellets from the different synthesis routes, as displayed in Figure 8. The Vickers hardness of the FAST samples is about 660 HV0.1, and the values for the PLS samples are nearly the same, i.e., 670−680 HV0.1. These values are, however, nearly twice as large as the values obtained for
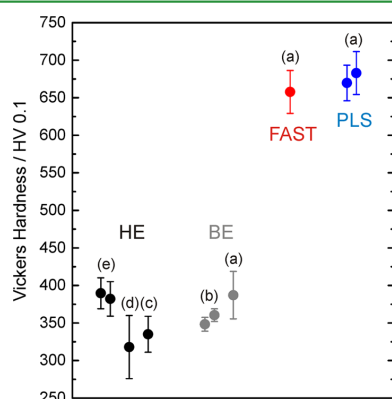
Figure 8. Comparison of Vickers hardness of FAST and PLS prepared HAP samples with hardness of bovine enamel (BE) and human enamel (HE): (a) this study, (b) ref 35, (c) ref 36, (d) ref 37, and (e) ref 38.

samples from bovine and human enamel. The reason is the very high density of the sintered HAP samples which contain no organic matrix between the grains.

3.3. Outlook. To illustrate the potential for the utility of such HAP samples, the adsorption of bovine serum albumin (BSA) proteins is demonstrated on the surface of a PLS prepared HAP sample in Figure 9. Despite the small size of the
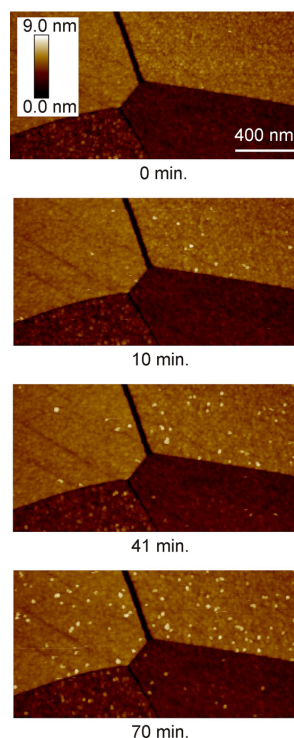
Figure 9. Different states of BSA protein adsorption on the surface of a PLS prepared HAP sample.

proteins in the range of 200−300 nm^3, individual specimens (white spots) can be detected due to the low surface roughness of the particular HAP grains. It is also obvious that the time dependence of protein adsorption is different on each grain giving evidence that the adsorption rate probably depends either on the texture of an individual grain or on its roughness. Since crystallographic orientation and residual roughness are, however, correlated according to the AFM data in Figure 4, it is not possible at this state to reveal the real origin of varying protein adsorption rates. Such issues will be discussed in detail in our future works. Furthermore, we will adopt the hydroxyapatite samples to investigate salivary protein adsorption under *in vivo* conditions in the oral cavity, thereby focusing on the effect of pure hydroxyapatite and excluding any influence of the individual enamel's properties on the adsorption process.

4. CONCLUSIONS

We presented two types of sintering techniques for the synthesis of HAP samples. Both procedures provide HAP samples with very similar properties in terms of surface

roughness, chemical composition, crystal structure, density, and microhardness. The most prominent difference (at least for the preparation parameters used here) concerns the average grain size. The FAST synthesis provides samples with the smallest average grain size and the smallest distribution in grain size; i.e., it results in the most homogeneous samples. For the PLS technique, the average grain area is nearly 4 times larger. At first sight, the less complex PLS technique seems therefore the preferred method. However, PLS samples are more brittle. This issue was not studied quantitatively, but our experience shows that this drawback holds only in case that large shear forces are applied, as e.g. during machine polishing. In usual sample handling, such as sample transfer or sample mounting, it plays a minor role.

On a macroscopic scale, i.e., for areas extending several tens or hundreds of μm^2, the surface roughness of both kinds of sintered HAP samples cannot compete with the roughness of current model systems such as silicon wafers. When restricting the areas to the range of a few μm^2, however, the roughness of individual grains is in the sub-nanometer range. Therefore, on this μm^2 scale, the sintered HAP samples can take the role of a new real-life model system, especially in such cases where the interaction between solids and very small bioparticles, such as proteins, are of particular interest.

■ ASSOCIATED CONTENT

ⓢ Supporting Information

The Supporting Information is available free of charge on the ACS Publications website at DOI: 10.1021/acsami.6b10089.

Figures S1 and S2; Table S1 (PDF)

■ AUTHOR INFORMATION

Corresponding Authors
*E-mail: f.mueller@mx.uni-saarland.de (F.M.).
*E-mail: k.jacobs@physik.uni-saarland.de (K.J.).

Author Contributions
C.Z. and T.F. contributed equally to this work.

Notes
The authors declare no competing financial interest.

■ ACKNOWLEDGMENTS

■ REFERENCES

(1) Kasemo, B. Biological surface science. *Surf. Sci.* **2002**, *500*, 656−677.

(2) Dufrene, Y. F. Using nanotechniques to explore microbial surfaces. *Nat. Rev. Microbiol.* **2004**, *2*, 451−460.

(3) Wilson, C. J.; Clegg, R. E.; Leavesley, D. I.; Pearcy, M. J. Mediation of biomaterial-cell interactions by adsorbed proteins: A review. *Tissue Eng.* **2005**, *11*, 1−18.

(4) Norde, W. Adsorption of proteins from solution at the solid-liquid interface. *Adv. Colloid Interface Sci.* **1986**, *25*, 267−340.

(5) Schmitt, Y.; Hähl, H.; Gilow, C.; Mantz, H.; Jacobs, K.; Leidinger, O.; Bellion, M.; Santen, L. Structural evolution of protein-biofilms: Simulations and experiments. *Biomicrofluidics* **2010**, *4*, 032201.

(6) Loskill, P.; Hähl, H.; Thewes, N.; Kreis, C. T.; Bischoff, M.; Herrmann, M.; Jacobs, K. Influence of the subsurface composition of a material on the adhesion of staphylococci. *Langmuir* **2012**, *28*, 7242−7248.

(7) Loskill, P.; Zeitz, C.; Grandthyll, S.; Thewes, N.; Müller, F.; Bischoff, M.; Herrmann, M.; Jacobs, K. Reduced adhesion of oral bacteria on hydroxyapatite by fluoride treatment. *Langmuir* **2013**, *29*, 5528−5533.

(8) Beaussart, A.; El-Kirat-Chatel, S.; Herman, P.; Alsteens, D.; Mahillon, J.; Hols, P.; Dufrêne, Y. F. Single-Cell Force Spectroscopy of Probiotic Bacteria. *Biophys. J.* **2013**, *104*, 1886−1892.

(9) Van der Mei, H. C.; Rustema-Abbing, M.; de Vries, J.; Busscher, H. J. Bond Strengthening in Oral Bacterial Adhesion to Salivary Conditioning Films. *Appl. Environ. Microbiol.* **2008**, *74*, 5511−5515.

(10) Rabe, M.; Verdes, D.; Seeger, S. Understanding protein adsorption phenomena at solid surfaces. *Adv. Colloid Interface Sci.* **2011**, *162*, 87−106.

(11) Hähl, H.; Evers, F.; Grandthyll, S.; Paulus, M.; Sternemann, C.; Loskill, P.; Lessel, M.; Huesecken, A.; Brenner, T.; Tolan, M.; Jacobs, K. Subsurface Influence on the Structure of Protein Adsorbates as Revealed by in Situ X-ray Reflectivity. *Langmuir* **2012**, *28*, 7747−7756.

(12) Müller, F.; Zeitz, C.; Mantz, H.; Ehses, K.-H.; Soldera, F.; Schmauch, J.; Hannig, M.; Hüfner, S.; Jacobs, K. Elemental Depth Profiling of Fluoridated Hydroxyapatite: Saving Your Dentition by the Skin of Your Teeth? *Langmuir* **2010**, *26*, 18750−18759.

(13) Lee, H.; Scherer, N. F.; Messersmith, P. B. Single-molecule Mechanics of Mussel Adhesion. *Proc. Natl. Acad. Sci. U. S. A.* **2006**, *103*, 12999−13003.

(14) Schroeder, H. E. *Orale Strukturbiologie: Entwicklungsgeschichte, Struktur und Funktion normaler Hart- und Weichgewebe der Mundhöhle und des Kiefergelenks*, 5th ed.; Thieme Georg Verlag: Stuttgart, 2000.

(15) Hannig, M.; Hannig, C. Nanomaterials in preventive dentistry. *Nat. Nanotechnol.* **2010**, *5*, 565−568.

(16) Weatherell, J.; Robinson, C.; Hallsworth, A. Variations in the Chemical Composition of Human Enamel. *J. Dent. Res.* **1974**, *53*, 180−192.

(17) Barros, J.; Grenho, L.; Manuel, C. M.; Ferreira, C.; Melo, L.; Nunes, O. C.; Monteiro, F. J.; Ferraz, M. P. Influence of Nanohydroxyapatite surface properties on *Staphylococcus Epidermis* Biofilm Formation. *J. Biomater. Appl.* **2014**, *28*, 1325−1335.

(18) Barros, J.; Grenho, L.; Fernandes, M. H.; Manuel, C. M.; Melo, L. F.; Nunes, O. C.; Monteiro, F. J.; Ferraz, M. P. Anti-sessile Bacterial and Cytocompatibility Properties of CHX-loaded Nanohydroxyapatite. *Colloids Surf., B* **2015**, *130*, 305−314.

(19) Prokopiev, O.; Sevostianov, I.; Genin, J.; McGee, S. M.; Woodward, C. Microstructure and elastic properties of sintered hydroxyapatite. *Int. J. Fract.* **2004**, *130*, L183−L190.

(20) Ramesh, S.; Aw, K. L.; Tolouei, R.; Amiriyan, M.; Tan, C. Y.; Hamdi, M.; Purbolaksono, J.; Hassan, M. A.; Teng, W. D. Sintering properties of hydroxyapatite powders prepared using different methods. *Ceram. Int.* **2013**, *39*, 111−119.

(21) Yeh, J. J.; Lindau, I. Atomic subshell photoionization cross sections and asymmetry parameters: 1 ≤ Z ≤ 103. *At. Data Nucl. Data Tables* **1985**, *32*, 1−155.

(22) Shirley, D. High-Resolution X-Ray Photoemission Spectrum of the Valence Bands of Gold. *Phys. Rev. B* **1972**, *5*, 4709−4714.

(23) Nishikawa, S.; Kikuchi, S. Diffraction of Cathode Rays by Mica. *Nature* **1928**, *121*, 1019−1020.

(24) Sternitzke, V.; Kaegi, R.; Audinot, J.-N.; Lewin, E.; Hering, J. G.; Johnson, C. A. Uptake of Fluoride from Aqueous Solution on Nano-

Sized Hydroxyapatite: Examination of a Fluoridated Surface Layer. *Environ. Sci. Technol.* **2012**, *46*, 802−809.

(25) Sternitzke, V.; Janousch, M.; Heeb, M. B.; Hering, J. G.; Johnson, C. A. Strontium hydroxyapatite and strontium carbonate as templates for the precipitation of calcium-phosphates in the absence and presence of fluoride. *J. Cryst. Growth* **2014**, *396*, 71−78.

(26) Gerth, H. U. V.; Dammaschke, T.; Schäfer, E.; Züchner, H. A three layer structure model of fluoridated enamel containig CaF2, Ca(OH)2 and FAp. *Dent. Mater.* **2008**, *23*, 1521−1528.

(27) Reyes-Gasga, J.; Martínez-Pinero, E. L.; Brès, É.F. Crystallographic structure of human tooth enamel by electron microscopy and X-ray diffraction: hexagonal or monoclinic. *J. Microsc.* **2012**, *248*, 102−109.

(28) Natter, H.; Schmelzer, M.; Löffler, M.-S.; Krill, C. E.; Fitch, A.; Hempelmann, R. Grain-Growth Kinetics of Nanocrystalline Iron Studied in Situ by Synchrotron Real-Time X-ray Diffraction. *J. Phys. Chem. B* **2000**, *104*, 2467−2476.

(29) Natter, H.; Hempelmann, R. Nanocrystalline copper by pulsed electrodeposition: The effects of organic additives, bath temperature, and pH. *J. Phys. Chem.* **1996**, *100*, 19525−19532.

(30) Krill, C. E.; Helfen, L.; Michels, D.; Natter, H.; Fitch, A.; Masson, O.; Birringer, R. Size-dependent grain-growth kinetics observed in nanocrystalline Fe. *Phys. Rev. Lett.* **2001**, *86*, 842−845.

(31) Kril, C. E.; Birringer, R. Estimating grain-size distributions in nanocrystalline materials from X-ray diffraction profile analysis. *Philos. Mag. A* **1998**, *77*, 621−640.

(32) Sato, K.; Shikida, M.; Yamashiro, T.; Tsunekawa, M.; Ito, S. Roughening of Single-Crystal Silicon Surface Etchedby KOH Water Solution. *Sens. Actuators, A* **1999**, *73*, 122−130.

(33) Scherrer, P. Bestimmung der Größe und der inneren Struktur von Kolloidteilchen mittels Röntgenstrahlung. *Göttinger Nachrichten* **1918**, *2*, 98−100.

(34) Williamson, G. K.; Hall, W. H. X-Ray Line Broadening from Filed Aluminium and Wolfram. *Acta Metall.* **1953**, *1*, 22−31.

(35) Mundra, S.; Mohan, V.; Gwyer, J.; Young, N.; Franklin, S. E.; Gerhardt, L.-C. Hardness, friction and wear studies on hydrogen peroxide treated bovine teeth. *Tribol. Int.* **2015**, *89*, 109−118.

(36) Aydin, B.; Pamir, T.; Baltaci, A.; Orman, M. N.; Turk, T. Effect of storage solutions on microhardness of crown enamel and dentin. *Eur. J. Dent.* **2015**, *9*, 262−266.

(37) Chuenarrom, C.; Benjakul, P.; Daosodsai, P. Effect of indentation load and time on Knoop and Vickers microhardness tests for enamel and dentin. *Mater. Res.* **2009**, *12*, 473−476.

(38) Akal, N.; Over, H.; Olmez, A.; Bodur, H. Effects of carbamide peroxide containing bleaching agents on the morphology and subsurface hardness of enamel. *J. Clin. Pediadr. Dent.* **2001**, *25*, 293−296.

Addendum VIII – Enhanced Adhesion of *S. mutans* to Hydroxyapatite After Exposure to Saliva

Authors: C. Spengler[1], N. Thewes[1], F. Nolle[1], T. Faidt[1], N. Umanskaya[2], M. Hannig[2], M. Bischoff[3] and K. Jacobs[1]

[1] Department of Experimental Physics, Saarland University, 66041 Saarbrücken, Germany.
[2] Clinic of Operative Dentistry, Periodontology and Preventive Dentistry, Saarland University, Homburg, Germany
[3] Institute of Medical Microbiology and Hygiene, Saarland University, Homburg, Germany.

Author contributions:
*Experiments were designed by **C. Spengler**, N. Thewes, T. Faidt and N. Umanskaya. Experimental results were achieved by **C. Spengler** and F. Nolle. The article was written by **C. Spengler**, N. Thewes, M. Bischoff and K. Jacobs. Scientific work was directed by M. Hannig, M. Bischoff and K. Jacobs.*

Abstract - *Streptococcus mutans* cells form robust biofilms on human teeth and are strongly related to caries incidents. Hence, understanding the adhesion of *S. mutans* in the human oral cavity is of major interest for preventive dentistry. In this study, we report on AFM-based single cell force spectroscopy measurements of *S. mutans* cells to hydroxyapatite surfaces. We observe for almost all measurements a significant difference in adhesion strength for *S. mutans* as well as for *S. carnosus* cells. However, the increase in adhesion strength after saliva exposure is much higher for *S. mutans* cells compared to *S. carnosus* cells. Our results demonstrate that *S. mutans* cells are welladapted to their natural environment, the oral cavity. This ability promotes the biofilm-forming capability of that species and hence the production of caries-provoking acids. In consequence, understanding the fundamentals of this mechanism may pave a way towards more effective caries-reducing techniques.

WILEY | Journal of Molecular Recognition

SPECIAL ISSUE ARTICLE

Enhanced adhesion of *Streptococcus mutans* to hydroxyapatite after exposure to saliva[†]

Christian Spengler[1] | **Nicolas Thewes[1]** | **Friederike Nolle[1]** | **Thomas Faidt[1]** | **Natalia Umanskaya[2]** | **Matthias Hannig[2]** | **Markus Bischoff[3]** | **Karin Jacobs[1]**

[1]Experimental Physics, Saarland University, Saarbrücken, Saarland, Germany

[2]Clinic of Operative Dentistry, Periodontology and Preventive Dentistry, Saarland University, Homburg, Saarland, Germany

[3]Institute of Medical Microbiology and Hygiene, Saarland University, Homburg, Saarland, Germany

Correspondence
Karin Jacobs, Experimental Physics, Saarland University, Saarbrücken, Saarland, Germany.
Email: k.jacobs@physik.uni-saarland.de

Funding information
German Research Foundation (DFG), Grant/Award Number: SFB 1027

Abstract

Streptococcus mutans cells form robust biofilms on human teeth and are strongly related to caries incidents. Hence, understanding the adhesion of *S. mutans* in the human oral cavity is of major interest for preventive dentistry. In this study, we report on atomic force microscopy–based single-cell force spectroscopy measurements of *S. mutans* cells to hydroxyapatite surfaces. We observe for almost all measurements a significant difference in adhesion strength for *S. mutans* as well as for *Staphylococcus carnosus* cells. However, the increase in adhesion strength after saliva exposure is much higher for *S. mutans* cells compared to *S. carnosus* cells. Our results demonstrate that *S. mutans* cells are well adapted to their natural environment, the oral cavity. This ability promotes the biofilm-forming capability of that species and hence the production of caries-provoking acids. In consequence, understanding the fundamentals of this mechanism may pave a way towards more effective caries-reducing techniques.

KEYWORDS

hydroxyapatite, saliva, single-cell force spectroscopy, *Streptococcus mutans*

1 | INTRODUCTION

It is known for decades that *Streptococcus mutans* is very closely related to the development of caries and other diseases in the oral cavity.[1-3] Furthermore, it can also enter the bloodstream through wounds in the oral cavity and travel from there through the body and even reach the coronary artery, where it can cause severe cardiovascular diseases.[4] The main pathogenicity of this organism arises when the cell adheres to appropriate surfaces, since with this step, the formation of a biofilm is initiated.

The process of caries formation is thereby influenced by substratum (eg, enamel, fluoridated, or not) and saliva.[5-8] On exposure to saliva, a proteinaceous surface coating—called pellicle—is formed almost immediately on all solid substrates.[9] This conditioning layer changes the properties of the substrate. The nature of the chemical groups exposed at the surface mainly defines the adhesion forces.[8]

Most studies focus on the adhesion of oral bacteria to salivary agglutinin (SAG) that is adsorbed to the oral pellicle on tooth surfaces.[10-12]

Additionally, it has been shown that the characteristics of biofilm formation by *S. mutans* depend on many parameters like for example oxygen content or the presence of specific enzymes in the bacterial cell.[13,14] Next to other constituents, the salivary sucrose content increases adhesion to surfaces significantly and is also a key factor in the production of biofilms.[15] Furthermore, by using genetically modified *S. mutans* cells, the function of many proteins in adhesion processes and biofilm formation on SAG was identified.[10-12]

Atomic force microscopy (AFM)-based force spectroscopy offers a unique tool to quantitatively investigate crucial parameters of initial bacterial adhesion. By using this technique, cantilevers functionalized with specific proteins of the bacterial cell wall provide access to probe molecular interactions between these proteins and various substrate surfaces. For example, the binding between SAG and the P1 adhesin of *S. mutans*, which is crucial for adhesion, has been characterized and quantified.[16,17]

For this AFM-based force spectroscopy study, we prepared cantilevers with single, viable bacterial cells to probe the interaction of the entire bacterial cell with the substratum dependent on a pretreatment of the cell.[18] Thereby, substrate parameters are kept constant. For force spectroscopy, a controlled, low roughness of the substratum is a precondition, since on rough, natural teeth surfaces, the contact

---

area between bacterial cell and surface is unpredictable. Therefore, as a model tooth material with low roughness and still high biological relevance, we used pressed, sintered, and polished high-density pellets of hydroxyapatite (HAP), which is the mineral component of human tooth enamel.[8]

To highlight the adaption of *S. mutans* cells for the human oral cavity and salivary environments, we performed the exact same experiments with *Staphylococcus carnosus* cells. *Staphylococcus carnosus* is an apathogenic representative of the genus *Staphylococci* that is used in meat production and has no affinity for the oral cavity.[19-22]

2 | MATERIALS AND METHODS

2.1 | Bacteria

Streptococcus mutans strain ATCC 25175 was cultured from a deep-frozen stock solution on mitis salivarius agar selective for this species for 3 days.[23,24] For every experiment, 1 colony from these plates (not older than 2 wk) was transferred into 5 mL of sterile Todd Hewitt broth and cultured for 24 hours at 37°C under agitation (150 rpm). Afterwards, 40 μL of this solution were transferred into 4 mL of fresh Todd Hewitt broth and cultured for another 16 hours at 37°C and 150 rpm resulting in an optical density at 600 nm of 0.2 to 0.3. To remove extracellular material, we washed cell suspensions as follows: 1 mL of the culture was centrifuged for 3 minutes at 17 000 × g. Afterwards, the supernatant was replaced by fresh phosphate buffered saline (PBS) and vortexed for 10 seconds. Then, the procedure was repeated 2 more times and the final solution was stored at 4°C for not longer than 6 hours.

For comparison, we used the apathogenic, nonoral species *S. carnosus* strain TM300.[19-22] These cells were grown from a deep-frozen stock solution on a blood agar plate for 3 days, and a fresh plate was used not longer than 2 weeks. Before every experiment, 1 colony was suspended in 5 mL tryptonic soy broth and cultured overnight at 37°C and 150 rpm. From this solution, 40 μL were inoculated in 4 mL fresh tryptonic soy broth and grown for another 2.5 hours resulting in an optical density at 600 nm of 0.3 to 0.4. Then, 1 mL of this suspension was washed 3 times as described above and afterwards stored at 4°C for not longer than 6 hours.

2.2 | Surfaces

Hydroxyapatite pellets were produced by pressing and sintering of pure HAP powder (Sigma Aldrich, Steinheim, Germany) resulting in an overall density of more than 97% of the density of a single crystal, following a standard procedure published elsewhere.[25] To increase their smoothness, we treated pellets with abrasive paper and polishing solutions of decreasing particle size (final polishing step with a diamond suspension of 30 nm particle size). Subsequently, the samples were etched in an ultrasonic bath for 7 seconds in sodium acetate buffer (pH 4.5) to remove residues from the final polishing step. Finally, HAP pellets feature a root mean square roughness of around 1 nm or less, as determined by AFM.[25]

In preparation for every experiment, the HAP samples were cleaned for 5 minutes in an ultrasonic bath in an aqueous solution of 1% Mucasol (Merz Pharma, Frankfurt a. M., Germany). Afterwards, they were rinsed in an ultrasonic bath of pure deionized water (0.055 $\frac{\mu S}{cm}$, Thermo Fischer Scientific, Waltham, Massachusetts) for another 5 minutes and dried in a stream of pure nitrogen.

2.3 | Collecting of saliva

On overall 5 different days, about 5 mL each of saliva were collected from a volunteer with good oral health by chewing on parafilm (50% paraffin and 50% polyethylene), and spitting into a sterile test tube. The volunteer refrained from eating and drinking (except for water) for 1 hour after brushing the teeth with normal toothpaste. The saliva sample was collected 30 minutes after renewed tooth brushing without toothpaste. Afterwards, the saliva samples were filtered first through a 2 μm and then through a 0.45 μm filter. Subsequently, they were frozen to -20°C. After the collection of all 5 samples, they were thawed, mixed
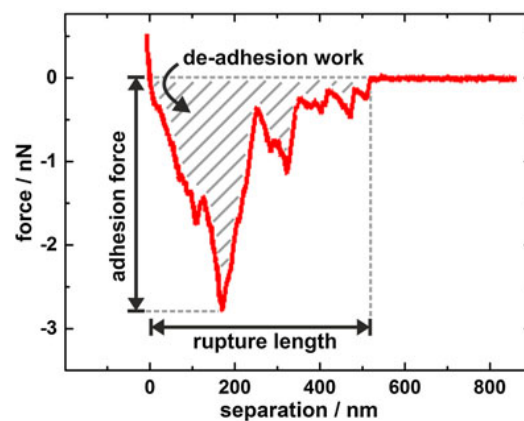
FIGURE 2 Retraction part of a typical force-distance curve, recorded with a single *Streptococcus mutans* cell on HAP, displaying the main experimental measures
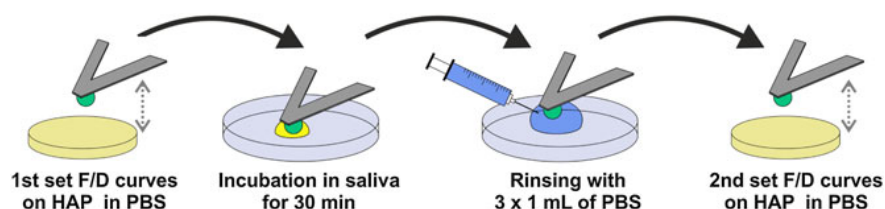
FIGURE 1 Scheme of the experimental procedure to expose a bacterial cell (green) to saliva

VIII. Addendum VIII – Enhanced Adhesion of S. mutans to Hydroxyapatite After Exposure to Saliva

together, and again frozen to -20°C. For every experiment, a fresh sample was thawed and "vortexed" for 30 seconds to ensure proper mixing of all saliva components.

2.4 | Force-distance measurements

Force-distance measurements were performed on a Bioscope Catalyst (Bruker-Nano, Santa Barbara, California) with single bacterial cells immobilized on soft cantilevers, prepared by a method published earlier.[18] We used tipless cantilevers (MLCT-0, Bruker) with a nominal spring constant of 0.03 $\frac{N}{m}$ and a deflection sensitivity of 25 $\frac{nm}{V}$. Cantilevers were calibrated before each set of experiments. The force trigger, which defines the maximum force with which the bacterial probe is pressed onto the substrate, was set to 300 pN, and the lateral distance between each single curve on the HAP surface was 1 μm. For the influence of the binding kinetics to be tested, the force trigger can be held constant for a certain time, called surface delay (SD) time.[26-28] We used SD of 0, 2, and 5 seconds. Thereby, 0 second stands for a very short contact time of some ms.[29] For every bacterial cell, first 3 sets of 40 force-distance curves (1 set for each SD time) were collected in PBS (pH 7.3) on a bare HAP surface. Next, the bacterial cell—still immobilized on the cantilever—was covered with 50 μL of filtered saliva for 30 minutes. Then, the cantilever was washed 3 times with 1 mL of pure PBS each to remove possible leftovers of the saliva solution. The thickness of the salivary layer remaining on the dopamin-coated cantilever can be estimated to be in the

range of some tens of nanometers at the maximum.[30] Since this is orders of magnitude smaller than the diameter of the bacterial cell, the cell itself serves as a spacer so that this salivary layer cannot make contact to the HAP surface in following force-distance measurements. Afterwards, the second 3 sets of force-distance curves were collected with the exact same parameters as before (see Figure 1). Subsequently, the measured force-distance curves were quantified for adhesion force (minimal force during retraction), rupture length (distance between cell and HAP surface at which the last connection breaks), and de-adhesion work (area under the retraction curve), as shown[26] in Figure 2.

Altogether, 10 individual *S. mutans* cells and 5 individual *S. carnosus* cells were tested, and with 1 and the same bacterial cell, in sum 240 force-distance curves on the HAP surface were taken (120 before and 120 after saliva exposure). A possible deterioration due to the measurement can be excluded, since with increasing number of scans, no systematic change in the force curves (eg, a decreasing adhesion) can be observed. This is in accordance with earlier studies.[26]

2.5 | Statistical analysis

Statistical analysis of all data distributions before and after saliva exposure was performed using a Mann-Whitney-U test of the software Matlab (MathWorks, Natick, Massachusetts). Significance levels are indicated in the graphs by asterisks denoting the following levels of significance: $*: p < .05$, $**: p < .01$, and $***: p < .001$.
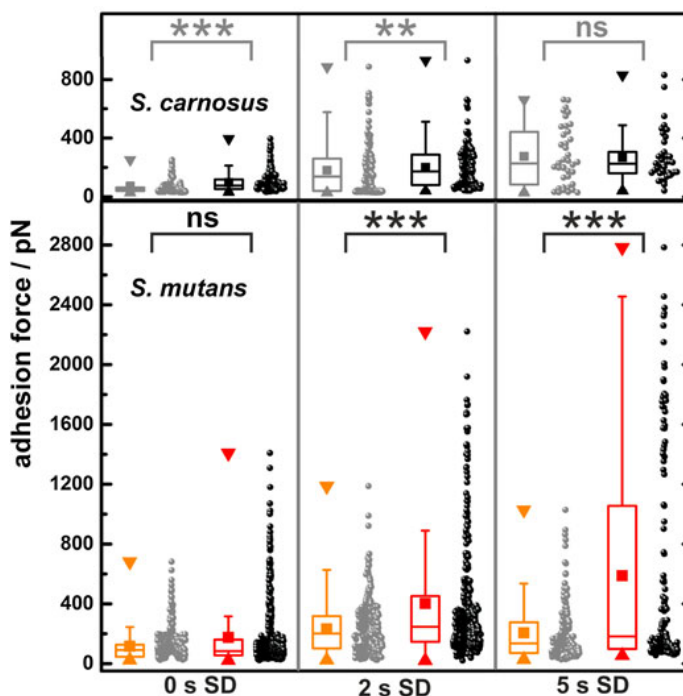
FIGURE 3 Adhesion forces of *Streptococcus mutans* (lower panel) and *Staphylococcus carnosus* cells (upper panel) to hydroxyapatite pellets before (light color) and after (dark color) saliva exposure for different surface delay (SD) times. For details of the box-and-whisker representation, see text

3 | RESULTS

Figure 3 depicts adhesion forces of 10 individual *S. mutans* and 5 individual *S. carnosus* cells before and after exposure to saliva. Three different SD times have been tested to study the influence of contact time to adhesion strength. Overall, the adhesion forces cover a range of 0 to 2800 pN for *S. mutans* cells and only 0 to 950 pN for *S. carnosus* cells. Within the same surface delay panel of Figure 3, *S. mutans* cells develop stronger adhesion forces after saliva exposure for SD times from 2 seconds onwards. Comparatively, *S. carnosus* cells exhibit much smaller differences in adhesion force before and after exposure. For this trend to be displayed, the results in Figure 3 are shown as box-and-whisker plots, where the median is marked by the horizontal line in the box and the whiskers are defined as 1.5 times the extent of the interquartile range (IQR).[31] These measures quantify what is already visible by the eye: For both bacterial species, for $SD > 0$ seconds, larger adhesion forces (median as well as average) are recorded, but the median is not significantly affected by saliva treatment. For *S. mutans* cells, however, mean adhesion force, IQR as well as the whiskers gain clearly in size by saliva exposure. In some force-distance measurements, the treatment causes an especially enforced adhesion.

Similarly, as displayed in Figure 4, the rupture lengths of *S. mutans* cells are especially increased after inoculation: No matter of the applied SD time, mean values of the rupture length increase by almost an order of magnitude after treatment. Before, rupture lengths are in the range of some tens of nanometers, whereas after the saliva treatment, they

increase up to several hundreds of nanometers with a mean value of around 200 nm and maxima up to 1200 nm. For *S. carnosus* cells, rupture lengths on the HAP surface are in general smaller than for *S. mutans* cells and the relative increase after saliva treatment is much smaller, only about a factor of 2.

An even stronger effect of saliva treatment can be observed by examining the work that is necessary to remove the entire bacterial cell from the surface (see Figure 5). For *S. mutans* cells, the mean value (as well as the IQR and the whiskers) is strongly increased: From a mean value of around 10 000 $k_B T$ at 0-second SD to a mean value of roughly 30 000 $k_B T$ at 5-second SD. Remarkably, at closer inspection, data points seem to develop a bimodal distribution at long SD times. Thereby, the median of the de-adhesion work stays almost unchanged.

To highlight this trend, Figure 6 shows histograms of the de-adhesion work of *S. mutans* and *S. carnosus* cells on HAP after the exposure to saliva for different SD times. With increasing surface delay, a second regime of large values of de-adhesion work occurs for *S. mutans* cells. Simultaneously, the portion of force-distance curves with a de-adhesion work below 20 000 $k_B T$ decreases with increasing SD time. For SD = 5 seconds, the mean value of the second regime in the histogram is located at values of the de-adhesion work of around 110 000 $k_B T$. It is interesting to note that for *S. mutans*, the different adhesion strengths become directly apparent in the way the shape of the force-distance curves changes with increasing SD times (8 curves are exemplarily shown as inset to Figure 6): All curves display local minima, and the deepest is taken as a measure for the adhesion force. However, for a SD of 5 seconds, the deepest minimum in the retraction
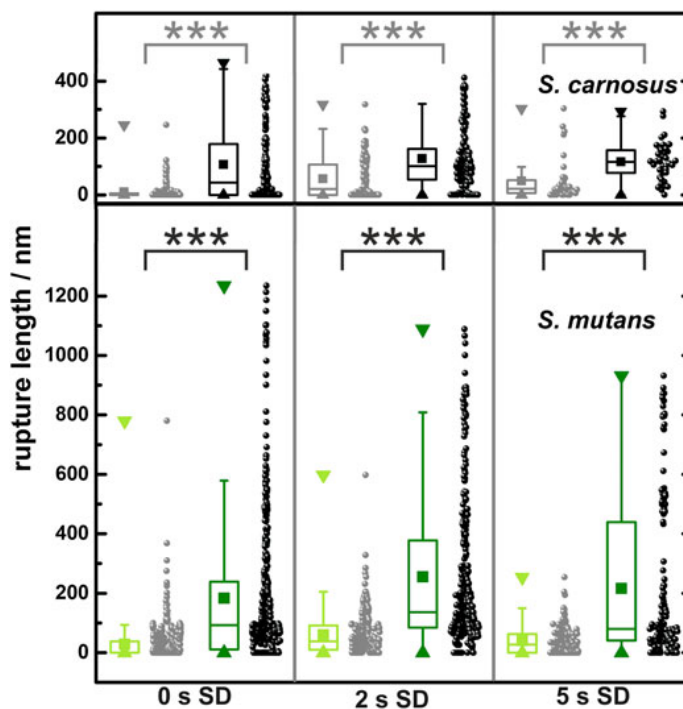
FIGURE 4 Rupture lengths for *Streptococcus mutans* (lower panel) and *Staphylococcus carnosus* cells (upper panel) removed from hydroxyapatite pellets before (light color) and after (dark color) saliva exposure for different surface delay (SD) times. For details of the box-and-whisker representation, see text

VIII. Addendum VIII — Enhanced Adhesion of *S. mutans* to Hydroxyapatite After Exposure to Saliva
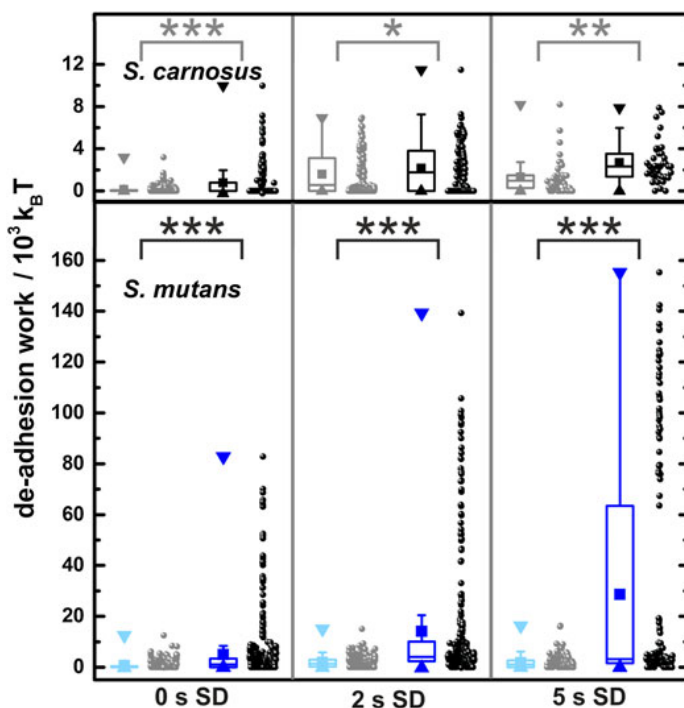
FIGURE 5 De-adhesion work of *Streptococcus mutans* (lower panel) and *Staphylococcus carnosus* cells (upper panel) on hydroxyapatite pellets before (light color) and after (dark color) saliva exposure for different surface delay (SD) times. For details of the box-and-whisker representation, see text. Note the 4-fold stretched energy scale in the upper panel
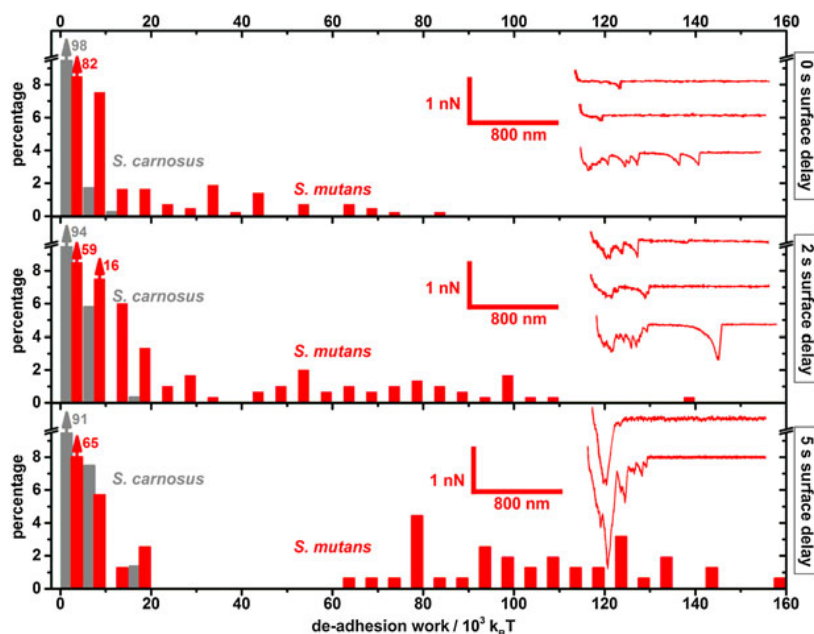
FIGURE 6 De-adhesion work histograms of *Streptococcus mutans* (red) and *Staphylococcus carnosus* cells (gray) for different surface delay times after saliva exposure. As insets, exemplary force-distance curves of *S. mutans* cells are shown. Note, that all distributions are significantly different from each other with a significance level $p < .001$

216

curve is much deeper than following local minima, whereas for curves with smaller SD times, all occurring local minima are in the same range of forces.

For *S. carnosus* cells, the scenario is completely different (see gray bars in Figure 6): The de-adhesion work is more than 1 order of magnitude smaller than for *S. mutans* cells. Also, for all SD times, the histogram of the de-adhesion work features only 1 regime and this is located at quite low values of around $10\,000\,k_B T$.

4 | DISCUSSION

Bacterial cells in the human mouth always run the risk of getting washed out, ie, of getting swallowed. Therefore, the evolutionary success of mouth colonizing cells relies first of all on their ability to adhere in the oral environment. Here, we investigated the adhesion strength of cells of the mouth colonizing species *S. mutans* to HAP pellets before and after exposure of the cells to human saliva using AFM-based single-cell force spectroscopy. Our results demonstrate that the strength of adhesion between *S. mutans* cells and HAP increases significantly and strongly after exposure of the cells to saliva. In contrast, treating *S. carnosus* cells (whose natural habitat is not the human mouth) in saliva increases the cells' adhesive strength to HAP pellets only slightly. Hence, *S. mutans* cells exhibit a specific mechanism that enhances their adhesion in the human oral environment. This mechanism may be a result of the evolutionary adaption of this bacterial species to its natural habitat, the human oral cavity. Moreover, our study demonstrates that for a firm adhesion of *S. mutans* cells to HAP surfaces, it is not necessary that SAG is present on the substratum, rather, even the exposure of the bacterial cell to a salivary environment is sufficient.

Open questions are why adhesion is enhanced by saliva inoculation and why *S. mutans* cells are especially responsive to the treatment. This study focusses on the former. The observation can be explained by the common notion how bacterial adhesion proceeds: The adhesion process relies on the consecutive binding of bacterial cell wall macromolecules to a substratum.[32,33] The binding strength of a single contact point cannot be altered by a saliva treatment of the bacterial cell. Therefore, saliva treatment must increase the number of contact points, for instance, by a larger number of macromolecules that tether to the surface. Two ways are possible to accomplish the latter: either certain salivary components link to the bacterial cell wall via *S. mutans*-specific surface molecules (or domains) or *S. mutans* produces additional cell wall macromolecules when exposed to its natural salivary environment.

We can name some properties of this additional macromolecules, using results of this study: In force-distance curves, the adhesion force value is defined as the minimum force during retraction. The distance at which this point appears is related to the mechanical properties—in particular the length—of the contact forming macromolecules. In our measurements, the minimal force is usually located at separating distances of less than 200 nm (see insets in Figure 6). Hence, adhesion forces are dominated by molecules with an untensioned length of less than 200 nm that tether to the surface. These forces, however, are only slightly influenced by the saliva treatment. In contrast, the rupture lengths feature a strong increase after saliva inoculation. This implies

that the additional macromolecules that contribute to the adhesion after saliva treatment are longer than the surface macromolecules responsible for adhesion before saliva treatment. The effect of saliva treatment has the strongest impact on the de-adhesion work. This is likely the result of the combination of 2 effects, the slight increase in adhesion forces as well as the significantly larger rupture lengths.

The adhesion strength moreover increases with SD time. This trend can be observed for many different bacterial force-distance curves.[26] After saliva treatment, longer SD times can additionally amplify the increase in adhesion force because additional macromolecules have more time to find a suitable position to tether to the HAP surface. This means that for a longer SD time, more new macromolecules find such a binding site and therefore, the increase in adhesion force due to the salivary treatment even grows with longer SD times. In contrast, SD times do not cause longer rupture lengths, because in this case, it is sufficient that few (or in the extreme case only a single) additional, long macromolecules tether to the surface. For an adequately high number of additional, long macromolecules, already the initial contact between bacterial cell and surface leads to such a binding event and hence, an additional contact time does not have an influence.

It is also possible that for longer SD times not only more bonds originate but also existing bonds develop a stronger binding to the surface. This phenomenon, called bond strengthening, has been measured for *Streptococci* as well as for *Staphylococci*.[34,35] However, in the present study, this effect cannot be the primary reason for enhanced adhesion because bond strengthening usually appears when specific interactions between binding molecules of the cell and molecules on the surface are involved. In our case, although, the substratum is a bare, smooth HAP surface, where no specific binding is expected. Furthermore, bond strengthening is usually observed for contact times notably longer than the 5 seconds of this study. Yet, it was not possible with the present setup to apply longer SD times while keeping the force trigger constant. It shall be probed in the future if for much longer SD times, most data will fall into the second regime of the de-adhesion work histogram.

5 | CONCLUSIONS

In this study, we have analyzed the adhesion properties of *S. mutans* cells to HAP surfaces. To monitor the adhesion process, AFM-based single-cell force spectroscopy was used on ultra smooth, high-density HAP pellets. It has been shown that adhesion force, rupture length, and de-adhesion work increase significantly when the cell has been inoculated in human saliva compared to adhesion without salivary treatment. Thereby, rupture length and de-adhesion work are notably enlarged, which leads to the interpretation that especially long macromolecules contribute to this. These macromolecules either stem from the saliva or are produced by *S. mutans* cells, stimulated by the contact to saliva. By comparing identical measurements of *S. mutans* and *S. carnosus* cells, it has been shown that the adaption to a salivary environment is a particular property of *S. mutans* cells and is far less pronounced for *S. carnosus* cells. Future studies may now further analyze saliva properties and identify salivary components that are responsible for this enhanced adhesion. That way, new pathways may open up in caries prevention by applying saliva-influencing agents after tooth brushing.

VIII. Addendum VIII – Enhanced Adhesion of S. mutans to Hydroxyapatite After Exposure to Saliva

REFERENCES

1. Hamada S, Slade HD. Biology, immunology, and cariogenicity of Streptococcus mutans. *Microbiol Rev*. 1980;44(2):331–384.

2. Loesche WJ. Role of Streptococcus mutans in human dental decay. *Microbiol Rev*. 1986;50(4):353–380.

3. Mitchell TJ. The pathogenesis of Streptococcal infections: from tooth decay to meningitis. *Nature Rev Microbiol*. 2003;1:219–230.

4. Abranches J, Zeng L, Bélanger M, et al. Invasion of human coronary artery endothelial cells by Streptococcus mutans OMZ175. *Oral Microbiol Immunol*. 2009;24:141–145.

5. Selwitz RH, Ismail AI, Pitts NB. Dental caries. *Lancet*. 2007;369:51–59.

6. Takahashi N, Nyvad B. Caries ecology revisited: microbial dynamics and the caries process. *Caries Res*. 2008;42(6):409–418. https://doi.org/10.1159/000159604.

7. Filoche S, Wong L, Sissons CH. Oral biofilms: Emerging concepts in microbial ecology. *J Dent Res*. 2010;89(1):8–18. https://doi.org/10.1177/0022034509351812.

8. Loskill P, Zeitz C, Grandthyll S, et al. Reduced adhesion of oral bacteria on hydroxyapatite by fluoride treatment. *Langmuir*. 2013;29(18):5528–5533. https://doi.org/10.1021/la4008558.

9. Hannig C, Hannig M. The oral cavity - a key system to understand substratum-dependent bioadhesion on solid surfaces in man. *Clin Oral Investig*. 2009;13(2):123–139. https://doi.org/10.1007/s00784-008-0243-3.

10. Ray CA, Gfell LE, Buller TL, Gregory RL. Interactions of streptococcus mutans fimbria-associated surface proteins with salivary components. *Clin Diagn Lab Immunol*. 1999;6(3):400–404.

11. Yoshida A, Ansai T, Takehara T, Kuramitsu HK. LuxS-based signaling affects streptococcus mutans biofilm formation. *Appl Environ Microbiol*. 2005;71(5):2372–2380.

12. Miller JH, Avilés-Reyes A, Scott-Anne K, et al. The collagen binding protein cnm contributes to oral colonization and cariogenicity of Streptococcus mutans OMZ175. *Infect Immun*. 2015;83(5):2001–2010. https://doi.org/10.1128/IAI.03022-14.

13. Ahn S-J, Burne RA. Effects of oxygen on biofilm formation and the AtlA autolysin of Streptococcus mutans. *J Bacteriol*. 2007;189:6293–6032. doi:10.1128/JB.00546-07.

14. Ahn S-J, Ahn S-J, Wen ZT, Brady LJ, Burne RA. Characteristics of biofilm formation by Streptococcus mutans in the presence of saliva. *Infect Immun*. 2008;76(9):4259–4268.

15. Costa EM, Silva S, Tavaria FK, Pintado MM. Study of the effects of chitosan upon Streptococcus mutans adherence and biofilm formation. *Anaerobe*. 2013;20:27–30. https://doi.org/10.1016/j.anaerobe.2013.02.002.

16. Brady LJ, Piacentini DA, Crowley PJ, Oyston PCF, Bleiweis AS. Differentiation of salivary agglutinin-mediated adherence and aggregation of mutans streptococci by use of monoclonal antibodies against the major surface adhesin P1. *Infect Immun*. 1992;60(3):1008–1017.

17. Sullan RMA, Li JK, Crowley PJ, Brady LJ, Dufrêne YF. Binding forces of Streptococcus mutans P1 adhesin. 2015;9(2):1448–1460. https://doi.org/10.1021/nn5058886.

18. Thewes N, Loskill P, Spengler C, Hümbert S, Bischoff M, Jacobs K. A detailed guideline for the fabrication of single bacterial probes used for atomic force spectroscopy. *Eur Phys J E Soft Matter*. 2015;38(12):140. https://doi.org/10.1140/epje/i2015-15140.

19. Schleifer KH, Fischer U. Description of a new species of the genus Staphylococcus: Staphylococcus carnosus. *Int J Syst*. 1982;32(2):153–156.

20. Barriere C, Leroy-Sétrin S, Talon R. Characterization of catalase and superoxide dismutase in Staphylococcus carnosus 833 strain. *J Appl Microbiol*. 2001;91:514–516.

21. Rosenstein R, Nerz C, Biswas L, Resch A. Genome analysis of the meat starter culture bacterium Staphylococcus carnosus TM300. *Appl Environ Microbiol*. 2009;75(3):811–822. https://doi.org/10.1128/AEM.01982-08.

22. Rosenstein R, Götz F. Genomic differences between the food-grade Staphylococcus carnosus and pathogenic Staphylococcal species. *Int J Med Microbiol*. 2010;300:104–108. https://doi.org/10.1016/j.ijmm.2009.08.014.

23. Gold OG, Jordan HV, Van Houte J. A selective medium for Streptococcus mutans. *J Microbiol Methods*. 1973;18:1357–1364.

24. Coykendall AL. Proposal to elevate the subspecies of Streptococcus mutans to species status, based on their molecular composition. *Int J Syst Bacteriol*. 1977;27(1):26–30.

25. Zeitz C, Faidt T, Grandthyll S, et al. Synthesis of hydroxyapatite substrates: bridging the gap between model surfaces and enamel. *Appl Mater Inter*. 2016;8(39):25848–25855. https://doi.org/10.1021/acsami.6b10089.

26. Thewes N, Loskill P, Jung P, et al. Hydrophobic interaction governs unspecific adhesion of Staphylococci: a single cell force spectroscopy study. *Beilstein J Nanotechnol*. 2014;5:1501–1512. https://doi.org/10.3762/bjnano.5.163.

27. Zeng G, Müller T, Meyer RL. Single-cell force spectroscopy of bacteria enabled by naturally derived proteins. *Langmuir*. 2014;30(14):4019–4025. https://doi.org/10.1021/la404673q.

28. Herman-Bausier P, El-Kirat-Chatel S, Foster TJ, Geoghegan JA, Dufrêne YF. Staphylococcus aureus fibronectin-binding protein a mediates cell-cell adhesion through low-affinity homophilic bonds. *mBio*. 2015;6(3):e00413–15.

29. Beaussart A, El-Kirat-Chatel S, Herman P, et al. Single-cell force spectroscopy of probiotic bacteria. *Biophys J*. 2013;104:1886–1892.

30. Macakova L, Yakubov GE, Plunkett MA, Stokes JR. Influence of ionic strength changes on the structure of pre-adsorbed salivary films. A response of a natural multi-component layer. *Coll Surf B*. 2010;77(1):31–39.https://doi.org/10.1016/j.colsurfb.2009.12.022.

31. Mcgill R, Tukey JW, Larsen WA. Variations of box plots. *Am Stat*. 1978;32(1):12–16. https://doi.org/10.2307/2683468.

32. Thewes N, Thewes A, Loskill P, et al. Stochastic binding of Staphylococcus aureus to hydrophobic surfaces. *Soft Matter*. 2015;11(46):8913–9046. https://doi.org/10.1039/c5sm00963d.

33. Song L, Hou J, van der Mei HC, Veeregowda DH, Busscher HJ, Sjollema J. Antimicrobials influence bond stiffness and detachment of oral bacteria. *J Dent Res*. 2016;95(7):793–799. https://doi.org/10.1177/0022034516634631.

34. van der Mei HC, Rustema-Abbing M, de Vries J, Busscher HJ. Bond strengthening in oral bacterial adhesion to salivary conditioning films. *Appl Environ Microbiol*. 2008;74(17):5511–5515.

35. Boks NP, Busscher HJ, van der Mei HC, Norde W. Bond-strengthening in staphylococcal adhesion to hydrophilic and hydrophobic surfaces using atomic force microscopy. *Langmuir*. 2008;24(22):12990–12994.

How to cite this article: Spengler C, Thewes N, Nolle F, Faidt T, Umanskaya N, Hannig M, Bischoff M, Jacobs K. Enhanced adhesion of Streptococcus mutans to hydroxyapatite after exposure to saliva. *J Mol Recognit*. 2017;30:e2615. https://doi.org/10.1002/jmr.2615

Danksagung

Ich bedanke mich bei all den Menschen, die durch ihre fachliche und moralische Unterstützung diese Arbeit möglich gemacht haben.

In erster Linie gilt mein Dank Prof. Dr. Karin Jacobs für die Möglichkeit, in ihrer Gruppe zu promovieren. Sie hat mir sowohl Freiheiten gelassen, meine eigenen Ideen zu verwirklichen, als auch konkrete Projekte entwickelt und vorangetrieben. Deshalb empfand ich das Arbeiten immer als sehr angenehm und bin gerne zur Uni gekommen. Danke auch für die Möglichkeit, an diversen Konferenzen im In- und Ausland teilzunehmen.

Ebenfalls gilt mein Dank Prof. Dr. Markus Bischoff für die Zweitbegutachtung der Arbeit und viele wissenschaftliche Impulse aus „biologischer Sicht“.

Im Verlauf der Jahre hatte ich das Vergnügen mit zahlreichen Kollegen und Kolleginnen zusammenzuarbeiten, die allesamt zu einer produktiven und freundschaftlichen Atmosphäre innerhalb unserer Arbeitsgruppe beigetragen haben. Den folgenden Menschen sei namentlich gedankt: Dr. Peter Loskill, dem ich es wahrscheinlich zu verdanken habe, dass ich mich überhaupt mit der Physik biologischer Materie beschäftigt habe. Dr. Hendrik Hähl, dessen riesiger Wissensschatz mir vom ersten Semester bis zum Ende der Promotion stets ein Quell der Erkenntnis war. Dr. Samuel Grandthyll, der meist alles hat fallen und liegen lassen, um selbst bei den scheinbar unwichtigsten Problemen zu helfen. Dr. Jean-Baptiste Fleury der AG Seemann, der eigentlich für alle Probleme eine Lösung wusste, auch wenn dies nicht immer offensichtlich war. Dr. Philipp Jung, der wirklich immer zu erreichen war, wenn mir ’mal wieder biologische Sachverhalte unklar waren. Dr. Joshua D. McGraw und Thomas Faidt, den besten Banknachbarn, die ich mir vorstellen konnte – quasi wechselwirkungsfrei, wenn gearbeitet wurde, jedoch perfekte Interaktionspartner in der restlichen Zeit. Dr. Nicolas Thewes und Dr. Mischa Klos, meinen virtuellen Banknachbarn, zu denen mein Verhältnis mehr als kollegial war und ist. PD Dr. Frank Müller, für schnelle und gute Antworten zu allen wissenschaftlichen Fragestellungen und für unterhaltsame Alltagsgeschichten. Ganz besonders zu erwähnen sind an dieser Stelle Judith Rech und Monika Schuck für ihre Hilfe bei zahlreichen administrativen Problemen und der Weitergabe aktueller Gruppen-Neuigkeiten.

Mein Dank gebührt ebenso den vielen Bachelor-, Master- und Staatsexamens-Studenten und -Studentinnen, an deren Betreuung ich beteiligt sein durfte; insbesondere Friederike Nolle und Johannes Mischo, die mittlerweile zu einer lieben Kollegin und einem lieben Kollegen geworden sind. Außerdem gilt mein Dank den vielen Kooperationspartnern und -partnerinnen inner- und außerhalb der Uni Saarland.

Danke fürs Korrekturlesen an Max und Laura John.

Nicht zuletzt bedanke ich mich bei meiner Familie und meinen Freunden für die Unterstützung im und die Ablenkung vom Studium.